STUDY ON NATURAL DYE EXTRACT FROM *Melastoma malabathricum* AND NANOSTRUCTURED TiO_2 AS COMPONENTS IN DYE-SENSITIZED SOLAR CELLS

NORKASMANI BINTI AZIZ

FACULTY OF SCIENCE
UNIVERSITY OF MALAYA
KUALA LUMPUR

2019

STUDY ON NATURAL DYE EXTRACT FROM *Melastoma malabathricum* AND NANOSTRUCTURED TiO_2 AS COMPONENTS IN DYE-SENSITIZED SOLAR CELLS

NORKASMANI BINTI AZIZ

THESIS SUBMITTED IN FULFILMENT OF THE
REQUIREMENTS FOR THE DEGREE OF
DOCTOR OF PHILOSOPHY

DEPARTMENT OF PHYSICS
FACULTY OF SCIENCE
UNIVERSITY OF MALAYA
KUALA LUMPUR

2019

UNIVERSITI MALAYA
ORIGINAL LITERARY WORK DECLARATION

Name of Candidate: **NORKASMANI BINTI AZIZ**

Matric No: **SHC130104**

Name of Degree: **DOCTOR OF PHILOSOPHY (EXCEPT MATHEMATICS & SCIENCE PHILOSOPHY)**

Title of Thesis ("this Work"): **STUDY ON NATURAL DYE EXTRACT FROM *Melastoma malabathricum* AND NANOSTRUCTURED TiO_2 AS COMPONENTS IN DYE-SENSITIZED SOLAR CELLS**

Field of Study: **EXPERIMENTAL PHYSICS**

I do solemnly and sincerely declare that:

(1) I am the sole author/writer of this Work;
(2) This Work is original;
(3) Any use of any work in which copyright exists was done by way of fair dealing and for permitted purposes and any excerpt or extract from, or reference to or reproduction of any copyright work has been disclosed expressly and sufficiently and the title of the Work and its authorship have been acknowledged in this Work;
(4) I do not have any actual knowledge nor do I ought reasonably to know that the making of this work constitutes an infringement of any copyright work;
(5) I hereby assign all and every rights in the copyright to this Work to the University of Malaya ("UM"), who henceforth shall be owner of the copyright in this Work and that any reproduction or use in any form or by any means whatsoever is prohibited without the written consent of UM having been first had and obtained;
(6) I am fully aware that if in the course of making this Work I have infringed any copyright whether intentionally or otherwise, I may be subject to legal action or any other action as may be determined by UM.

Candidate"s Signature Date:

Subscribed and solemnly declared before,

Witness"s Signature Date:

Name:

Designation:

UNIVERSITI MALAYA

PERAKUAN KEASLIAN PENULISAN

Nama: **NORKASMANI BINTI AZIZ**

No. Matrik: **SHC130104**

Nama Ijazah: **DOKTOR FALSAFAH (KECUALI MATEMATIK& FALSAFAH SAINS)**

Tajuk Tesis ("Hasil Kerja ini"): **Kajian berkenaan ekstrak anthocyanin daripada *Melastoma Malabathricum* dan TiO_2 yang berstruktur nano sebagai kompenen dalam sel solar pemeka warna**

Bidang Penyelidikan: **EKSPERIMEN FIZIK**

Saya dengan sesungguhnya dan sebenarnya mengaku bahawa:

(1) Saya adalah satu-satunya pengarang/penulis Hasil Kerja ini;

(2) Hasil Kerja ini adalah asli;

(3) Apa-apa penggunaan mana-mana hasil kerja yang mengandungi hakcipta telah dilakukan secara urusan yang wajar dan bagi maksud yang dibenarkan dan apa-apa petikan, ekstrak, rujukan atau pengeluaran semula daripada atau kepada mana-mana hasil kerja yang mengandungi hakcipta telah dinyatakan dengan sejelasnya dan secukupnya dan satu pengiktirafan tajuk hasil kerja tersebut dan pengarang/penulisnya telah dilakukan di dalam Hasil Kerja ini;

(4) Saya tidak mempunyai apa-apa pengetahuan sebenar atau patut semunasabahnya tahu bahawa penghasilan Hasil Kerja ini melanggar suatu hakcipta hasil kerja yang lain;

(5) Saya dengan ini menyerahkan kesemua dan tiap-tiap hak yang terkandung di dalam hakcipta Hasil Kerja ini kepada Universiti Malaya ("UM") yang seterusnya mula dari sekarang adalah tuan punya kepada hakcipta di dalam Hasil Kerja ini dan apa-apa pengeluaran semula atau penggunaan dalam apa jua bentuk atau dengan apa juga cara sekalipun adalah dilarang tanpa terlebih dahulu mendapat kebenaran bertulis dari UM;

(6) Saya sedar sepenuhnya sekiranya dalam masa penghasilan Hasil Kerja ini saya telah melanggar suatu hakcipta hasil kerja yang lain sama ada dengan niat atau sebaliknya, saya boleh dikenakan tindakan undang-undang atau apa-apa tindakan lain sebagaimana yang diputuskan oleh UM.

Tandatangan Calon Tarikh:

Diperbuat dan sesungguhnya diakui di hadapan,

Tandatangan Saksi Tarikh:

Nama:

Jawatan:

STUDY ON NATURAL DYE EXTRACT FROM *Melastoma malabathricum* AND NANOSTRUCTURED TiO_2 AS COMPONENTS IN DYE-SENSITIZED SOLAR CELLS

ABSTRACT

Dye-sensitized solar cells (DSSCs) or Graetzel cells are third generation solar cells. A huge variety of dyes including natural dyes can be used as sensitizers to provide the charge carriers. In the present work, anthocyanin that contains delphidin-3-glucoside and delphidin-3,5-glucoside has been extracted from the fruit pulp of *Melastoma malabathricum.* This study investigates the parameters that affect anthocyanin extraction from *Melastoma malabathricum* using the response surface method (RSM). Acidified methanol has been used for the anthocyanin extraction temperature between 30 and 80 °C. The fruit pulps of *Melastoma malabathricum* have been soaked between 60 to 180 min in trifluoroacetic acidified methanol content between 0.5 to 3%. These compounds are extracted for use in dye sensitized solar cells. Dye-sensitized solar cells were fabricated by sandwiching the polyacrylonitrile-based polymer electrolytes between TiO_2/dye photoelectrode and platinum, Pt counter electrode, respectively. A simple technique was developed to fabricate a large-area TiO_2 electrode layer using electrospun for dye-sensitized solar cells (DSSCs) via electrospinning technique. The electropsun TiO_2 was further characterized in order to investigate the potential of these nanostructures to be used as component in DSSCs fabrications. The structures and properties of the electrospun solid and mesoporous TiO_2 have been characterized by FESEM and XRD. For the first DSSC systems which contain commercial P25 TiO_2, 5 wt.% of anthocyanin dyes (A3) exhibited the maximum efficiency of $(1.054 \pm 0.012)\%$. TiO_2 nanoparticle/electrospun composite electrodes have been designed to increase the efficiency of dye adsorption in DSSCs application. 10 wt.% NRs and 90 wt.% of NPs (B1) resulted in improved efficiency up to $(1.351\pm 0.013)\%$. The performance of NPs-NRs composite based DSSC was further improved by addition of sucrose and sucrose-

DCA additives. For DSSC (NP-NRs) composite systems, the use of sucrose-DCA successfully improved the performances of DSSCs based *Melastoma malabathricum* anthocyanin. The performance was improved by addition of 6 wt.% sucrose-DCA compared to sucrose without DCA additive, in which the J_{sc}, V_{oc}, FF, efficiency, R_s, R_{sh} and R_2 values were (6.360 ± 0.059) mA cm^{-2}, (0.473 ± 0.0.005) V, (0.656 ± 0.006), (1.974 ± 0.014) %, (0.013 ± 0.003) $\Omega\text{-cm}^2$, (2.918 ± 0.019) $\Omega\text{-cm}^2$ and (38.20 ± 0.17) Ω, respectively.

Keywords: Anthocyanin, Natural dye, *Melastoma malabathricum*, Tio_2, dye-sensitized solar cells (DSSCs), electrospinning.

KAJIAN BERKENAAN PEWARNA SEMULAJADI DARIPADA *Melastoma malabathricum* DAN TiO_2 YANG BERSTRUKTUR NANO SEBAGAI KOMPONEN DALAM SEL SOLAR PEMEKA WARNA

ABSTRAK

Sel solar pemeka warna (DSSCs) atau sel Graetzel adalah sel solar generasi ketiga. Pelbagai jenis pewarna termasuk pewarna semulajadi boleh digunakan sebagai pemeka warna untuk menyediakan pembawa caj. Dalam konteks ini, anthocyanin yang mengandungi delphidin-3-glukosid dan delphidin-3,5-glukosid telah diekstrak daripada pulpa buah *Melastoma malabathricum*. Kajian ini menyiasat berkenaan parameter yang mempengaruhi ekstrak antosianin daripada *Melastoma malabathricum* menggunakan kaedah permukaan tindak balas (RSM). Methanol berasid telah digunakan untuk pengekstrakan antosianin antara 30 dan 80 °C. Pulpa buah *Melastoma malabathricum* telah direndam selama 60 hingga 180 minit dalam methanol trifluoroacetic acid dari 0.5 hingga 3%. Sebatian ini diekstrak untuk digunakan dalam sel solar pemeka warna. Sel solar pemeka warna dipasang dengan mengapit elektrolit poliakrilonitril berasaskan TiO_2/photoelekrod dan platinum kaunter elektrod. Teknik yang mudah ini dibangunkan untuk membuat lapisan elektrod TiO_2 yang mempunyai permukaan luas menggunakan elektrospun untuk sel solar pemeka warna (DSSCs) melalui teknik elektroputaran. Elektropsun TiO_2 dicirikan lagi untuk menyiasat potensi struktur nano ini untuk digunakan sebagai komponen fotoanod dalam fabrikasi DSSCs. Struktur dan sifat TiO_2 elektrospun dan mesopori telah dicirikan dengan menggunakan FESEM dan XRD. Untuk sistem DSSC pertama yang mengandungi TiO_2 P25 komersial, 5 wt.% of anthocyanin dyes (A3) mencapai kecekapan maksimum iaitu (1.054 ± 0.012)%. Komposit TiO_2 nanopartikel/electrospun elektrod telah direka untuk meningkatkan kecekapan penyerapan pewarna dalam aplikasi DSSCs. 10 wt.% NRs dan 90 wt.% of NPs (B1) menunjukan peningkatan kecekapan sehingga (1.351± 0.013)%. Prestasi (NRs-NPs) DSSC system dipertingkatkan lagi dengan menambah 6 wt.% sucrose-DCA dibandingkan dengan prestasi sukros tanpa acid DCA dengan nilai J_{sc}, V_{oc}, FF, efficiency, R_s, R_{sh} dan R_2 (6.360 ± 0.059) mA cm^{-2}, (0.473 ± 0.0.005) V, (0.656 ± 0.006), (1.974 ± 0.014) %, (0.013 ± 0.003) Ω-cm^2, (2.918 ± 0.019) Ω-cm^2 and (38.20 ± 0.17) Ω, respectively.

Kata kunci: Antosianin, pewarna semulajadi, *Melastoma malabathricum*, TiO_2, Sel solar pemeka warna(DSSCs),elektroputaran.

ACKNOWLEDGEMENT

First and foremost, I would like to express my heartiest gratitude to my supervisor, **Professor Dr. Abdul Kariem Bin Hj Mohd Arof** for his patience, continuous supervision, guidance, advice, and support in completing this thesis. I express my humble gratitude to my supervisor for his willingness to spare me his time and guide me to complete my study. All his guidance, patience and encouragement throughout this study are greatly appreciated.

I would like to take this opportunity to thank **Yang Di-Pertuan Agong scholarship (BYDPA)** and **Public Service Department (JPA)** for providing me financial support for the completing this research works. I would also like to thank the **University of Malaya** for the awarded grant.

Finally but not least, I would like to thank both of my parents, husband, son and siblings for their support. I am grateful and touched for the support from my beloved mother, Saudah binti Ab kadir, my father, Aziz bin Hj yusof, my husband Mohd Azuan bin Mohd Daud and my son Mohd Afif Firdaus Mohd Azuan for their constant encouragement and understanding throughout the years of my study. I also would like to thanks all my friends especially Centre ionic University of Malaya (CIUM) group members for their moral support and encouragement in making this research a success.

TABLE OF CONTENTS

ABSTRACT…………………………………………………………………… iii

ABSTRAK……………………………………………………………………… v

ACKNOWLEDGEMENT……………………………………………………… vii

TABLE OF CONTENTS……………………………………………………… viii

LIST OF FIGURES…………………………………………………………..xiv

LIST OF TABLES…………………………………………………………….. xvii

LIST OF SYMBOLS AND ABBREVIATIONS……………………………………xx

CHAPTER 1: INTRODUCTION…………………………………………………….. 1

1.1 Background……………………………………………………………… 1

1.2 Problem statements……………………………………………………… 3

1.3 Objective of this study…………………………………………………… 6

1.4 Scope of study…………………………………………………………… 7

CHAPTER 2: LITERATURE REVIEW…………………………………………….. 9

2.1 Solar cells………………………………………………………………… 9

2.1.1 Dye sensitized solar cell and workin principle………………………..9

2.1.2 Component of DSSCs……………………………………………… 12

2.2 Sensitizer for DSSCs……………………………………………………… 12

2.2.1 Natural sensitizer from plant……………………………………... 13

2.2.2 Basic structure of anthocyanin…………………………………… 14

2.2.3 Antocyanin sensitized DSSC……………………………………….. 16

2.2.4 Extraction of anthocyanin…………………………………………... 18

2.2.5 Response surface methodology (RSM)……………………………... 18

2.2.6 *Melastoma malabathricum* as source for sensitizer………………… 20

2.3 TiO_2 semiconductor………………………………………………….. 21

2.3.2 Electrospinning……………………………………………………22

2.3.3 History of Electrospinning: Some Historical Facts………………… 23

2.3.4 Electrospinning process…………………………………………….. 23

2.4 Factors effecting the properties of electrospun fiber………………………25

2.5 Solution parameter that effect the properties of electrospun fiber…………… 25

2.5.1 Viscosity…………………………………………………………. 25

2.5.2 Concentration……………………………………………………... 25

2.5.3 Molecular weight…………………………………………………… 26

2.5.4 Conductivity and surface charge density…………………………… 26

2.6 Processing parameter……………………………………………………… 26

2.6.1 Applied Voltage…………………………………………………….. 26

2.6.2 Flow rate……………………………………………………………. 27

2.6.3 Distance: Tip to collector distance (TCD)………………………….. 27

2.7 Application of electrospun nano fiber…………………………………….. 28

2.7.1 Energy generation application……………………………………… 29

2.7.2 Synthesis of TiO_2 by combination Sol gel and electrospinning……..29

2.8 Electrolyte………………………………………………………………… 30

2.9 Counter Electrode………………………………………………………… 31

2.10 Additive……………………………………………………………………32

2.11 Summary…………………………………………………………………... 32

CHAPTER 3: METHODOLOGY…………………………………………………... 33

3.1 Introduction………………………………………………………………... 33

3.2 Optimization of anthocyanin extraction from fruit pulps of Melastoma malabathricum (pokok senduduk) by response surface methodology (RSM)……………………………………………………………………34

3.2.1 Materials…………………………………………………………. 34

3.2.2 Experimental Design: Response Surface Methodology (RSM)……. 35

3.2.3 Anthocyanin extraction of *Melastoma malabathricum* based on BBD……………………………………………………………37

3.2.4 Total anthocyanin content... 38

3.2.5 Colour Analysis for obtaining L*, a*, b*, C, H, saturation and anthocyanin content... 39

3.3 Analytical ultra performance liquid chromatography with electrospray ionization tandem mass spectrometry (UPLC-ESI-MS/MS)..................... 43

3.4 Synthesis of TiO_2 nanostructure for semiconductor photoanode............... 43

3.4.1 Materials... 43

3.4.2 Preparation of TiO_2 by sol-gel synthesis..................................... 44

3.4.3 Preparation of TiO_2 by electrospinning...................................... 44

3.4.4 Effect of polymer concentrations on nanofiber formation............. 45

3.4.5 Effect of applied voltage on nanofiber formation......................... 46

3.5 Characterization of TiO_2 nanostructure.. 47

3.5.1 Field Emission Scanning Electron Microscope (FESEM)............. 47

3.5.2 Energy Dispersive X-Ray Analysis (EDX)................................ 47

3.5.3 X-Ray Diffraction (XRD)... 48

3.6 Preparation of samples for DSSCs application.................................... 48

3.6.1 Fluorine-doped Tin Oxide (FTO) Glass Cleaning Process............ 48

3.6.2 Preparation of photoanode using commercial TiO_2........................... 49

3.6.3 Preparation of TiO_2 composite photoanode............................. 50

3.6.4 Preparation of platinum (Pt) electrode.................................. 51

3.6.5 Gel polymer electrolyte preparation (GPE).............................. 52

3.6.6 Extraction Preparation of Anthocyanin from *Melastoma malabathricum* for DSSC of dye sensitizer for DSSCs................ 53

3.6.7 Additive... 53

3.6.8 Fabrication of dye sensitized solar cells (DSSCs)...................... 53

3.7 Characterizations... 54

3.7.1 Visible Spectroscopy... 55

3.7.2 *J-V* Analysis... 56

3.7.3 Short Circuit Photocurrent Density (J_{sc})................................ 56

3.7.4 Open Circuit Photovoltage (V_{oc}).. 57

3.7.5 Fill Factor (FF)..57

3.7.6 Series Resistance..57

3.7.7 Shunt Resistance... 58

3.7.8 Solar Energy to Electricity Conversion Efficiency (η)................ 59

3.7.9 Incident photon to current efficiency (IPCE)............................59

3.7.10 Electrochemical Impedance Spectroscopy (EIS)........................ 60

3.8 Summary... 60

CHAPTER 4: RESULTS FOR IDENTIFICATION AND OPTIMIZATION OF ANTHOCYANIN EXTRACTION FROM FRUIT PULPS OF *Melastoma malabathricum* BY RESPONSE SURFACE METHODOLOGY (RSM)........... 61

4.1 Introduction... 61

4.2 Identification of anthocyanin extraction from fruit pulps of Melastoma malabathricum by UPLC-ESI-MS/MS... 61

4.3 Response surface methodology (RSM)... 63

4.3.1 A box-behnken design (BBD) analaysis of L*, a*, b*, C, H°, saturation and anthocyanin content.......................................63

4.3.2 Stastical analysis for determination of appropriate polynomial equation to represent rsm model... 66

4.4 Validation of the model for L*, a*, b*, C, H^0, saturation and anthocyanin content... 80

4.5 Analysis of response model graph on L*, a*, b*, C, H^0, saturation and anthocyanin content... 82

4.5.1 Analysis of response model graph on lightness, L* of anthocyanin extract from *Melastoma malabathricum*................................82

4.5.2 Analysis of response model graph on redness, a* coordinate of anthocyanin extract from *Melastoma malabathricum*..................83

4.5.3 Analysis of response model graph on blueness, b* coordinate of anthocyanin extract from *Melastoma malabthricum*.................... 85

4.5.4 Analysis of response model graph on colour Chromaticity, C of anthocyanin extract from *Melastoma malabathricum*................. 86

4.5.5 Analysis of response model graph on colour Hue angle, H^0 of anthocyanin extract from *Melastoma malabathricum*................. 87

4.5.6 Analysis of response model graph on colour saturation, S of anthocyanin extract from *Melastoma malabathricum*……………… 88

4.5.7 Analysis of response model graph on anthocyanin content of anthocyanin extract from *Melastoma malabathricum*……………….90

4.6 Optimization of the models for L*, a*, b*, C, H^0, saturation and anthocyanin content……………………………………………………….. 91

4.7 Colour differences (ΔE) based on L*, a* and b* colour coordinate…………. 94

4.8 Summary……………………………………………………………………... 96

CHAPTER 5: RESULTS FOR SYNTHESIS AND CHARACTERIZATION OF TIO_2 NANOSTRUCTURE…………………………………………………… 97

5.1 Introduction…………………………………………………………………... 97

5.2 Morphology studies on electrospun TiO_2 nanofiber obtained from combined method of sol gel with electrospinning…………………………….98

5.2.1 Effect of PVP concentration on nanofiber morphology……………..98

5.2.2 Effect of applied voltage on nanofiber morphology………………. 102

5.3 Effect of calcination temperature on TiO_2 nanorod morphology and average diameter…………………………………………………………...109

5.4 Energy Dispersive analysis X-Rays: Elemental Microanalysis of TiO_2 nanorod……………………………………………………………………… 111

5.5 XRD of electrospun TiO_2 nanorod obtained from combined method of sol gel with electrospinning…………………………………………………….. 112

5.6 Morphology studies on composite TiO_2 nanoparticle (P25) (NP) and nanorod (NR)………………………………………………………………………….113

5.7 Summary………………………………………………………………………. 115

CHAPTER 6: RESULTS FOR DSSC APPLICATIONS……………………….. 116

6.1 Introduction…………………………………………………………………… 116

6.2 Effect of Melastoma malabathricum‟s anthocyanin concentration as natural sensitizer for dssc using commercial tio_2 in mesoporous layer……...116

6.2.1 Visible spectroscopy analysis for different concentrations of anthocyanin sensitizer…………………………………………... 116

6.2.2 *J-V* analysis of commercial TiO_2 semiconductor with different anthocyanin extracts (1%, 3%, 5%, 7% and 9%)…………………. 118

6.2.3 Incident photon-to-current conversion efficiency (IPCE) characterization at different weight percentages of anthocyanin dye………………………………………………… 120

6.2.4 Electrochemical impedance spectroscopy (EIS) characterization at different weight percentages of anthocyanin dye………………..121

6.3 Effect of different percentage of tio$_2$ nanorods on composite dsscs (NPs - NR) system………………………………………………………….. 124

6.3.1 Visible studies of different weight percentages of TiO$_2$ nanorods in (NPs - NRs) system…………………………………………... 124

6.3.2 *J-V* characterization of DSSCs sensitized at different weight percentages of TiO$_2$ nanorods…………………………………... 125

6.3.3 Incident photon-to-current conversion efficiency (IPCE) characterization at different weight percentages of TiO$_2$ nanorods……………………………………………………………… 126

6.3.4 Electrochemical impedance spectroscopy (EIS) characterization at different weight percentages of TiO$_2$ nanorods…………………. 128

6.4 Effect of Different Additives Addition on Composite DSSCs System…….. 129

6.4.1 Visible studies at different weight percentages of sucrose……….. 129

6.4.2 *J-V* characterization of DSSCs sensitized at different weight percentages of additives…………………………………………….131

6.4.3 Incident photon-to-current conversion efficiency (IPCE) characterization at different weight percentages of additives…….... 134

6.4.4 Electrochemical impedance spectroscopy (EIS) characterization at different weight percentages of additives……………………… 135

6.5 Summary………………………………………………………………… 140

CHAPTER 7: DISSCUSSIONS…………………………………………………..142

CHAPTER 8: CONCLUSIONS AND SUGGESTIONS FOR FUTURE WORKS……………………………………………………………………………160

REFERENCES ………………………………………………………………...163

LIST OF PUBLICATIONS AND PAPERS PRESENTED……………………… 178

LIST OF FIGURES

Figure 2.1 : Schematic diagram working principle of DSSC. 10

Figure 2.2 : Types of DSSC sensitizer. 13

Figure 2.3 : Types of plant pigments. 13

Figure 2.4 : Basic structure of anthocyanin. 14

Figure 2.5 : Attachment of anthocyanin to a metallic ion 17

Figure 2.6 : Step involve in response surface methodology. 19

Figure 2.7 : Fruit pulp of *M.malabathricum.* 20

Figure 2.8 : Schematic electrospinning setups (a) Standing or vertical setup and (b) horizontal. 24

Figure 2.9 : Electrospinning applications in different fields 28

Figure 3.1 : Fruit pulp of *Melastoma malabathricum* 35

Figure 3.2 : Flow chart of optimization of anthocyanin by RSM approach. 36

Figure 3.3 : CIELab colour space describing colour in three dimensions, luminance, L*, the red-green axis, a*, and the blue-yellow axis, b*. 40

Figure 3.4 : Schematic diagram of electrospinning setup. 45

Figure 3.5 : TiO_2 photoanode (a) before, (b) after immersed into anthocyanin dye solutions. 50

Figure 3.6 : Pt coated FTO counter electrode. 51

Figure 3.7 : PAN-based gel polymer electrolytes 52

Figure 3.8 : Fabrication of dye sensitized solar cells (DSSCs) 54

Figure 3.9 : *J-V* curve plot in DSSCs 56

Figure 3.10 : Solar cell equivalent circuit that shows the series (Rs) and shunt resistant (R_{sh}). 58

Figure 4.1 : Mass spectrometer UPLC-ESI-MS/MS of anthocyanin from *Melastoma mabathricum.* 62

Figure 4.2 : Normal plot residual for response of (a) L*, (b) a*, (c) b*,(d) H, (e) S and (g) anthocyanin content 81

Figure 4.3 : (a) Cube graph analysis for response of Lightness, L* of anthocyanin extractionfrom *Melastoma malabathricum* (b) 3D Response surface model for Lightness, L* at 80 ^{0}C............................ 83

Figure 4.4 : (a) Cube graph analysis for response of redness, a* coordinate in CIElab of anthocyanin extraction from *Melastoma malabathricum* (b) 3D Response surface model for colour redness, a* at 80 ^{0}C.. 84

Figure 4.5 : (a) Cube graph analysis for response of blueness,b* coordinate in CIElab of anthocyanin extraction from *Melastoma malabathricum*, (b) 3D Response surface model for colour blueness, b* at 80 ^{0}C. 85

Figure 4.6 : (a) Cube graph analysis for response of colour chromaticity, C of anthocyanin extraction from *Melastoma malabathricum,* (b) 3D Response surface model for colour chromaticity, C at 80 ^{0}C............. 87

Figure 4.7 : (a) Cube graph analysis for response of Hue angle, ^{0}H of anthocyanin extraction from *Melastoma malabathricum*(b)3D Response surface model for hue angle, H^{0} at 80 ^{0}C............................ 88

Figure 4.8 : (a) Cube graph analysis for response of colour saturation,S of anthocyanin extraction from Melastoma malabathricum,(b) 3D Response surface model for colour saturation, S at 80 ^{0}C................... 89

Figure 4.9 : (a) Cube graph analysis for response of anthocyanin content of anthocyanin extraction from Melastoma malabathricum, (b) 3D Response surface model for anthocyanin content response at 80 ^{0}C. 90

Figure 4.10 : Relationship between anthocyanin content with different sample of extractions. 95

Figure 4.11 : Relationship between colour difference (ΔE^*) with different sample of extractions. 95

Figure 5.1 : FESEM images of synthesized TiO$_2$ NanoFiberss. at (a) P1, 8% PVP ; (b) P2,9 % PVP (c) P3, 10 % PVP, (d) P4,11 % PVP ; (e) P5, 12 % PVP... 98

Figure 5.2 : Analysis of average fiber diameter for (a) 10% PVP (P3), (b) 11% PVP (P4), (c) 12% PVP (P5) nanofibers. 100

Figure 5.3 : Analysis of average bead diameter for (a) 10 % PVP (P3), (b) 11 % PVP (P4), (c) 12 % PVP (P5) nanofiber.. 101

Figure 5.4 : FESEM images of synthesized TiO2 NanoFiberss.of P5 sample at (a) 15kV (V1), (b) 16 kV (V2), (c) 17 kV (V3), (d) 18 kV (V4), (e) 19 kV (V5), (f) 20 kV (V6) and (g) 21 kV (V7)......................... 103

Figure 5.5 : Analysis of average fiber diameter of TiO_2 nanofibers of P5 sample at (a) 16 kV (V2), (b) 17 kV (V3), (c) 18 kV (V4), (d) 19 kV (V5), (e) 20 kV (V6) and (f) 21 kV (V7) 105

Figure 5.6 : Analysis of average bead diameter of TiO_2 NanoFiberss.of P5 sample at (a) 16 kV, (b) 17 kV, (c) 18 kV, (d) 20 kV and (e) 21 kV 106

Figure 5.7 : FESEM of TiO_2 comercial (a) P25 nanoparticle and TiO_2 nanorod after calcination at (b) 400 ^{0}C, (d) 500 ^{0}C and (f) 600 ^{0}C. .. 110

Figure 5.8 : Analysis of average fiber diameter of TiO_2 nanorod after calcination at (a) 400, (b) 500 and (c) 600 ^{0}C. 111

Figure 5.9 : EDX spectrum for TiO_2 nanorod. 112

Figure 5.10 : XRD spectrum for TiO_2 nanorod sintered at (a) 400, (b) 500 and (c) 600 ^{0}C... 112

Figure 5.11 : FESEM images of the TiO_2 multi-electrodes with different nanorod/nanoparticle ratios (nanorods: (a,b) 10%, (N1)(c,d) 20 %(N2) ,(e,f) 30 %(N3), (g,h) 40 % (N4) and (i,j) 50 % (N5) 114

Figure 6.1 : Visible spectroscopy of different percentage of anthocyanin extract from Melastoma malabathricum. 117

Figure 6.2 : Visible spectroscopy of TiO_2 semiconductor that immersed in different anthocyanin extract (1%, 3%, 5%, 7% and 9%). 118

Figure 6.3 : *J-V* analysis of commercial TiO_2 semiconductor with different anthocyanin extracts (1%, 3%, 5%, 7% and 9%). 119

Figure 6.4 : IPCE curves of DSSCs sensitized by anthocyanin from *Melastoma malabathricum* at different percentage (1%, 3%, 5%, 7% and 9%)... 120

Figure 6.5 : The equivalent circuit used to fit the experimental data. 121

Figure 6.6 : EIS for DSSCs based anthocyanin sensitized at different weight percentages of anthocyanin from *Melastoma malabathricum* at different percentage (1%, 3%, 5%, 7% and 9%) 122

Figure 6.7 : The absorption spectra of composite electrodes based on different percentages (10, 20, 30, 40 and 50 wt.%) of TiO_2 nanorods sensitized at 5 wt.% of *Melastoma malabathricum* anthocyanin dyes 124

Figure 6.8 : *J-V* curve for composite DSSCs fabricated from TiO_2 nanoparticle-nanorod samples with nanorod percentages of 10, 20, 30, 40 and 50 wt.% sensitized at 5 wt.% anthocyanin dyes. 126

Figure 6.9 : IPCE curves for composite DSSCs fabricated from TiO_2 nanoparticle-nanorod samples with nanorod percentages of 10, 20, 30, 40 and 50 wt.% sensitized at 5 wt.% anthocyanin dyes. 127

Figure 6.10 : EIS for composite DSSCs fabricated from TiO_2 nanoparticle-nanorod samples with nanorod percentages of 10, 20, 30, 40 and 50 wt. % sensitized at 5 wt.% anthocyanin dyes. 128

Figure 6.11 : The absorption spectra of anthocyanin-pigmented TiO_2 composite electrodes with 10 wt.% TiO_2 NRs at different weight percentage of additives (2, 4, 6, 8 and 10 wt.% sucrose). 130

Figure 6.12 : The absorption spectra of anthocyanin-pigmented TiO_2 composite electrodes with 10 wt.% TiO_2 NRs at different weight percentage of additives (2, 4, 6, 8 and 10 wt.% sucrose-DCA). 131

Figure 6.13 : *J-V* curve for composite DSSCs fabricated with 10 wt.% TiO_2 NRs at different weight percentage of additives (2, 4, 6, 8 and 10 wt.% sucrose).. 132

Figure 6.14 : *J-V* curve for composite DSSCs fabricated with 10 wt.% TiO_2 NRs at different weight percentage of additives (2, 4, 6, 8 and 10 wt.% sucrose-DCA) 133

Figure 6.15 : IPCE curve for anthocyanin-pigmented TiO_2 composite electrodes with 10 wt.% TiO_2 NRs at different weight percentage of (a) sucrose additives (2, 4, 6, 8 and 10 wt.% sucrose), (b) sucrose-DCA additive (2, 4, 6, 8 and 10 wt.% sucrose-DCA). 134

Figure 6.16 : EIS for composite DSSCs fabricated with 10 wt.% TiO_2 NRs at different weight percentage of additives (2, 4, 6, 8 and 10 wt.% sucrose) 136

Figure 6.17 : EIS for composite DSSCs fabricated with 10 wt.% TiO_2 NRs at different weight percentage of additives (2, 4, 6, 8 and 10 wt.% sucrose-DCA) 137

Figure 6.18 : Summarized of (a) J_{sc} *(b)* η, (c) R_s, (d) R_{sh} and (e) R_2 values for four different sytems studied. 138

Figure 7.1 : Structure of delphinidin 152

LIST OF TABLES

Table 2.1 : Basic structure of six common anthocyanin 15

Table 2.2 : Photovoltaic parameters of anthocyanin dye based DSSCs. 17

Table 3.1 : Indepedent variables and their level used for BBD.......................... 35

Table 3.2 : Experimental runs of BBD design.. 38

Table 3.3 : BBD design table.. 42

Table 3.4 : Effect of polymer concentrations on nanofiber formation 45

Table 3.5 : Effect of applied voltage on nanofiber formation for P5 (12 wt%) ... 46

Table 3.6 : Different compositions of TiO_2 nanorod and commercial TiO_2 nanoparticle (P-25) mixture for DSSC photoanode 51

Table 4.1 : Experimental runs of BBD design and the response 65

Table 4.2 : Sequential model sum of squares (SMSS) analysis for (a) L* (b) a*, (c) b*, (d) C, (e) H°, (f) saturation and (g) anthocyanin content response. 67

Table 4.3 : Model summary statistics analysis for (a) L* (b) a*, (c) b*, (d) C, (e) H°, (f) saturation and (g) anthocyanin content response.......... 70

Table 4.4 : ANOVA analysis of the reduced quadratic model for L* 73

Table 4.5 : ANOVA analysis of the reduced quadratic model for a*.................. 74

Table 4.6 : ANOVA analysis of the reduced quadratic model for b*.................. 75

Table 4.7 : ANOVA analysis of the reduced quadratic model for C................... 76

Table 4.8 : ANOVA analysis of the reduced quadratic model for H^0 77

Table 4.9 : ANOVA analysis of the reduced quadratic model for S 78

Table 4.10 : ANOVA analysis of the reduced quadratic model for anthocyanin content.. 79

Table 4.11 : Summary table for desirability goal of L*,a*, b*, C, H^0, S, and anthocyanin content... 92

Table 4.12 : Optimization table based on desirability goal for L*,a*, b*, C, H^0, S, and anthocyanin content. 93

Table 4.13 : Colour differences (ΔE) of extraction from fruit pulp of *Melastoma malabathricum.* 94

Table 5.1 : Summary table for effect of different wt(%) of PVP on morphology of nanofiber 102

Table 5.2 : Summary table for effect of different applied kV and applied electric field on morphology of nanofiber 108

Table 5.3 : Percentage of anatase and Rutile TiO_2 sintered at 400, 500 and 600 ^{0}C 113

Table 6.1 : Values of V_{oc}, J_{sc}, FF, η, R_s and R_{sh} of DSSC fabricated using different wt% of M.malabathricum anthocyanin as dye materials 120

Table 6.2 : R_s, R_1, R_2, R_3 values for DSSCs based anthocyanin sensitized at different weight percentages (1%, 3%, 5%, 7% and 9%) of dyes.... 123

Table 6.3 : J_{sc}, V_{oc}, FF, η, R_s and R_{sh} values for composite DSSCs fabricated from TiO_2 nanoparticle-nanorod samples with nanorod percentages of 10, 20, 30, 40 and 50 wt.% sensitized at 5 wt.% anthocyanin dyes. 126

Table 6.4 : R_s, R_1, R_2, R_3 values for composite DSSCs fabricated from TiO_2 nanoparticle-nanorod samples with nanorod percentages of 10, 20, 30, 40 and 50 wt.% sensitized at 5 wt.% anthocyanin dyes. 129

Table 6.5 : J_{sc}, V_{oc}, FF, η, R_s and R_{sh} values for composite DSSCs fabricated with 10 wt.% TiO_2 NRs at different weight percentage of additives (2, 4, 6, 8 and 10 wt.% sucrose) 132

Table 6.6 : J_{sc}, V_{oc}, FF, η, R_s and R_{sh} values for composite DSSCs fabricated with 10 wt.% TiO_2 NRs at different weight percentage of additives (2, 4, 6, 8 and 10 wt.% sucrose-DCA) 133

Table 6.7 : Rs, R_1, R_2, R_3 values for composite DSSCs fabricated with 10 wt.% TiO_2 NRs at different weight percentage of additives (2, 4, 6, 8 and 10 wt.% sucrose) 136

Table 6.8 : R_s, R_1, R_2, R_3 values for composite DSSCs fabricated with 10 wt.% TiO_2 NRs at different weight percentage of additives (2, 4, 6, 8 and 10 wt.% sucrose-DCA) 137

LIST OF SYMBOLS AND ABBREVIATIONS

η : Efficiency

FF : Fill factor

V_{oc} : Open circuit voltage

J_{sc} : Short circuit current density

R_s : Series resistance

R_{sh} : Shunt resistance

ANOVA : Analysis of varience

BBD : Box Benkhen Design

BMII : 1-butyl-3-methylimidazolium iodide

CO_2 : Carbon dioxide

Cy : Cyanidin

DCA : Deoxycholic acid

Dp : Delphinidin

DSSCs : Dye-sensitized solar cells

EDX : Energy dispersive x-ray analysis

EIS : Electrochemical impedance spectroscopy

FESEM : Field emission scanning electron microscopy

GPE : Gel polymer electrolyte

IL	:	Ionic liquid
IPCE	:	Photon to current efficiency
LiL	:	Lithium iodide
MON	:	Metal oxide nanoparticles
MOS	:	Metal oxide semiconductor
Mv	:	Malvidin
NP	:	Nanoparticle
NPs-NRs	:	Nanorod-nanoparticle
NR	:	Nanorod
Pg	:	Pelargonidin
Pn	:	Peonidin
PV	:	Photovoltaic
PVP	:	Polyvinyl pyrrolidone
RSM	:	Response surface methodology
SMSS	:	Sum of squares
TCD	:	Tip to collector distance
TFA	:	Trifluoroacetic acidified
TiO_2	:	Titinium dioxide
TPAI	:	Tetrapropylammonium iodide

TTIP	:	Titanium (IV) isopropoxide
UV-Vis	:	Ultraviolet visible spectroscopy
XRD	:	X-ray diffraction

CHAPTER 1: INTRODUCTION

1.1 Background

The increase in energy consumption is one of the most critical and greatest challenges that the world faces right now. With a persistently growing human population and upgraded living standards, more energy will be needed. Society calls for energy production to meet basic human requirements (Edenhofer et al., 2011). Thus, in order to overcome this issue many efforts and research have been done. At present, the world is depending on fossil fuels (coal, oil and gas). Nevertheless, with rising global energy demands, fossils fuels are facing depletion since they are non-renewable (Kaygusuz, 2012). The use of energy from fossil fuels can be considered to face two main problems. The first is the limited resources and the second is their environmental impact. Combustion of fossil fuels has led to the ecological pollution and global warming resulting in greenhouse effect (Perera, 2018). For these two reasons, there is increased global awareness that has urged alternative energy resources to be formed to meet global needs. The supply of clean green energy is considered as one of the most important challenges faced in the 21st century (Kaygusuz, 2012). Acquiring new energy sources and controlling the negative effects to climate changes are challenges for a sustainable future (Abbasi & Abbasi, 2010; Kaygusuz, 2012). Therefore, to overcome this problem, economical and environmentally friendly alternative sustainable energy resources need to be established and used (Gong et al*.,* 2012; Susanti et al*.,* 2014).

The world‟s climate has been changing since time beginning, but the fast rate of change in recent years is worrying. CO_2 growth rate has escalated for nearly 4 decades (Asumadu-Sarkodie & Owusu, 2015) and the concern to keep global warming below 2 °C has been continuing for more than 10 years (McConell, 2002; Asumadu-Sarkodie & Owusu, 2015). The use of fossil fuels that has led to rapid growth in carbon dioxide emission is the cause of the green-house effect. Data accumulated in 2010 certified that the use of fossil fuels is the cause of gaseous release that exceeded pre-industrial levels (Edenhofer et al., 2011). Thus „cleaner" and „greener" energies to be developed must result in decreased environmental impacts and production. Renewable energy technologies must provide moderation of gas release and reduce universal warming (Panwar et al., 2011).

Renewable energy is defined as energy that is derived from sources such as sunlight, wind, hydro, rain, waves, geothermal and heat that are always in existence. Renewable energies are expected to be capable of supplying endless energy for mankind. Solar energy is a capable future energy resource since it is abundant, clean, safe, and economical and allows energy generation in remote rural areas (Edenhofer et al., 2011). Sunlight into electricity conversion by photovoltaic cells has many advantages over many electricity techniques. It is also very effective compared to other available renewable energy resources. Other attractive features of photovoltaic include cell as being environmental friendly, and does not pollute. Photovoltaic cells generate electricity without requiring mechanical or moving parts (Husain et al., 2018). Therefore, photovoltaic cells are sustainable and can continuously work for a longer period of time and are maintenance-free compared to other power generation technologies (Hosenuzzaman et al., 2015). However, the high cost per watt electricity generated currently limits its application (Husain et al., 2018). The cost has however been reduced.

The first generation photovoltaic (PV) solar such as the single multi-crystalline silicon based solar cells has entirely controlled the market. The second generation solar cell is a modification of the developed first generation PVs which has a lower manufacturing cost. Finally, the third generation solar cells include organic PV cells. Although the cost of the second generation solar cells is reduced, the third generation solar cells promise to be even cheaper. The dye sensitized solar cell is an example of third generation cells (Cuce at al., 2015). The dye sensitized solar cells have been drawing considerable attention due to their low fabrication cost, variety of colors, easy manufacturing process, clean, eco-friendly and exhibit relatively high power conversion efficiency (Song et al., 2005).

Dye-sensitized solar cells (DSSCs) have shown promising future as the alternative option to replace silicon-based solar cells (Song et al., 2005). The DSSC device can be distinguished from the classical solid-state junction device. This can be done by replacing the p-n junction with a metal oxide semiconductor (MOS) in contact with a liquid, gel or solid electrolyte. The electrolyte acts as a medium for charge transport (Grätzel, 2003). Generally, a photoelectrochemical cell or DSSC device comprises (i) photoanode or working electrode, (ii) a metal counter electrode and (iii) a redox electrolyte. The photoanode consist of a dye capped nanocrystaline porous semiconductor. For the conventional systems, p-n junctionact as both the light absorber and charge carrier transporter. In DSSC, light absorption is carried out by the dye and charge separation occurs at the interface of the dye and the MOS (Grätzel, 2005; Ludin et al., 2014).

1.2 Problem statements

Commercial dyes in DSSCs are usually synthetic dyes, such as diruthenium (II), commercially coded as N719 and N3, both of which enhance the light to electricity conversion efficiency. DSSCs utilizing nanoporous TiO_2 electrodes and sensitized with ruthenium containing dyes have derived high efficiencies, but these dyes are costly. They are also ecologically unfriendly and contain ruthenium, a heavy metal. Thus although low cost, natural dyes have been tested for DSSCs, the challenge remains (Senthil et al., 2013). Dyes and pigments derived from plants, for example, chlorophyll, anthocyanin, tannin, and carotene, are cheap and do not pose any environmental issues (Kushwaha et al., 2013), but efficiency of DSSCs employing them as sensitizer are mostly low. Natural dyes sensitizers offer an alternative to the synthetic dyes. They are easy to prepare, abundant, cheap, biodegradable, environmental friendly and do not contain heavy metal (Adedokun et al., 2018). Most of the reported efficiencies from DSSCs employing natural dyes are less than one percent, only a few achieved efficiency more than one percent (Hug et al*.,* 2014). Research in natural DSSCs is still in its infancy. The low efficiency of DSSCs when sensitized with „green" dyes as compared to that of synthetic dyes presents a tremendous scope for the search of efficient dye sensitizers. This is because one of the prime factors governing efficiency of the cell is the sensitizer.

Good sensitizers should be able to absorb in the entire visible range. Good sensitizing effect is also influenced by the dye extracting medium, i.e. solvents (Adedokun et al., 2018). For efficient extraction, the solvent must be able to completely dissolve the target compound. *Melastoma malabathricum* is a natural dye that contains anthocyanin (Abdullah et al*.,* 2006; Wong, 2008). Anthocyanin from *Melastoma malabathricum* used as sensitizer and has been reported with efficiency only 0.039% (Rus et al., 2013). Reports show that anthocyanin from *Melastoma malabathricum* has potential to be a good sensitizer since it is in abundance, economical and cheap (Rus et al., 2013). Thus, research on anthocyanin from this source is vital in order to enhance the performance of natural DSSCs. There are many factors that influence the extraction of natural sensitizer. The extraction parameters influence the yield of natural anthocyanin extraction. Different species have different optimal conditions to extract the anthocyanin content. Hence, it is important to obtain the required optimization parameter to obtain the highest amount of anthocyanin extraction from *Melastoma malabathricum* to increase efficiency of DSSCs.

Modification of TiO_2 photoanode is needed in order to further increase efficiency of the DSSCs employing anthocyanin from *Melastoma malabathricum* as sensitizer. In this effort, TiO_2 nanoparticle/nanorod composite electrodes have been designed to offer electron transfer paths without loss of the high surface area for dye adsorption. This is where nanomaterials are useful. Nanomaterials show flexibility in surface functionalities and greater mechanical performance compared to other material forms (Asagoe et al., 2007). A number of techniques that include phase separation, self-assembly and electrospinning have been used to make polymer nanofibers in recent years. The electrospinning process seems to be a suitable method to develop continuous nanofibers from several polymers since other methods are time comsuming (Asagoe et al., 2007).

Electrospinning offers a simple method to produce nanofibers with a broad range of diameters ranging from micrometer to nanometer. Structure, morphology, bead and nanofiber diameters are easily controlled by varying solution concentration, viscosity, surface tension, and conductivity of the solution (Demir et al., 2002). Numerous metal oxide nanofibers including titanium oxide, silica, cobalt oxide, nickel oxide, tin oxide, zirconium oxide, palladium oxide and zinc oxide have been prepared using electrospinning approaches. The TiO_2 electrodes for use in DSSCs were fabricated by mixing TiO_2 nanorods and the commercially available TiO_2 nanoparticles. The TiO_2 multi-electrodes improved the DSSC efficiency (Deitzel et al., 2001).

1.3 Objective of this study

In this thesis, DSSCs devices are fabricated from a combination of relatively popular materials containing environmental friendly natural dye, inexpensive, inert and non-toxic TiO_2 photoanode, low cost redox mediator-containing gel electrolyte and platinum counter electrode which acts as a catalyst for electron regeneration. All these DSSC components have important roles to play in promoting good efficiency. The cell performance can be enhanced by adding additives. The objectives in this study are summarized as follows:

1. To confirm the type of anthocyanins present in the solvent extract of fruit pulp of *Melastoma malabathricum* by analytical ultra performance liquid chromatography with electrospray ionization mass spectrometry (UPLC-ESI-MS/MS).
2. To optimize the extraction parameters for anthocyanin extraction from the fruit pulp of *Melastoma malabathricum* via response surface methodology (RSM).
3. To optimize electrospinning parameter for production of uniform and beadless TiO_2 nanofibers. The beadless TiO_2 nanofiber will also be calcined at different temperature to obtain TiO_2 nanorod.
4. To study the effect of anthocyanin concentration from the fruit pulp of *Melastoma malabathricum* on the efficiency of DSSCs employing commercially purchased TiO_2. The optimized anthocyanin concentration that obtained will also be utilized for DSSCs employing unique composite photoanode that consist of commercial nanoparticle TiO_2 (NPs) and nanorod (NRs) obtained by combining sol-gel and electrospinning techniques. The optimum amount of nanorods for inclusion in the TiO_2 composites was also determined.

5. To study the influence of additives sucrose and sucrose-deoxycholic acid (sucrose-DCA) addition in optimized anthocyanin extract from fruit pulp of *Melastoma malabathricum* on the efficiency of composite DSSCs.

1.4 Scope of study

This thesis consists of eight chapters. The first chapter begins with an introduction to the thesis. Chapter 2 gives an overview of synthetic and natural sensitizers, selection and properties of materials used and a review about DSSCs as well as its working principle. Chapter 3 describes the details of sample preparation and characterizations such as visible spectroscopy, electrochemical impedance spectroscopy (EIS) and DSSC fabrication. Chapter 4 encompasses investigation to comfirm the major anthocyanin type extracted from *Melastoma malabathricum* and optimization of anthocyanin extraction parameters using response surface methodology (RSM). The optimized anthocyanin extracted from *Melastoma Malabathricum* extraction will be used as sensitizer in DSSC application at different concentration. Chapter 5 presents morphology results of TiO_2 nanostructures produced by combination of soft chemistry and elctrospinning method. Surface morphology and fiber formation of electrospinning nanofibers were investigated using FESEM. The optimized PVP samples were further analysed in order to obtain beadless nanofibers. Hence, the effect of applied voltage on average fiber and bead diameters were studied. The successfully formed beadless nanofibers obtained were subjected to different calcination temperatures. Nanorods were obtained after grinding the nanofibers. The structure of nanorods were determined by x-ray diffraction (XRD). The anatase TiO_2 nanorods were used to form the nanoparticle/nanorod composites. The morphology of the composite at various nanorods to nanoparticles ratios were observed via FESEM. Chapter 6 describes results of different weight percentages of optimized anthocyanin from *Melastoma malabathricum* in DSSC application. The optimized wt.% of anthocyanin extact, which exhibit the highest efficiency of DSSCs will be used in further studies. The goal of this work is to evaluate the potential of TiO_2 nanorod-nanoparticle (NPs-NRs) composite photoanode materials in DSSCs. The optimum amount of nanorods for inclusion in the TiO_2 composites was also determined. To further increase the efficiency, sucrose and sucrose-DCA were added as additives in the optimized anthocyanin extract and used as sensitizer in DSSCs with composite photoanode. Chapter 7 discusses all results obtained and Chapter 8 concludes the thesis with some suggestions for future work that will help to increase the body of knowledge in the vast literature on TiO_2 nanorod and DSSCs.

CHAPTER 2: LITERATURE REVIEW

2.1 Solar cells

Photovoltaic is cells or solar cells that convert light to electricity. To date, there are three generations of solar cells. Currently in used are the first generation solar cells. It is quite costly although the price has already dropped and very pure silicon is needed (Lund, 2009). The second generation solar cells have efficiency lower compared to first generation cells. However, this type of solar cells is much inexpensive compared to the first generation. Materials in this second generation are copper indium gallium selenide (CIGS), amorphous silicon (a-Si) and cadmium telluride (CdTe) (Sharma et al., 2015). Although the price is lower, however manufacturers face difficulty on consumer acceptance. This is because, the solar cells contain harmful component to our environment and health (Charles et al., 2005). Nanophotovoltaic solar cells technology is classified as third generation solar cells (Sharma et al., 2015). In 2011, Razykov and coworkers stated some of ongoing research in this field such are quantum dot solar cells (QDs), quantum well solar cells (QWSCs)(Charles et al., 2005), dye-sensitized solar cells (DSSCs), organic and Polymeric solar cells (Hegedus, 2011). All devices have diverse potential applications and dissimilar ways of approached to compensate between the manufacture cost and efficiency trade of. Nevertheless, a greener solar cell technology should be emphasized while retaining low price materials and production methods with adequate efficiency. Definitely, it is not yet extensively commercializes (Lund et al., 2009).

2.1.1 Dye sensitized solar cell and working principles

DSSC is a material that can convert sunlight into electricity through sensitization of wide band-gap semiconductors. The efficiency of DSSC generally be influenced by dyes or colourant used as sensitizers, which absorb sunlight and convert solar energy into electric energy and the ability of dye to anchor with TiO_2 on the surface of semiconductor (Jinchu et al., 2014). The previous research on DSSCS of semiconductors focused on flat electrodes, but these systems were encountering an essential problem (Hamman et al., 2007). Effective injection of electron into semiconductor is depending on the first monolayer that adsorbs dye. The effective surface area of monolayer for light harvesting can be increased by utilization of TiO_2 nanoporous (Wurfe et al., 2008).

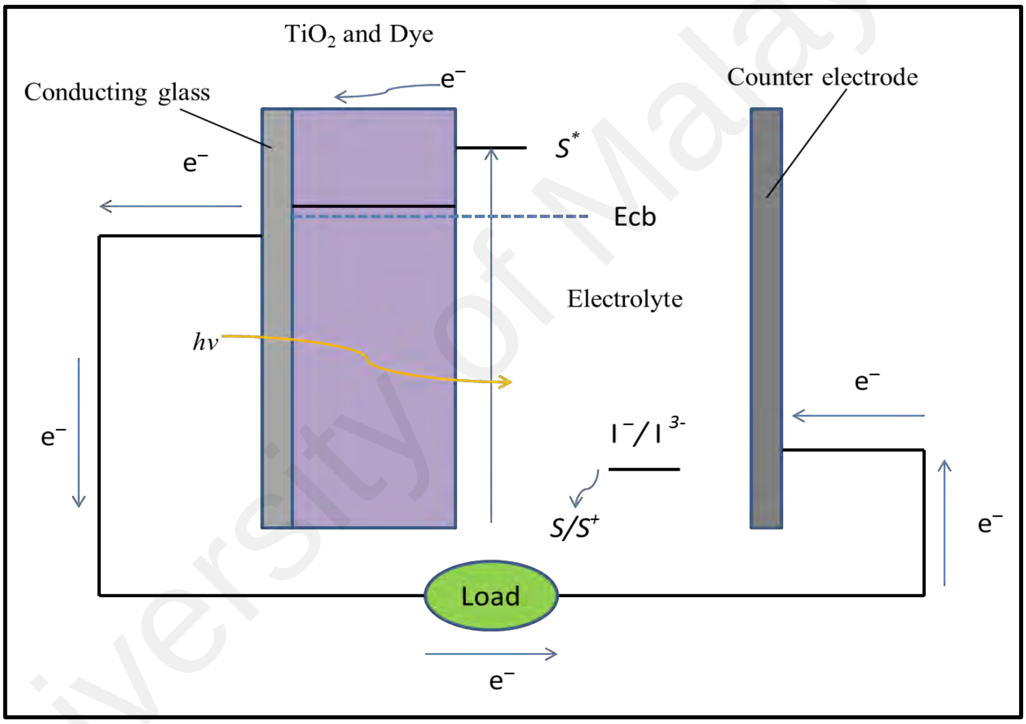

Figure 2.1: Schematic diagram working principle of DSSC.

An interesting feature in the TiO_2 nanocrystalline film is effective of charge transport of the photo-generated electrons passing through all the particles (Wurfe et al., 2008). Attractive performance of TiO_2 nanocrystalline photoanode based solar cells was first reported by Grätzel (Agarwala et al., 2011). Nanoporous semiconductors such as ZnO, SnO_2 and TiO_2, were act as electron electronic conductor and electron acceptor. The current flows that travel across the TiO_2 nanocrystaline film to the charge collecting and then to external circuit results from injection of electron of the photo-excited dye. Continuous conversion of light energy is assisted by regeneration of the reduced dye sensitizer either using a reversible redox couple which is usually I_3^-/I^- or via the electron donation from a p-type semiconductor (Chen et al., 2013). Figure 2.1 show the schematic diagram on the working principle of DSSCs.

Sensitizer (*S*) absorbed photon and get excited. The electron injected by excited molecule (S^*) into the conduction band of the semiconductor as show in reaction (2.1) below before the oxidized dye can reduce to its original state reaction (2.5). The oxidized dye (S^+) is regenerated by iodide in the electrolyte as fast as possible to ensure efficient DSSC (reaction 2.2), which normally arises more quickly than reduction by photo-injected electrons in the TiO_2 (reaction 2.6). The tri-iodide formed by dye regeneration reaction is reduced at the counterelectrode (reaction 2.4). Electrons in the TiO_2 are affected by two competing processes: (i) Recombination with tri-iodide in the electrolyte (reaction 2.6) and (ii) diffusion through the mesoporous TiO_2 to the front electrode. The operating cycle of DSSC can be summarized in the following chemical reaction (Wenger, 2010)

$S + hv \longrightarrow S^*$	Photo excitation reaction	(2.1)
$S^* \longrightarrow S^+ + e^-$	Charge injection reaction	(2.2)
$S^+ + 2I^- \longrightarrow S + I_2$	Dye regeneration reaction	(2.3)
$I_3 + 2e^- \longrightarrow 3I^-$	Electrolyte regeneration reaction	(2.4)
$S^* \longrightarrow S$	Dye relaxation reaction	(2.5)
$S^+ + e^- \longrightarrow S$	Recombination via dye	(2.6)

2.1.2 Component of DSSCs

DSSC comprises a transparent conducting oxide TCO glass (Tachan et al., 2010) that has been coated with fluorine doped tin oxide or indium doped tin oxide. TCO should be of low resistance but high transparency. It is the photoanode and counter electrode substrate. It transmits light and collects electrons at the counter electrode. The photoelectrode comprises a metal oxide nanoparticles (MON) such as ZnO, TiO_2, or SnO deposited on the TCO. MON should have as large surface area as possible for dye adsorption. Grätzel & O'Regan (2003) developed Ruthenium complexes as sensitizers and achieved approximately 7.1% efficiency under AM 1.5 light irradiation. The TCO-TiO_2 assembly is soaked in dye solution to form the photonanode. The electrolyte (liquid, solid or gel) containing Iodide and tri-iodide redox couple for electron transfer from the counter electrode to the photoanode (Peter, 2007). The light-to-energy conversion efficiency of the DSSC depends on the relative energy levels of the semiconductor and dye. It also depends on the kinetics of electron transfer processes at the sensitized semiconductor and electrolyte interface. The rate of these processes depends on the properties of its components. In order to improve the DSSC perfomance: 1) Architecture of TiO_2 nanoparticles must lead to better electron transportation and diffusion, 2) Electrolyte should exhibit faster redox reaction and stability at high temperatures and 3) Dye molecules should absorb in a wider spectral range (McConnel, 2002).

2.2 Sensitizer for DSSCs

Ruthenium based dyes used in DSSCs have exhibited efficiency that ranged from 8% to 11%. Commonly used are red dye (N3) and black dye (N719) (Nazeeruddin et al., 1993; Nazeeruddin et al., 2001). They are however not cheap, toxic and not readily available (Zhou et al., 2011). Os(II), Pt(II), Re(I), Cu(I) and Fe(II) are other metal complexes investigated. The different types of sensitizers are shown in Figure. 2.2.

Some examples of synthetic organic sensitizers that have been used include triphenylamine (Heo et al., 2013), porphyrin (Zhou et al., 2011) and perylene (Mikroyannids et al., 2009).

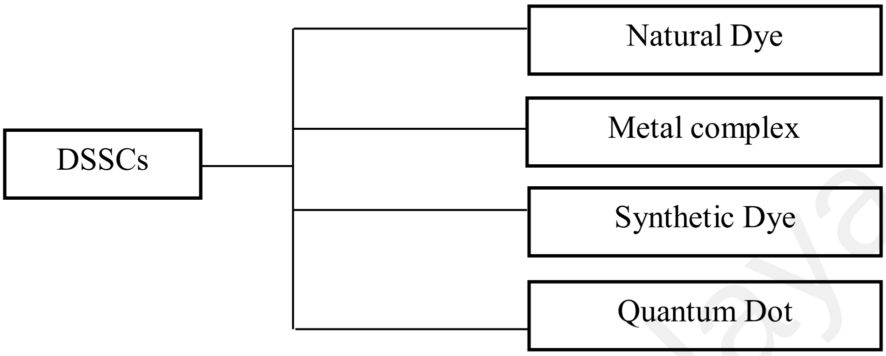

.

Figure 2.2: Types of DSSC sensitizer.

2.2.1 Natural sensitizer from plant

Many plants have been studied to extract the coloured material for solar cells. Pigments capture visible light. Pigments can be synthetic and natural. Plant pigments include chlorophylls, carotenoids, anthocyanin and betalain as in Figure 2.3 (Delgado-Vargas et al., 2000). Anthocyanins are flavonoids that impart fruits and flowers with red and blue colors. For example, the colours of strawberry and cranberry are attributed to the many different anthocyanins (Delgado-Vargas et al., 2000).

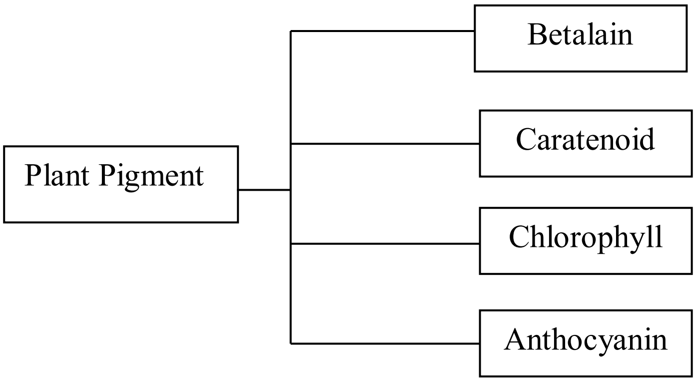

Figure 2.3: Types of plant pigments.

Anthocyanins are water-soluble (Castaneda et. al., 2009). They act in plants as antioxidants, antimicrobials and photoreceptors (Guisti and Wrolstad, 2003). Anthocyanin is influenced by various factors such as pH aggregation and temperature (Castaneda et. al., 2009).

2.2.2 Basic structure of anthocyanin

Anthocyanins contain of anthocyanidin, sugar(s) and acyl group(s). Flavyllium cation is the main part of anthocyanins. The flavylium cation is absorbing around 500 nm and results in the pigments to look red. Anthocyanidins has a C6-C3-C6 carbon skeleton basic structure (Guisti and Wrolstad, 2003). According to Andersen & Jordheim (2006), the number of hydroxyl groups and the position of their attachment, the type of sugars and how many sugar bonded to the molecule as well as the number of aliphatic and aromatic acids attached to sugar at B ring make up the different anthocyanin as in Figure 2.4.

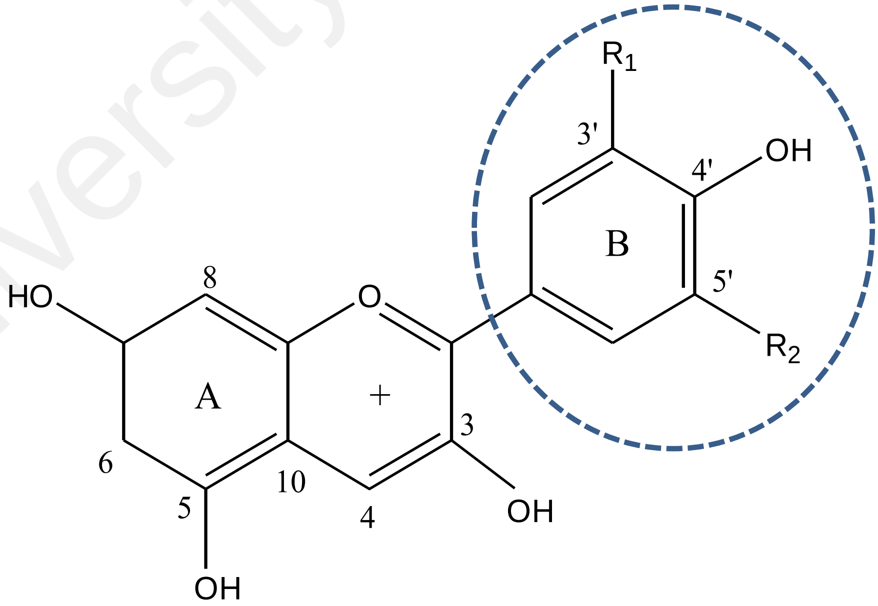

Figure 2.4: Basic structure of anthocyanin.

There are six common anthocyanidins in higher plants peonidin (Pn), pelargonidin (Pg) malvidin (Mv), cyanidin (Cy), delphinidin (Dp) and petunidin (Pt) that only differ by the hydroxylation and methoxylation pattern on their B-rings as listed in Table 2.1. As mentioned, anthocyanidins are very unstable, but the sugar in their glycosylated attachment improves their stability and solubility (Giusti & Wrolstad, 2003). The most common sugar moieties include glucose and galactose, to name a few (Andersen & Jordheim, 2006).

Table 2.1: Basic structure of six common anthocyanin.

Type of anthocyanin	Basic structure
(a) Pelagornidin	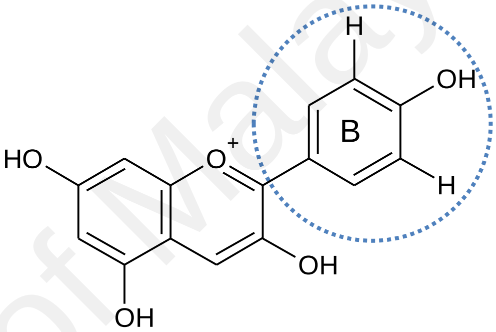
(b) Cyanidin	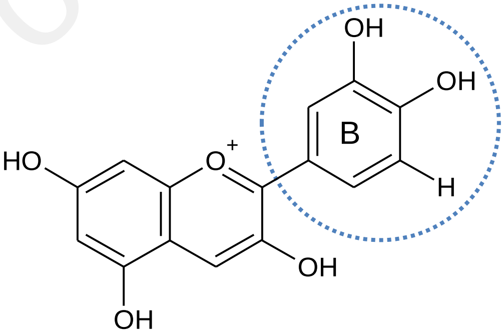
(c) Peonidin	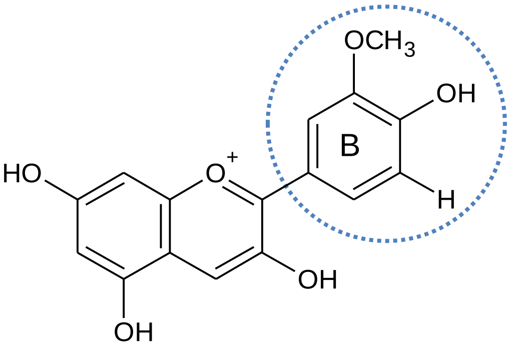

Table 2.1, continued.

(d) Delphinidin	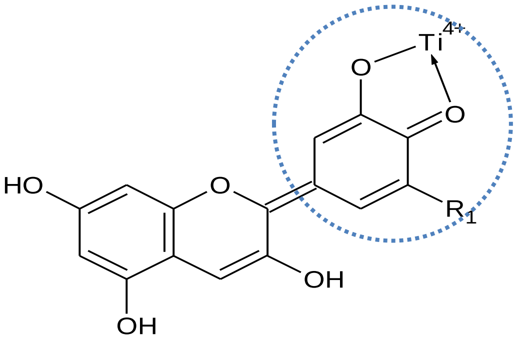
(e) Petunidin	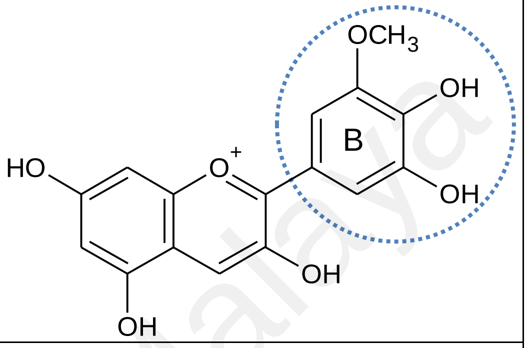
(f) Malvidin	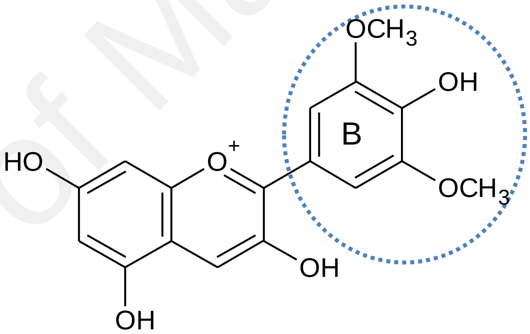

2.2.3 Antocyanin sensitized DSSC

Employment of anthocyanin in DSSCs can offer a “green” substitute to the ruthenium based DSSC. Recently, anthocyanins have been actively studied because they are cost effective and able to absorb photons and convert them to electrons effectively (Furukawa et al., 2009). Anthocyanins ordinarily absorb light which have wavelengths from 450 nm to 600 nm.

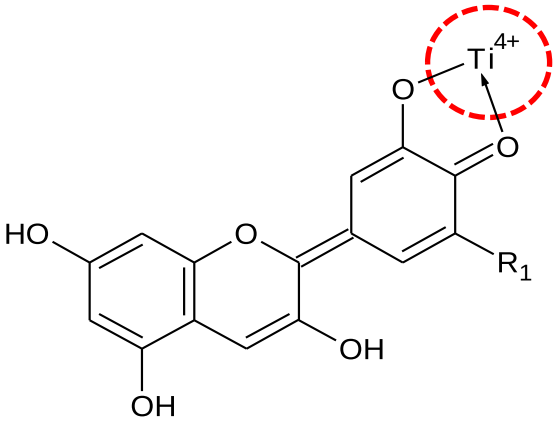

Figure 2.5: Attachment of anthocyanin to a metallic ion (TiO_2).

The plant that contains anthocyanin is normally blue, purple and red in color. The joining of nanoparticles to the anthocyanin dye can potentially broaden the absorption spectra and enhance cell efficiency (Furukawa et al., 2009). Hydroxyl and carbonyl groups of anthocyanin molecule can attach to semiconductor surface and provide pathways for the excited electron to enter the conduction band of semiconductor (Hao et al., 2006). Complexation of anthocyanin pigments have shown that the pigment binds with metal ions such as aluminum, iron, titanium and chromium as in Figure 2.5 (Fernando & Senadeera, 2008). Different anthocyanin extracted from different plant will result in different solar cell performance (Polo & Iha, 2006).

Table 2.2: Photovoltaic parameters of anthocyanin dye based DSSCs.

Anthocyanin sensitizer	J_{sc}	V_{oc}	FF	Efficiency
Mangosteen pericap	2.69	0.686	0.63	1.17
Hibiscus surattensis	5.45	0.39	0.54	1.14
Sesbania grandiflora	4.40	0.41	0.57	1.02

Fill factor (*FF*), energy conversion efficiency (η), open circuit voltage (V_{oc}), and short circuit current (J_{sc}) are analyzed in order to evaluate the performance of natural dye sensitizer in DSSC. Several researchers have been studied some anthocyanin sources (see Table 2.2) in DSSCS as photosensitizers for DSSC (Adedokun et al., 2018).

According to Furukawa et al. (2009), anthocyanin based sensitizers are cheaper than Ru based sensitizers. It is also reported that pigments such as curcumin (*Curcuma longa*), has exhibited efficiency of 1.10%, safflower (*Carthamus tinctorium L.*), (0.6%), gardenia yellow (*Gardenia jasminoides*) (0.90%) and red cabbage (*Brassica oleracea*) (1.56%) (Polo & Iha, 2006).

2.2.4 Extraction of anthocyanin

Extraction is the essential step in the commercialization of anthocyanins. Common solvent used to extract anthocyanin are acidified solutions of methanol, ethanol, acetone and water. Numerous plant parts contain anthocyanin which can be extracted using different solvents. The choice of solvent is important. This is because the solvent will affect the yield of anthocyanin extract. Furukawa et al. (2009) stated that type of solvent will affect the concentration of the dyes. Binding between the dye and semiconductor surface also depend on the nature of the solvent being used (Polo & Iha, 2006). To date, developing efficient extraction method in order to increase the yield of anthocyanin remains a challenge (Ludin et al., 2014).

2.2.5 Response surface methodology (RSM)

There are many factors that affect the anthocyanin extraction. Based on previous studies, many factors affect anthocyanin extraction. The main factors that influence the yield of anthocyanin are solvent composition, extraction time, extraction temperature, solvent to solid ratio and extraction soaking time (Borges et al., 2011; Wijingaard et al*.*, 2010; Abad- Garcial, 2014). According to Naczk & Shahidi (2006) prolonged soaking time at high temperatures will result in decomposition of the desired product. Anthocyanins can be extracted using acidified alcohols, water, or mixtures into which a little acid is added to avoid material destruction (Borges et al., 2011). RSM is a popular method that can optimize the extraction condition of the natural pigment (Abad-Garcia et al., 2014). The parameters affecting the process are independent variables (input), and responses (output) are dependent variables. RSM investigates the relationship between independent and dependent variables and distinguishes the condition optimal for extraction of a system (Borges et al., 2011). RSM, the experimental design method used are Box-Behnken designs (BBD) and central composite design (CCD) (Saleem and Soma, 2014). Central composite rotatable design (CCRD) and face central composite design (FCCD) are rarely used (Wang et al., 2009; Sahin & Samli, 2013).

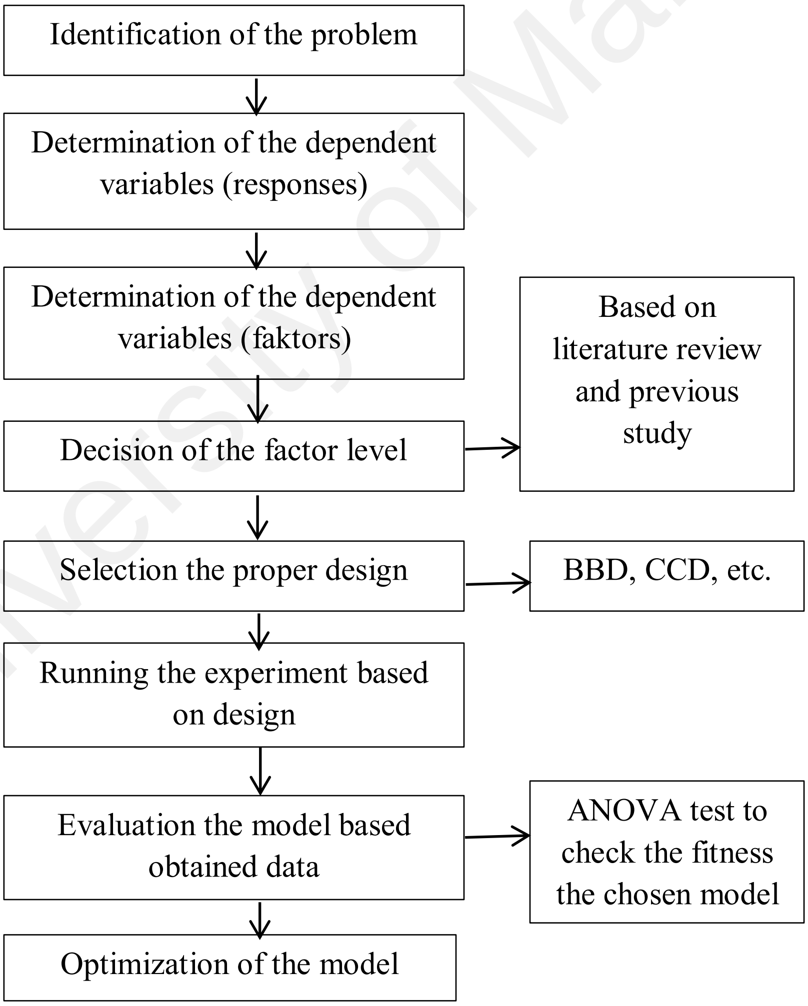

Figure 2.6: Step involve in response surface methodology.

The experimental data are evaluated to fit a statistical model (Linear, Quadratic, Cubic or 2FI (two factor interaction). The coefficients of the model are represented by constant term, A, B and C (linear coefficients for independent variables), AB, AC and BC (interactive term coefficient), A^2, B^2 and C^2 (quadratic term coefficient). Correlation coefficient (R^2), adjusted determination coefficient (Adj-R^2) and adequate precision are used to check the model adequacies; the model is adequate when its P value < 0.05, lack of fit P value > 0.05, $R^2 > 0.9$ and Adeq Precision >4. Differences between means can be tested for statistical significance using analysis of variance (ANOVA) (Sahin et al., 2017). The advantages offered by the RSM can be summarized as determining the interaction between the independent variables, modeling the system mathematically, and saving time and cost by reducing the number of trials (Maran et al., 2013). The steps that must be followed in order to apply this method correctly are shown in Figure 2.6.

2.2.6 *Melastoma malabathricum* as source for sensitizer

Melastoma malabathricum is a member of Melastomataceae family (Abdullah et al., 2006). It has been chosen as a source of natural sensitizer for DSSC.

Figure 2.7: Fruit pulp of *Melastoma malabathricum.*

Melastoma malabathricum is locally known as "*pokok senduduk*". Its flowers are purplish and its leaves are oblong. The fruits are deep purplish blue fruits, Figure 2.7. The seeds are orange in colour (Wong, 2008). The stems and leaves of *"pokok senduduk"* are rough and covered with bristles. The flowers of *"pokok senduduk"*, are in a clusters and formed the shoot tip (Wong, 2008). The fruit is known to contain anthocyanins and tannins (Abdullah et al*.,* 2006; Wong, 2008).

2.3 TiO_2 semiconductor

TiO_2 is the most versatile among other semiconductors. It delivers the highest efficiencies, is chemically stable, non-toxic, and available in large quantities. Its anatase nanocrystalline form gives the highest efficiency surface area, porosity, pore diameter, transparency and film thickness arfer optimized (Zukalová et al., 2005). It has wide bandgap and its HOMO and LUMO are suitably aligned with the electrolyte and dye respectively. The band gap for the rutile phase is of 3 eV and for the anatase is 3.2 eV. This is due to strong photon absorption at 413 and 388 nm respectively. In the dark, this semiconductor oxide is insulating (Kang et al., 2008).

Due to the nanometer size (~20nm), a single electron injection produces an electron number density of 10^{17} cm^{-3} resulting a conductance in the order of 10^{-4} S cm^{-1} and the electron diffusion coefficient of 10^{-4} cm^2 $S^{-1.}$ (Zukalová et al., 2005). TiO_2 nanotubes and TiO_2 nanorods have also produced comparable efficiency (Kang et al., 2008). Intensive researches have been carried out on nanorods structure in DSSC in order to examine of surface structure effect on DSSCs performance. This is because one-dimensional (1-D) structured TiO_2 nanorods have shown improved electrical and optical properties in the photoanodes of DSSCs (Cozzoli et al., 2003). Thus, intensive study in this TiO_2 nanorod has gain intention to researcher in DSSCs application in order to more improve DSSCs performance.

2.3.1 TiO_2 nanorod

TiO_2 nanorods are 1-D materials, that are densely TiO_2 packed nanoparticles. I-D nanorods can behave as single crystal and be involved in fast electron transport, are able to reduce possibilities for electron recombination. TiO_2 film with 1-D nanorods helps the electrolyte to enter the pores in the photoelectrode easily (Park et al., 2006). They can provide pathway for electrons and minimize the electron recombination (Ramakrishna et al., 2006). TiO_2 nanorod can scatter sunlight and make incident light stays longer in the cell. Much research has been conducted to study the effects of the 1-D structured TiO_2 on the photoelectrode (Jung et al., 2013). However, the efficiencies of these DSSCs are still low as compared to those based on TiO_2 nanoparticles. The main drawback is the smaller specific surface area of the TiO_2 nanoarrays (Baxter et al., 2006) which can lead to insufficient dye absorption and result in lower cell performance (Kumar et al., 2012). Therefore, engineering the elaborate microstructure of 1D nanomaterials to provide a large specific surface area becomes a hot issue. Among the methods to synthesis TiO_2 fibrous materials, electrospinning technique has become a popular method to prepare inorganic oxide nanofibers in recent years due to its simplicity and low cost. The microstructure of electrospun fibers can be control by optimizing the experimental parameters (Chen et al., 2013).

2.3.2 Electrospinning

Electrospinning is a widely used for the electrostatic fiber synthesis. It employs electrical forces for the formation of fibers with synthetic and natural polymer solutions (Ahn et al., 2006; Reneker & Yarin, 2008). Electrospinning can produce unique natural nanofibers/nanomats with pore structure that can easily controlled (Ramakrishna et al., 2005).

2.3.3 History of Electrospinning: Some Historical Facts

Electrospinning was first noticed by Rayleigh in 1897 (Chew et al., 2006). However it was Taylor"s work in 1969 on the electrical operation of rapid stream of liquid forced out of an orifice that laid the foundation of electrospinning. The word "electrospinning", was obtained from electrostatic spinning. However, its beginning can be traced back to 8 decades ago. Patents were successfully produced by Formhals from 1934 to 1944 that described an experimental method for producing of polymer filaments using electrospinning method (Chew et al., 2006; Huang et al., 2003; Dzenis, 2004).

An easy method to produce a smooth droplet of about 0.1 mm in diameter was designed by Vonnegut and Newbauer in 1952. An apparatus to produce light and ultra - thin fabrics that were non-woven by electrical spinning was patented by Simon in 1966 (Dzenis, 2004). An apparatus for electrospinning acrylic fibers was made by Baumgarten in 1971. These fibers had diameters between 0.05 and 1.1 µm. Since the 1980s, electrospinning process has gained a lot of attention due to of interest in nanotechnology. Fibers with radii of nanometers in length were easily fabricated using this technique (Huang et al., 2003). This technique has become so popular that according to Li & Xia (2003) more than 200 institutes all over the world studied numerous characteristics of the electrospinning and fiber production (Li & Xia, 2003).

2.3.4 Electrospinning process

Electrospinning uses electrostatic forces. Fibers are formed from melt or polymer solutions. The fibers diameter are range from micrometer to nanometer. The surface area is larger compared to that produced from conventional spinning procedures (Li & Xia, 2003). A direct current voltage of magnitude several tens of kilovolts is required to initiate electrospinning (Chew et al., 2006). At present, two electrospinning system are

2.4 Factors effecting the properties of electrospun fiber

Electrospinning are governed by solution, operational and enviromental parameters. Conductivity, viscosity, surface tension and molecular weight are solution parameters. The tips to collector distance, applied electric field, and feeding or flow rate are process or operational parameters. All these parameters affect morphology of the fibres. Proper manipulations of these parameters can give fiber morphologies and diameters that are desired (Kim et al., 2005). Ambient or environmental parameters include temperature and humidity also affects the electrospun nanofibers properties (Li & Xia, 2003).

2.5 Solution parameter that effect the properties of electrospun fiber

2.5.1 Viscosity

Very low viscosity yields irregular fibers. Very high viscosity will make polymer solution jets difficult to be ejected from the needle tip. Hence an optimum viscosity is necessary (Sukigara et al., 2003). Viscosities ranging between 1 and 215 poise has been reported (Deitzel et al., 2001). Polyethylene oxide (PEO) of different viscocities to produce nanofibers have been studied by Fong et al. (1999). They claimed that uniform nanofibers can be produced using viscosities between 1 and 20 poise (Kim et al., 2005).

2.5.2 Concentration

A minimum solution concentration is needed for fibers to form. It is now known that beads and fibers are gained at low solution concentration. On increasing concentration, the bead shapes changes from round to rod-like. Further increased in polymer concentration can resulting the formation of large diameters that is uniform. This is due to the resistant at higher viscosity (Ki et al., 2005; Haghi & Akbari, 2007). Researchers have found that, increased in solution concentration will increase the fiber diameter (Ki et al., 2005; Jun et al., 2003; Deitzel et al., 2001).

2.5.3 Molecular weight

The polymer molecular weight affects surface tension, viscosity, dielectric strength and conductivity in electrospinning process (Haghi & Akbari, 2007). If the molecular weight is too low, the solution forms beads instead of fibers. The use of high molecular weight polymer results in a solution that results larger fibers diameters. High molecular weight of the polymer will increase the solution viscosity due to polymer chain entanglements in a solution (Ki et al., 2005; Jun et al., 2003).

2.5.4 Conductivity and surface charge density

Conductivity and surface charge density play an important role in control the fiber morphology. According to Jun et al. (2003), solution conductivity is attributed to the type of polymer, doping, salt and solvent used. As the conductivity is increased nanofiber diameter decreased significantly. Influence of ions with addition of salt on the morphology electrospinning‟s fibers was studied by Zong et al. (2002).

It was stated that with the addition of ionic salts like NaCl to the electrospinning precursor resulted in uniform fiber with no bead. The fibers obtained also have smaller radii that range from 200 to 1000 nm. The modification of solution parameter by addition of salt to increase the solution conductivity has been utilize for other polymers such as PVA (Kim et al., 2005), polyamide-6 (Mit- Uppatham et al., 2004), polyacrylic acid (PAA), (Kim et al., 2005), and PEO (Fong et al., 1999).

2.6 Processing parameter

2.6.1 Applied Voltage

In the electrospinning process the voltage applied to the solution is important. Fibers are formed when threshold voltage is attained. The required applied voltage induces necessary charges to the solution and initiates the process. The shape of the initiating drop that leaves the needle tip changes with spinning parameters that include the feed rate, viscosity and voltage (Demir et al., 2002). Some observed that, researchers have suggested at higher voltages more polymer is ejected and this leads to large fibers to form (Kim et al., 2005; Demir et al., 2002). Some researchers stated that electrostatic repulsive force on the fluid increased when electric field strength increased. This favors the formation of a narrow of fibers. In many cases, however a high voltage results in a better solution stretching since the stronger columbic forces in the jet. This is happen due to the greater electric field and solvent evaporation from the fiber result in decrease in fiber diameter. However, at very high voltage the probabilities of the beads to produce is also greater (Deitzel et al., 2001; Demir et al., 2002).

2.6.2 Flow rate

The flow rate during electrospinning process influences the material transfer rate and the jet velocity. A lower feed rate will provide sufficient time for solvent evaporation (Yuan et al., 2010). Fiber and the pore radii have been observed to increases with solution flow rate increased for polystyrene (PS) fibers. Modification of the flow rate affects the morphologies structure of fibers. Several researches have shown that feed rate and fiber surface structure and size are correlated (Megelski et al., 2002; Zong et al., 2002). Higher feed rates lead to form fiber with beads since there is insufficient time for drying before the solution reaches the collector (Yuan et al., 2004; Kim et al., 2005; Zhou et al., 2005).

2.6.3 Distance: Tip to collector distance (TCD)

The syringe to collector distance is another strategy to manage fiber size and surface structure. It is now known that a minimal distance is necessary for the fibers to dry before they reach the collector. Beads have been observed if the the TCD are either too short or too long (Lee et al., 2009; Geng et al., 2005; Ki et al., 2005). The influence of syringe to the collector distance on surface structure is not as important as other parameters. This has was shown in the case of gelatin (Ki et al., 2005), poly (vinylidene fluoride), (Zhou et al., 2005), PVA (Kim et al., 2005) and chitosan (Geng et al., 2005). Flatter fibers can be formed at small TCD.

2.7 Application of electrospun nano fiber

In recent times, scientists have started to investigate numerous uses of electrospun fibers mats. This is due to fibers mat offer a number of benefits such as very high porosity, enhanced mechanical properties and high surface to volume ratio. This is because, in the electrospinning procedure, the process and solution can be simply manipulated to get the preferred fiber morphology and structure (Lee et al., 2009).

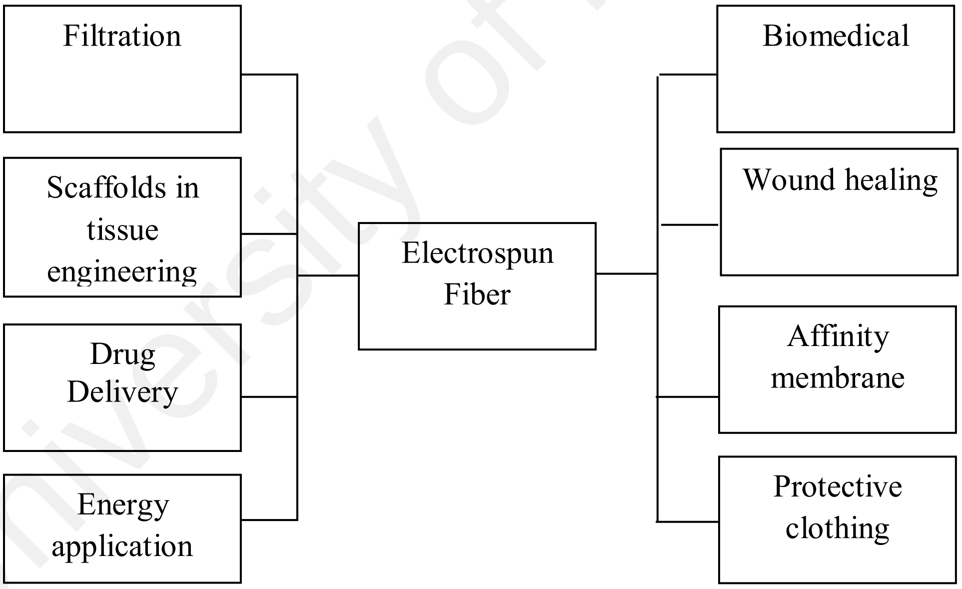

Figure 2.9: Electrospinning applications in different fields.

Fibre can be spun into various shapes using numerous polymers. Thus electrospinning is well known as versatile technique (Doshi and Reneker, 1995; Subiah et al., 2005). Application electrospinning in many fields are schematically shown in Figure 2.9.

2.7.1 Energy generation application

Potential used of polymeric conductive membranes include as photovoltaic device, electrostatic dissipation, electromagnetic interference protective, corrosion protection, used in fabrication of small electronic devices for example, sensors, Schottky junctions and actuators etc.(Senecal et al., 2002; Norris et al., 2000). These small fibers join integrated arrays of nanomachines to larger scale systems. Moreover, the Korea Institute of Science and Technology owns a patent on the fabrication of a lithium secondary battery comprising a fibrous film made by electrospinning (Norris et al., 2000). Additional fascinating development of a hybrid solar cell are employing conductive electrospun polymers doped with nanocrystalline semiconductor particles and photovoltaic dyes (Ziegler et al. 2005). Norris et al. (2000) and Ziegler et al. (2005) have been prepared numerous flexible photovoltaic membranes by utilising electrospun polyacrylonitrile (PAN) nanofiber dyed with copper phthalocyanine. Application of electrospun nanofiber in photovoltaic devices has intensively increased because of their low production cost and simple method (Ziegler et al. 2005).

2.7.2 Synthesis of TiO_2 by combination Sol gel and electrospinning

The methods to fabricate the 1D-structured TiO_2, include dip coating, electrospinning, and electrochemical methods. Sol gel is another common method that can be used to produce titania with high surface area (Jung et al., 2000). Recently, there have been determinations to synthesize metal oxide nanofibers using sol gel technique (Sarkar et al., 2012; Hilliard et al., 2017). The sol-gel method is commonly known as “soft chemistry” compared to more conventional industrial methods in glass and ceramic manufacturing that very high temperatures were needed (Sui et al., 2011). The sol-gel chemistry involves two distinct stages: solution and gelation: a sol is a colloidal suspension of solid particles, while a gel is an interconnected network of solid phase particles (Levy et al., 2015). The benefits of sol-gel approaches include: low operation temperatures, high yield and cost effective. Watthanaarun et al. (2005) reported another method which is combination of sol gel and electrospinning method. In this combination method, solution were prepared by adding high molecular weight polymer into solvent by utilized sol gel method before subjected to electrospinning process. The advantage using sol gel method in preparation of solution for electrospinning is easy to control the viscosity and concentration of polymer solution (Ziegler et al. 2005). Electrospinning is a flexible method. It is a simple methodology to yield polymeric inorganic nanofibers. The nature of the fiber structure e.g. morphology, and bead diameter can be controlled by tuning solution concentration, viscosity and surface tension. Many metal oxide nanofibers and nanotubes, including the oxides of silica, titanium, cobalt oxide, nickel oxide, zirconium, zinc and palladium have been prepared effectively by electrospinning method. The precursor electrospinnable metal oxides are prepared using sol-gel method. The usual catalyst used is acetic acid (Chen et al., 2013).

TiO_2 nanorods were prepared by electrospinning, sintering, and mechanical grinding. For preparing the electrospinning solution titanium isopropoxide (TIP,), poly(vinyl pyrrolidone) and acetic acid as catalyst were mixed followed by stirring at room temperature for a fixed time. The viscous gel solutions were electrospun into fibres at appropriate applied voltage and needle tip to a collector distance. The sintering step was carried out to acquire pure nanofibers. TiO_2 electrospun nanofibers were calcined for 3 h at 600 ^oC and then ground to form nanorods (Park et al., 2013)

2.8 Electrolyte

The electrolyte facilitates charge transport between photoanode and the counter cathode. Efficient charge transports between the electrodes with the efficiently regenerate the oxidized dye (Shelke et al., 2013). The electrolyte is prepared in the liquid state, but solid-state form can also be prepared (Yu et al., 2011). The significant disadvantage of DSSC using liquid electrolyte is less stable due to the volatility of the organic solvent in electrolyte. For the sake of commercialize and marketing, durability is a crucial component. This may be overcome by substituting the liquid electrolytes with gel electrolytes and this can be made by adding organic or inorganic (or both) materials. The benefits of gel electrolytes are non-combustible reaction products at the electrode surface, limited internal shorting and non-leakage of electrolytes (Pujiarti et al., 2018). In the previous decades, many investigations have been conducted on gel electrolyte, and great achievements have been reported. Although the pore and the surface of the TiO_2 is covered the dye, triiodide reduction by the photogenerated electrons results in dark current. Since the triiodide ions are relatively small it can either cross dye layer or enter the nano pores which cannot be entered by the dye molecules (Grätzel et al., 2005).

2.9 Counter Electrode

Another component where I^- is reduced in the counter electrode. It comprises of FTO glass deposited with platinum (Pt). Benefits of Pt are its great catalytic activity towards the iodide/triiodide redox reaction. Pt is an expensive element. Therefore, to keep the cell manufacturing costs low, only a few nanometer layer of Pt is needed. Pt is also chemically stable in the electrolyte. The function of the counter electrode is to transfer the electrons arriving from the external circuit back to the redox electrolyte. Hence, it must be well conducting and exhibit a low overvoltage for reduction of the redox couple. In addition, it may serve as mirror, reflecting the light transmitted by the photoelectrode to traverse it a second time, thus enhancing light absorption with a giving amount of dye (Radwan et al., 2015).

2.10 Additive

Additive is the substance added to sensitizer to improve a particular characteristic of DSSC. The additive usually constitutes a small percentage (Florio & Miller, 2004). Carbohydrates are known to possess plenty of hydroxyl groups which are non-ionizable under normal conditions, making them hard to bind with TiO_2 crystalline. However, it has been shown carbohydrate molecules can interact and aggregate with one another through hydrogen bonds and van der Waals‟ interactions (Spillmann & Burger, 1996). Biological examples include the cross-linking among hydrocarbon chains that leads to stable three-dimensional structures in cellulose, pectin and agarose, as well as the interactions among the oligosaccharides in glycolipids and glycoproteins on cell surfaces that provide adhesion force between cells (Bucior et al., 2004). Compared with monosaccharaides (glucose and fructose), disaccharides (maltose and sucrose) in general exhibited higher V_{oc}, FF and J_{sc}. In addition in DSSC, the dye needs attaching groups (-COOH, $-H_2PO_3$, $-SO_3H$, etc.) to improve the chemical bonding with the semiconductor surface and possibly to work as bridges for electron injection (Radwan et al., 2015). Since deoxycolic acid, DCA has –COOH (Chien et al., 2014) thus perhaps will combine with TiO_2 and improve the DSSC performance.

2.11 Summary

This chapter can be summarized that anthocyanin from *Melastoma malabathricum* is suitable alternative as natural sensitizer. Based on the literature review, RSM is promised method to optimized anthocyanin yield. Nanorod can be produce by electrospinning process and can be further utilized as component of photoanode for DSSC application.

CHAPTER 3: METHODOLOGY

3.1 Introduction

In the present work, the experimental and preparation method were divided into three sections. The first section will be focusing on natural dyes extract from *Melastoma malabathricum*. In this part, the preparation for identification of natural dyes from fruit pulps of *Melastoma malabathricum* using UPLC-ESI-MS/MS in order to prove and confirm the presence of anthocyanin content will be presented. Results from this analysis showed the presence of three types of anthocyanin which are delphinidin-3,5-glucoside, delphinidin-3-glucoside and proanthocyanidin. Hence, it will considered that the natural dye from fruit pulp of *Melastoma malabathricum* extract contain of anthocyanin compound. These extracts were also subjected to absorption spectroscopy which exhibited a peak at 523 nm. According to Castanena et al. (2009), the absorption peak of anthocyanin range within 450 to 600 nm and this findings for anthocyanin absorption is within the range stated in the reference. Hence, in this work, we designate the natural dye from fruit pulp of *Melastoma malabathricum* as anthocyanin since the highest colourant content were attribute to the anthocyanin content. anthocyanin from *Melastoma malabathricum* was used as the natural sensitizer in the DSSC fabrication. The anthocyanin extraction was first being optimized using response surface methodology (RSM) to obtain the optimized extraction parameters (addition of trifluoroacetic acid (TFA) to methanol, soaking time and extraction temperature) that can produce the highest yield of anthocyanin dyes. The commercial and synthesized TiO_2 were used for the preparation of different types of semiconductor photoanode. The TiO_2 nanofibers were synthesized by combining sol gel with electrospinning methods. Further grinding of TiO_2 nanofibers produced TiO_2 nanorods. These have preferred morphologies that yield high specific area. The nanorods were mixed with TiO_2 nanoparticles in the preparation of the working electrode. The cell containing only commercial TiO_2 nanoparticles were also fabricated. Sucrose and sucrose-DCA were added as additive to the anthocyanin dye in order to improve performance of natural dye sensitized solar cells. The electrolyte in this work was gel polymer electrolyte (GPE) using PAN as polymer host and I_2 added to form redox mediators. EC and PC were used as the solvent to dissolve the polymer and salts. At the same time EC and PC act as the plasticizers. Lithium iodide (LiI) and tetrapropylammonium iodide (TPAI) were used as the doping salts in the PAN-based GPE host to supply the iodide ions which acts as charge carriers in the electrolyte. 1-butyl-3-methylimidazolium iodide (BMII) ionic liquid (IL) was introduced in the GPE to increase the concentration of ion for enhancing the GPE conductivity. This optimized composition of the gel polymer electrolytes was based on the works of Bandara et al. (2015). The natural dye sensitizer was characterized using absorbtion spectroscopy, ultra performance liquid chromatography with electrospray ionization tandem mass spectrometry (UPLC-ESI-MS/MS) and CIE colour system. The synthesized TiO_2 was characterized using x-ray diffraction (XRD), field emission scanning electron microscopy (FESEM), energy dispersive x-ray analysis (EDX). The complete DSSCs using commercial and synthesized TiO_2 as a photoanode material were investigated via electrical *J-V* characterizations and incident photon to current efficiency (IPCE).

3.2 Optimization of anthocyanin extraction from fruit pulps of *Melastoma malabathricum* (pokok senduduk) by response surface methodology (RSM)

3.2.1 Materials

Fresh mature fruits of *Melastoma Malabathricum* as in Figure 3.1 were obtained from Kelantan, a state in Malaysia. The fully ripened fruits were peeled before they were freeze-dried.

Figure 3.1: Fruit pulp of *Melastoma malabathricum.*

The freeze-dried powder of fruit pulps of *Melastoma Malabathricum* were sieved to obtain 500 μm particles. Samples were stored at -20°C in amber bottles and kept until required for analysis. Methanol from systerm and trtrifluoroacetic acid (TFA) from Merck were used in *Melastoma malabathricum's* anthocyanin extraction. Potassium chloride (KCl) buffer (pH 1) and sodium acetate (CH_3CO_2Na) buffer (pH 4.5) from Sigma Aldrich were used for total anthocyanin analysis.

3.2.2 Experimental Design: Response Surface Methodology (RSM)

RSM was used to design the best condition for anthocyanin removal from fruit pulp of *Melastoma malabathricum*. RSM is an empirical optimization method and had been proven to investigate the relationship between experimental outputs (or responses) and independent factors or parameters (Borges et al., 2011).

Table 3.1: Indepedent variables and their level used for BBD.

Variables	Factors	Levels		
	X	-1	0	1
Trifluoroacetic acid (%)	A	0.5	1.75	3
soaking time (min)	B	60	120	180
Extraction temperature (°C)	C	30	55	80

In this study the independent factors were designated as A, B and C. In this approach, experimental lay out and statistical studies were accomplished using the Design-Expert software (version 6.0.8, Stat Ease Inc., Minneapolis, MN, USA). A three-level-three factor Box Benkhen Design (BBD) was used for evaluation of the best independent parameters of TFA concentration, extraction time and temperature. TFA concentration was designated as A, soaking time as B and extraction temperature as C. The levels are -1 for minimum and 1 for maximum. Extraction temperature, soaking time and Trifluoroacetic acid (TFA) content are listed in Table 3.1. The simplified step of RSM approach to optimize anthocyanin extraction shown in Figure 3.2.

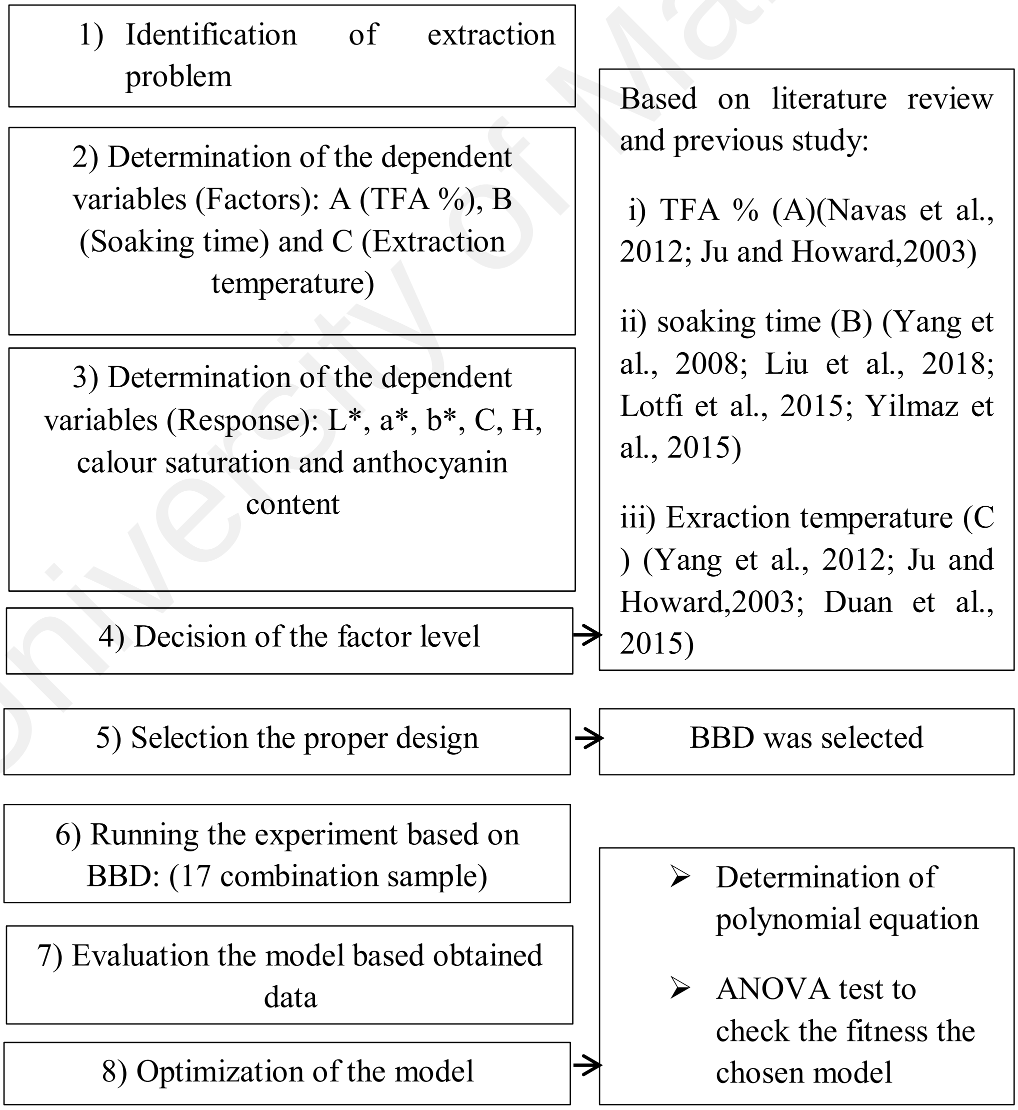

Figure 3.2: Flow chart of optimization of anthocyanin by RSM approach.

The response values were lightness (L*), hue angle (H^{o}), redness, a*, blueness,b*, C, colour saturation and anthocyanin content. The response function (Y) was separated into linear (A, B and C) quadratic (A^2, B^2 and C^2) and interactive components, (AB, AC and BC) according to the equation (3.1)

$$Y = b_0 + b_1A + b_2B + b_3C + b_{11}A^2 + b_{22}B^2 + b_{33}C^2 + b_{12}AB + b_{13}A + b_{23}BC \qquad (3.1)$$

Here b_0 is the cut-off on the vertical axis. Following Borges et al. (2011), b_1, b_2, and b_3 are linear coefficients, b_{11}, b_{22}, and b_{33} are squared coefficients; b_{12}, b_{13}, and b_{23} are interaction coefficients. Analysis of variance (ANOVA) was performed to check the significance of the selected model.

3.2.3 Anthocyanin extraction of *Melastoma malabathricum* based on BBD

Polar solvent can dissolve anthocyanins. Normally anthocyanins extraction from plants is done using acidified methanol. Hence, the pH of solvent is lowered. This impedes anthocyanin degradation (Cacace et al., 2002). 0.03g of freeze-dried *Melastoma malabathricum* fruit pulp was placed into 16 mL of methanol that has been acidified with different concentrations of TFA (0.5, 1.75, 3%). The mixtures were soaked at different temperatures 30 °C, 55 °C and 80 °C for 60, 120 and 180 min. 17 combination samples were prepared based on the BBD as in Table 3.2.

The prepared extractions were then centrifuged for 15 minutes at 5,000 rpm. The supernatant liquids were then filtered using whatman No.1 filter paper to remove any traces of residue. All experiments were performed in triplicate and the average value of the measurement was used. The experimental results obtained then analysed. These 17 samples were then subjected to visible spectroscopy to calculate total anthocyanin content and CIE colour analysis.

Table 3.2: Experimental runs of BBD design.

	Factor 1	Factor 2	Factor 3
Sample	A:TFA (%)	B:Soaking time (min)	C:Extraction temperature (°C)
1	0.5	60	55
2	3.0	60	55
3	0.5	180	55
4	3.0	180	55
5	0.5	120	30
6	3.0	120	30
7	0.5	120	80
8	3.0	120	80
9	1.75	60	30
10	1.75	180	30
11	1.75	60	80
12	1.75	180	80
13	1.75	120	55
14	1.75	120	55
15	1.75	120	55
16	1.75	120	55
17	1.75	120	55

3.2.4 Total anthocyanin content

The total anthocyanin content was determined following the spectrophotometric pH differential method (Lee et al., 2009). Samples were then diluted separately with 0.025 M potassium chloride (KCl) buffer (pH 1) and 0.4 M sodium acetate (CH_3CO_2Na) buffer (pH 4.5) that purchased from Sigma aldrich. Absorbance (A) of the mixture was measured at $A_{\lambda\text{vis-max}}$ and at 700 nm using Visible spectrophotometer. Absorbance was calculated as equation (3.2)

$$A=[(A_{\lambda\text{vis-max}} - A_{700})\text{pH1.0- } (A_{\lambda\text{vis-max}} - A_{700})\text{pH4.5} \qquad (3.2)$$

The total anthocyanin content was calculated as in the following equation 3.2 (Wrolstad et al., 2005):

$$\text{anthocyanin content}\left(\frac{\text{mg}}{\text{L}}\right) = \frac{A \times \text{MW} \times \text{ DF } \times \text{V} \times 1000}{\varepsilon \times \text{l} \times \text{c}} \qquad (3.3)$$

Here A is the absorbance obtained from equation (3.2). MW = 449.2 g/mol. DF=the dilution factor, ε is the molar absorptivity (26900), l =1cm, the cell path length and c is the sample concentration (mg/L).

3.2.5 Colour Analysis for obtaining L*, a*, b*, C, H, saturation and anthocyanin content

Avantes (AvaSoft 7.6) visible spectrophotometer with colour analysis software (CIE system) was used to record the spectral characteristics (in transmission mode, from 380 to 780 nm with a 2 nm bandwith). Colorimetric calculations were carried out using the CIE system via the CIELab colour coordinates. According to Birse (2007) the use of absorbance profiles and λ_{max} values are difficult for non-expert person to understand. This is because the λ_{max} value requires an understanding of absorbance values, wavelengths and colours before making a suitable judgment. Furthermore, absorbance spectrum from visible spectroscopy is not that straightforward in telling us the precise colour of a sample. This is because varying degrees of absorbance at different wavelength may imply that the colour observed is not simply red or orange. CIELab colour values are a more proper measurement for the colour of natural colourant. CIElab system can be used to describe all the colours visible to the human eye. Thus, colours can be precisely described using CIELab colour co-ordinates.

After procedure 3.2.4 and 3.2.5, we have obtained results for experiments proposed by BBD (Table 3.3). BBD analysis was performed to determine the effects of extraction parameters on the selected responses. The relationship between the output responses (L*, a*, b*, C, H°, saturation and anthocyanin content) and the input process variables (TFA content, soaking time and extraction temperature) are defined using a number of evaluation step. The evaluation step involved sequential model sum of squares (SMSS), model summary statistics and ANOVA as in the flow chart mentioned before in Figure 3.2. These steps were carried out in order to determine appropriate polynomial equations to represent the relationships between the input parameters. After determining the appropriate polynomial equation, the validation steps were carried out in order to check the residuals. The residuals give the difference between the experimental value and predicted value. This step is important to estimate experimental error. Finally, the extraction of anthocyanin from *Melastoma malabathricum* fruit pulp was optimized numerically. This step is to find the combination of factor levels that satisfy the responses and factors. The optimized combination of extraction parameters (TFA content, soaking time, extraction temperature) will be used for the anthocyanin natural colourant extraction for application as sensitizer in DSSC.

Table 3.3: BBD design table.

Sample	Factor 1	Factor 2	Factor 3	Response 1	Response 2	Response 3	Response 4	Response 5	Response 6	Response 7
	A:TFA (%)	B:Soaking Time (min)	C:Extraction temperature (°C)	L (%)	a*	b*	C	H°	Saturation	Anthocyanin content (mg/L)
1	0.5	60	55							
2	3	60	55							
3	0.5	180	55							
4	3	180	55							
5	0.5	120	30							
6	3	120	30							
7	0.5	120	80							
8	3	120	80							
9	1.75	60	30							
10	1.75	180	30							
11	1.75	60	80							
12	1.75	180	80							
13	1.75	120	55							
14	1.75	120	55							
15	1.75	120	55							
16	1.75	120	55							
17	1.75	120	55							

3.3 Analytical ultra performance liquid chromatography with electrospray ionization tandem mass spectrometry (UPLC-ESI-MS/MS)

An analytical ultra-performance liquid chromatography with electrospray ionization tandem mass spectrometry, UPLC-ESI-MS/MS (Perkin Elmer FX15) was used to identify the athhocyanin presents in *Melastoma malabathricum*. The anthocyanin fractions were examined with the AB Sciex 3200Q Trap, with reverse-phase column (Phenomenex Aqua C18) of 50 mm × 2.0 mm × 5 μM. Different solvents were used: (A) water with 0.1% formic acid and 5 mM ammonium formate and (B) acetonitrile with 0.1% formic acid and 5 mM ammonium formate with rapid screening at 15 min run time, setting up the subsequent gradients: from 10% B to 90% B from 0.01 min to 8 min, held for 3 min and back to 10% A in 0.1 min and reequilibrated for 5 min. The samples were dissolved in acidified methanol and filtered through a nylon filter of 0.22 µm. The electrospray ionization (ESI) was run in negative and positive ion modes set conditions: full scan, i.e. between 100 and 1200 m/z, MS/MS scan at 50 and 1200 m/z; 4500 V capillary voltages; nebulizer N2 purified gas, 40 psi, and 400 °C source temperature.

3.4 Synthesis of TiO_2 nanostructure for semiconductor photoanode

3.4.1 Materials

Titanium (IV) isopropoxide (TTIP), was purchased from Sigma–Aldrich and used as a precursor in electrospinning. Polyvinyl pyrrolidone (PVP) (MW: 1,300,000, Aldrich) was the polymer host for the electrospinning solution. The solvent for the electrospinning solution were ethanol (95.0%, Aldrich) and N, N-dimethylformamide, DMF (99.0%, Aldrich). The catalyst was acetic acid (99.0%, Aldrich).

3.4.2 Preparation of TiO_2 by sol-gel synthesis

In the present work, the combination of two methods (sol-gel and electrospinning) was implemented in order to produce TiO_2 nanofiber. The sol-gel method was employed to produce the precursor for TiO_2 which will be used in the electrospinning solution. After obtaining the nanofibers from electrospinning, the nanofibers were sintered to get pure TiO_2 nanofibers. Nanorod will be obtained after mechanical grinding. 0.44 g of PVP was dissolved in 3 mL ethanol in a glass bottle. In order to optimize the polymer concentration, different amounts of PVP polymer (0.44, 0.50, 0.56, 0.62 and 0.68 g) were used for the preparation of electrospinning solution. To ensure stable and continuous electrospinning, 1 mL of DMF which is a polar organic solvent was added to PVP solution. Subsequently, a polymerization catalyst of 1.2 mL acetic acid was added to the solution. 0.6 mL of (TTIP) precursor was added and the sol gel was stirred for 30 min to obtain homogeneous solutions. In order to optimize fiber formation and investigate the influence of electrospinning setup, the same procedure with the optimized amount of polymer concentration, were used to prepare the TiO_2 sol-gel solution. All the above procedures were conducted in a controlled environment in order to minimize the moisture content.

3.4.3 Preparation of TiO_2 by electrospinning

The electrospinning setup consisted of a 1 mL syringe and needle, a syringe pump, a high positive voltage supply, and aluminum foil wrapped around a rotating drum collector as shown in Figure 3.4. 1 mL sample containing TiO_2 solution from sol gel method will be transferred to a syringe that was attached to a syringe pump with a fixed flow rate, and electrospun by applying high voltage with the distance from the needle tip to collector that has been fixed.

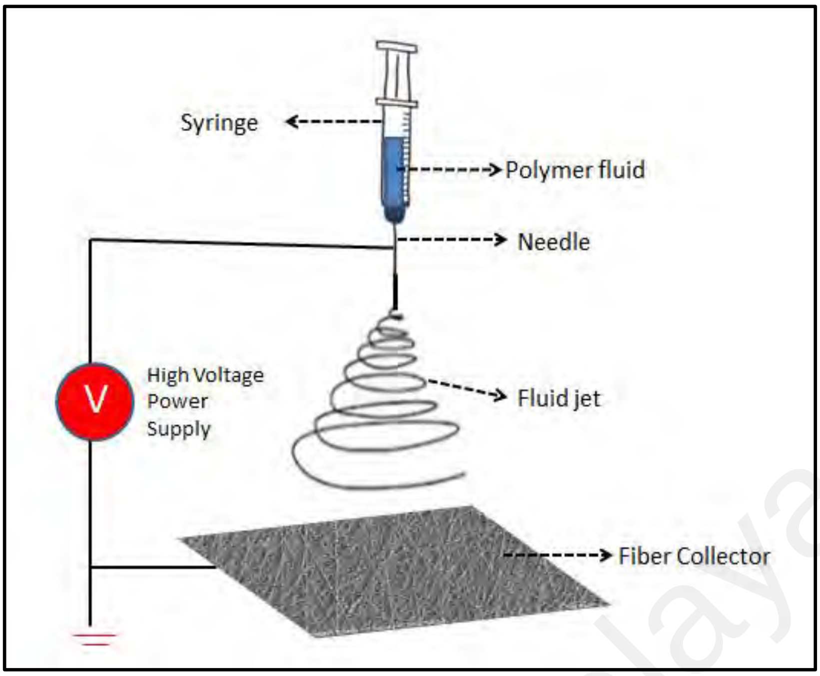

Figure 3.4: Schematic diagram of electrospinning setup.

3.4.4 Effect of polymer concentrations on nanofiber formation

In this study, the concentration of polymer will be investigated to produce beadless fiber and to study the relationship between solution concentration and fiber diameter. In order to study the optimized polymer concentration that can produce beadless TiO_2 nanofibers, flow rate, TCD and applied voltage were set constant for all different polymer concentrations in the electrospinning process. This was done to ensure that only the polymer concentration was the variables. The electric fields are the same for all samples.

Table 3.4: Effect of polymer concentrations on nanofiber formation.

Designation	PVP (wt.%)	PVP (g)	TTIP (mL)	Ethanol (mL)	DMF (mL)	Acetic acid (mL)
P1	8	0.44	0.6	3	1	1.2
P2	9	0.50	0.6	3	1	1.2
P3	10	0.56	0.6	3	1	1.2
P4	11	0.62	0.6	3	1	1.2
P5	12	0.68	0.6	3	1	1.2

Table 3.4 displays the experimental conditions for the preparation of the TiO_2 polymer solution with different polymer concentrations. During the experiments, the flow rate of the spinning solution was fixed at 2 mL/h, the distance from TCD and applied voltage was set at 14 cm and 17 kV, respectively. The optimized wt% of PVP was subjected to further studies.

3.4.5 Effect of applied voltage on nanofiber formation

In electrospinning, an essential element is the applied voltage. Only after achieving the threshold voltage, fiber formation occurs. The threshold voltage charged the solution and initiated the process. Thus in this work, the applied voltage in electrospinning process will be intensively study in order to investigate the relationship between fiber formation and bead formation with applied voltage.

Table 3.5: Effect of applied voltage on nanofiber formation for P5 (12 wt.%).

Sample designation	Distance (wt.%)	Applied voltage (kV)	Applied Electric Field (kV/cm)
V1	14	15	1.07
V2	14	16	1.14
V3	14	17	1.21
V4	14	18	1.28
V5	14	19	1.35
V6	14	20	1.43
V7	14	21	1.50

At higher voltage the chances of bead formation is high (Deitzel et al., 2001; Demir et al., 2002). To study the applied voltage effect on nanofiber formation, TCD was set constant as listed in Table 3.5. The electrospun PVP-TiO_2 composite was collected as white film on a grounded Aluminium (Al) foil wrapped on the rotating drum. The sheet was peeled off from the Al foil and then were sintered at different temperatures of 400, 500, 600 °C, respectively for 5 h in order to remove PVP and to obtain pure TiO_2 nanofibers with anatases crystallite form (Chen et al., 2013).

3.5 Characterization of TiO_2 nanostructure

3.5.1 Field Emission Scanning Electron Microscope (FESEM)

FESEM provides ultra-high resolution imaging at low accelerating voltages and small working distances. FESEM will be used to study morphology of the fibers produced. FESEM is capable of detecting fiber diameters and morphologies. For FESEM, samples are acquired to be electrically conductive especially at high magnification. Hence the electrospun polymers were coated with gold or platinum. FESEM is an effective tool to investigate the surface of a solid nanoscale material. This technique offers higher resolution and large depth focus compared to an optical and electron microscope (Jun et al., 2003). Surface morphology and fiber formation of electrospinning nanofibers and the photoanode films were investigated in this study by using FESEM (Hitachi Su8220). To study the morphology of nanofibers from electrospinning, the samples were prepared in membrane fiber while nanorods and nanoparticle samples are in powder form. The investigation also involved the morphology of coated photoanode film prepared. All samples were coated with thin layer of platinum by sputtering technique to make them conducting and to avoid any possible charging effect during FESEM analysis. The morphology of the samples were then evaluated using Image J to measure the diameter and particle size.

3.5.2 Energy Dispersive X-Ray Analysis (EDX)

EDX is a relatively simple but powerful technique. It can identify the elements and their composition. The EDX equipment is affixed to FESEM apparatus. EDX is non-destructive method. EDX operates by detecting X-rays produced by a sample. An electron beam excites atoms in a sample and X-rays with energy characteristic of the atoms and a spectrum is obtained (Jun et al., 2003). In this study, the synthesized nanofiber of TiO_2 was characterized using EDX (Hitachi model).

3.5.3 X-Ray Diffraction (XRD)

XRD is a rapid technique to analyses the phase of a crystalline material. It provides information on the unit cell of a material (Cozzoli et al., 2003). XRD can be used to study crystal structures and atomic spacing. XRD is based on the constructive interference of monochromatic X-rays. The interaction of the incident rays with the sample produces constructive interference (and a diffracted ray) when conditions satisfy by Bragg‟s law (3.5) (Cozzoli et al., 2003):

$$2\ d \sin \theta = n\ \lambda \tag{3.5}$$

where d is lattice atomic spacing, θ is the scattering angle (Bragg‟s angle), n is reflection order and λ is x-ray wavelength. In the present study, XRD analysis was used to identify the nature of the nanostructured materials to confirm phase structure. The XRD analysis was performed using Olympus BTX Benchtop XRD Diffractometer. The data were collected using Cu-Kα radiation from the range of diffraction angle from 2θ = 5° to 55° with X-ray wavelength, = 1.5406 Å. For the XRD measurements, the samples were prepared in powder form. XRD patterns were analyzed using Origin 8.1 software. The XRD peaks were indexed by comparing with the similar diffraction pattern reported in the literature.

3.6 Preparation of samples for DSSCs application

3.6.1 Fluorine-doped Tin Oxide (FTO) Glass Cleaning Process

FTO glass has been used as current collector. Also, its transparency ensures efficient absorption of solar spectrum by the sensitizer. Its high conductivity allows efficient transport of electrons to the outer circuit. The FTO glass was cut into 1 cm x 2 cm rectangular pieces. Cleaning of the FTO substrate surface is vital to remove any contaminants. This is done to enhance the wettability of chemical precursors or doctor blade paste that used in DSSC fabrication. The FTO substrate then immersed in detergent for 5 minutes and rinsed with distilled water twice. After that, the FTO were immersed and rinsed several time with acetone. The dried and cleaned FTO glass was immersed in propanol until boiling (353 K) to eliminate any remaining organic impurities on the FTO surface. The FTO glasses were dried again and then kept in a petri dish and sealed with parafilm prior to use.

3.6.2 Preparation of photoanode using commercial TiO_2

15 nm size (P90) and 21 nm size (P25) TiO_2 nanoparticles from Sigma-Aldrich were used in preparation of photoanode. In the preparation of first layer (compact layer) TiO_2 (P90) powder of 0.5 g mass were mixed with 2 mL of nitric acid, HNO_3 (pH 1) and ground for 30 min using a mortar and pestle. Nitric acid from Sigma-Aldrich was added to make it acidic and to improve adhesion between TiO_2 nanoparticles and FTO glass. This blocking or compact layer is to help prevent the electrolyte from entering the FTO glass which may cause shorting.

The TiO_2 paste was spin-coated on the conducting FTO glass at 2350 rpm for 60 s before being sintered at 723 K for 30 min. During the coating process, an adhesive tape was used to cover a part of the FTO glass for electrical contacts. For the second porous layer, 0.5 g of TiO_2 (P25) powder were mixed with 2 mL solution of nitric acid, HNO_3 (pH 1) and ground for 30 min using a mortar and pestle. 0.1 g of poly (ethylene glycol) (PEG) and 0.1 g of Triton X-100 surfactant were added to the TiO_2 (P25) slurry and ground again to get a homogeneous paste. PEG was added to create porosity when it evaporated on heating process. PEG was purchased and Triton X-100 was purchased from Sigma-Aldrich. The surfactant is to ensure wetting of the solution onto the FTO glass (Yusuf et al., 2016). The solution paste can then be applied on the compact layer by the doctor blade technique. The doctor bladed layer was then sintered again at 723 K

3.6.6 Extraction Preparation of Anthocyanin from *Melastoma malabathricum* for DSSC of dye sensitizer for DSSCs

For DSSCs using commercial TiO_2 system, a mass of 0.1 g (1 wt.%) of *Melastoma malabathricum* freeze-dried powder was mixed with 9.9 g of methanol with trifluoroacetic acid content of 0.5%. The mixture was soaked at 80 °C for 132 min. The solutions were then centrifuged for 15 minutes at 5,000 rpm. The procedure were repeated for different concentration of *Melastoma.malabathricum* anthocyanin (1wt%, 3 wt%, 5 wt%, 7 wt% and 9 wt.%).The concentration of *Melastoma malabathricum* anthocyanin that gave highest efficiency were used for composite system. It is to be noted that extraction parameters were the optimized parameters obtained after stage 8 of Figure 3.2.

3.6.7 Additive

Different additive were added to enhance the performance of composite system DSSCs with optimum nanorod amount. The additives used for this study were sucrose and sucrose-DCA. The mixture of sucrose and DCA additive is in 1:1 ratio. The additives were added into optimized anthocyanin extract at different percentage (2%, 4%, 6%, 8% and 10%).

3.6.8 Fabrication of dye sensitized solar cells (DSSCs)

DSSCs sensitized with anthocyanin from *Melastoma malabathricum*, active area 0.196 cm^2 were prepared by placing the prepared GPE on the TiO_2/dye photoanode and covering the GPE with the platinum (Pt) counter electrode. The optimized gel polymer electrolyte of PAN-TPAI-LiI-BMII with I^-/I^-_3 redox mediator was used as the charge transport medium in DSSCs. In this study, the DSSC configuration was glass/FTO/TiO_2/anthocyanin/electrolyte/Pt/ FTO/glass as displayed in Figure 3.8.

- The mixture of TiO_2 nanoparticles (P-25) and 10% TiO_2 nanorod semiconductor (optimize nanorod percentage added which gave highest efficiency) that immersed in anthocyanin-additive (sucrose and sucrose-DCA) at different additive percentage (2%, 4%, 6%, 8% and 10 wt.%). For sucrose system sample designated as C1, C2, C3, C4 and C5. While for sucrose-DCA system sample were designated as D1, D2, D3, D4 and D5 respectively.

The composite photoanode of the DSSC sample that subjected to FESEM analysis as in procedure 3.5.1 were:

- The mixture of TiO_2 nanoparticles (P-25) and electrospinning TiO_2 nanorod semiconductor at different percentage of nanorod (10%, 20%, 30%, 40% and 50%).

3.7.1 Visible Spectroscopy

In visible spectroscopy, the sample absorbs photons, from the electromagnetic radiation field. The intensity of the absorption varies with the wavelength of the electromagnetic radiation. This makes the absorption spectrum. Absorption spectroscopy was performed between 300 and 800 nm. The electromagnetic spectrum is the complete range of all wavelengths and frequencies. It starts from a very low level energy with longer wavelengths and low frequencies and has the potential to turn into a very high level energy when it consists of shorter wavelengths and higher frequencies. Each of the different types of radiation occupies a definite place in the spectrum, but their divisions are not very definite. Most organic molecules are transparent to some regions of the electromagnetic spectrum. This may be the ultraviolet (UV), wavelength between 190 and 399 nm and visible (VIS), wavelengths from 400 nm to 800 nm. All samples were scanned from 400 to 800 nm using visible spectroscopy (JASCO V-730) model.

3.7.2 *J-V* Analysis

Photocurrent density-photovoltage or *J-V* characteristics of the DSSCs were measured using the Autolab potentiostat-galvanostat instrument under the exposure of light illumination (1000 W m^{-2}) with 0.196 cm^2 active area. The TiO_2 photoanode was connected to the counter/reference wire while the Pt electrode was connected to the working electrode wire. The two wires were then connected to the Autolab potentiostat-galvanostat. Figure 3.9 shows the normal of *J-V* curve plotted for the DSSCs measurement (Jinchu et al., 2014).

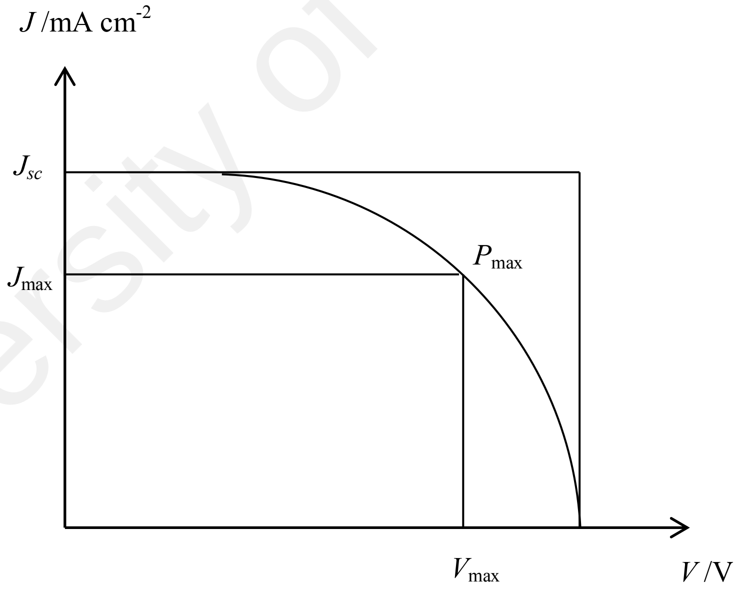

Figure 3.9: *J-V* curve plot in DSSCs.

3.7.3 Short Circuit Photocurrent Density (J_{sc})

The short-circuit current is the current through the solar cell when the voltage across the solar cell is zero (i.e., when the solar cell is short circuited). Usually written as J_{sc}, the short-circuit current. J_{sc} is the photocurrent per unit area (mA cm^{-2}). It is strongly related to the IPCE. The short-circuit current depends on a number of factors which are area of the solar cell, number of photon, the spectrum to incident light and optical properties (Radwan et al., 2015).

3.7.4 Open Circuit Photovoltage (V_{oc})

The open-circuit voltage, $V_{oc,}$ is the maximum voltage available from a solar cell, and this occurs at zero current. The open-circuit voltage corresponds to the amount of forward bias on the solar cell due to the bias of the solar cell junction with the lightgenerated current (Saji et al., 2010; Jinchu et al.,2014)

3.7.5 Fill Factor (FF)

The fill factor (*FF*) is a measure of the maximum power output from a solar cell. It represents the squareness of the *J-V* curve and is defined as the ratio of the maximum power to the product of V_{oc} and J_{sc} for the solar cell:

$$\mathrm{FF} = \frac{J_{opt}V_{opt}}{J_{sc}V_{oc}} \tag{3.6}$$

where, V_{opt} and J_{opt} are the voltage and current at maximum power point. Fill factor, being a ratio of the same physical parameters, has no unit. Fill factor is a function of the series and shunt resistance of the solar cell. For DSSCs, it reflects the extent of electrical and electrochemical losses during cell operation. To obtain higher fill factor improvement of the shunt resistance and decrement of the series resistance, with reduction of the voltage for diffusion and charge transfer is required (Saji et al., 2010)

3.7.6 Series Resistance

Series resistance, R_s in a solar cell is the result of contact resistance and charge transfer resistance in the semiconductor material. Series resistance reduces the fill factor affecting the maximum power output, while excessively high value of R_S can also reduce the short-circuit current. The open-circuit voltage is not affected since, at V_{oc} the total current flow through cell itself and hence through the series resistance is zero (Jinchu et al., 2014).

3.7.7 Shunt Resistance

Significant power losses caused by the presence of a shunt resistance, R_{sh}, are typically due to manufacturing defects, rather than poor solar cell design. In DSSC low shunt resistance provides a substitute path for light generated current and hence lowers the power output which in turns decreases fill factor. The shunt resistance R_{sh} is attributed to slow back electron transfer rate from TiO_2 to electrolyte in TiO_2/ dye/ electrolyte interface. The effect of low shunt resistance is reduced fill factor and lower open-circuit voltage affecting the maximum power output. The short-circuit voltage is not affected unless for a very low value, since at J_{sc} the total current flows through the outer path and hence through the shunt resistance is low. An approximation of the shunt resistance can be calculated from the slope of the *J-V* curve at the short circuit current point (Zhou et al., 2011). Figure 3.10 present the solar cell equivalent circuit that shows the series (R_s) and shunt resistance (R_{sh}).

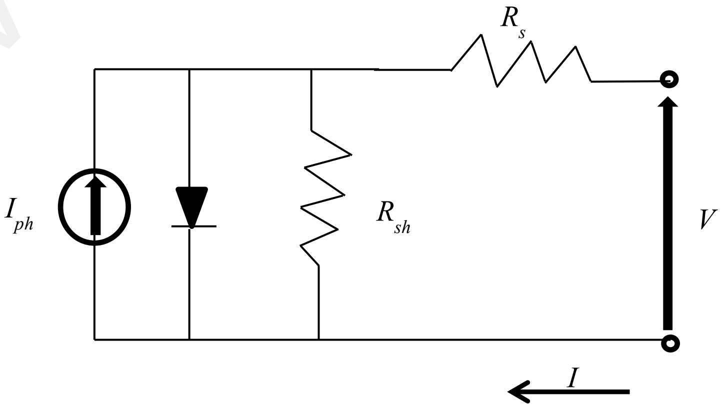

Figure 3.10: Solar cell equivalent circuit that shows the series (R_s) and shunt resistant (R_{sh}).

3.7.8 Solar Energy to Electricity Conversion Efficiency (η)

The overall solar energy to electric power conversion efficiency (η), the key parameter of the device, measures how much power is converted by the cell in comparison to the amount of absorbed light that reaches the device. It is given by the ratio of the maximum output power to the incident solar power (Pin). The overall sunlight to electric power conversion efficiency of a DSSC is given by the following expression (Saji et al., 2010):

$$\eta(\%) = \frac{J_{sc}V_{oc}FF}{P_{in}} \times 100\% \tag{3.7}$$

where, Pin is the power input from the sunlight. Efficiency is generally expressed in percentage.

3.7.9 Incident photon to current efficiency (IPCE)

The spectral response of the dye sensitized solar cell depends on the absorption properties of the dye. The incident photon to current conversion efficiency (IPCE), also known as external quantum efficiency (EQE), is one of the key parameters of quantitative characterization of the solar cell performance for the fact that IPCE shows the spectral response of solar cells to various incident wavelengths. It measures how efficiently the incident light of a specific wavelength is converted into electron/hole pairs, by measuring the ratio between the number of electrons generated by the solar cell and collected at the external circuit and the number of photons of a given wavelength shining on the solar cell (Jinchu et al., 2014). In this study, all samples were scanned from 300 to 900 nm using Newport-Oriel model. The IPCE are calculated following equation (Jinchu et al., 2014):

$$IPCE\ (\lambda) = \frac{1240\ \times J_{sc}}{\lambda \times \phi} \tag{3.8}$$

where J_{sc} is the short circuit current (mA/cm^2), λ is the wavelength (nm) and ϕ is the incident radiative light flux (W/m^2).

3.7.10 Electrochemical Impedance Spectroscopy (EIS)

EIS has also proven to be a powerful technique for studying the fundamental components and processes in solar cells, and is now widely applied to the study of DSSCs as well. In this study AUT 85988 advanced electrochemical system (Metrohm Autolab B.V. PGSTAT 128N Netherlands) was used to measure the impedance of in the frequency range between 10 mHz to 100 kHz DSSCs under 1000 W m^{-2} light illumination. The potential of each DSSC was set at their open circuit voltage (V_{oc}), respectively.

3.8 Summary

This chapter can be summarized that the optimization of anthocyanin were analysed using RSM method. The optimized extraction was applied in commercial P25 TiO_2 nanoparticles as sensitizer by vary concentration of anthocyanin. The optimized anthocyanin concentration were further utilized in composite (NPs-NRs) at diferent nanorod ratio. The morphology TiO_2 nanostructure obtained were observed using FESEM. The characteristic of DSSCs samples were analysed using visible spectroscopy, *J-V* analysis, IPCE and EIS. The detail method, apparatus and characterization are presented in this chapter.

CHAPTER 4: RESULTS FOR IDENTIFICATION AND OPTIMIZATION OF ANTHOCYANIN EXTRACTION FROM FRUIT PULPS OF *Melastoma malabathricum* BY RESPONSE SURFACE METHODOLOGY (RSM)

4.1 Introduction

Chapter 4 begins with confirmation of major anthocyanin type from fruit pulp of *Melastoma malabathricum* using mass spectrometer UPLC-ESI-MS/MS. In this study, BBD was chosen to optimize anthocyanin extraction from *Melastoma malabathricum* with three independent variables (A: wt % of trifluoroacetic acid, B: soaking time and C: extraction temperature). The response variables were the CIE measurement in terms of lightness, L*, redness, a*, blueness, b*, chromaticity, C, hue angle, H°, saturation,S and anthocyanin content. The relationship between the output responses (L*, a*, b*, C, H°, saturation and anthocyanin content) and the input factor variables (TFA content, soaking time and extraction temperature) are defined using RSM modelling approach which justify the polynomial mathematical equations that represent both relationship. Determination of the process parameters and potential interactions affecting the all response values were done by carrying out analysis of variance (ANOVA). The desirability function method was employed to produce the ideal optimized extraction conditions for anthocyanin extraction from fruit pulp of *Melastoma malabathricum*.

4.2 Identification of anthocyanin extraction from fruit pulps of *Melastoma malabathricum* by UPLC-ESI-MS/MS

Figure 4.1 shows the mass spectra of anthocyanin-rich extract of *Melastoma malabathricum* taken using the mass spectrometer UPLC-ESI-MS/MS. Based on UPLC-ESI-MS/MS study, the main types of anthocyanin detected is (a) delphinidin-3,5-glucoside, (b) delphinidin-3-glucoside and (c) proanthocyanindin based on ACD/ACD/Labs advanced chemometrics mass fragmentation predictive software.

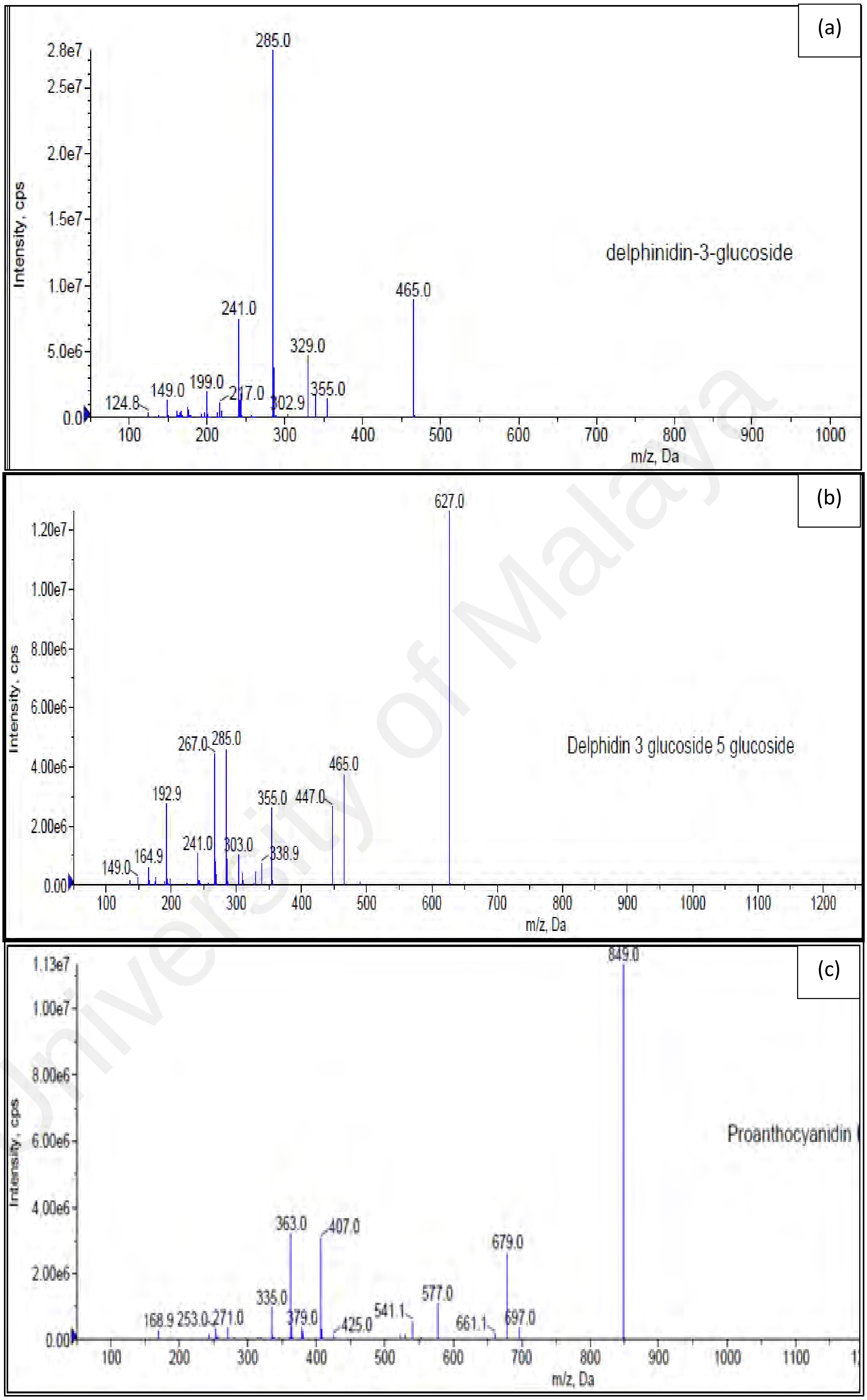

Figure 4.1: Mass spectrometer UPLC-ESI-MS/MS of anthocyanin from *Melastoma mabathricum.*

4.3 Response surface methodology (RSM)

4.3.1 A box-behnken design (BBD) analaysis of L*, a*, b*, C, H°, saturation and anthocyanin content

In this study, BBD was used in order to design the experiment with three independent variables which were (A: % wt of trifluoroacetic acid, B: soaking time and C: extraction temperature) at three levels (-1, 0, 1). The minimum factor were set at (-1) and maximum factor at (1). The midpoint (0) was generated by BBD. For the identification of minimum and maximum level are based on previous study and literature review. The minimum factor level decided for TFA content were 0.5 % while 3 % for maximum factor level. The minimum factor level decided for TFA content were 0.5 % while 3 % for maximum factor level. This range were chosen based on studied conducted by Navas et al. (2012) and Ju & Howard (2003). The minimum factor level decided for soaking time were 60 min while 180 min for maximum factor level. This range were selected based on other researchers (Yang et al., 2008; Liu et al., 2018; Lotfi et al., 2015; Yilmaz et al., 2015). The minimum factor levels decided for extraction temperature were 30 ^{0}C while 30 ^{0}C for maximum factor level. This range were selected based on other researchers (Yang et al., 2008; Sharif et al., 2010; Duan et al., 2015).

The response variables were the CIE measurement in terms of lightness, L*, redness, a*, blueness, b*, chromaticity, C, hue angle, H°, colour saturation, S and anthocyanin content. 17 run as in Table 4.1 that generated from BBD that have centre points. Centre point was used to determine the experimental error. This combination of factor was carried out in order to find out the optimal extraction conditions. 17 samples were prepared according to different combination factors that generated by BBD and were subjected for CIE colour analysis and anthocyanin content. The experimental results were included to the BBD table as recorded in Table 4.1. BBD analysis was performed to determine the effects of extraction parameters on the selected responses. The relationship between the output responses (L*, a*, b*, C, H°, S and anthocyanin content) and the input factors (TFA content, soaking time and extraction temperature) are defined using a number of evaluation step.

Table 4.1: Experimental runs of BBD design and the response.

	Factor 1	Factor 2	Factor 3	Response 1	Response 2	Response 3	Response 4	Response 5	Response 6	Response 7
Sample	A:TFA (%)	B:Soaking Time (min)	C:Extraction temperature °C	L (%)	a*	b*	C	H°	Saturation,S	Anthocyanin content mg/L
1	0.5	60	55	76.33	46.40	-4.19	46.59	354.84	0.6104	3074.77
2	3.0	60	55	71.12	57.07	-0.64	57.07	359.36	0.8025	4022.58
3	0.5	180	55	70.88	56.07	-2.94	56.15	357.00	0.7922	3850.49
4	3.0	180	55	74.59	51.18	-1.74	51.21	358.05	0.6866	3214.22
5	0.5	120	30	72.17	52.17	-3.42	52.28	356.25	0.7244	3263.50
6	3.0	120	30	71.21	56.25	-0.54	56.25	359.45	0.7899	4117.36
7	0.5	120	80	73.00	59.50	-0.77	59.50	359.26	0.8151	4596.25
8	3.0	120	80	70.01	55.58	-0.62	55.58	359.36	0.7939	3768.00
9	1.75	60	30	76.46	50.38	-7.26	50.90	351.80	0.6657	3256.04
10	1.75	180	30	73.95	52.63	-6.43	53.02	353.03	0.7169	3371.17
11	1.75	60	80	75.43	50.25	-7.12	50.75	351.94	0.6728	3333.00
12	1.75	180	80	73.70	55.98	-4.47	56.16	355.43	0.7620	3640.92
13	1.75	120	55	71.86	59.58	-5.11	59.80	355.10	0.8322	3839.50
14	1.75	120	55	73.40	56.42	-6.42	56.78	353.51	0.7737	3798.73
15	1.75	120	55	73.23	53.48	-7.03	53.94	352.51	0.7366	3610.59
16	1.75	120	55	72.49	56.36	-5.82	56.66	354.10	0.7816	3833.24
17	1.75	120	55	73.55	54.15	-6.18	54.50	353.49	0.7409	3881.10

4.3.2 Stastical analysis for determination of appropriate polynomial equation to represent rsm model

Data obtained from the 17 run sample were analysed using sequential model sum of squares (SMSS), model summary statistics and analysis of varience (ANOVA) as shown in Table 4.2, 4.3 and 4.4 respectively in order to determine suitable polynomial equations to show the relationships between the input parameters (TFA content coded as A, soaking time coded as B and extraction temperature coded as C) and the all response study. These tests were done to decide about the suitability of models to represent the L*, a*, b*, C, H°, saturation and anthocyanin content response.

4.3.2.1 Sequential model sum of squares (SMSS), for L*, a*, b*, C, H°, saturation and anthocyanin content response

Experimental data were first evaluated by using SMSS in order to choose the appropriate model. For the SMSS, the maximum order polynomial was selected when the additional model are significant. In this analysis, the aliased model will be eliminated. Table 4.2 (a) to (g) showed the SMSS tested output for L*, a*, b*, C, H°, saturation and anthocyanin content response which showed that the cubic is an aliased model. Thus the cubic model will not favorable for this analysis. The quadratic models are suggested as the appropriate model since the model have lower p-value ($p=0.0021$) designed for L* response which shows strength of significance as in Table 4.2(a). Table 4.2(b) showed the SMSS output for a* response which also indicates the cubic model was found to be aliased. The quadratic are suggested as the appropriate model since the model are found to have lower p-value which is $p= 0.0639$ which shows strength of significance. Another model studied for response of b* ($p=0.0002$), C($p=0.0579$), H° ($p=0.0001$), saturation ($p=0.026$) and anthocyanin content ($p=0.0032$) as in Table 4.2(c), Table 4.2 (d), Table 4.2 (e), Table 4.2(f) and Table 4.2 (g) respectively, also gave similar results which showed that quadratic model are suggested since have lower p value. To further check the adequacy of the model, the next step that needs to perform was model summary stastistic.

Table 4.2: Sequential model sum of squares (SMSS) analysis for (a) L* (b) a*, (c) b*, (d) C, (e) H°, (f) saturation and (g) anthocyanin content response.

(a) Sequential model sum of squares (SMSS) analysis for L* model

Source	Sum of Squares	DF	Mean Square	F Value	Prob > F	
Mean	90940.81	1	90940.81			
Linear	8.889175	3	2.963058	0.82659	0.5025	
2FI	21.07393	3	7.024642	2.75188	0.0982	
Quadratic	22.00351	3	7.334502	14.57243	0.0021	Suggested
Cubic	1.492275	3	0.497425	0.979704	0.486	Aliased
Residual	2.03092	4	0.50773			
Total	90996.3	17	5352.724			

(b) Sequential model sum of squares (SMSS) analysis for a* model.

Source	Sum of Squares	DF	Mean Square	F Value	Prob > F	
Mean	50161.3	1	50161.3			
Linear	33.8599	3	11.2866	0.91266	0.4618	
2FI	79.596	3	26.532	3.26865	0.0675	
Quadratic	50.6383	3	16.8794	3.86978	0.0639	Suggested
Cubic	7.63773	3	2.54591	0.44479	0.7342	Aliased
Residual	22.8953	4	5.72382			
Total	50355.9	17	2962.11			

(c)Sequential model sum of squares (SMSS) analysis for b* model.

Source	Sum of Squares	DF	Mean Square	F Value	Prob > F	
Mean	328.24	1	328.24			
Linear	14.77	3	4.92	0.83	0.4996	
2FI	7.42	3	2.47	0.36	0.786	
Quadratic	64.94	3	21.65	33.3	0.0002	Suggested
Cubic	2.52	3	0.84	1.65	0.3124	Aliased
Residual	2.03	4	0.51			
Total	419.92	17	24.7			

Table 4.2, continued.

(d)Sequential model sum of squares (SMSS) analysis for C model

Source	Sum of Squares	DF	Mean Square	F Value	Prob > F	
Mean	50564.03	1	50564.03			
Linear	31.04658	3	10.34886	0.862171	0.4852	
2FI	77.71315	3	25.90438	3.307118	0.0657	
Quadratic	49.73074	3	16.57691	4.057507	0.0579	Suggested
Cubic	7.185325	3	2.395108	0.44741	0.7326	Aliased
Residual	21.41312	4	5.35328			
Total	50751.12	17	2985.36			

(e) Sequential model sum of squares (SMSS) analysis for H^0 model

Source	Sum of Squares	DF	Mean Square	F Value	Prob > F	
Mean	2149161	1	2149161			
Linear	17.43918	3	5.813058	0.731387	0.5515	
2FI	6.689625	3	2.229875	0.230754	0.8729	
Quadratic	90.49255	3	30.16418	34.37931	0.0001	Suggested
Cubic	2.534275	3	0.844758	0.936674	0.5014	Aliased
Residual	3.60748	4	0.90187			
Total	2149282	17	126428.3			

(f) Sequential model sum of squares (SMSS) analysis for S model

Source	Sum of Squares	DF	Mean Square	F Value	Prob > F	
Mean	9.483572	1	9.483572			
Linear	0.010155	3	0.003385	0.897856	0.4685	
2FI	0.024395	3	0.008132	3.303786	0.0658	
Quadratic	0.017545	3	0.005848	5.791211	0.026	Suggested
Cubic	0.001142	3	0.000381	0.256917	0.8534	Aliased
Residual	0.005927	4	0.001482			
Total	9.542736	17	0.561337			

(g)Sequential model sum of squares (SMSS) analysis for anthocyanin content model

Source	Sum of Squares	DF	Mean Square	F Value	Prob > F	
Mean	2.30E+08	1	2.30E+08			
Linear	2.54E+05	3	84802.34	0.5	0.6869	
2FI	1.34E+06	3	4.48E+05	5.28	0.0193	
Quadratic	7.17E+05	3	2.39E+05	12.69	0.0032	Suggested
Cubic	86846.35	3	28948.78	2.58	0.1909	Aliased
Residual	44848.68	4	11212.17			
Total	2.32E+08	17	1.37E+07			

4.3.2.2 Model summary statistics for L*, a*, b*, C, H°, saturation and anthocyanin content response

Model summary statistics were carried out to further check the adequacy of the selected model. Model summary statistics output in Table 4.3 show that the cubic model was eliminated as it is aliased. Thus, the cubic models cannot be preferred for further modeling of output data. The quadratic model for L* in Table 4.3(a) show the highest values for the R^2 (0.9365), adjusted R^2 (0.8549) and predicted R^2 (0.5125) compared to the linear and 2FI (two-factor interaction) models. Table 4.3 (b) shown that quadratic model for a* response resulted in highest values for the R^2 (0.8431), adjusted R^2 (0.6414) and predicted R^2 (0.1883). While for b* response as in Table 4.3 (c) resulted in highest values for the R^2 (0.9504), adjusted R^2 (0.8866) and predicted R^2 (0.5259). As in Table 4.3 (d) for C response showed the highest values for the R^2 (0.8471), adjusted R^2 (0.6506) and predicted R^2 (0.2067) respectively. For H^0 response in Table 4.3(e) showed high value of R^2 (0.9491), adjusted R^2 (0.8838) and predicted R^2 (0.6175) compared to 2FI model. As in Table 4.3 (f) and Table 4.3(g) for S and anthocyanin content response also show the highest values for the R^2 which were 0.8805 and 0.9462 respectively. For all model studied, the quadratic model was not only found to have maximum R^2, adjusted R^2, predicted R^2, but also exhibited low p-values. Hence the quadratic model was chosen for further analysis. These analyses suggested the relationship between input parameters and resultant L*, a*, b*, C, H°, saturation and anthocyanin content response can be modeled using quadratic equations. To more improve the model, the next step that needs to carry out was ANOVA based on the how significant the input parameters affect the response studied. At this stage, the insignificant factors will be eliminating. Thus after this step, then appropriate quadratic equation will be determine.

Table 4.3: Model summary statistics analysis for (a) L* (b) a*, (c) b*, (d) C, (e) H°, (f) saturation and (g) anthocyanin content response.

(a)Model summary statistics analysis for L* response.

Source	Std Dev.	R-Squared	Adjusted R-Squared	Predicted R-Squared	
Linear	1.8933	0.1602	-0.0336	-0.7179	
2FI	1.5977	0.5399	0.2639	-1.1970	
Quadratic	0.7094	0.9365	0.8549	0.5125	Suggested
Cubic	0.7126	0.9634	0.8536		Aliased

(b)Model summary statistics analysis for a* response.

Source	Std. Dev.	R-Squared	Adjusted R-Squared	Predicted R-Squared	
Linear	3.5166	0.1739	-0.0167	-0.5459	
2FI	2.8491	0.5829	0.3327	-0.3812	
Quadratic	2.0886	0.8431	0.6414	0.1883	Suggested
Cubic	2.3925	0.8824	0.5295		Aliased

(c)Model summary statistics analysis for b* response.

Source	Std. Dev.	R-Squared	Adjusted R-Squared	Predicted R-Squared	
Linear	2.43	0.1611	-0.0324	-0.5794	
2FI	2.64	0.2421	-0.2126	-2.1599	
Quadratic	0.81	0.9504	0.8866	0.5259	Suggested
Cubic	0.71	0.9778	0.9114		Aliased

(d)Model summary statistics analysis for C response

Source	Std. Dev.	R-Squared	Adjusted R-Squared	Predicted R-Squared	
Linear	3.4646	0.1659	-0.0265	-0.5522	
2FI	2.7987	0.5813	0.3301	-0.3457	
Quadratic	2.0213	0.8471	0.6506	0.2067	Suggested
Cubic	2.3137	0.8855	0.5421		Aliased

(e)Model summary statistics analysis for H° response

Source	Std. Dev.	R-Squared	Adjusted R-Squared	Predicted R-Squared	
Linear	2.8192	0.1444	-0.0530	-0.6305	
2FI	3.1086	0.1998	-0.2803	-2.4443	
Quadratic	0.9367	0.9491	0.8838	0.6175	Suggested
Cubic	0.9497	0.9701	0.8805		Aliased

Table 4.3, continued

(f)Model summary statistics analysis for S response

Source	Std. Dev.	R-Squared	Adjusted R-Squared	Predicted R-Squared	
Linear	0.0614	0.1716	-0.0195	-0.5819	
2FI	0.0496	0.5839	0.3343	-0.5052	
Quadratic	0.0318	0.8805	0.7269	0.5346	Suggested
Cubic	0.0385	0.8998	0.5993		Aliased

(g)Model summary statistics analysis for anthocyanin content response

Source	Std. Dev.	R-Squared	Adjusted R-Squared	Predicted R-Squared	
Linear	410.64	0.104	-0.1028	-0.8305	
2FI	291.23	0.6533	0.4453	-0.5939	
Quadratic	137.16	0.9462	0.8770	0.4034	Suggested
Cubic	105.89	0.9817	0.9267		Aliased

4.3.2.3 Analysis of variance (ANOVA) selected model for L*, a*, b*, C, H°, saturation and anthocyanin content response

Summary of analysis of variance (ANOVA) for the selected quadratic polynomial model for L*, a*, b*, C, H°, saturation and anthocyanin content response was performed to check the adequacy and fitness of the developed models. This step is very important in order to improve the quadratic polynomial model by eliminate the terms factor that are not significant and known as reduce quadratic polynomial model. Determination of the process parameters and potential interactions affecting the L*, a*, b*, C, H°, saturation and anthocyanin content response were done by carrying out analysis of variance (ANOVA) on the quadratic response surface reduced model since some of factor terms need to eliminate to improve the model studied. ANOVA analysis of L* response is summarized in Table 4.4. At a 95% confidence level, a model was considered significant, if the p value less than 0.05. The “Model F-value” of 17.48 is significance of the model. Possibly that the deviation is due to noise is only 0.01%.

Based on the significant p-value of less than 0.05, TFA content(A), (0.0158), soaking time (B), (p=0.0081), interaction between TFA content and soaking time,(AB) (p=0.0001), TFA content quadratic term (A^2), (p=0.0012), soaking time quadratic term (B^2), (p=0.0003) were the significant influencing factors of the resultant L* values. These indicate that most of the variation in the response could be explained by the developed models. p-values greater than 0.05 indicates that the model terms are not significant as referred by extraction temperature term with p=0.3928. This insignificant model term was not being reduced since the extraction temperature terms are required to support the hierarchy of the reduced quadratic model. The overall model for L* is significant since p is equal to 0.0001, therefore this model can be accepted and used to explain the experimental data.

The lack of fit analysis also supported the accuracy of selected model. Lack-of-Fit is the variation due to the model inadequacy. The F-value of 0.70 in Table 4.4 implies that the model is accurate. Therefore, there is no evidence to indicate that the models do not adequately explain the variation in the responses. The ANOVA of response surface reduced quadratic regression model demonstrated that the quadratic models were highly significant, evident from Fisher‟s F-test with high F value and low p- value.

Adequacy of the developed models was tested by performing coefficient of determination (R^2), adjusted coefficient of determination (R^2 adj) and predicted coefficient of determination (predicted R^2). R^2 is defined as the ratio of of sum of squares due to regression to the total sum of squares and is interpreted as the proportion of the variability in the data explained by the ANOVA. The values of R^2 was 0.9315 is relatively high values which imply that more than 93% of experimental data can be explained by the reduced model. The adjusted R^2 value corrects the R^2 value for the sample size and for the number of terms in the model. The values of adjusted R^2 were 0.8782, in which are also high and indicate a high correlation between the observed and the predicted values. The predicted R^2 was 0.7017 is in reasonable agreement with the R^2 adj. The predicted R^2 should fall no more than 0.2 below the adjusted R^2. Meanwhile, the adequate precision measures the signal to noise ratio. A ratio greater than 4 is desirable. The ratio of 15.4730 indicates an adequate signal. This model can be used to navigate the design space.

Table 4.4: ANOVA analysis of the reduced quadratic model for L*.

Source	Sum of Squares	DF	Mean Square	F Value	Prob > F	
Model	51.69	7	7.38	17.48	0.0001	significant
A	3.71	1	3.71	8.79	0.0158	
B	4.84	1	4.84	11.45	0.0081	
C	0.34	1	0.34	0.81	0.3928	
A^2	9.16	1	9.16	21.68	0.0012	
B^2	13.91	1	13.91	32.92	0.0003	
AB	19.89	1	19.89	47.09	< 0.0001	
AC	1.03	1	1.03	2.44	0.1528	
Residual	3.80	9	0.42			
Lack of Fit	1.77	5	0.35	0.70	0.6542	not significant
Pure Error	2.03	4	0.51			
Cor Total	55.49	16				

Table 4.5 shows the ANOVA analysis of reduced quadratic model for a* response. With F- value of 6.83 with p = 0.0051 implies the a* model is significant. The “Lack of Fit F-value” of 0.28 and p value is 0.9038 implies that the lack of fit is not significant relative to pure error. Interaction between TFA content and soaking time (AB) resulted in more significant value, p=0.0023 compared to AC and BC which resulted in p value equal to 0.0587 and 0.3718 respectively. The values of R^2 was 0.8415 is relatively high values which imply that more than 84% of experimental data can be explained by the reduced model. The adjusted R^2 value corrects the R^2 value for the sample size and for the number of terms in the model. The value of adjusted R^2 was 0.7183, in which are also high and indicate a high correlation between the observed and the predicted values.

The predicted R^2 was 0.5683 is agreeable with the adjusted R^2 of 0.7183. Adequate precision measures the signal to noise ratio. A ratio greater than 4 is desirable (Kaur et al., 2018). The ratio of 9.4838 indicates an adequate signal. This model can be used to navigate the design space.

Table 4.5: ANOVA analysis of the reduced quadratic model for a*.

Source	Sum of Squares	DF	Mean Square	F Value	Prob > F	
a* Model	163.79	7	23.4	6.83	0.0051	significant
A	4.4	1	4.4	1.28	0.2867	
B	17.29	1	17.29	5.04	0.0513	
C	12.18	1	12.18	3.55	0.0921	
B^2	50.33	1	50.33	14.69	0.004	
AB	60.53	1	60.53	17.66	0.0023	
AC	16.04	1	16.04	4.68	0.0587	
BC	3.03	1	3.03	0.88	0.3718	
Residual	30.84	9	3.43			
Lackof Fit	7.95	5	1.59	0.28	0.9038	not significant
Pure Error	22.9	4	5.72			
Cor Total	194.63	16				

The “Model F-value” of 18.02 with p= 0.0001 implies the model is significant for b* response as in Table 4.6. The “Lack of Fit F-value” 1.6 implies that the lack of fit is not significant. There is a 33.36% chance that “Lack of Fit F-value” this large due to deviation. The ANOVA of response surface reduced quadratic regression model demonstrated that the quadratic models were highly significant, evident from Fisher‟s F-test with high F value and low p- value. Based on ANOVA, the significant p-value of less than 0.05, TFA content (A, p= 0.0087), extraction temperature (C, p=0.0187), TFA content quadratic term (A^2) ($p < 0.0001$) and interaction between TFA content with soaking time (AB) (p=0.0269) were the significant influencing factors of the resultant b* values. This indicates that most of the variation in the response could be explained by the developed models. P-values greater than 0.05 indicates that the model terms are not significant as referred by soaking time term with p=0.1537. This insignificant model term was not being reduced since the soaking time term are required to support the hierarchy of the reduced quadratic model. The overall model for b* is significant since P is equal to 0.0001, therefore this model can be used to explain the experimental data.

Table 4.6: ANOVA analysis of the reduced quadratic model for b*

Source	Sum of Squares	DF	Mean Square	F Value	Prob > F	
b*Model	85.58	7	12.23	18.02	0.0001	significant
A	7.57	1	7.57	11.15	0.0087	
B	1.65	1	1.65	2.43	0.1537	
C	5.56	1	5.56	8.2	0.0187	
A^2	63.58	1	63.58	93.7	< 0.0001	
B^2	1.53	1	1.53	2.26	0.1674	
AB	4.73	1	4.73	6.97	0.0269	
AC	1.86	1	1.86	2.75	0.1319	
Residual	6.11	9	0.68			
Lack of Fit	4.08	5	0.82	1.6	0.3336	not significant
Pure Error	2.03	4	0.51			
Cor Total	91.68	16				

Adequacy of the developed models was tested by performing regression analysis. The values of R^2 was 0.9334 is relatively high values which imply that more than 93.34 % of experimental data can be explained by the reduced model. The value of adjusted R^2 was 0.8816, in which are also high and indicate a high correlation between the observed and the predicted values. The predicted R^2 was 0.6951 is in reasonable agreement with the adjusted R-squared of 0.8816 since predicted R^2 should fall no more than 0.2 below the adjusted R^2. Meanwhile, the adequate precision measures the signal to noise ratio. The ratio of 12.2 indicates an adequate signal since more than 4. This model can be used to navigate the design space.

Table 4.7 shows the quadratic response surface reduced model for C response. Soaking time quadratic term, (B^2) (p=0.0036) and interaction between TFA content with soaking time (AB) (p=0.0020) and interaction between TFA content with extraction temperature (AC, p=0.0556) were the significant influencing factors of the resultant C values. The overall model for C is significant since P is equal to 0.0047, therefore this model can be accepted and used to explain the experimental data. The values of R^2 was 0.84489 is relatively high values which imply that more than 84.49% of experimental data can be explained by the reduced model. The predicted R^2 was 0.5795 is in reasonable agreement with the adj R-squared of 0.7242 since predicted R^2 should fall no more than 0.2 below the adjusted R^2. The ratio of 9.608302 indicates an adequate signal.

Table 4.7: ANOVA analysis of the reduced quadratic model for C.

Source	Sum of Squares	DF	Mean Square	F Value	Prob > F	
CModel	158.07	7	22.58	7	0.0047	significant
A	3.91	1	3.91	1.21	0.2996	
B	15.76	1	15.76	4.89	0.0544	
C	11.38	1	11.38	3.53	0.0931	
B^2	49.31	1	49.31	15.29	0.0036	
AB	59.44	1	59.44	18.44	0.0020	
AC	15.56	1	15.56	4.83	0.0556	
BC	2.71	1	2.71	0.84	0.3835	
Residual	29.02	9	3.22			
Lack of Fit	7.61	5	1.52	0.28	0.8999	not significant
Pure Error	21.41	4	5.35			
Cor Total	187.09	16				

TFA content (p= 0.0083), soaking time (p= 0.0603), TFA content quadratic term (p < 0.0001), were the significant influencing factors of the resultant H° values. The overall model for H° is significant since p is equal to 0.0003 as in Table 4.8, therefore this model can be accepted and used to explain the experimental data. The values of R^2 was 0.946255 is relatively high values which imply that more than 84.49% of experimental data can be explained by the reduced model. The adjusted R^2 value corrects the R^2 value for the sample size and for the number of terms in the model. The predicted R^2 was 0.723726 is in reasonable agreement with the adj R-squared of

0.89251 since predicted R^2 should fall no more than 0.2 below the adjusted R^2. Meanwhile, the adequate precision measures the signal to noise ratio. The ratio of 11.5126 indicates an adequate signal. This model can be used to navigate the design space for H^{o} response.

Table 4.8: ANOVA analysis of the reduced quadratic model for H^{0}.

Source	Sum of Squares	DF	Mean Square	F Value	Prob > F	
H^{0}Model	114.2727	8	14.2841	17.60	0.0003	significant
A	9.8346	1	9.8346	12.12	0.0083	
B	3.8781	1	3.8781	4.78	0.0603	
C	3.7265	1	3.7265	4.59	0.0645	
A^2	88.0031	1	88.0031	108.47	< 0.0001	
B^2	3.9286	1	3.9286	4.84	0.0589	
AB	3.0102	1	3.0102	3.71	0.0902	
AC	2.4025	1	2.4025	2.96	0.1236	
BC	1.2769	1	1.2769	1.57	0.2451	
Residual	6.4903	8	0.8113			
Lack of Fit	2.8829	4	0.7207	0.80	0.5834	not significant
Pure Error	3.6075	4	0.9019			
Cor Total	120.7631	16				

Based on the significant ANOVA in Table 4.9, p-value of less than 0.05, soaking time (B) (p= 0.0436), interaction between TFA content and soaking time (AB) (p=0.0012), soaking time quadratic term (B^2), (p=0.0028), were the significant influencing factors of the resultant S values. The overall model for S is significant since P is equal to 0.0063, therefore this model can be accepted and used to explain the experimental data. The values of R^2 was 0.8744 which is is relatively high values which imply that more than 87.44% of experimental data can be explained by the reduced model. The adjusted R^2 value corrects the R^2 value for the sample size and for the number of terms in the model. The predicted R^2 was 0.6036 is in reasonable agreement with the adj R-squared of 0.7489 since predicted R^2 should fall no more than 0.2 below the adjusted R^2. Meanwhile, the adequate precision measures the signal to noise ratio. A ratio greater than 4 is desirable. The ratio of 9.0404 indicates an adequate signal. This model can be used to navigate the design space.

Table 4.9: ANOVA analysis of the reduced quadratic model for S.

Source	Sum of Squares	DF	Mean Square	F Value	Prob > F	
S Model	0.051735	8	0.006467	6.9642	0.0063	significant
A	0.002138	1	0.002138	2.3021	0.1677	
B	0.005324	1	0.005324	5.7334	0.0436	
C	0.002693	1	0.002693	2.8999	0.1270	
A^2	0.000731	1	0.000731	0.7868	0.4009	
B^2	0.016856	1	0.016856	18.1523	0.0028	
C^2	0.00012	1	0.00012	0.1295	0.7283	
AB	0.022157	1	0.022157	23.8605	0.0012	
AC	0.001879	1	0.001879	2.0237	0.1927	
Residual	0.007429	8	0.000929			
Lack of Fit	0.001502	4	0.000375	0.2534	0.8939	not significant
Pure Error	0.005927	4	0.001482			
Cor Total	0.059164	16				

Extraction temperature(c), p= 0.0045, interaction between TFA content and soaking time (p=0.0001) (AB), interaction between TFA content and extraction temperature (AC), (p=0.0001), soaking time quadratic term (B^2) (0.0001), TFA content quadratic term (A^2) were the significant influencing factors of the resultant anthocyanin content values as in Table 4.10. These indicate this variation in the response could be explained by the developed models. The overall model for anthocyanin content is significant since p is equal to 0.0001, therefore this model can be accepted and used to explain the experimental data. The value of R^2 was 0.9424 which imply that more than 87.44% of experimental data can be explained by the reduced model. The predicted R^2 was 0.7144 is in reasonable agreement with the adj R^2 of 0.8975 since predicted R^2 should fall no more than 0.2 below the adjusted R^2. Meanwhile, the adequate precision measures the signal to noise ratio. The ratio of 16.603 indicates an adequate signal since more than 4. This model can be used to navigate the design space for anthocyanin response.

Table 4.10: ANOVA analysis of the reduced quadratic model for anthocyanin content.

Source	Sum of Squares	DF	Mean Square	F Value	Prob > F	
Model	2.31E+06	7	3.29E+05	21.02	<0.0001	significant
A	14208.77	1	14208.77	0.91	0.3658	
B	19052.5	1	19052.5	1.22	0.2987	
C	2.21E+05	1	2.21E+05	14.12	0.0045	
A^2	85171.45	1	85171.45	5.44	0.0446	
B^2	6.55E+05	1	6.55E+05	41.83	0.0001	
AB	6.27E+05	1	6.27E+05	40.04	0.0001	
AC	7.07E+05	1	7.07E+05	45.15	< 0.0001	
Residual	1.41E+05	9	15666.59			
Lack of Fit	96150.6	5	19230.12	1.72	0.3106	not significant
Pure Error	44848.68	4	11212.17			
Cor Total	2.45E+06	16				

4.3.2.4 Appropriate polynomial equation to represent RSM model for L*, a*, b*, C, H°, saturation and anthocyanin content response

Appropriate polynomial equation to represent RSM model for L*, a*, b*, C, H°, saturation and anthocyanin content response are listed below as equation (4.1) to (4.7) Where A is TFA%, B is the soaking time and C is the extraction temperature. This equation is used to calculate the predicted value in order to optimize the response model studies. This predicted value is further evaluated and compared with experimental value in order to estimate experimental error.

$$\mathrm{L}^* = 72.91 - 0.68\,A - 0.78B - 0.21C - 1.48\,\mathrm{A}^2 - 0.17\mathrm{C}^2 + 2.23\mathrm{AB} - 0.51\mathrm{A} + 0.19\mathrm{BC} \tag{4.1}$$

$$\mathrm{a}^* = 56 + 0.005\,A + 2.438B + 1.11C - 0.71\,\mathrm{A}^2 - 4.53\mathrm{B}^2 + 0.84C^2 - 2.67\mathrm{AB} - 1.75\mathrm{AC} + 0.87\mathrm{BC} \tag{4.2}$$

$$\mathrm{b}^* = -5.94 - 0.97\,A + 0.45\mathrm{B} - 0.83\mathrm{C} - 3.88\,\mathrm{A}^2 - 0.60\,\mathrm{B}^2 - 1.09\,\mathrm{AB} - 0.68\,\mathrm{AC} \tag{4.3}$$

$$\mathrm{C}^{*} = 56.14 + 0.70\ \mathrm{A} + 1.40\mathrm{B} - +1.19\ \mathrm{C} - 3.41\ \mathrm{B}^2 - 3.85\ \mathrm{AB} - 1.97\ \mathrm{AC} + 0.82\ \mathrm{BC} \quad (4.4)$$

$$\mathrm{H}^{0} = +353.86 + 1.11\mathrm{A} + 0.7\mathrm{B} + 0.68C + +4.57\mathrm{A}^2 - 0.96\mathrm{B}^2 - 0.17\mathrm{C}^2 + -0.87\ \mathrm{AB} - 0.022\ \mathrm{AC} \quad (4.5)$$

$$\mathrm{S} = +0.77 - +0.016\ \mathrm{A} + 0.026\mathrm{B} - 0.21C + 0.018\ \mathrm{A}^2 - -0.063\mathrm{B}^2 - 0.0053\ \mathrm{C}^2 - 0.074\mathrm{B} - 0.51\mathrm{AC} + 0.19\mathrm{BC} \quad (4.6)$$

$$\text{Anthocyanin content } = +3793.35 + 42.14\ \mathrm{A} + 48.80\mathrm{B} + 166.26\ \mathrm{C} + 142.03\ \mathrm{A}^2 - 393.97\ \mathrm{B}^2 - 396.02\ \mathrm{AB} - 420.53\ \mathrm{AC} \quad (4.7)$$

4.4 Validation of the model for L*, a*, b*, C, H^0, saturation and anthocyanin content

Data attained were further examined to check the residuals. The residuals are the differences between the experimental and predicted value. Normality of the residuals was observed by plotting the normal probability plot of residuals which represents the normal distribution of the residuals. Normal percentage probability versus studentized residuals were constructed to evaluate correlation and to identify the satisfactory of developed models. Figure 4.2(a) to 4.2 (g) shows the normal probability plots of residuals. It is observed that residuals followed normal distribution well as majority of the data points are reasonably close to a straight line. This indicates that experimental results are correlated well with predicted value. The error terms are considered normally distributed since the data points is close to the straight line. Obvious S-shape pattern were not observed in this figure. S-shape is not preferable because its indicates that there are some abnormalities with obtained experiment data. The plotted graph shows the values were low (value between -3 and 3). This suggested that the variance of observation is constant for the response value (Shafiʿī et al. 2013). If the value of the studentized residual exceeds ±3, the data should be investigated for checking errors.

Obtaining a smaller residual value is favored as this shows the degree of deviancy from predicted model. Therefore, theoretical validations of the reduced models for L*, a*, b*, C, H, saturation and anthocyanin content response was confirmed.

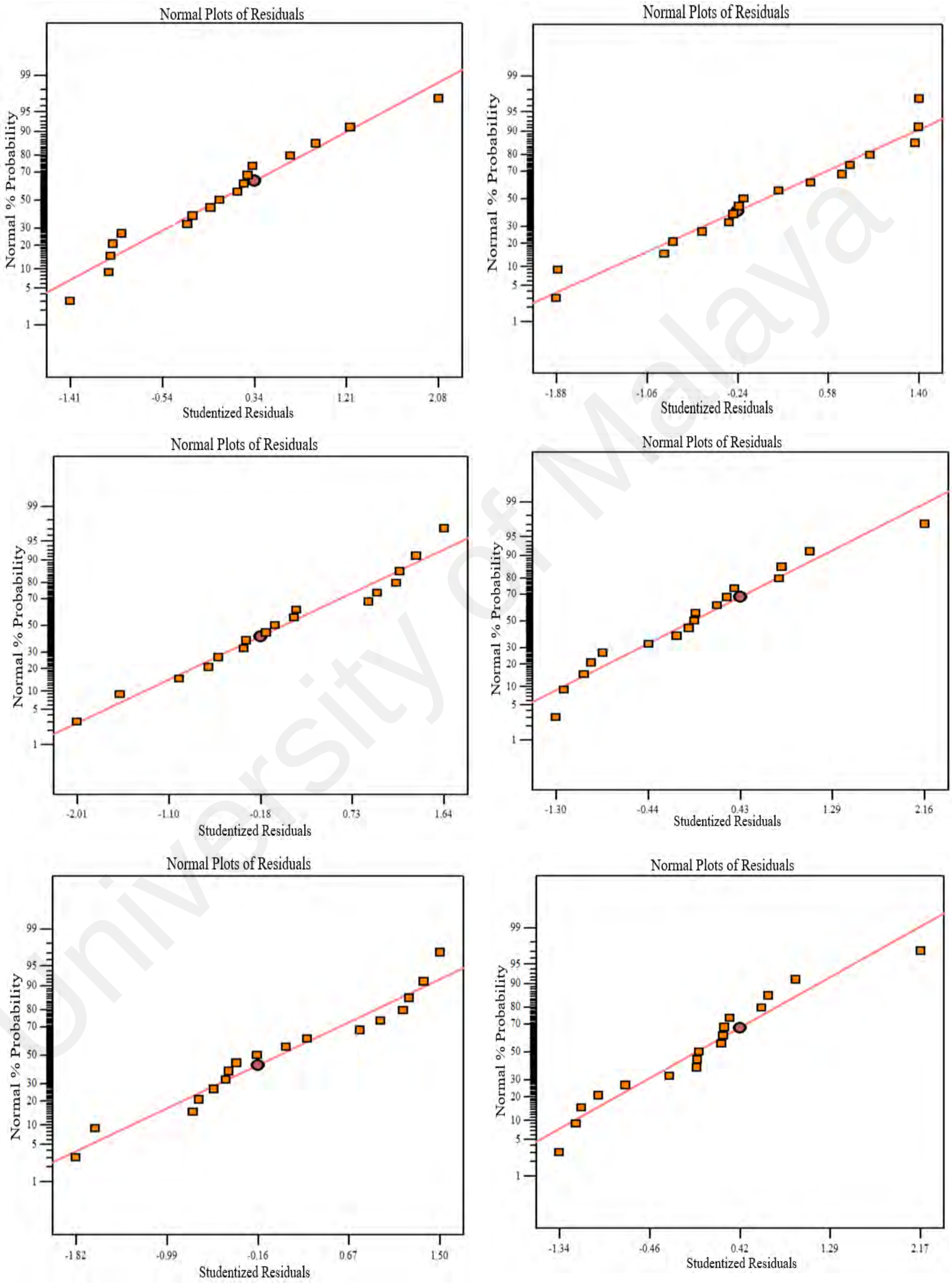

Figure 4.2: Normal plot residual for response of (a) L*, (b) a*, (c) b*, (d) H, (e) S and (g) anthocyanin content.

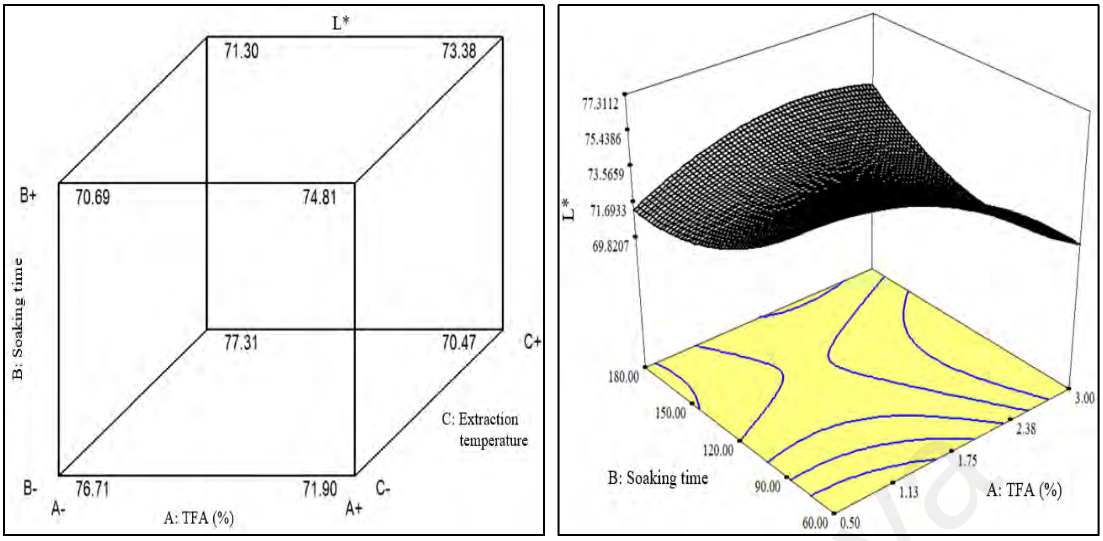

Figure 4.3: (a) Cube graph analysis for response of Lightness, L* of anthocyanin extractionfrom *Melastoma malabathricum* (b) 3D Response surface model for Lightness, L* at 80 ^{0}C.

Figure 4.3 (b) shows the 3D response surface for the influence of soaking times and TFA concentrations on L* responses. Each plot shows the effect of varying two parameters while holding the other parameter constant at 80 ^{0}C. Interaction between two factors (A: TFA content and B: soaking time) have a stronger effect in L* response for anthocyanin extraction from fruit pulp of *Melastoma malabathricum* at 80 ^{0}C. As can be seen in Figure, L* response decreased significantly with increasing soaking time and TFA concentration until TFA content reach 2.38. At greater than 2.38% TFA content the L* value start to increase. At 3% TFA, L* value increased with increasing soaking period until 180 min. Therefore it directly noticed that, anthocyanin content of sample at 80 ^{0}C obviously depend on percentage of TFA added and soaking time.

4.5.2 Analysis of response model graph on redness, a* coordinate of anthocyanin extract from *Melastoma malabathricum*

Based on cube graph in Figure 4.4(a), it can be clearly noticed that, a* value for sample with 0.5% TFA content, increased from 44.50 to 52.96 with increasing soaking time up till 180 min. a* value decreased with increased in extraction temperature. At 30

°C a* value was 53.35 and decreased to 50.32 at 80 °C. In addition, the increase in TFA content from 0.5% to 3% TFA for 60 min soaking time resulted in rapid increased in a* value up to 53.35. Nevertheless, at 3% TFA content and at low temperature of 30 °C, a* value decreased to 51.41 although soaking time was 180 min.

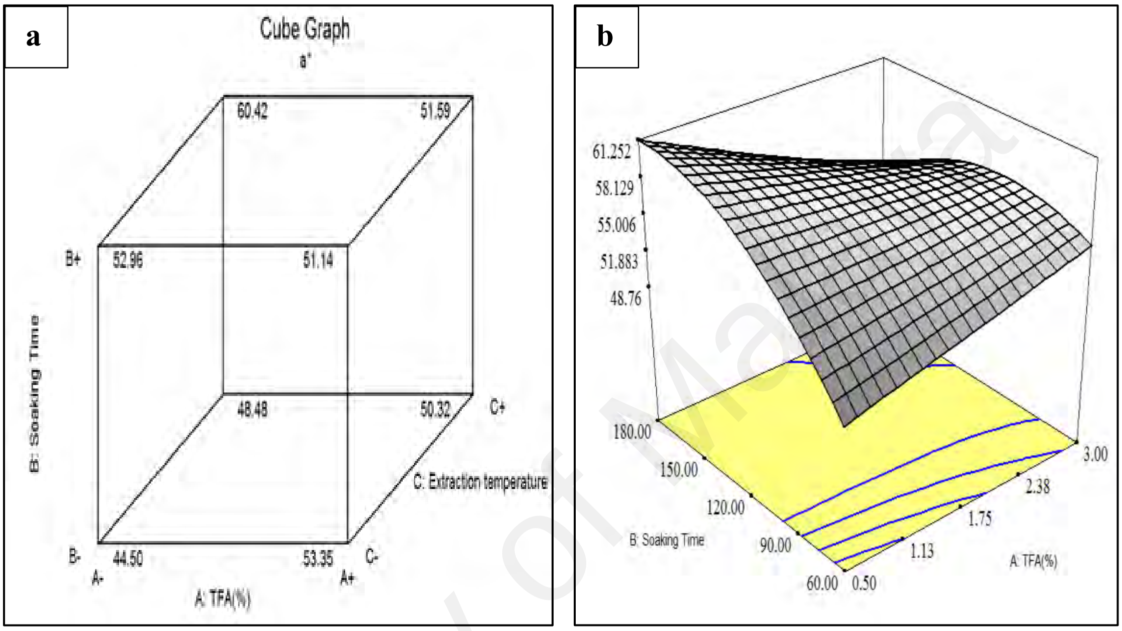

Figure 4.4: a) Cube graph analysis for response of redness, a* coordinate in CIElab of anthocyanin extraction from *Melastoma malabathricum* (b) 3D Response surface model for colour redness, a* at 80 ^{0}C.

Figure 4.4 (b) shows the 3D Response surface model for colour redness, a* at 80 ^{0}C. Interaction between two factors (A: TFA content and B: soaking time) have a stronger effect in a* coordinate. As can be seen in Figure above, a* coordinate response increased significantly with increasing soaking time and TFA concentration. Increasing the soaking time at 80 ºC will increase redness of the sample (a* value in the CIElab system). It is clearly noticed that at 0.5% TFA concentration a* value increased continuously until the soaking time of 180 min. Based on Figure 4.4(b), it can be observed that at 0.5% TFA at 80 ºC a* value increased with increasing soaking period until 180 min. At 3% TFA, a* value slightly increase with icreasing soaking time up to 180 min.

4.5.3 Analysis of response model graph on blueness, b* coordinate of anthocyanin extract from *Melastoma malabthricum*

The Cube graph shown in Figure 4.5(a) describes how the three independent variables affect blueness b* response of sample extraction from *Melastoma malabathricum*, in CIElab colour coordinate. Based on this figure, it can be clearly noticed that, b* value for sample with 0.5% TFA content, decreased from -6.69 to -3.61 with increasing soaking time up till 180 min at 30 °C. b* value decreased with increased in extraction temperature. At 30 °C the b* value was – 1.20 decreased to -0.90 at 80 °C. In addition, the increase in TFA content from 0.5% to 3% TFA for 60 min soaking time resulted in rapid decreased in b* value up to -1.20. Nevertheless, at 3% TFA content and at low temperature of 30 °C, b* value increased to -2.47 with soaking time was 180 min.

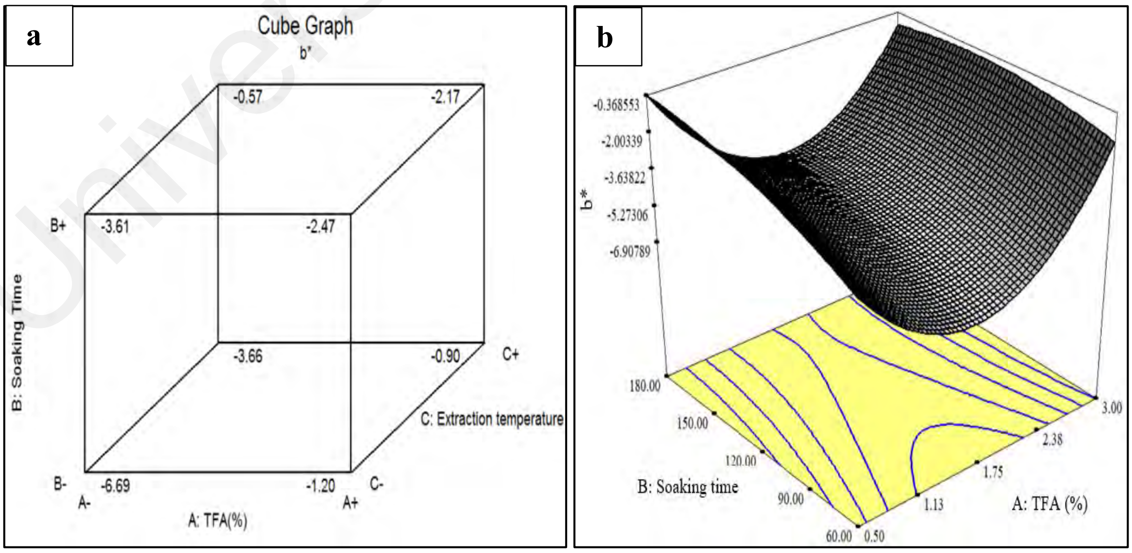

Figure 4.5: (a) Cube graph analysis for response of blueness,b* coordinate in CIElab of anthocyanin extraction from *Melastoma malabathricum*, (b) 3D Response surface model for colour blueness, b* at 80 ^{0}C.

Figure 4.5(b) shows the 3D Response surface model for, b* response at 80 ^{0}C. Interaction between two factors (A: TFA content and B: soaking time) have a stronger effect in b* coordinate. As can be seen in figure above, b* coordinate response increased significantly with increasing soaking time and TFA concentration. Increasing the soaking time at 80ºC will increase blueness of the sample b* value in the CIElab system. It is clearly noticed that at 3% TFA concentration b* value increased continuously until the soaking time of 180 min. It can be detected that at lowest soaking time with increasing TFA content at 80 ºC, b* value increased until 1.75% TFA. At greater than 1.75% TFA, the b* value decreased.

4.5.4 Analysis of response model graph on colour Chromaticity, C of anthocyanin extract from *Melastoma malabathricum*

The Cube graph shown in Figure 4.6 (a) show C response in CIElab colour coordinate. Based on this figure, it can be clearly noticed that, C value for sample with 0.5% TFA content, increased from 44.43 to 53.30 with increasing soaking time up till 180 min at 30 °C. C value increased up to 61.28 with increasing extraction temperature for sample with 0.5% TFA. However at 3%FA the C value decreased from 57.48 to 54.28 when the temperature rised to 80 ^{0}C. Nevertheless, at 3% TFA content and at low temperature of 30 °C, C value decreased to 50.94 although soaking time was 180 min. Figure 4.6 (b) shows the 3D Response surface model for choromaticity, C response at 80 ^{0}C. Interaction between two factors (A: TFA content and B: soaking time) have a stronger effect in b* coordinate. As can be seen in Figure above, C response increased significantly with increasing soaking time and TFA concentration. Increasing the soaking time at 80ºC will increase C value in the CIElab system. It is clearly noticed that at 0.5% TFA concentration, C value increased continuously until the soaking time of 180 min.It can be observed that at lowest soaking time with increasing TFA content at 80 ºC, C value increased until 3% TFA. However at 3% TFA, the C value decreased with increasing soaking time up to 180 min.

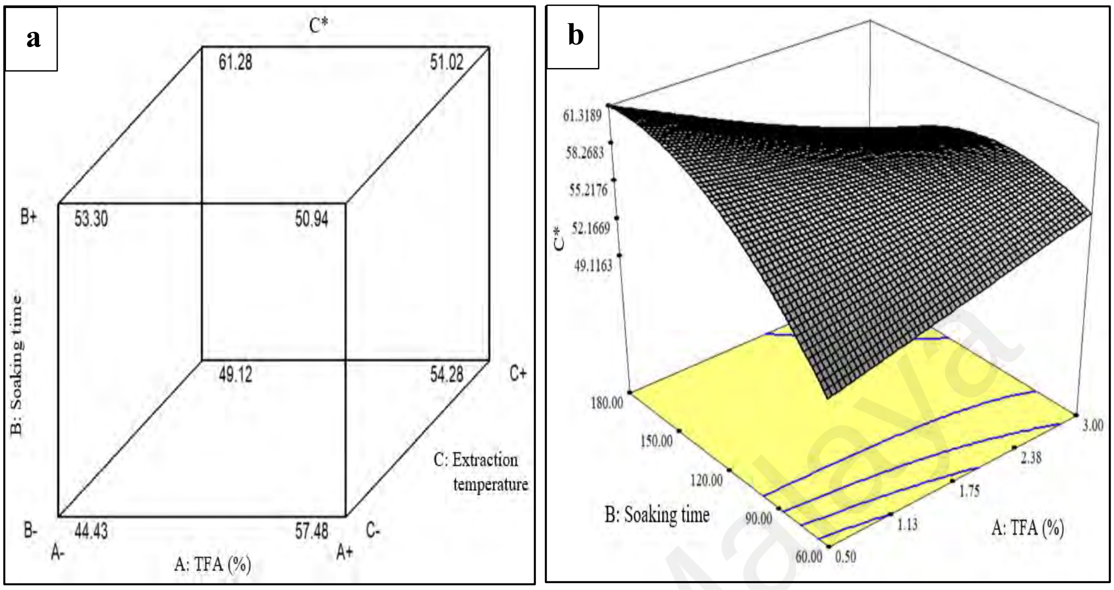

Figure 4.6: (a) Cube graph analysis for response of colour chromaticity, C of anthocyanin extraction from *Melastoma malabathricum,* (b) 3D Response surface model for colour chromaticity, C at 80 ^{0}C.

4.5.5 Analysis of response model graph on colour Hue angle, H^0 of anthocyanin extract from *Melastoma malabathricum*

Figure 4.7(a) show cube graph of hue angle, H^0 response in CIElab colour coordinate. Based on this figure, it can be clearly noticed that, H^0 value for sample with 0.5% TFA content, increased from 353.90 to 355.90 with increasing soaking time till 180 min at 30 °C. H^0 value increased with increased in extraction temperature from 353.90 to 355. 68. At 30 °C the H^0 value was 359.40 and slightly decreased to 358.09 at 80 °C. In addition, the increase in TFA content from 0.5% to 3% TFA for 60 min soaking time resulted in rapid increased in value up to 359.40. Nevertheless, at 3% TFA content and at low temperature of 30 °C, H^0 value decreased to 357.93 although soaking time was 180 min.

Figure 4.7(b) shows the 3D Response surface model for hue angle response, H^0 at 80 ^{0}C. Interaction between two factors (A: TFA content and B: soaking time) have a stronger effect in H^0 response. As can be seen in Figure above, H^0 response increased significantly with increasing soaking time and TFA concentration. Increasing the soaking time at 80ºC will increase H^0 value in the CIElab system. It is clearly noticed that at 0.5% TFA concentration, H^0 value increased continuously until the soaking time of 180 min. based on figure also, it can be detected that at lowest soaking time with increasing TFA content at 80ºC, H^0 value increased until 1.75% TFA however at greater than 1.75% TFA, the H^0 value decreased with increasing soaking time up to 180 min.

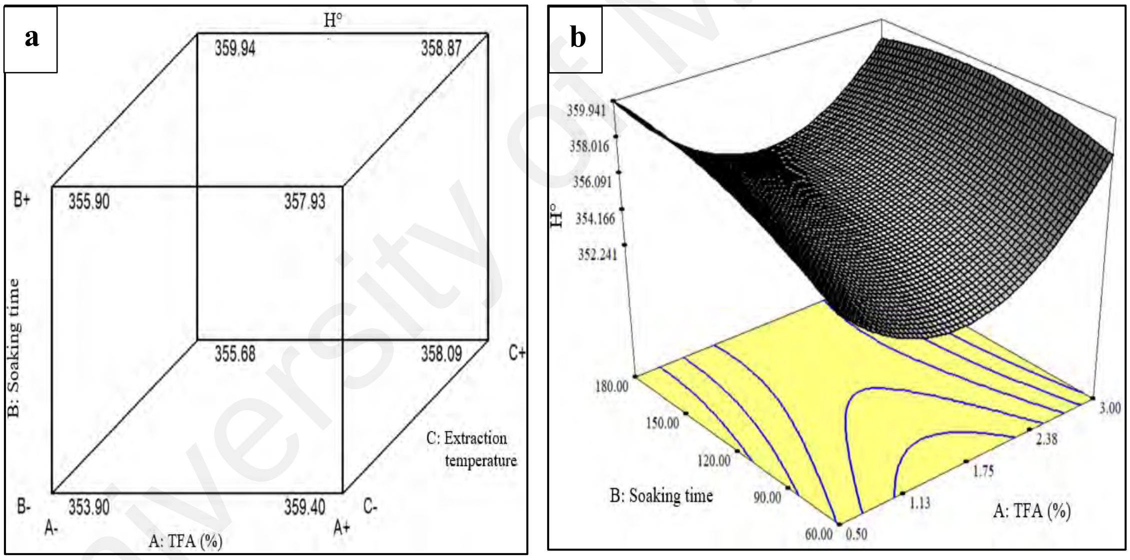

Figure 4.7: a) Cube graph analysis for response of Hue angle, ^{0}H of anthocyanin extraction from *Melastoma malabathricum*(b) 3D Response surface model for hue angle, H^0 at 80 ^{0}C.

4.5.6 Analysis of response model graph on colour saturation, S of anthocyanin extract from *Melastoma malabathricum*

The saturation, S is the calculation of an area visualized by an observer which the scalar value derived from the CIELab parameters colour values. This determined as the chromaticity to lightness or the ratio of C to L*, and effectively reduces the CIELab coordinates from three to single value, S. Based on this Figure 4.8(a) it can be clearly noticed that, S value for sample with 0.5% TFA content, increased from 0.56 to 0.76 with increasing soaking time up to 180 min. S value decreased with increased in extraction temperature. At 30 °C the S value was 0.79 and decreased to 0.78 at 80 °C. In addition, the increase in TFA content from 0.5% to 3% TFA for 60 min soaking time resulted in rapid increased in S value up to 0.79. Nevertheless, at 3% TFA content and at low temperature of 30 °C, S value decreased to 0.69 although soaking time was 180 min. Figure 4.8(b) shows the 3D Response surface model for colour saturation, S response, at 80 ^{0}C. Interaction between two factors (A: TFA content and B: soaking time) have a stronger effect in S response. As can be seen in Figure above, S response increased significantly with increasing soaking time and TFA concentration. Increasing the soaking time at 80ºC will increase S value in the CIElab system. It is clearly noticed that at 0.5% TFA concentration, S value increased continuously until the soaking time of 180 min. based on figure also, it can be detected that at lowest soaking time with increasing TFA content at 80ºC , S value increased until 3% TFA. However at 3% TFA, the S value decreased with increasing soaking time up to 180 min.

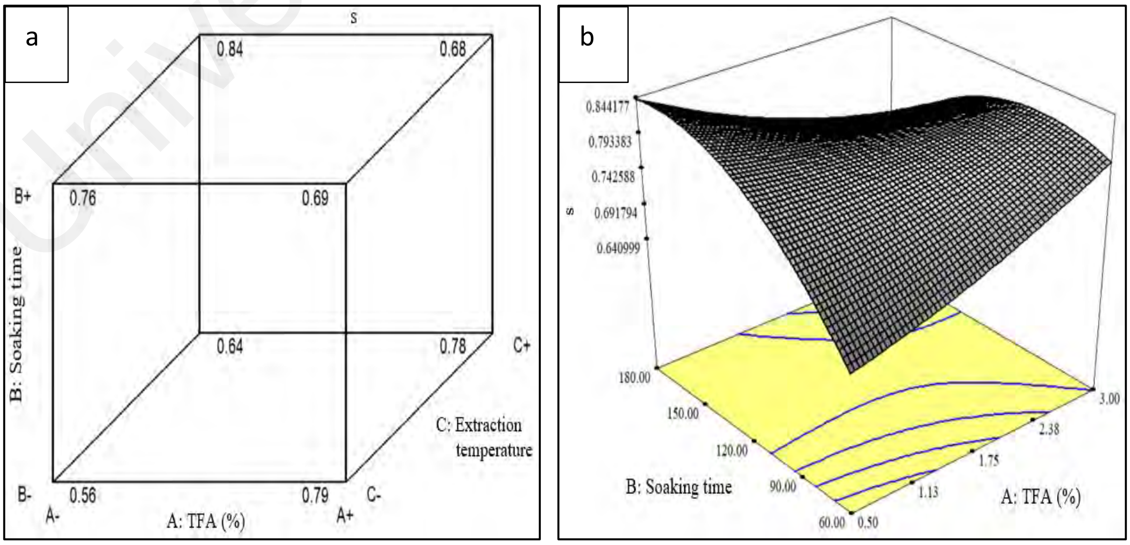

Figure 4.8: (a) Cube graph analysis for response of colour saturation, S of anthocyanin extraction from Melastoma malabathricum, (b) 3D Response surface model for colour saturation, S at 80 ^{0}C.

4.5.7 Analysis of response model graph on anthocyanin content of anthocyanin extract from *Melastoma malabathricum*

According to Figure 4.9(a) it can be clearly noticed that, anthocyanin content value for sample with 0.5% TFA content, increased up to ~3357.30 mg/L with increasing soaking time up till 180 min at 30 °C. Anthocyanin content value increased with increased in extraction temperature up to ~3641 mg/L. While anthocyanin content continue to increase up ~4530 mg/L with increasing soaking time. At 30 °C the anthocyanin content value was ~4185 mg/L and decreased to ~3676 mg/L with increasing extraction temperature. In addition, the increase in TFA content from 0.5% to 3% TFA for 60 min soaking time resulted in rapid increased in anthocyanin content value up to ~4185 mg/L. Nevertheless, at 3% TFA content and at low temperature of 30 °C, anthocyanin content value decreased to ~3490 mg/L although soaking time was 180 min

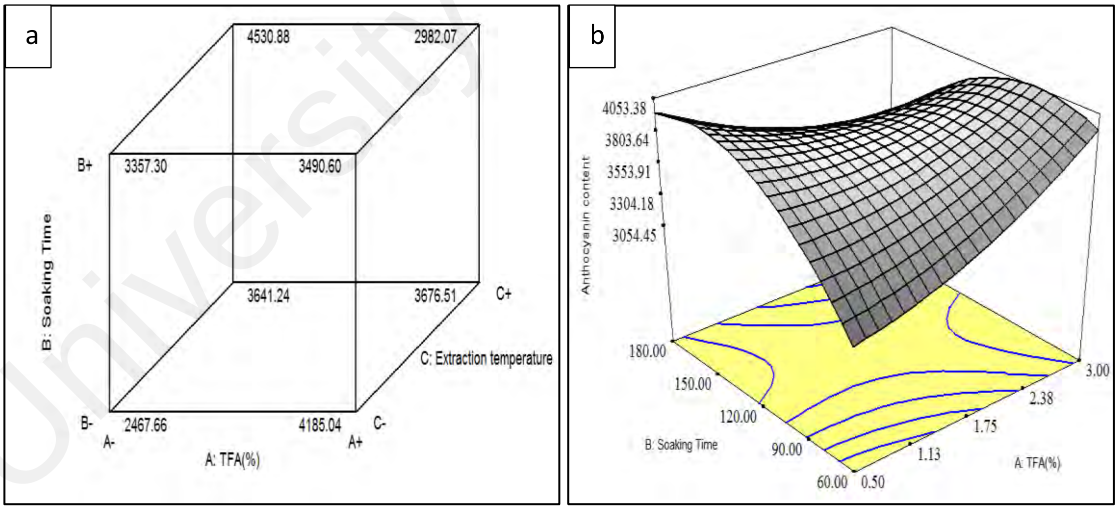

Figure 4.9: (a) Cube graph analysis for response of anthocyanin content of anthocyanin extraction from Melastoma malabathricum, (b) 3D Response surface model for anthocyanin content response at 80 ^{0}C.

Figure 4.9(b) shows the 3D Response surface model for anthocyanin content response, at 80 ^{0}C. Interaction between two factors (A: TFA content and B: soaking time) have a stronger effect in S response. As can be seen in Figure above, anthocyanin content response increased significantly with increasing soaking time and TFA concentration. Increasing the soaking time at 80ºC will increase anthocyanin content value in the CIElab system. It is clearly noticed that at 0.5% TFA concentration, anthocyanin content value increased continuously until the soaking time of 180 min. based on figure also, it can be detected that at lowest soaking time with increasing TFA content at 80 ºC, anthocyanin content value increased until 3% TFA. However at 3% TFA, the anthocyanin content value decreased with increasing soaking time up to 180 min.

4.6 Optimization of the models for L*, a*, b*, C, H^0, saturation and anthocyanin content

The extraction of anthocyanin from fruit pulp of *Melastoma malabathricum* f was optimized numerically in order to find the combination of factor levels that simultaneously satisfy the responses and factors. To execute this, the desirability function method was employed to produce the ideal extraction conditions for antnocyanin extraction. The set goals are either none, maximum, minimum, target, or in a range of variables or factors and responses before being grouped into one desirability function. To obtain a suitable set of conditions that satisfy the goals, the three factors (i) TFA content (0.5 to 3%), (ii) Soaking time (60–180 min), and (iii) extraction temperature (30 °C–80 °C) were set within range. For the present study, the responses, L*,a*, b*, C, H^o, saturation are set within the range while anthocyanin content were set to be maximized as seen in Table 4.11 which shows the summary of desirability goals. The goals were established from maximum points using computative optimization.

Table 4.11: Summary table for desirability goal of L*,a*, b*, C, H^0, S, and anthocyanin content.

Lower Name	Upper Goal	Lower Limit	Upper Limit
TFA(%)	is in range	0.5	3
Soaking Time	is in range	60	180
Extraction temperature	is in range	30	80
L	is in range	70.01	76.46
a*	is in range	46.4	59.58
b*	is in range	-7.26	-0.54
C	is in range	46.59	59.8
H°	is in range	351.8	359.45
Saturation	is in range	0.610376	0.832174
Anthocyanin content	maximize	3074.77	4596.25

Table 4.12 shows the optimization table output based on desirability goal for L*,a*, b*, C, H^0, S, and anthocyanin content. Based on the table it can be observed that there are several combinations of variable that could meet all the goals set. For this study, the optimized condition with the highest desirability, 0.973 are TFA content (0.5%), soaking period (132.43 min) and temperature of extraction of 80 ºC.

Table 4.12: Optimization table based on desirability goal for L*,a*, b*, C, H^0, S, and anthocyanin content.

Number	TFA(%)	Soaking Time	Extraction temperature	L	a*	b*	C	H°	Saturation	Anthocyanin content	Desirability	
1	**0.5**	**132.43**	**80**	**71.9436**	**59.58**	**-0.9785**	**59.723**	**359.177**	**0.822541**	**4555.27**	**0.973**	**Selected**
2	0.5	132.87	79.75	71.9247	5.96E+01	-0.9844	59.7229	359.172	0.822773	4551.3	0.97	
3	0.51	132.67	80	71.9549	5.96E+01	-1.0514	59.7225	359.102	0.822403	4549.61	0.969	
4	0.52	132.94	80	71.967	5.96E+01	-1.1308	59.7218	359.021	0.822252	4543.37	0.965	
5	0.5	134.27	78.99	71.8692	59.58	-1.0160	59.7223	359.144	0.823447	4538.11	0.962	
6	0.5	127.11	80	72.1579	59.1272	-1.0938	59.2824	359.016	0.815483	4527.21	0.955	
7	0.5	141.52	75.43	71.5886	59.58	-1.0646	59.7197	359.113	0.826761	4481.7	0.925	
8	2.96	93.58	30	71.3653	58.1072	-0.6395	58.2792	359.45	0.806915	4282.49	0.794	
9	2.96	95.02	30	71.3623	58.1006	-0.6434	58.2722	359.45	0.807077	4282.29	0.794	
10	2.98	117.83	30	71.548	57.5127	-0.6585	57.6834	359.45	0.800918	4229.64	0.759	

4.7 Colour differences (ΔE) based on L*, a* and b* colour coordinate

The colour differences (ΔE) of extraction from fruit pulp of *Melastoma malabathricum* was calculated based on L*, a* and b* colour coordinate following equation (4.8):

$$\Delta E^* = \sqrt{(L_2^* - L_1^*)^2 + (a_2^* - a_1^*)^2 + (b_2^* - b_1^*)^2} \tag{4.8}$$

Table 4.13: Colour differences (ΔE) of extraction from fruit pulp of *Melastoma malabathricum.*

Sample	Anthocyanin content (mg/L)	Colour difference (ΔE)
1	3074.77	13.94
2	4022.58	3.08
3	3850.49	4.58
4	3214.22	8.53
5	3263.50	7.84
6	4117.36	3.72
7	**4596.25**	**0.00**
8	3768.00	4.93
9	3256.04	11.72
10	3371.17	8.95
11	3333.00	11.48
12	3640.92	5.15
13	3839.50	4.49
14	3798.73	6.45
15	3610.59	8.69
16	3833.24	5.97
17	3881.10	7.63

Table 4.13 lists the anthocyanin content in mg/L with the colour differences (ΔE*). From the table it show that the colour difference (ΔE*) vary between the sample studied. Figure 4.10 shows the relationship between anthocyanin content and the sample of extractions while Figure 4.11 present the relationship between colour difference

(ΔE*) and sample of extractions. Based on Figure 4.10 and 4.11 the relationship between anthocyanin content with sample of extractions and colour difference with sample of extractions, if assumed linear has a regression (R^2) of 0.9173 and 0.7369, respectively.

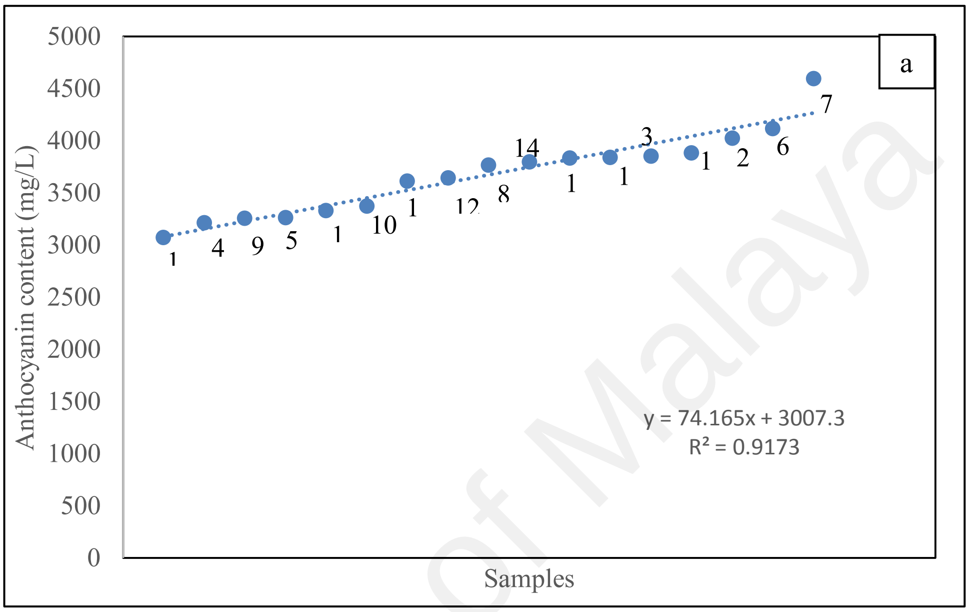

Figure 4.10: Relationship between anthocyanin content with different sample of extractions.

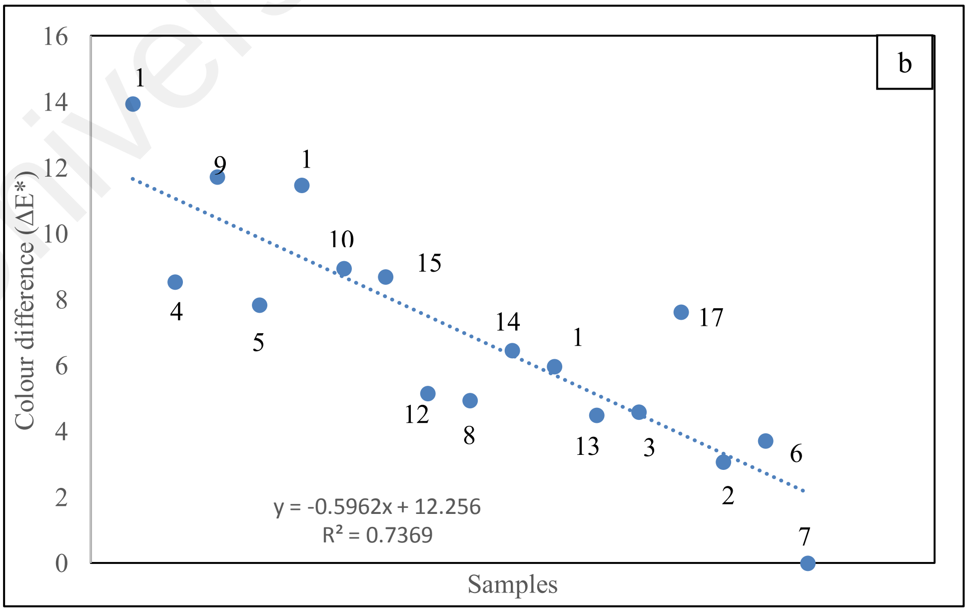

Figure 4.11: Relationship between colour difference (ΔE*) with different sample of extractions.

4.8 Summary

This chapter can be summarized that optimized condition for anthocyanin extraction for *Melastoma malabathricum* were TFA content (0.5%), soaking period (132 min) and temperature of extraction of 80 ºC which successfully obtained by RSM. This optimized condition of anthocyanin extraction will be further used as sensitizer in DSSC.

CHAPTER 5: RESULTS FOR SYNTHESIS AND CHARACTERIZATION OF TIO_2 NANOSTRUCTURE

5.1 Introduction

The morphology of TiO_2 nanostructures produced by the combination of sol gel and elctrospinning method will be presented in this chapter. This chapter begins with the study on relationship between concentration of solution with the average fiber diameter formation and average bead diameters. Surface morphology and fiber formation of electrospinning nanofibers were investigated using FESEM (Hitachi Su8220). The optimized PVP samples were further analysed to obtain beadless nanofibers. Hence, the influence of applied voltage on average fiber and bead diameters were studied. The successfully beadless nanofibers obtained in this work were subjected to different calcination temperatures and the morphology of the nanorods was examined.

The XRD analysis was performed and data were collected using Cu-Kα X-ray radiation between 2θ angles of 5° to 55°. For the XRD measurements, the samples were prepared in powder form. The sintered samples were ground to obtain nanorod shape of TiO_2. Nanorods with anatase structure were used to form nanoparticle/nanorod composite for DSSCs application. The morphology of the composites at various nanorods ratios was observed. Chemical analysis of prepared TiO_2 nanorods synthesized by electrospinning was carried out using energy dispersive analysis X-rays (EDX). The average fiber and average bead diameters were analysed by using image J software.

5.2 Morphology studies on electrospun TiO_2 nanofiber obtained from combined method of sol gel with electrospinning

5.2.1 Effect of PVP concentration on nanofiber morphology

The effects of PVP concentration in the spinning solutions on surface structure of the electrospun fibers are shown in Figure 5.1. Figure 5.1(a) to (e) show FESEM image of nanofibers at different percentages of PVP is from 8% PVP to 12% PVP, designated as P1, P2, P3, P4 and P5 respectively. As can be seen in Figure 5.1(a) and (b) at low solution concentrations of 8% (P1) and 9% (P2), cylindrical fibers were not formed and flat fibers were observed as inserted picture.

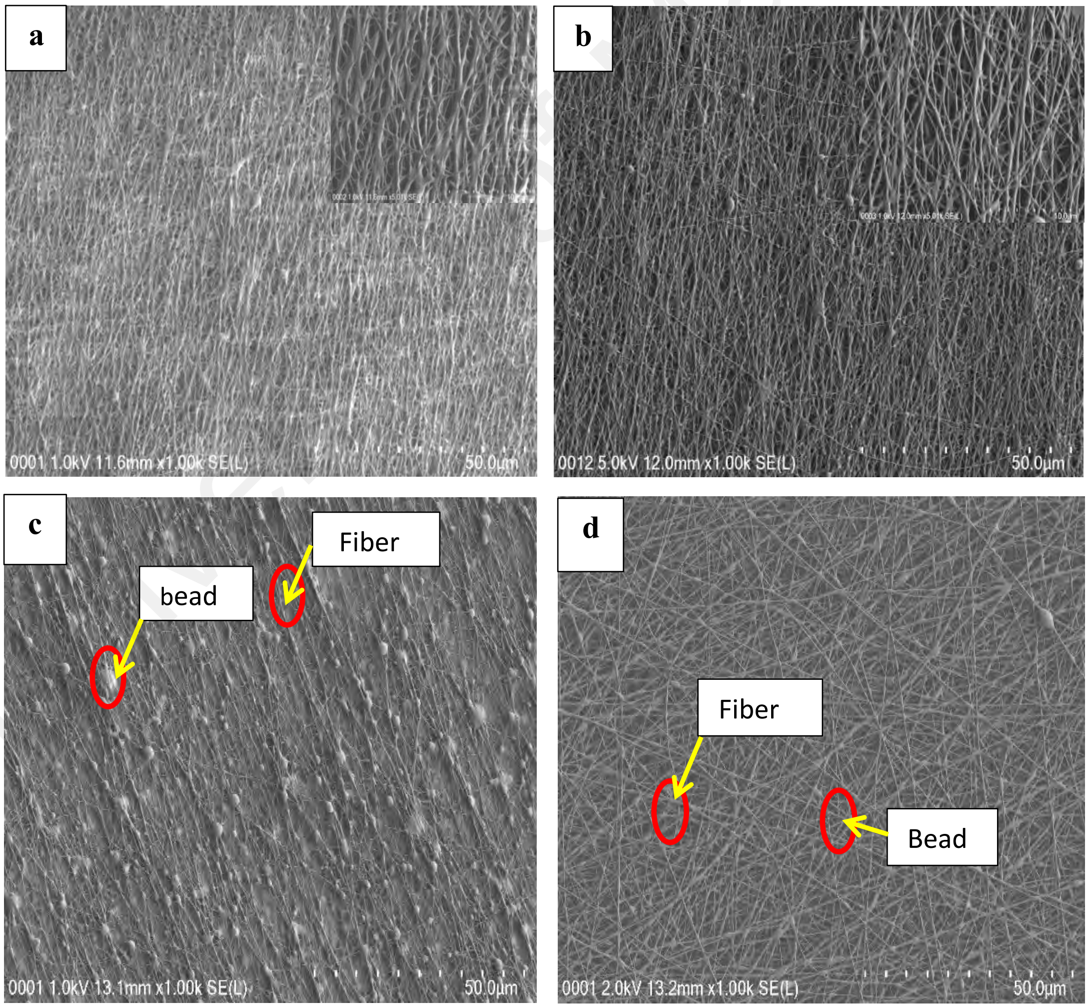

Figure 5.1: FESEM images of synthesized TiO_2 NanoFiberss. at (a) P1,8% PVP ; (b) P2,9% PVP (c) P3, 10% PVP, (d) P4,11% PVP ; (e) P5, 12% PVP.

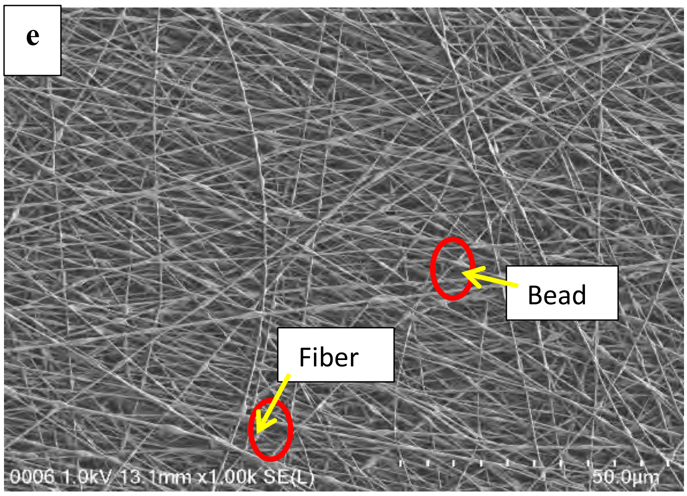

Figure 5.1, continued.

It could be noted that, flat fiber is not fovourable in this work, thus further analysis were not carried out for P1 and P2 samples. The mixture of cylindrical fibers and beads were observed at FESEM image depicted in Figure 5.1 (c) designated as P3 (10% of PVP). On increasing the solution concentration to 11% of PVP (P4 sample), Figure 5.1(d), less beads were obtained and the bead shapes changed from ball-like to rod-like shape. Finally further increase in PVP concentration to 12% (P5 sample) resulted in more uniform nanofiber with less beads present as in Figure 5.1(e). Based on the results acquired in Figure 5.1, it can be examined that increasing PVP concentration led to an increase in the fiber diameters with decreased bead diameters.

Fiber and bead sizes analysis were studied using Image J software. As can be seen in Figure 5.2 (a), average fiber diameter produced with 10% PVP (P3 sample) range from 96 nm to 211 nm with the most fibers having an average diameter of 120 nm. Increasing the concentrations of PVP to 11% (P4 sample), Figure 5.2(b), increased the average fiber diameter and most of fibers had an average fiber diameter up to 261 nm. Even the range of average fiber diameters showed an increase from 126 nm to 321 nm. Finally, on increase in PVP content to 12 % (P5 sample), the average fiber diameter range from 211 nm to 467 nm as shown in Figure 5.2 (c) which the most fiber having diameter of

307 nm. Analysis of bead diameter as in Figure 5.3(a) showed that low PVP concentration (P1) produced beads with diameter ranging from 1.93 µm to 2.94 µm with most bead having average bead diameter of 2.27 µm. However increase in PVP concerntration to 11% PVP (P2) resulted in most fibers having bead diameters of 1.45 µm as depicted in figure 5.3(b). It is observed that the bead diameter range from 1.04 µm to 1.66 µm. At 12% PVP(P5) most fibers having bead diameter of 0.36 µm. Even the range has decreased between 0.30 and 0.43 µm.

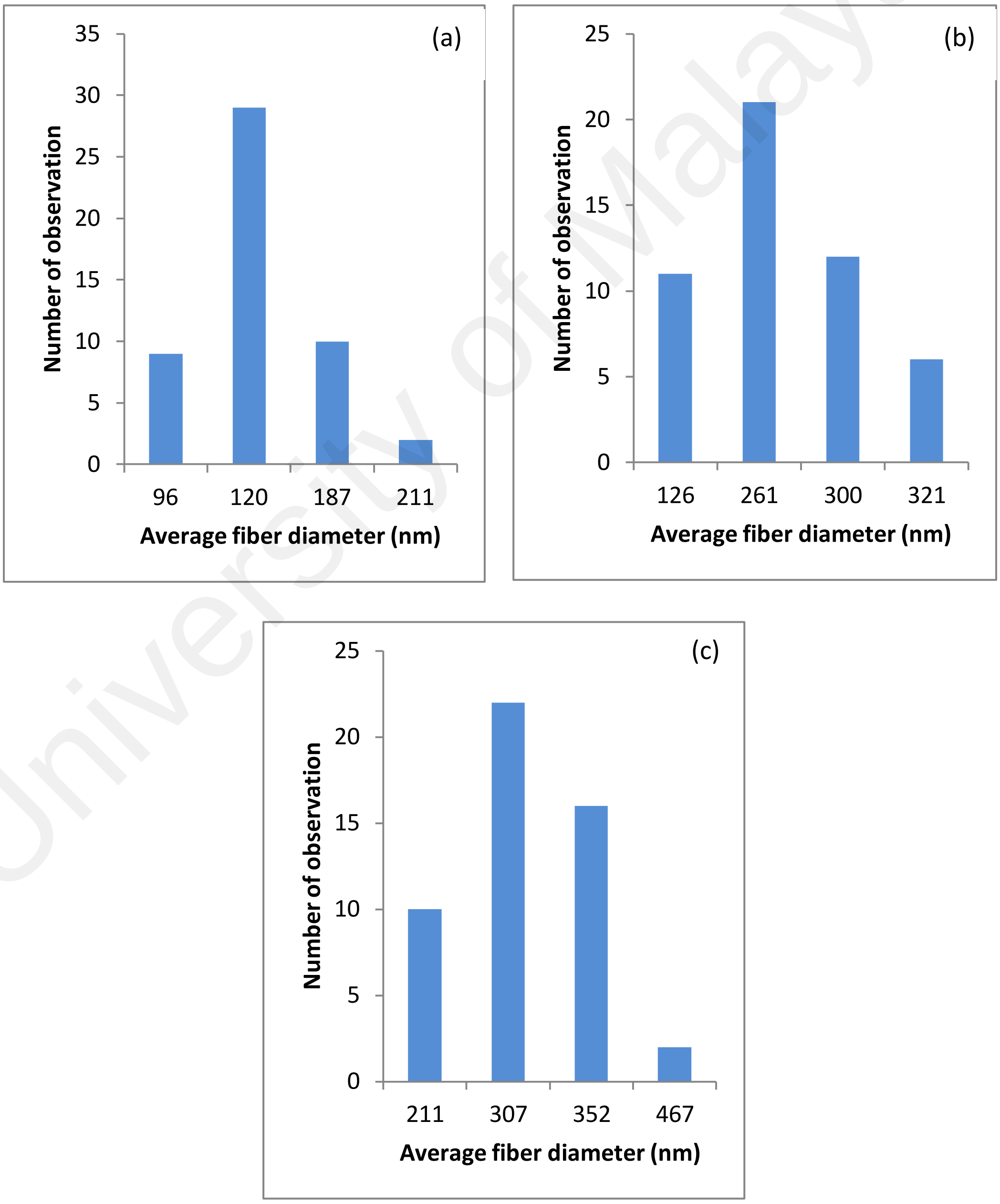

Figure 5.2: Analysis of average fiber diameter for (a) 10% PVP (P3), (b) 11% PVP (P4), (c) 12% PVP (P5) nanofibers.

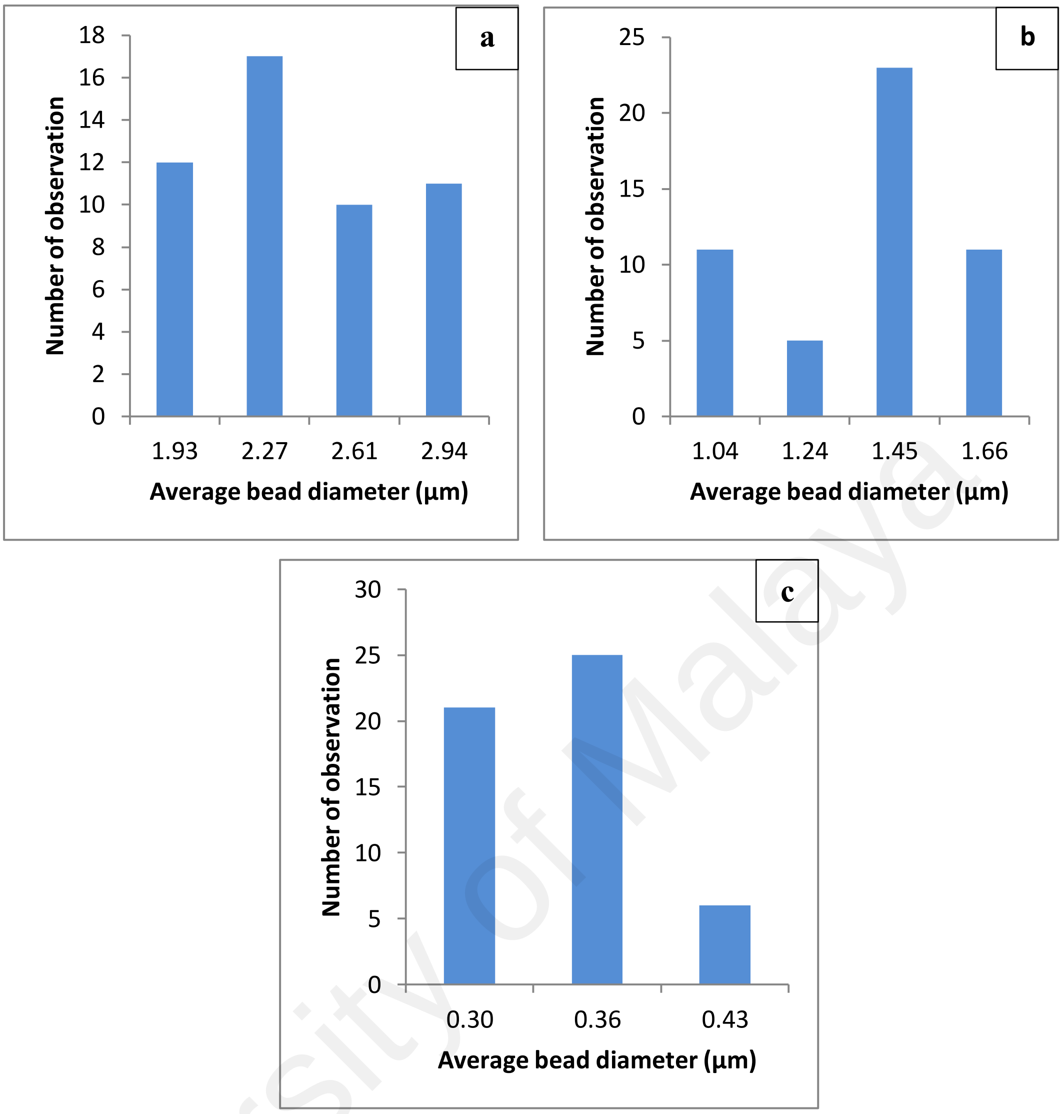

Figure 5.3: Analysis of average bead diameter for (a) 10% PVP (P3), (b) 11% PVP (P4), (c) 12% PVP (P5) nanofiber.

Table 5.1 summarizes the relationships between average fiber diameter and average bead diameter with respect to PVP concentration of the spinning solutions. These results indicate that PVP content has a significant effect on morphology electrospun nanofibers in terms of average fiber and bead diameters. From Table 5.1, it is observed that increasing PVP content from 10 wt.% (P3) to 12 wt.% (P5) showed that most of the fibers have diameters from 116 nm to 248 nm. It can be noted that, eventhough the average fiber diameter increased by increasing PVP content, the morphology still contain beads. Bead diameters were observed to decrease, with most beads had diameters from 2.3 µm to 0.4 µm for PVP content of 10 (P3) to 12 wt.% (P5). These showed that increase in PVP content will eliminate the formation of bead. The drawback is, the fiber diameter will be large and more polymers is needed. Thus, in order to establish beedless nanofiber with decreasing fiber diameter other processing parameters such as applied voltage must be considered.

Table 5.1: Summary table for effect of different wt(%) of PVP on morphology of nanofiber.

Designation	PVP (wt.%)	Average fiber diameter (nm)	Average bead diameter (µm)	Morphology of nanofiber
P1	8	-	-	Flat fiber
P2	9	-	-	Flat fiber
P3	10	120	2.3	Beaded fiber
P4	11	261	1.5	Beaded fiber
P5	12	307	0.4	Beaded fiber

5.2.2 Effect of applied voltage on nanofiber morphology

To examine the influence of applied voltage in a systematic manner, the applied voltage were changed from 15–21 kV while the other parameters were kept constant and the PVP concentration was 12 wt% (P5 sampel). This concentration was chosen because fiber morphology had the least beads. Thus, P5 composition was further experimented to produce beedless nanofibers by modifiying the applied voltage. The average fiber diameter and the average bead diameter were investigated using FESEM. Prior to FESEM, samples were sputtered with platinum. 50 fibers were chosen randomly from each FESEM image and analysed with Image J software to get bead and fiber diameters.

Figure 5.4 (a) to (g) depict the FESEM image of 12 wt.% of PVP sample (P5) with different applied voltages ranging from 15 kV to 21 kV and designated as V1, V2, V3, V4, V5, V6, V7 respectively. By changing the applied voltage morphology changed. Based on the Figure 5.4 (a), it was observed that at voltage 15 kV (V1 sample) flat fibers that are different from cylindrical geometry were formed. The morphology of fiber mat changed from flat fibers to cylindrical fiber when increased the applied voltage to 16 kV (V2 sample) as shown in Figure 5.4 (b). It was clearly noticed that even though cylindrical fibers had started to form, there were still many spherical beads present. Further increased of applied voltage to 17 kV (V3 sample) lesser beads were obtained as in Figure 5.4 (c) and the beads become more rod-like. When applied voltage was 18 kV (V4 sample) resulted in more uniform fibers with less bead are present as in Figure 5.4(d). Finally, when applied voltage increased to 19 kV (V5), it was found that, a uniform beadless fiber was formed as in Figure 5.4 (e). Thus, the cylindrical nanofiber without any bead successfully obtained. However, on increasing applied voltage to 20 kV (V6) and 21 kV (V7) beads begin to form again. Figure 5.4 (f) and (g) illustrated the morphology of electrospun fiber if the applied voltage increased beyond the 19 kV. Based the results obtained, it clearly observed that, at 20 kV, Figure 5.4 (f) the beaded fiber are started to formed again. Further increased kV up to 21 kV, resulted in mixture of beads and fiber. Thus, based on the result acquired in Figure 5.4, it can be infered that an applied voltage of 19 kV (V5) is the most suitable electrospinning parameters to produce an almost beadles fiber mat. Further analysis on applied voltage effect on fiber diameter and bead diameter were performed by using Image J software.

Figure 5.5 (a) to (f) show the distribution of TiO_2 of fiber diameter of TiO_2 of fibers P5 sample at (a) 16 kV, (b) 17 kV, (c) 18 kV, (d) 19 kV, (e) 20 kV and (f) 21 kV. As can be seen in Figure 5.5 (a), average fiber diameter of 12% PVP at 16 kV resulted in nanofiber range from 111 nm to 347 nm which with the highest numbers of fibers having diameter of 148 nm. At applied voltage of 17 kV (V3), Figure 5.5(b) the average fiber diameter range increased from 211 nm to 467 nm and most fibers had diameters of ~328 nm.

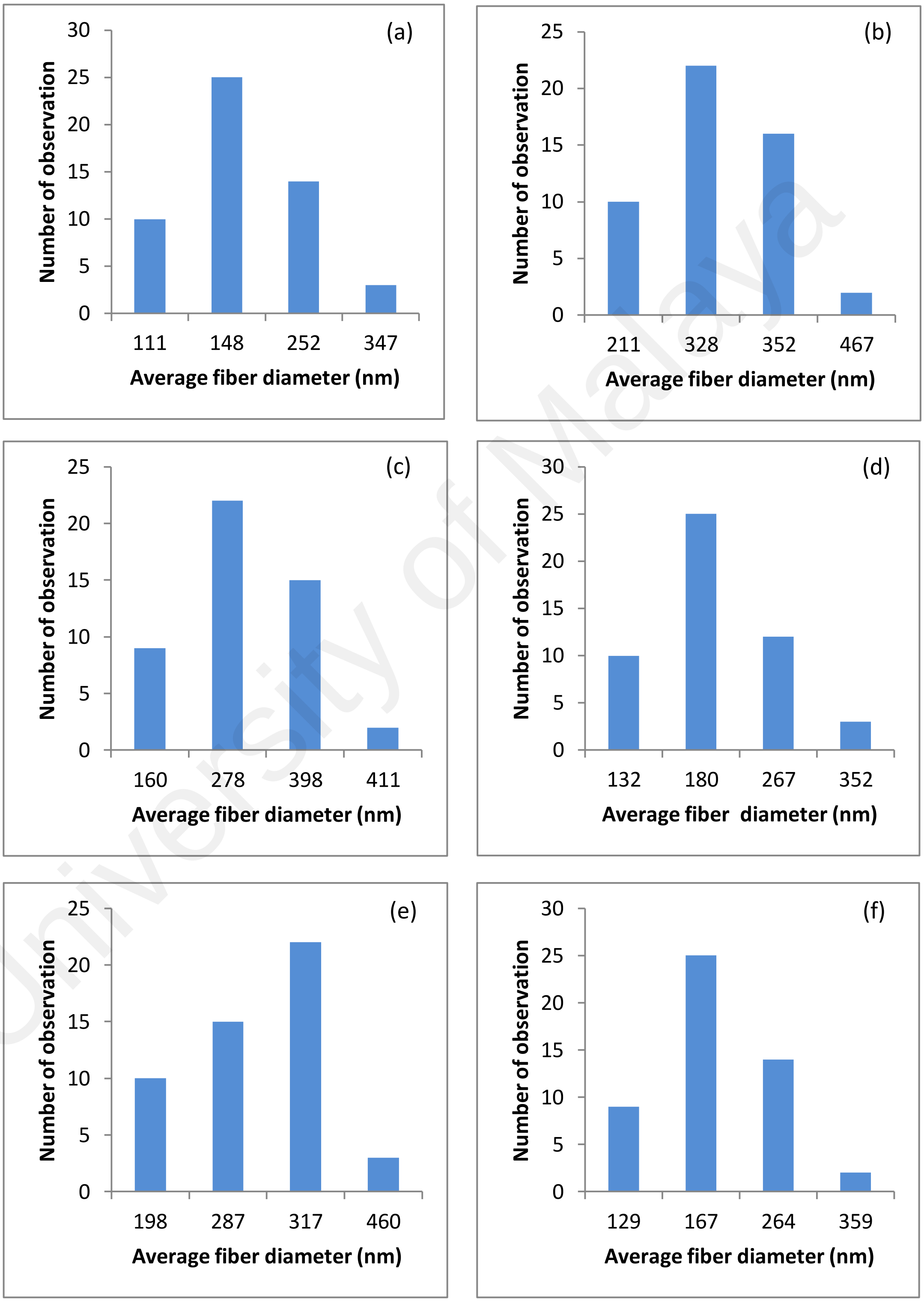

Figure 5.5: Analysis of average fiber diameter of TiO_2 nanofibers of P5 sample at (a) 16 kV (V2), (b) 17 kV (V3), (c) 18 kV (V4), (d) 19 kV (V5), (e) 20 kV (V6) and (f) 21 kV (V7).

However, on increase in applied voltage to 18 kV (V4) saw decrease in average fiber diameter with more than 20 out of 50 fibers chosen had average diameter of 278 nm and fiber range from 160 to 411 nm as shown in Figure 5.5 (c). Further increase in voltage to 19 kV (V5), as shown in Figure 5.5 (d), resulted in further decrease in average fiber diameter range from 132 nm to 352 nm and most of the fibers exhibit diameter of ~180 nm indicating that fibers with no bead have been formed. Increasing the applied voltage above 19 kV resulted in increased average fiber diameter, Figure 5.5 (e) and 5.5 (f). The voltage of 19 kV is the most suitable voltage to produce nanofibers with almost no bead.

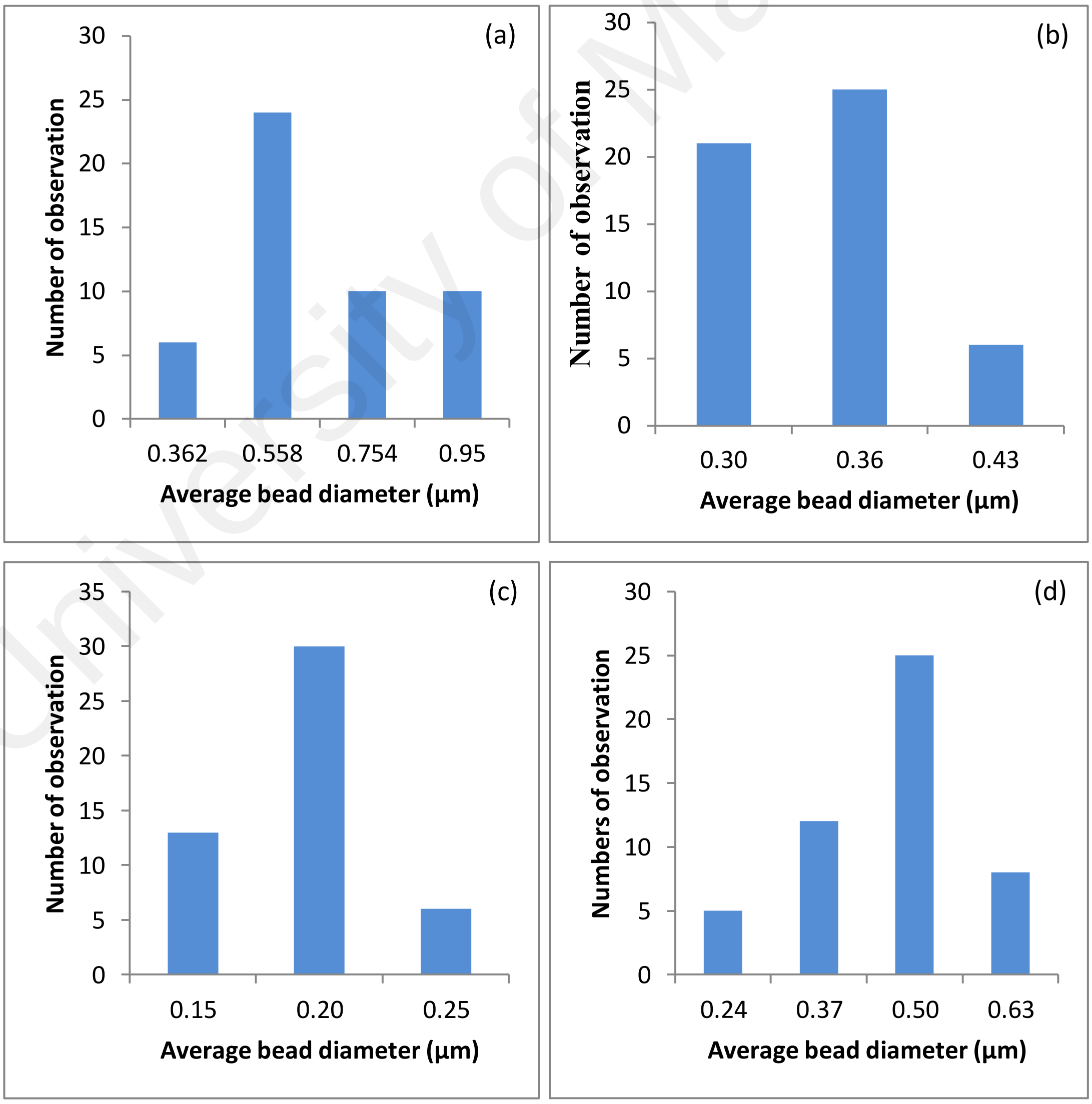

Figure 5.6: Analysis of average bead diameter of TiO_2 fiberss of P5 sample at (a) 16 kV, (b) 17 kV, (c) 18 kV, (d) 20 kV and (e) 21 kV.

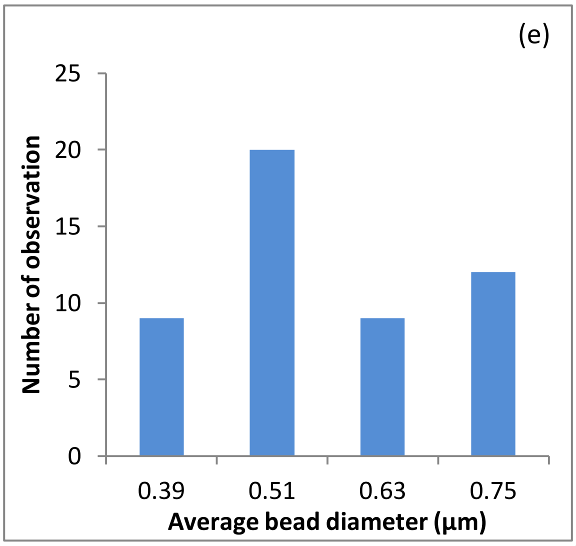

Figure 5.6, Continued.

Analysis of bead diameter as in Figure 5.6(a) showed that low applied voltage, 16 kV (V2) resulted in large diameter of beads ranging from 0.36 µm to 0.95 µm with the most bead having diameter of 0.56 µm. However on increasing applied voltage to 17 kV narrower bead diameters ranging from 0.30 µm to 0.430 µm with the most bead having diameter 0.36 µm as depicted in figure 5.6(b). It could be observed that, electric field of 1.21 kV/cm with 18 kV applied voltage as in Figure 5.6 (c) resulted in thinner beed with he most bead having diameter of 0.20 µm. Nevertheless, on incrased applied voltage to 20 kV resulted in increased average bead diameter which the most bead having a diameter of 0.50 µm, while the range of average bead diameter were 0.24 to 0.63 µm as shown in Figure 5.6 (d). It could be noted that, at higher applied voltage of 21 kV lead to bigger bead with the average bead diameter range from 0.39 µm to 0.75 µm.

Table 5.2 summarizes the relationships of the average fiber diameter and average bead diameter electrospun TiO_2. fibers with respect to applied voltage and applied electric field. These results indicate that applied voltage and applied electric field has a significant effect on morphology electrospun fibers in terms of average fiber diameter and bead diameter. Based on Table 5.2, it is more obviously that at very low applied voltage, 15 kV with electric field of 1.07 kV/cm, the flat fiber were formed. These types of fiber were classified as failure in fiber formation since there are different from wellknown cylindrical fibers (Nuansing et al., 2006). Thus the average fiber diameter and bead diameter were not calculated for this sample. Increasing applied voltage from 15 kV (V1) to 16 kV (V2) significantly change the morphology of fiber mat from flat to cylindrical fiber with applied electric field increased to 1.14 kV/cm. However the morphology of electrospun TiO_2. fiber which formed at this applied voltage is still beaded fiber with the most bead having diameter of 0.56 µm.

Table 5.2: Summary table for effect of different applied kV and applied electric field on morphology of nanofiber.

Applied voltage (kV)	Applied Electric Field (kV/cm)	Maximum Average fiber diameter (nm)	Maximum Average bead diameter (µm)	Morphology of nanofiber
15	1.07	-	-	Flat fiber
16	1.14	148	0.56	Beaded fiber
17	1.21	328	0.36	Beaded fiber
18	1.28	278	0.20	Beaded fiber
19	1.35	180	-	Beadlessfiber
20	1.43	317	0.50	Beaded fiber
21	1.50	167	0.51	Beaded fiber

It could be noted that the most TiO_2 fiber having diameter of 148 nm at 16 kV. Further increased the applied voltage to 18 kV with electric field of 1.28 kV/cm directly decrased the TiO_2. fiber diameter to 278 nm. It can be observed also the average bead diameter diminished to 0.20 µm. Finally, at 19 kV with electric field of 1.35 kV/cm, beadles and uniform cylindrical fibers was successfully obtained. Nonetheless, further increased in applied voltage and electric field up to 21 kV with electric field resulted of 1.5 kV/cm resulted in increased bead diameter up to 0.51 µm. These result inferred that increased in voltage applied will result in decreased the bead size and TiO_2. fiber diameter from 17 kV to 19 kV. Beyond 19 kV bigger fiber diameter and bead diameter were formed. Thus, based on the result obtained the optimum condition to form uniform electropun of TiO_2 nanofiber without any bead present were 19kV with electric field of 1.35 kV/cm and PVP content of 12 wt.%. These electrospun were further calcined to form nanorod TiO_2.

5.3 Effect of calcination temperature on TiO_2 nanorod morphology and average diameter

The electrospun PVP-TiO_2 was peeled-off from the Al foil and and then were sintered at different temperature of 400, 500, 600 °C, at 2 °C min^{-1} heating rate respectively for 5 h to determine the effect of different calcination temperature on morphology of nanorod. After the calcination the fiber was ground to form nanorod. The morphology of the TiO_2 nanorod was examined using FESEM. The average TiO_2 nanorod diameters were measured directly from selected FESEM images using image J software.

Figure 5.7 (a) showed the morphology of the P25 commercial nanoparticles. Meanwhile Figure 5.7 (b) to (d) depicts the morphology of TiO_2 nanorod sintered at 400, 500 and 600 ^{0}C respectively. At calcination temperature of 400 ^{0}C as in Figure 5.7 (b), it could be detected that nanorod formed was agglomerate, resulted in non-uniform distribution of nanorod. FESEM micrographs indicate that the nanorod is nearly uniform throughout the surface for the TiO_2 nanorod sintered at 500 ^{0}C as in Figure 5.7 (c). Based on FESEM obtained it could be noted that the morphology of TiO_2 after calcined and mechanical grinding were shows oriented rod-like structure. Thus, it could be observed that there is no significant change in shape when increase the calcination temperature from 400 ^{0}C to 600 ^{0}C. However it notices that from the depicted image, the diameter of nanorod change with different calcination temperature. Diameters of nanorods were determined using Image J software. Figure 5.8 (a) to (c) shows the result of average diameter for TiO_2 nanorod calcined at 400, 500 and 600 ^{0}C respectively. It can be observed the average TiO_2 nanorod diameter calcined at 400 ^{0}C ranges from 84 nm to 321 nm. At the calcination temperature of 500 ^{0}C average nanorod diameter decreased in the range from 52 nm to 281 nm and most of nanorod in 93 nm. The average diameter range increased at 600 °C from 97 to 334 nm.

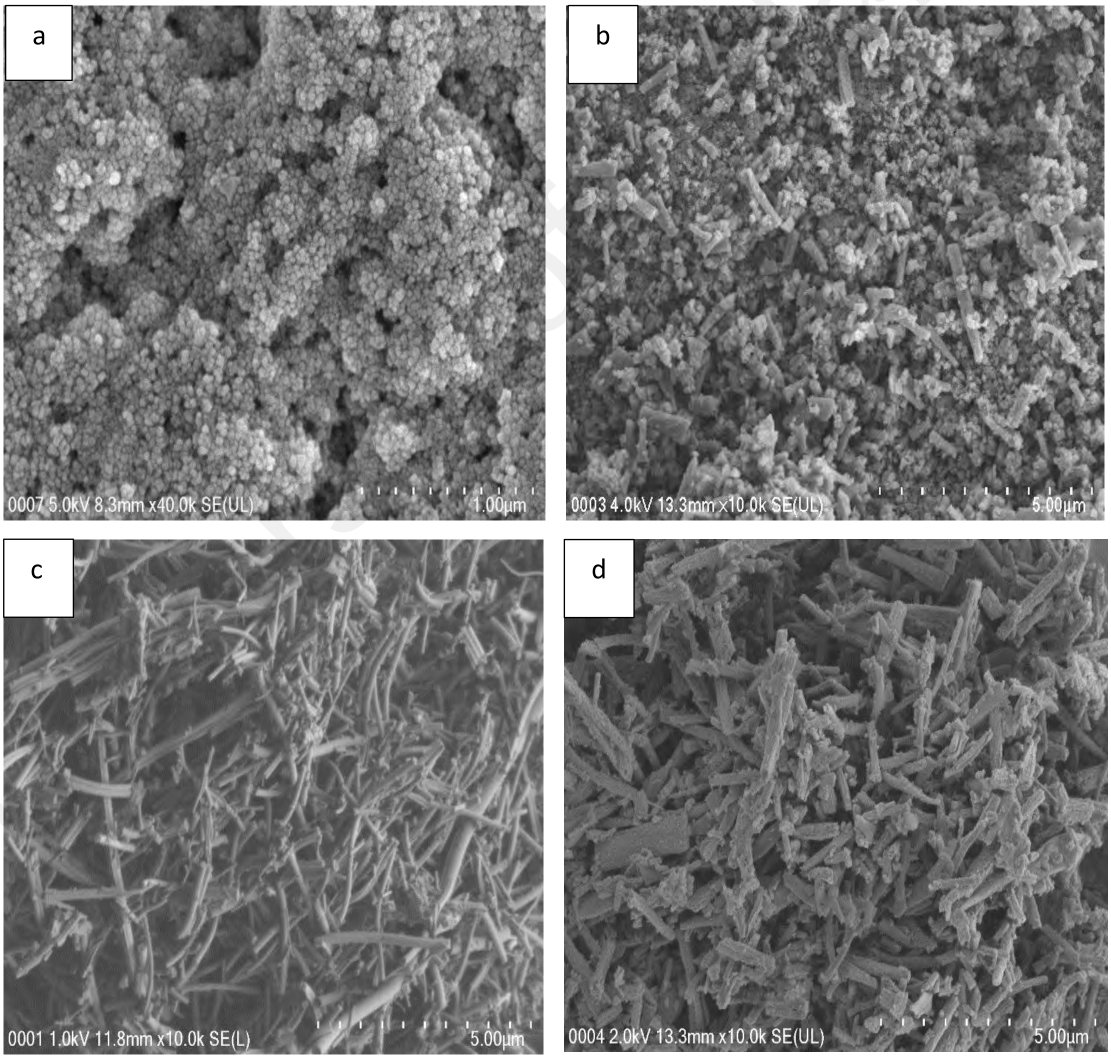

Figure 5.7: FESEM of TiO_2 comercial (a) P25 nanoparticle and TiO_2 nanorod after calcination at (b) 400 ^{0}C, (c) 500 ^{0}C and (d) 600 ^{0}C.

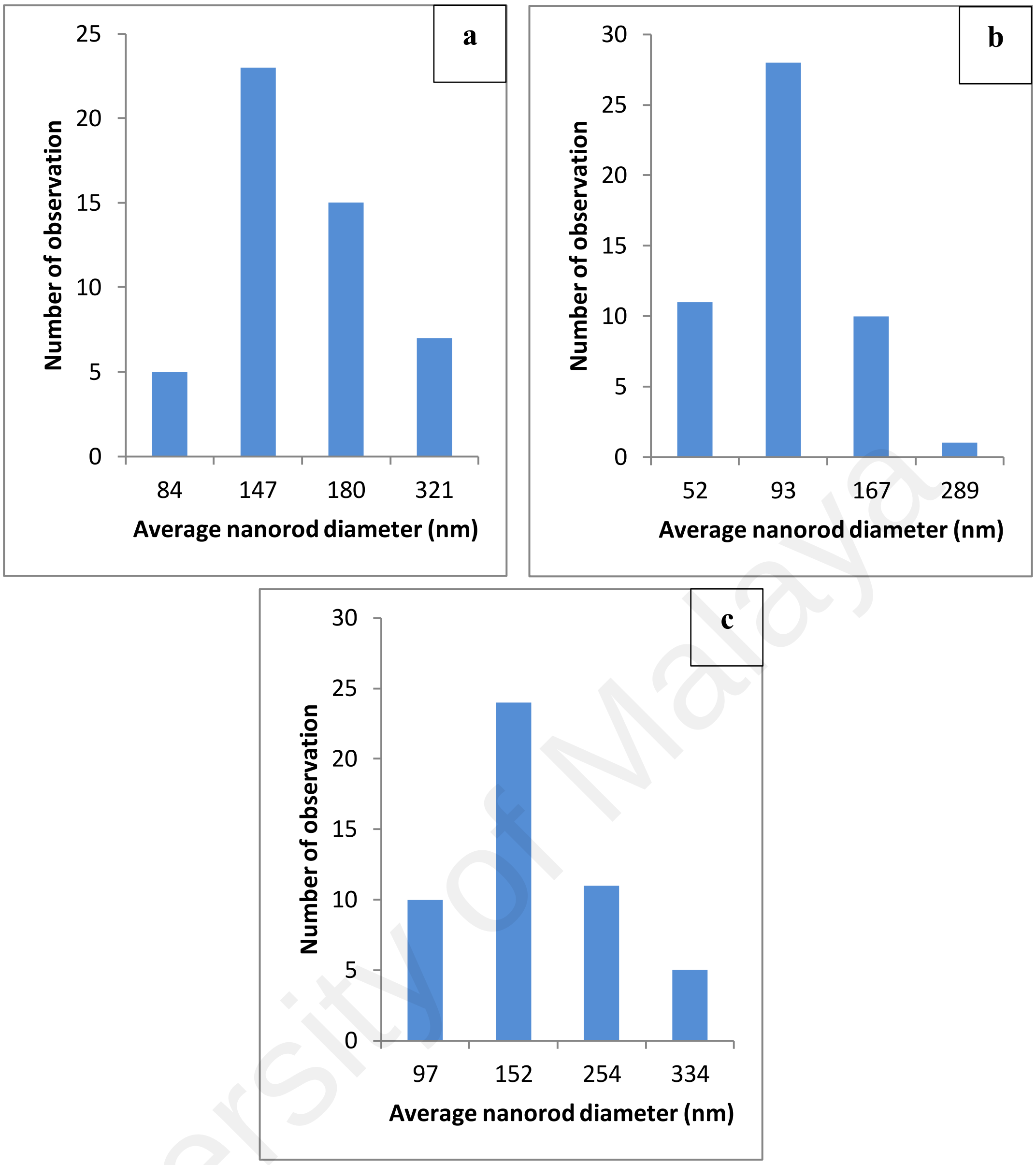

Figure 5.8: Analysis of average fiber diameter of TiO_2 nanorod after calcination at (a) 400, (b) 500 and (c) 600 ^{0}C.

5.4 Energy Dispersive analysis X-Rays: Elemental Microanalysis of TiO_2 nanorod

Chemical analysis of the prepared TiO_2 nanorods synthesized by electrospinning was accomplished using analysis of energy dispersive analysis of X-rays (EDX). EDX spectra of all investigated samples as in Figure 5.9 showed only Ti and O peak. Then the nanorods were pure TiO_2

As evident in Figure 5.10 (a) to (c) the highest intensity peak was at 25.26 ^{0}C for the (101) reflection plane that represents TiO_2 anatase phase. As shown in Figure 5.10 (b) nanorods calcined at 500 ^{0}C temperature have obvious peaks at 2θ values of 25.3^0 (101), 37.8^0 (004), 48.1^0 (200), 54.0^0 (105), 55.1^0(211), and 62.8^0 (204), suggesting that TiO_2 anatase phase had formed. Table 5.3 shows the percentage of anatase and rutile at different calcination temperature.It revealed that nanorod calcined at 500 ^{0}C resuted highest anatase percentage, 90% while sample calcined at 600 ^{0}C showed the lowest anatase value, 57%.

Table 5.3: Percentage of anatase and Rutile TiO_2 sintered at 400, 500 and 600 ^{0}C.

Calcination Temperature (^{0}C)	Anatase (%)	Rutile (%)
400	86	14
500	90	10
600	57	43

5.6 Morphology studies on composite TiO_2 nanoparticle (P25) (NP) and nanorod (NR)

To prepare the electrodes for DSSCs, TiO_2 nanorods fabricated via electrospinning and commercially available TiO_2 nanoparticles (P-25) were mixed in various ratios (10%, 20%, 30%, 40%, 50%) and designated as N1, N2, N3, N4, N5 respectively. The morphology of the mixture TiO_2 nanoparticle and nanorods were observed by using FESEM. Figure 5.11 (a) to (j) depicted the FESEM images of the TiO_2 multi-electrodes with the different nanorod/ nanoparticle ratios at low and high magnification. It could be observed that increased ratio from 10% to 50% nanorod resulted in increased in amount of nanorod present in the composite. Based on the result Figure 5.11 (g) and (j), rod like structure was clearly detected in composite electrode. Although the TiO_2

5.7 Summary

This chapter can be summarized that the morphology of electrospun TiO_2 nanofiber were observed. Polymer concentration and applied voltage affect the morphology of electrospun TiO_2. Uniform nanofiber with no bead obtained for sample V5 with 12% PVP and electrospun at 19kV. Calcination at 500 ^oC with 2^0 C/min heating rate formed a TiO_2 anatase phase. Further grinding TiO_2 nanorod obtained. This has been comfirmed by XRD analysis. Different morphology was observed for different addition of TiO_2 nanorod.

CHAPTER 6: RESULTS FOR DSSC APPLICATIONS

6.1 Introduction

Anthocyanin was extracted from *Melastoma malabathricum* using the optimized parameters determined via RSM. The anthocyanin was used to make DSSCs using commercial TiO_2 ups in the mesoporous layer to obtain the best anthocyanin concentration for best DSSCs performance in terms of efficiency. TiO_2 nanorods prepared using the combined sol-gel and electrospinning methods followed with sintering and grinding processes were mixed with commercial TiO_2 nanoparticles and used as the mesoporous layer in the composite DSSC system. The optimized anthocyanin concentration was used. This is to further improve the DSSC performance with the hope that in the presence of NRs, light harvesting may be improved. The composite DSSCs system was again fabricated, but with additive such as sucrose and sucrose-DCA added to the optimized anthocyanin system to determine the best anthocyanin-additive concentration that may further the efficiency. In this chapter, three types of DSSC systems have been studied.

6.2 Effect of *Melastoma malabathricum's* anthocyanin concentration as natural sensitizer for DSSC using commercial tio$_2$ in mesoporous layer

6.2.1 Visible spectroscopy analysis for different concentrations of anthocyanin sensitizer

Figure 6.1 shows visible spectroscopy of different percentages of anthocyanin extract from *Melastoma malabathricum*. It showed that, the anthocyanin extract from this spesies is able to absorb visible light from 400 nm to 600 nm. As can be seen in the figure on increasing anthocyanin from 1 wt.% to 5 wt.% the maximum absorbance from 0.65 to 1.0 at maximum wavelength of , λ= 523 nm. However further increased to 7 wt.% and 9 wt.% resulted in decreased in maximum absorption to 0.76 and 0.57

respectively. 5 wt.% anthocyanin content resulted in highest absorption, 1.00 at maximum wavelength of 523 nm. This result indicate that 5 wt.% of anthocyanin extract is optimum amount to achieve high visible absorption.

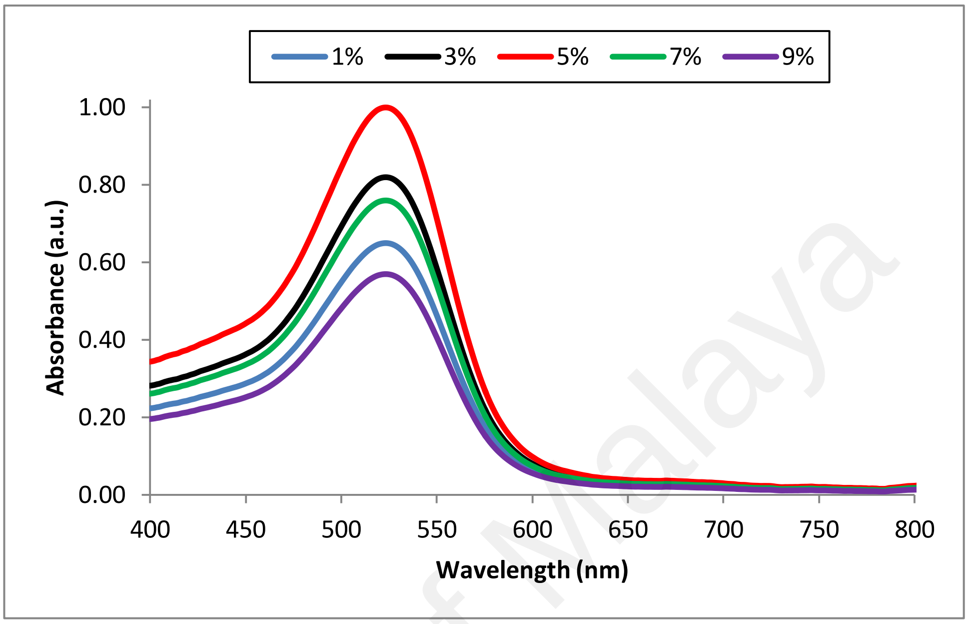

Figure 6.1: Visible spectroscopy of different percentage of anthocyanin extract from Melastoma malabathricum (1%, 3%, 5%, 7% and 9 wt.%).

Figure 6.2 presented the visible spectroscopy of the commercial TiO_2 semiconductor that have been immersed in different anthocyanin extracts (1%, 3%, 5%, 7% and 9%) designated as A1, A2, A3, A4 and A5 respectively. It clearly showed that absorption increased with increasing anthocyanin content from 1 wt.% (A1), (0.48) to 5 wt.%(A3), (0.66). Further increased in anthocyanin content from 7 wt.% (A4) to 9 wt.% (A5) decreased the maximum absorption of visible spectra to 0.39 and 0.30 respectively. The decrement is about ~0.36 compared to sample of commercial TiO_2 semiconductor immersed in 5 wt.% (A3) anthocyanin content. Based on the result obtained also, it can be seen that the maximum absorption wavelength of all samples shifted to the longer wavelength compared to sample of anthocyanin extract from 523 nm to 526 nm.

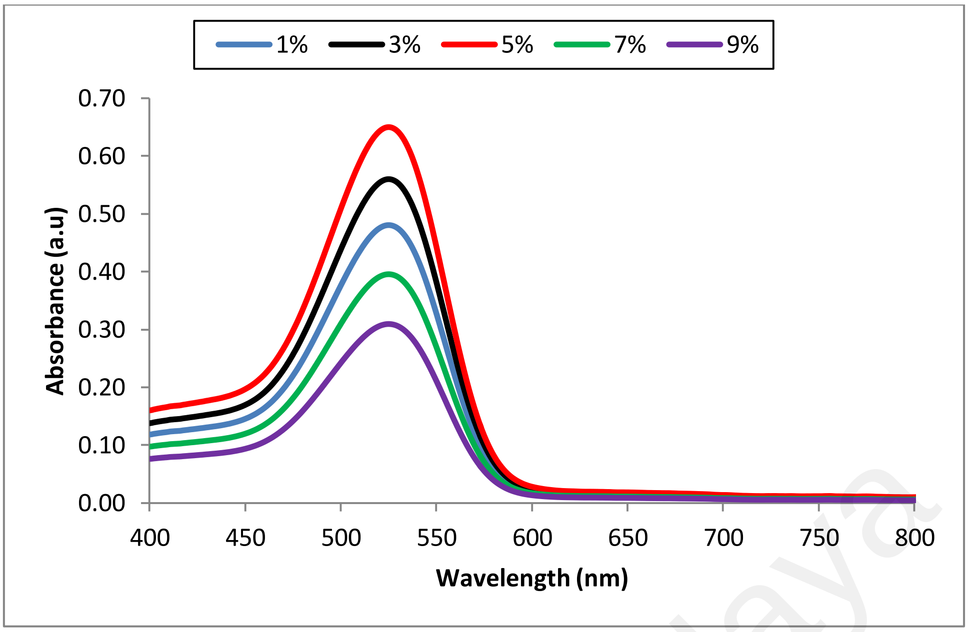

Figure 6.2: Visible spectroscopy of TiO_2 semiconductor that immersed in different anthocyanin extract (1%, 3%, 5%, 7% and 9%).

6.2.2 *J-V* analysis of commercial TiO_2 semiconductor with different anthocyanin extracts (1%, 3%, 5%, 7% and 9%)

Figure 6.3 represents *J-V* analysis of commercial TiO_2 semiconductor with different anthocyanin extracts (1%, 3%, 5%, 7% and 9%) designated as as A1, A2, A3, A4 and A5 respectively. Figure 6.3 shows the *J-V* curve for DSSCs with anthocyanin different concentration of anthocyanin extracted using the optimized parameters obtained via RSM. The open circuit voltage (V_{oc}), short circuit current density (J_{sc}), Fill factor (*FF*) and efficiency (η) along with their standard deviation values of the each cell was listed in Table 6.1. Based on the result, it can be seen that the DSSCs fabricated with TiO_2 electrode soaked in *Melastoma malabathricum* dye exhibited efficiency. The efficiency of the DSSC was observed to increase until it obtained the maximum of (1.054 ± 0.012) % with the TiO_2 electrode soaked in 5 wt.% of *Melastoma malabathricum* dye solution (A3 sample) and higher concentration, 9 wt.% (A5 sample) did not yield better result. The performance of cells with anthocyanin concentration higher than 5 wt.% was slightly decreased till it obtain the minimum of (0.551 ± 0.044)% with the TiO_2 electrode soaked in 9 wt.% of *Melastoma malabathricum* anthocyanin extract solution (A5 sample).

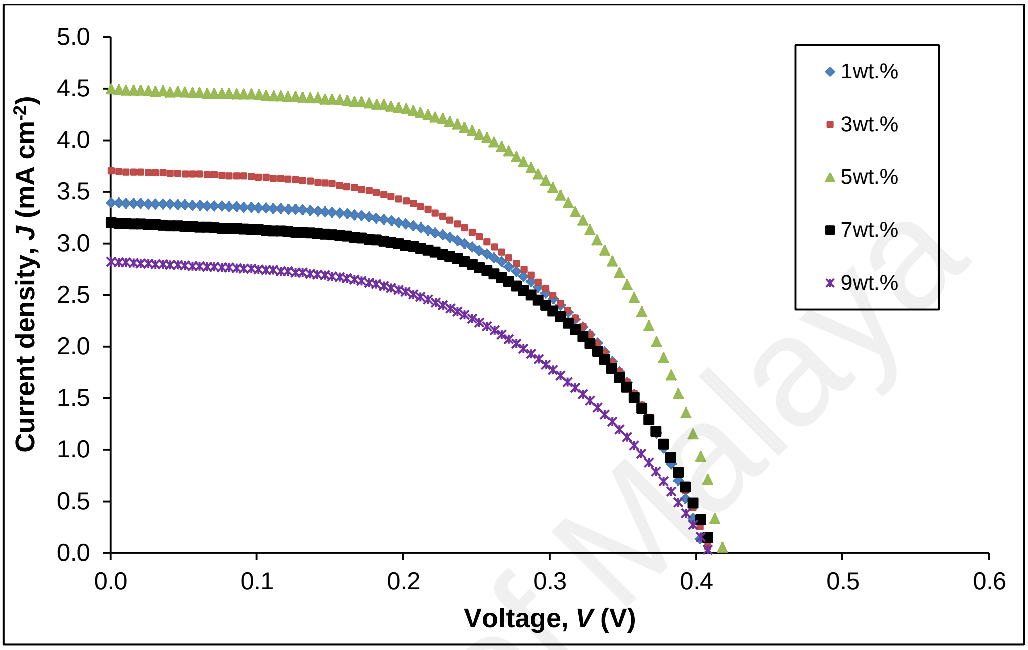

Figure 6.3: *J-V* analysis of commercial TiO_2 semiconductor with different anthocyanin extracts (1%, 3%, 5%, 7% and 9%).

It is clearly observed that the J_{sc} increased in line with the increase in efficiency as in Table 6.1. This showed that anthocyanin concentration helped in increasing the rate of electron injection from the dye excited state to the conduction band edge of TiO_2, thus increasing the efficiency of the DSSCs. From the results obtained in Table 6.1, R_s value decreased with increased anthocyanin concentration up to 5% from (0.030 ± 0.003) Ω–cm^2 to (0.022 ± 0.002) Ω–cm^2. The value of R_s is inversely proportional with the value of efficiency. Increased in anthocyanin concentration up to 9% resulted in increased of R_s value up to (0.046 ± 0.002) Ω–cm^2. The R_{sh} value increased with efficiency. As can be seen the DSSC with the highest efficiency of 5 wt.% anthocyanin (A3 sample) resulted in higher R_{sh} value, (1.620 ± 0.032) Ω–cm^2.

Table 6.1: Values of V_{oc}, J_{sc}, FF, η, R_s and R_{sh} of DSSC fabricated using different wt% of M.malabathricum anthocyanin as dye materials.

Wt.%	J_{sc} (mA cm^{-2})	V_{oc} (V)	FF	η (%)	R_s (Ω–cm^2)	R_{sh} (Ω–cm^2)
1	3.389±0.142	0.403 ± 0.010	0.534 ±0.009	0.729±0.021	0.030±0.003	1.447 ± 0.057
3	3.690±0.139	0.413 ± 0.008	0.540 ±0.008	0.823±0.014	0.029±0.003	1.572 ± 0.045
5	4.487±0.135	0.418 ± 0.004	0.569 ±0.008	1.054±0.012	0.022±0.002	1.620 ± 0.032
7	3.225±0.140	0.408 ± 0.010	0.535 ±0.012	0.704±0.089	0.033±0.002	1.230 ± 0.054
9	2.827±0.136	0.408 ± 0.011	0.477 ±0.014	0.551±0.044	0.046±0.002	1.173 ± 0.060

6.2.3 Incident photon-to-current conversion efficiency (IPCE) characterization at different weight percentages of anthocyanin dye

Figure 6.4 shows the IPCE of the prepared DSSCs sensitized by *Melastoma malabathricum* dye. As revealed in the figure, when the incident light wavelength is at 560 nm, the DSSC prepared using *Melastoma malabathricum* dye at 5 wt.% anthocyanin concentration (A3 sample) exhibited the highest IPCE value at around 21%.

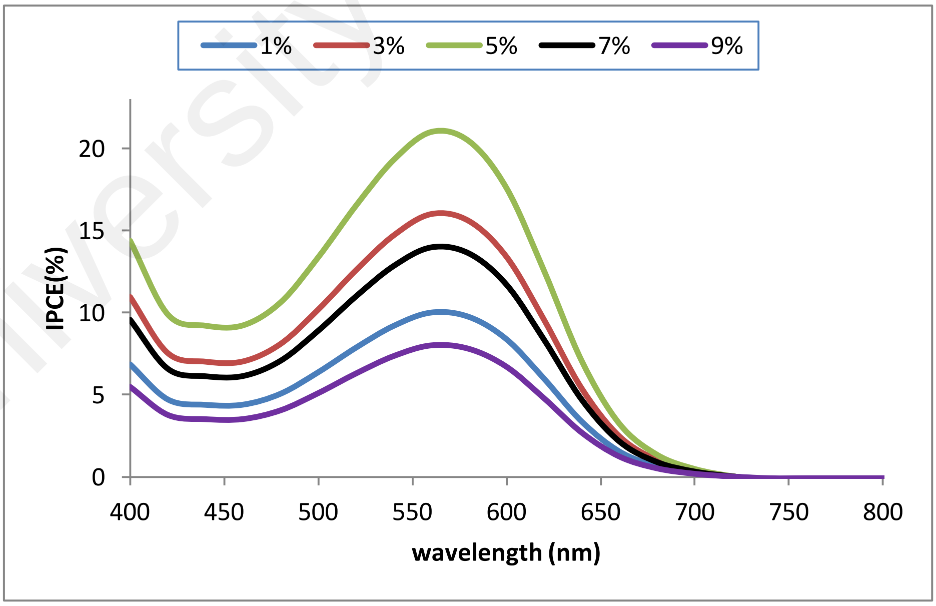

Figure 6.4: IPCE curves of DSSCs sensitized by anthocyanin from *Melastoma malabathricum* at different percentage (1%, 3%, 5%, 7% and 9 wt.%).

It can be observed that increased anthocyanin concentration from 1 wt.% to 5 wt.% directly increased the IPCE value from 10% to 21% respectively. Beyond 5 wt% the

counter electrode, the second semicircle, R_2 is the resistance of charge transfer at the TiO_2/dye/electrolyte interface and in the third semicircle, R_3 is ionic diffusion resistance in the electrolyte (Sarker et al., 2018). Based on the figure three semicircle were observed. Since other resistances are not affected by the use of different dye percentages, we focused on the differences in R_2 which represented as second semicircle.

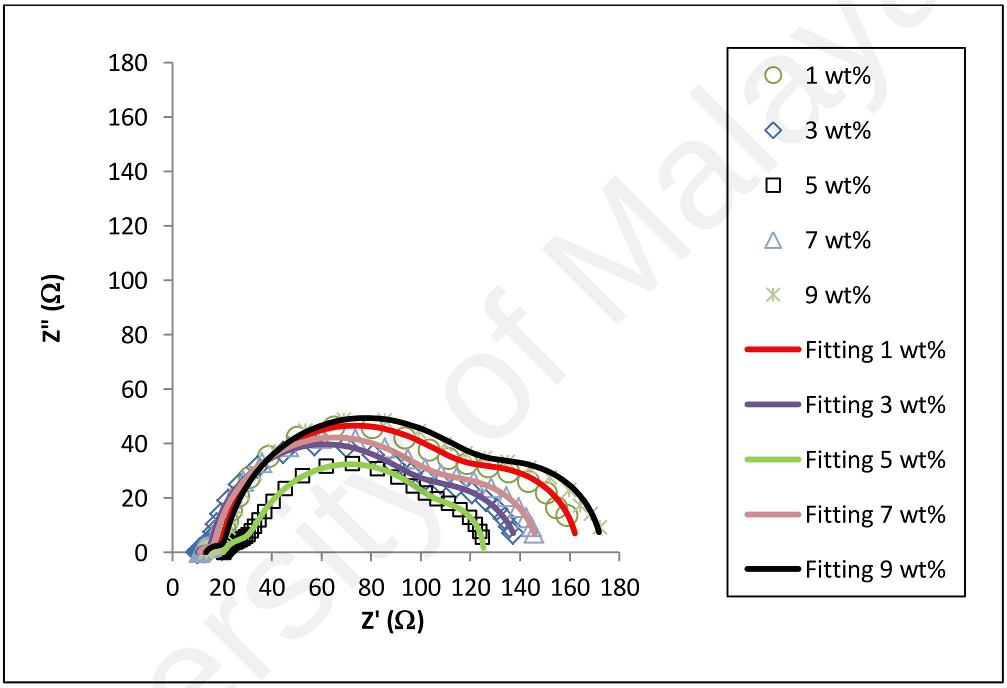

Figure 6.6: EIS for DSSCs based anthocyanin sensitized at different weight percentages of anthocyanin from *Melastoma malabathricum* at different percentage (1%, 3%, 5%, 7% and 9 wt.%).

The fitted graphs are also shown in Figure 6.6. These fitted graphs were used to evaluate the R_s, R_1, R_2 and R_3 value. As mentioned earlier in Chapter 3, R_s is ohmic serial resistance. R_1 in the first semicircle is the resistance of charge transfer at the Pt counter electrode, the second semicircle, R_2 is the resistance of charge transfer at the TiO_2/dye/electrolyte interface and in the third semicircle, R_3 is ionic diffusion resistance in the electrolyte (Sarker et al., 2018). Based on the figure three semicircle were observed. Since other resistances are not affected by the use of different dye percentages, we focused on the differences in R_2 which represented as second semicircle.

Table 6.2: R_s, R_1, R_2, R_3 values for DSSCs based anthocyanin sensitized at different weight percentages (1%, 3%, 5%, 7% and 9 wt.%) of dyes.

Wt.%	R_s (Ω)	R_1 (Ω)	R_2 (Ω)	R_3 (Ω)
1	13.05 ± 0.03	5.40 ± 0.14	91.80 ± 0.49	49.50 ± 0.14
3	8.75 ± 0.04	10.15 ± 0.17	81.55 ± 0.41	35.70 ± 0.19
5	20.45 ± 0.02	8.40 ± 0.10	68.95 ± 0.38	25.50 ± 0.11
7	12.50 ± 0.06	11.50 ± 0.18	84.40 ± 0.42	38.80 ± 0.20
9	13.47 ± 0.05	7.66 ± 0.15	96.00 ± 0.43	48.35 ± 0.19

The R_s, R_1, R_2 and R_3 values calculated for the DSSCs based anthocyanin at different percentages are presented in Table 6.2. The R_2 values of (68.95 ± 0.08) Ω is lower for the cell with 5 wt.% of anthocyanin dyes (A3) but cell with 9 wt.% of anthocyanin dyes (A5 sample) exhibited the highest R_2 value of (96.00 ± 0.13) Ω. Increased in concentration of anthocyanin dyes from 1 wt. % (A1) to 5 wt.% (A3) directly decreased the value of R_2 from (91.80 ± 0.49)Ω to (68.95 ± 0.38) Ω. The decrement is about 22.85Ω. Beyond 5 wt.% of anthocyanin content the value of R_2 started to increased up to (96.00 ± 0.43)Ω for 9 wt.% anthocyanin content. DSSCs sensitized with anthocyanin extracted from *Melastoma malabathricum* displays a good cell potential, further improvement can still be employing in order to enhance the performance of this cell. It is revealed that, the sample that immersed in 5 wt.% of *Melastoma malabathricum* anthocyanin dye (A3 sample) exhibit highest efficiency with lowest R_2 value. This sample was selected to further enhance the DSSCs performance by incorporating TiO_2 nanorods into the mesoporous TiO_2 nanoparticles.

6.3 Effect of different percentage of tio$_2$ nanorods on composite dsscs (NPs - NR) system

6.3.1 Visible studies of different weight percentages of TiO$_2$ nanorods in (NPs - NRs) system

The second DSSC systems were prepared by incorporated five different amounts of TiO$_2$ nanorods (NRs) (10, 20, 30, 40 and 50 wt.%) into mesoporous TiO$_2$ nanoparticles (NPs) designated as B1, B2, B3, B4 and B5. As mention before, 5 wt. % anthocyanin sensitizer (A3) were used since exhibit the highest efficiency (1.054 ± 0.012)% in the first system study. Figure 6.7 shows the absorption spectra of anthocyanin absorbed into the TiO$_2$ NRs-NPs composite electrode after immersed into dye solution. The absorption spectrum for pigmented composite electrode with anthocyanin extract from fruit pulp of *Melastoma malabathricum* displays a higher peak at wavelength, λ= 527 nm

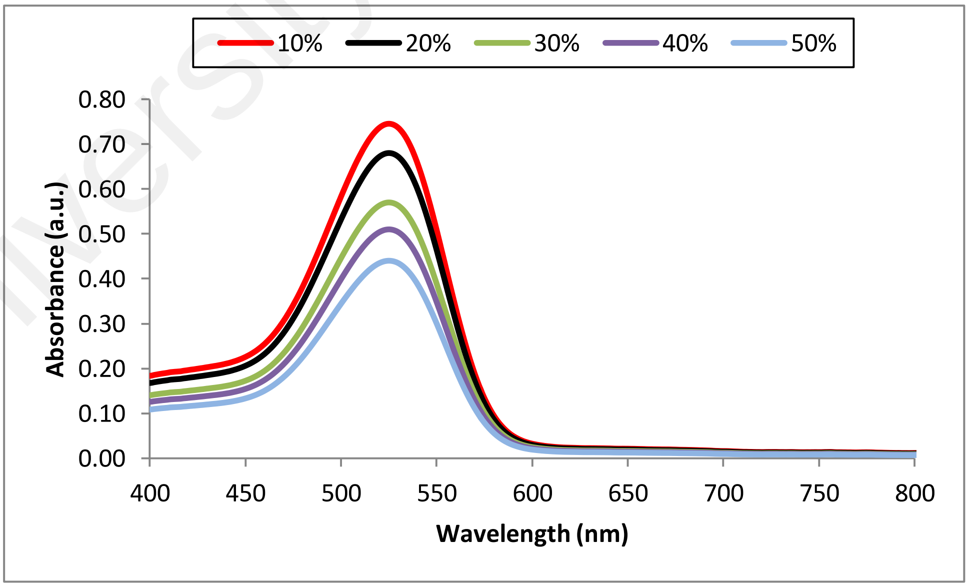

Figure 6.7: The absorption spectra of composite electrodes based on different percentages (10, 20, 30, 40 and 50 wt.%) of TiO$_2$ nanorods sensitized at 5 wt.% of *Melastoma malabathricum* anthocyanin dyes.

From the figures, it can be observed that the highest absorption of pigmented composite electrodes achieved by B1 samples with 10 wt.% addition of NRs. This composite electrode shows a slightly increased in absorption intensity of 0.74 compared to the commercial DSSCs sytems (NPs electrode) 0.71 with ~4.2% increments. This means that the composite electrode can absorb more anthocyanin dye compared to NPs electrode. This will lead to improvement of light-to-electricity conversion efficiency of the DSSC. However, as increased the nanorods percentages from 20 to 50 wt.% the maximum absorption continued to decrease.

6.3.2 *J-V* characterization of DSSCs sensitized at different weight percentages of TiO_2 nanorods

The effect of different weight percentage of NRs added on performance of composite DSSC was further investigated. The DSSCs were illuminated under 1000 W m^{-2} at room temperature. Figure 6.8 represent the *J-V* curves of the second systems (NPs-NRs composite). The J_{sc}, V_{oc}, FF, η, R_s and R_{sh} values are tabulated in Table 6.3. There was significant enhancement observed for J_{sc} and η values with 10 wt.% NR addition, designated as B1 attained highest J_{sc} of (4.711 ± 0.109) mA cm^{-2} and efficiency (η) of (1.351± 0.013)%.

The R_{sh} value observed also maximum at (2.228 ± 0.025) Ω-cm^2 with lower Rs values at (0.021 ± 0.002) Ω-cm^2 as seen in Figure 6.8 and Table 6.3. For comparison, the DSSC made using the commercial TiO_2 NPs in previous results had J_{sc}, η values of (4.487 ± 0.135) mA cm^{-2} and (1.054 ± 0.012)%, respectively. From this comparison, there was ~5% improvement in J_{sc} value while ~29% increase in η values. The increase in J_{sc} and η values are probably due to enhanced dye loading and light scattering effect (Chen et al., 2013). However, when increasing the percentages of TiO_2 nanorods from 20 to 50 wt.% the J_{sc}, η and Rsh values are observed to decrease continuously, as seen in Table 6.3. In contrast, the *Rs* value is observed to increase continuously from sample B2 to B5 sample. It revealed that 10 wt.% NRs inclusion to NPs composite is enough amount to improve the second system DSSCs.

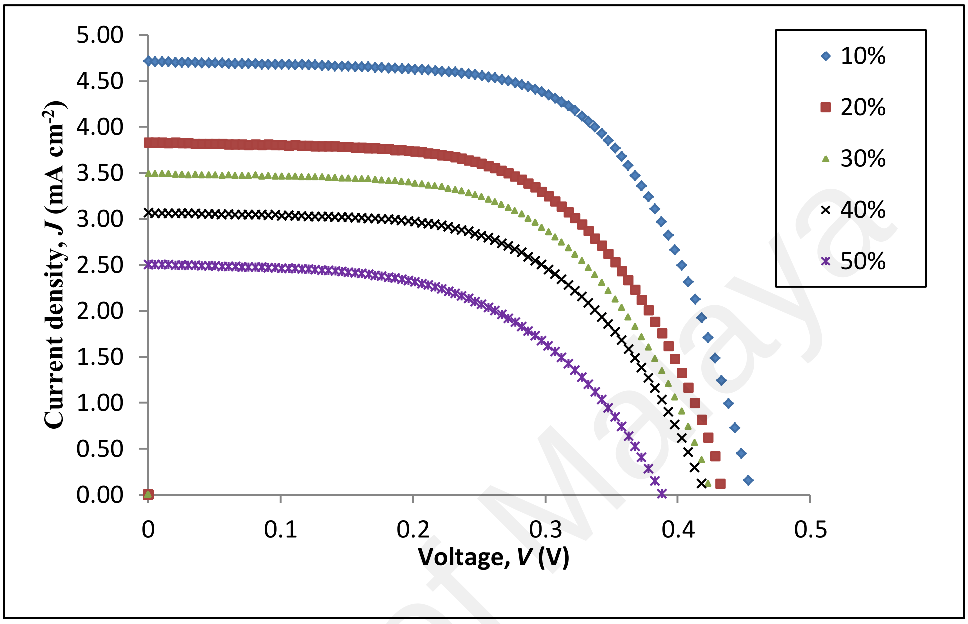

Figure 6.8: *J-V* curve for composite DSSCs fabricated from TiO_2 nanoparticle-nanorod samples with nanorod percentages of 10, 20, 30, 40 and 50 wt.% sensitized at 5 wt.% anthocyanin dyes.

Table 6.3: J_{sc}, V_{oc}, FF, η, R_s and R_{sh} values for composite DSSCs fabricated from TiO_2 nanoparticle-nanorod samples with nanorod percentages of 10, 20, 30, 40 and 50 wt.% sensitized at 5 wt.% anthocyanin dyes.

Wt.%	J_{sc} (mA cm^{-2})	V_{oc} (V)	FF	η (%)	R_s (Ω-cm^2)	R_{sh} (Ω-cm^2)
10%	4.711 ±0.109	0.458 ±0.004	0.626 ± 0.007	1.351 ±0.013	0.021±0.002	2.228 ±0.025
20%	3.824 ±0.112	0.432 ±0.007	0.594 ± 0.010	0.982 ±0.024	0.025±0.001	2.131 ±0.032
30%	3.470 ±0.115	0.423 ±0.010	0.581 ± 0.013	0.853 ±0.028	0.029±0.003	1.889 ±0.040
40%	3.061 ±0.123	0.418 ±0.020	0.581 ± 0.016	0.743 ±0.021	0.032±0.004	1.859 ±0.043
50%	2.516 ±0.128	0.388 ±0.012	0.536 ± 0.021	0.523 ±0.020	0.045±0.002	1.781 ±0.052

6.3.3 Incident photon-to-current conversion efficiency (IPCE) characterization at different weight percentages of TiO_2 nanorods

Figure 6.9 represented the incident photon to current conversion efficiency (IPCE) spectra of the composite photoanode made up of different percentages of TiO_2 nanorods (NRs) (10, 20, 30, 40 and 50 wt.%). These composite photoanode were sensitized with dye percentages of 5 wt.%. Previously, the IPCE of commercial DSSC system sensitized with 5 wt.% of anthocyanin dye exhibits a maximum of 21% at 580 nm. In the entire wavelength region of 300-800 nm, NP-NR composites photoanode reveals higher IPCE values than commercial system, which is compatible with the J_{sc} value obtained by photocurrent-voltage measurement. The IPCE peak for the CP1 electrode with 10 wt.% of NRs showed the highest photon to current conversion efficiency of 26 % at higher wavelength 600 nm. In order to estimate the light scattering effect, the NP-NR composite electrode showed higher IPCE values in the long wavelength region around 600-700 nm, suggesting that the NP-NR composite electrode provides an appreciable light scattering effect (Hong et al., 2014). This values is much higher than the value of 21% obtained for commercial sample without NR addition. The increment is about 7%. The IPCE peak for other composite electrodes continuously decreased in which the values were 17%, 13%, 10%, and 7% designated for D2 to D5 respectively.

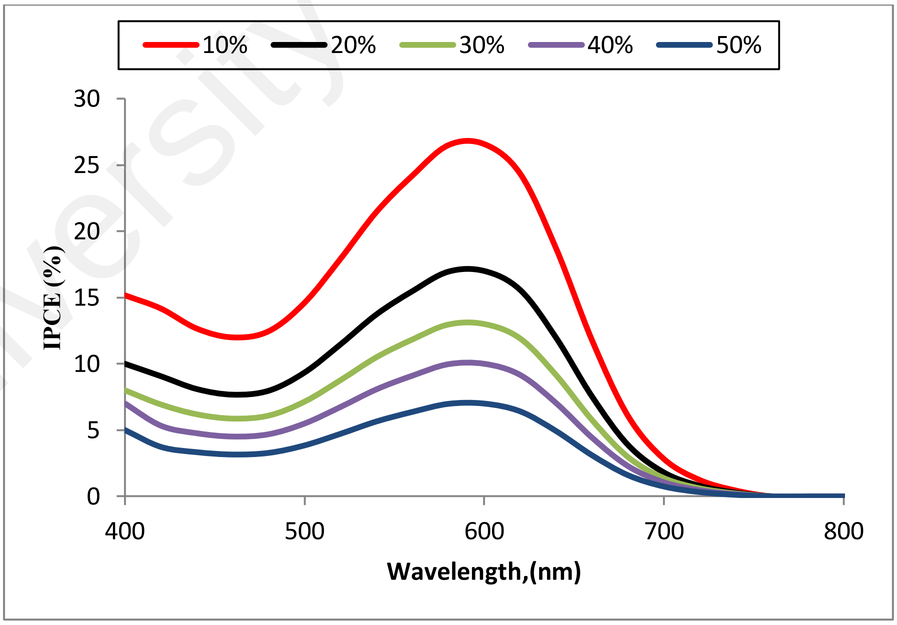

Figure 6.9: IPCE curves for composite DSSCs fabricated from TiO_2 nanoparticle-nanorod samples with nanorod percentages of 10, 20, 30, 40 and 50 wt.% sensitized at 5 wt.% anthocyanin dyes.

6.3.4 Electrochemical impedance spectroscopy (EIS) characterization at different weight percentages of TiO_2 nanorods

Figure 6.10 displays the Nyquist and fitting plots of the fabricated composite DSSCs at various nanorods weight ratios sensitized with 5 wt.% *Melastoma malabathricum* anthocyanin dyes. Rs, R_1, R_2, R_3 values calculated for the composite DSSCs based anthocyanin dyes are presented in Table 6.4. R_2 values of (62.40 ± 0.28) Ω, is observed to be lower for the cell with 10 wt.% nanorods. When increasing the NR percentages from B2 (20 wt.%) to B5 (50 wt.%), the R_2 values increased continuously, with the highest R_2 values (97.60 ± 0.46) Ω achieved by the B5 samples. This correlated with *J-V* analysis study which B5 (50 wt.%) resulted in lowest efficiency value. As expected, R_2 values affect the DSSCs performance whereby the highest efficiency performance associated with samples that possesses lowest R_2 values.

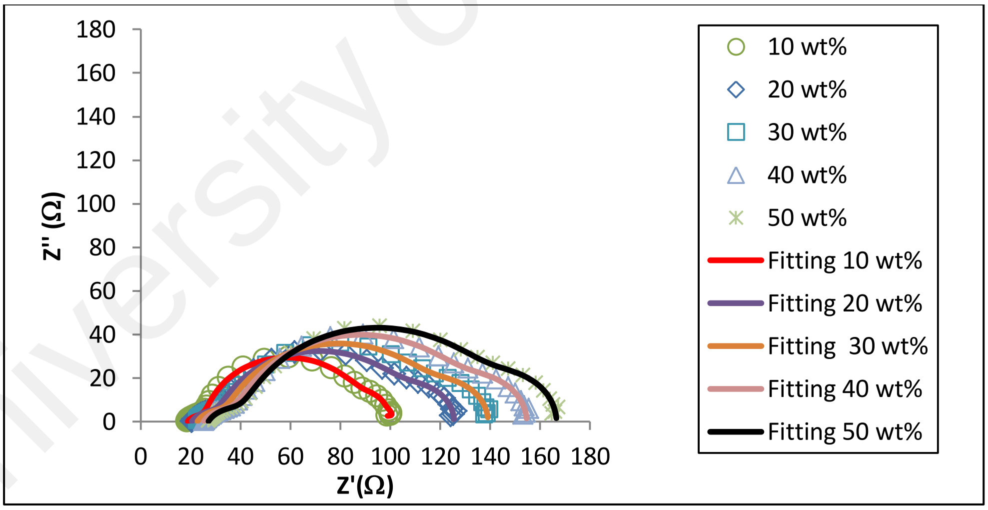

Figure 6.10: EIS for composite DSSCs fabricated from TiO_2 nanoparticle-nanorod samples with nanorod percentages of 10, 20, 30, 40 and 50 wt. % sensitized at 5 wt.% anthocyanin dyes.

DSSCs based anthocyanin extracted from *Melastoma malabathricum* resulted in improving cell performance with modification of photoanode with 10 wt.% of NRs(B1). In an effort to further ehance the performance of DSSCs based anthocyanin extracted from *Melastoma malabathricum*, DSSC were investigated by addition of additive which are sucrose (third design) and (fourth design) sucrose-DCA. The cell with highest efficiency and lower R_2 values (10 wt.% nanorods), B1 was further increased the performance by added of additive.

Table 6.4: R_s, R_1, R_2, R_3 values for composite DSSCs fabricated from TiO_2 nanoparticle-nanorod samples with nanorod percentages of 10, 20, 30, 40 and 50 wt.% sensitized at 5 wt.% anthocyanin dyes.

Wt.%	R_s (Ω)	R_1 (Ω)	R_2 (Ω)	R_3 (Ω)
10	19.50 ± 0.04	11.70 ± 0.15	62.40 ± 0.28	20.00 ± 0.12
20	20.45 ± 0.06	16.90 ± 0.16	72.00 ± 0.33	17.00 ± 0.15
30	22.00 ± 0.07	10.80 ± 0.18	80.56 ± 0.39	23.50 ± 0.19
40	23.00 ± 0.05	10.80 ± 0.21	86.80 ± 0.45	23.40 ± 0.13
50	27.09 ± 0.06	15.00 ± 0.10	97.60 ± 0.46	27.40 ± 0.15

6.4 Effect of Different Additives Addition on Composite DSSCs System

6.4.1 Visible spectroscopy studies at different weight percentages of sucrose

The performance of composite cell of B1 (10 wt.% NR) systems were further improved by adding the additives to the optimized anthocyanin dye (5 wt.%). Sucrose and sucrose-deoxycholic acid (sucrose-DCA) at five different weight percentages (2, 4, 6, 8 and 10 wt.%) was added into the optimized anthocyanin dye solutions. The B1 composite systems were immersed for 24 h into the solutions of anthocyanin-additives containing sucrose and sucrose-DCA separately. The sucrose added samples were designated as C1, C2, C3, C4 and C5 while sucrose-DCA were designated as D1, D2, D3, D4 and D5 respectively. Figure 6.11 shows the visible spectrum of TiO_2 composite electrode after immersed into anthocyanin-sucrose and Figure 6.12 shows absorption spectra for sample immersed in anthocyanin-sucrose-DCA *Melastoma malabathricum* anthocyanin solutions. The absorption spectrum for pigmented composite electrode sensitized with anthocyanin-sucrose at different percentages shows a higher peak at wavelength, λ= 529 nm. From the Figures 6.11, it can be detected that the highest absorption of pigmented composite electrodes for sucrose added samples achieved by 2 wt.% sucrose with intensity of 0.76.

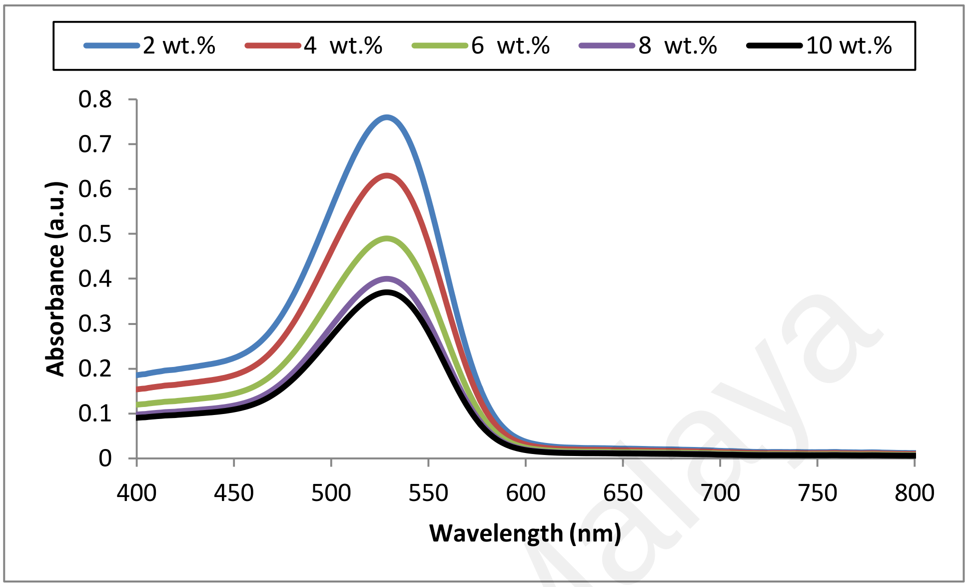

Figure 6.11: The absorption spectra of anthocyanin-pigmented TiO_2 composite electrodes with 10 wt.% TiO_2 NRs at different weight percentage of additives (2, 4, 6, 8 and 10 wt.% sucrose).

For anthocyanin-sucrose-DCA cells Figure 6.12, the higher peak observed shifted from 529 nm to highest wavelength, 532 nm for 6 wt.% sucrose-DCA. Highest absorption exhibited by 6 wt.% sucrose-DCA added with intensity of 1.000. The composites added sucrose-DCA additives showed a huge increased values compared to 10 wt.% NR-NPs composite without additives which the increment was ~35 %. This shows that by adding 2wt.% sucrose (C1 sample) and 6 wt.% sucrose-DCA (D3 sample) additives, help the composite electrode to absorb more anthocyanin dye. This trend is obviously observed for sample with 6 wt.% sucrose-DCA. Beside the ability to absorb to longer visible wavelength make it become favourable for DSSC application. Further increased the sucrose-DCA content up to 10 wt.% (D5) decreased the maximum absorption to 0.30. This shows that the optimum amount of sucrose-DCA additive needed is crucial in order to absorb more light in visible region. However, for sucrose without DCA additive, further addition percentages from 4 to 10 wt.%, the absorption spectra constantly decreased. It revealed that sucrose-DCA more suitable additive for anthocyanin sensitized solar cell compared to sucrose without DCA additive.

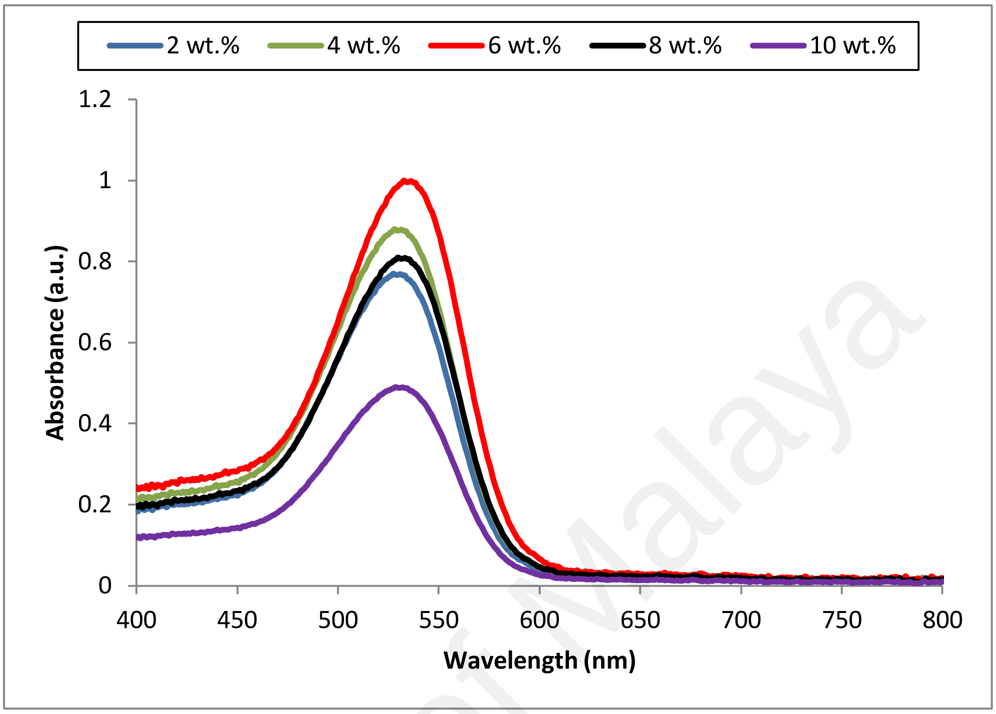

Figure 6.12: The absorption spectra of anthocyanin-pigmented TiO_2 composite electrodes with 10 wt.% TiO_2 NRs at different weight percentage of additives (2, 4, 6, 8 and 10 wt.% sucrose-DCA).

6.4.2 *J-V* characterization of DSSCs sensitized at different weight percentages of additives

The optimized composite photoanodes were subjected to *J-V* analysis to examine the effect of additive added on DSSC performances. DSSCs with B1 photoanode (10 wt.% NRs) were immersed for 24 h into anthocyanin-sucrose and anthocyanin-sucrose and anthocyanin-sucrose-DCA solution at five different percentages (2, 4, 6, 8 and 10 wt.% sucrose), respectively and measured under 1000 W m^{-2} at room temperature. Figure 6.13 illustrated the *J-V* curve of sample at different sucrose percentage while Figure 6.14 represent *J-V* curve for cell immersed in anthocyanin-sucrose-DCA. The J_{sc}, V_{oc}, FF, η, R_s and R_{sh} values are tabulated in Table 6.5 and 6.6. For comparison, the previous results for composite DSSC of 10 wt.% NR without additives addition had J_{sc}, η values of (4.711 ± 0.109) mA cm^{-2} and (1.351 ± 0.013)%, respectively. There were significant enhancement observed for J_{sc}, and η values due to addition of additives.

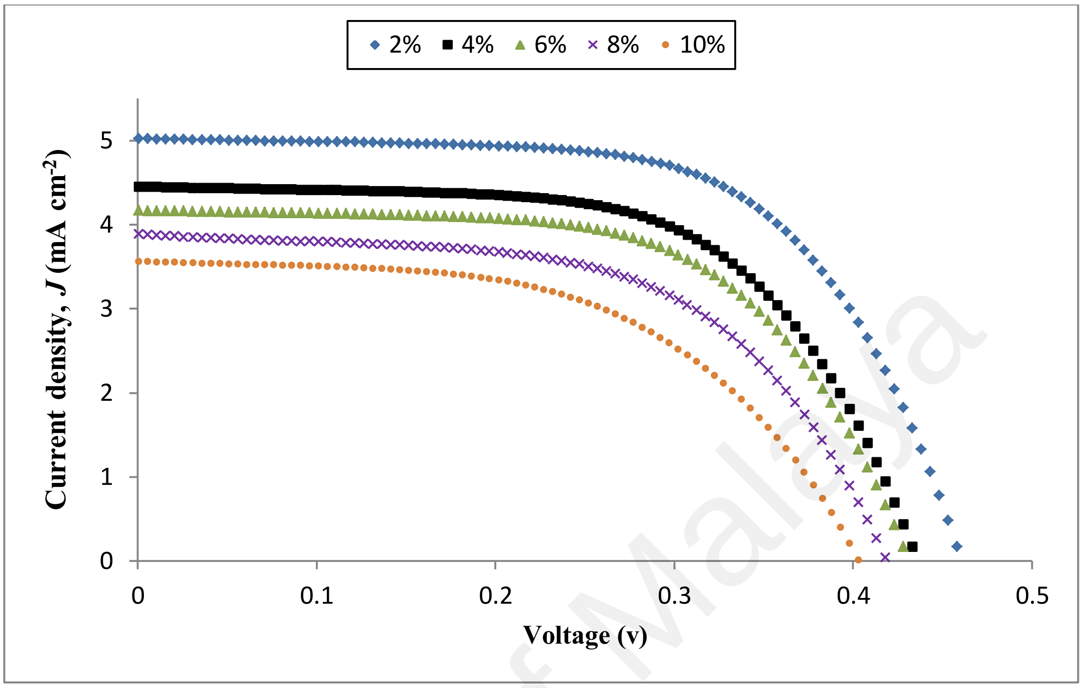

Figure 6.13: *J-V* curve for composite DSSCs fabricated with 10 wt.% TiO_2 NRs at different weight percentage of additives (2, 4, 6, 8 and 10 wt.% sucrose).

Table 6.5: J_{sc}, V_{oc}, FF, η, R_s and R_{sh} values for composite DSSCs fabricated with 10 wt.% TiO_2 NRs at different weight percentage of additives (2, 4, 6, 8 and 10 wt.% sucrose).

Wt.%	J_{sc} (mA cm^{-2})	V_{oc} (V)	FF	η (%)	R_s (Ω-cm^2)	R_{sh} (Ω-cm^2)
2%	5.020 ± 0.093	0.458 ± 0.010	0.635 ± 0.005	1.461 ± 0.024	0.019 ± 0.003	2.518±0.04
4%	4.457 ± 0.094	0.433 ± 0.011	0.619 ± 0.018	1.194 ± 0.021	0.021 ± 0.004	2.361±0.01
6%	4.174 ± 0.092	0.428 ± 0.012	0.617 ± 0.009	1.102 ± 0.020	0.023 ± 0.003	1.970±0.02
8%	3.868 ± 0.113	0.418 ± 0.009	0.594 ± 0.008	0.938 ± 0.013	0.025 ± 0.002	1.208±0.08
10%	3.569 ± 0.125	0.403 ± 0.019	0.546 ± 0.009	0.785 ± 0.028	0.031 ± 0.006	1.066±0.04

The composite DSSCs containing sucrose-DCA additives shown great improvement of photocurrent compared to that containing sucrose without DCA additives. There were slightly increased in J_{sc} and η values for 2 wt.% of sucrose (C1 sample) which the values were (5.020 ± 0.093) mA cm^{-2} and (1.461 ± 0.024)%, respectively as seen in Figure 6.13 and Table 6.5. Beyond 2 wt.% sucrose, the DSSCs efficiency start to decrease from (1.194 ± 0.021)% (4 wt.% sucrose-C2 sample) to (0.785 ± 0.028)% (10 wt.% sucrose-C5 sample). Since the efficiency of cell decrease thus, the J_{sc} also decreased from (4.457 ± 0.094) mA cm^{-2}. It shows that addition of sucrose additive only slightly improve the performance of composite photoanode DSSC.

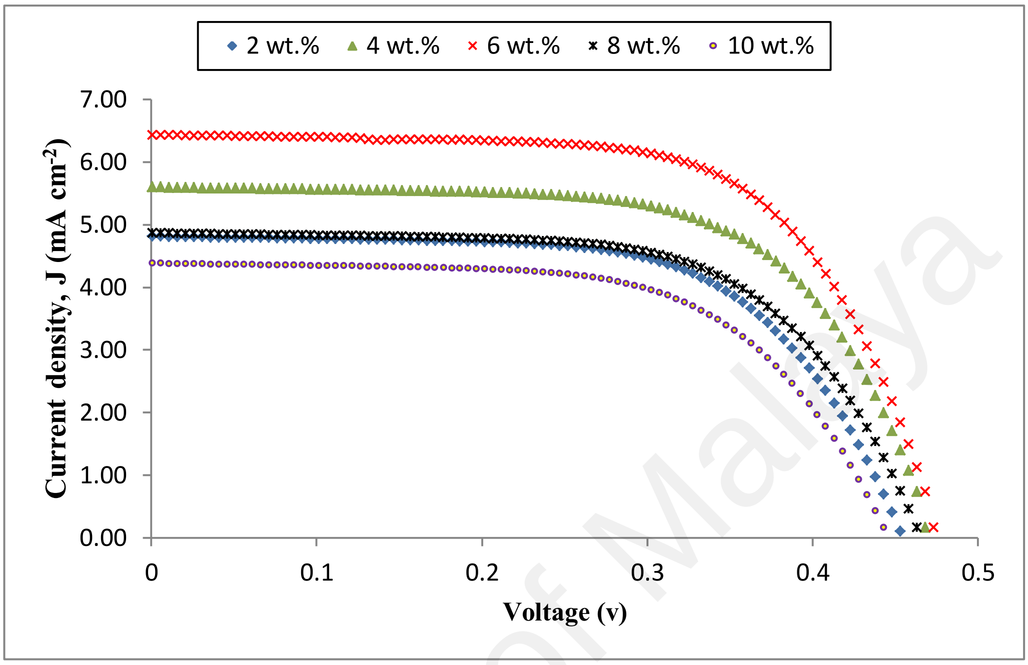

Figure 6.14: *J-V* curve for composite DSSCs fabricated with 10 wt.% TiO_2 NRs at different weight percentage of additives (2, 4, 6, 8 and 10 wt.% sucrose-DCA).

Table 6.6: J_{sc}, V_{oc}, *FF*, η, R_s and R_{sh} values for composite DSSCs fabricated with 10 wt.% TiO_2 NRs at different weight percentage of additives (2, 4, 6, 8 and 10 wt.% sucrose-DCA).

Wt.%	J_{sc} (mA cm^{-2})	V_{oc} (V)	*FF*	η (%)	R_s (Ω-cm^2)	R_{sh} (Ω-cm^2)
2%	4.809±0.079	0.453 ± 0.007	0.634 ±0.007	1.382 ±0.023	0.0197±0.004	2.228±0.032
4%	5.585±0.065	0.468 ± 0.005	0.649 ±0.013	1.697 ±0.029	0.0159±0.003	2.344±0.023
6%	6.360±0.059	0.473 ± 0.005	0.656 ±0.006	1.974 ±0.014	0.0133±0.003	2.918±0.019
8%	4.862±0.070	0.463 ± 0.010	0.638 ±0.011	1.436 ±0.020	0.0193±0.002	2.241±0.024
10%	4.386±0.073	0.443 ± 0.020	0.624 ±0.010	1.213 ±0.026	0.0212±0.006	2.105±0.023

However the efficiency greatly improved with addition of sucrose-DCA into *Melastoma malabathricum* sensitizer. The highest efficiency for sucrose-DCA series is exhibited by the 6 wt.% (D3 sample) with J_{sc} of (6.360 ± 0.059) cm^{-2} and η of (1.974 ± 0.014)%. These shows a huge increment of ~35% for J_{sc} value and ~46% for η values compared to the DSSC system without additives addition. The R_{sh} value observed also maximum at (2.918 ± 0.019) Ω-cm^2 with lower R_s values at 0.0133 Ω-cm^2 as seen in Figure 6.14 and Table 6.6. The addition of 2 wt.% (D1) to 6 wt.% (D3) successfully increased the performance DSSC. Beyond D3, 6 wt.% of sucrose-DCA to D5, 10 wt.% of sucrose-DCA addition the efficiency performance diminished till (1.213 ± 0.026) % for η values and (4.386 ± 0.073) mA cm^{-2} for J_{sc}. These results revealed that sample of 10% NRs-NPs composite immersed in anthocyanin from *Melastoma malabathricum* with addition 6 wt.% of sucrose-DCA (D3) improved the DSSC performance. Thus sucrose-DCA has a big impact as additive for this study. To further confirm this sample were subjected to IPCE analysis.

6.4.3 Incident photon-to-current conversion efficiency (IPCE) characterization at different weight percentages of additives

IPCE analysis was done for further investigation on the effects of additives on the DSSCs performance after *J-V* characterized. The IPCE spectra of the composite (10 wt.% NRs) photoanode sensitized at 5 wt.% anthocyanin with combination of sucrose and sucrose-DCA additives are shown in Figure 6.15.

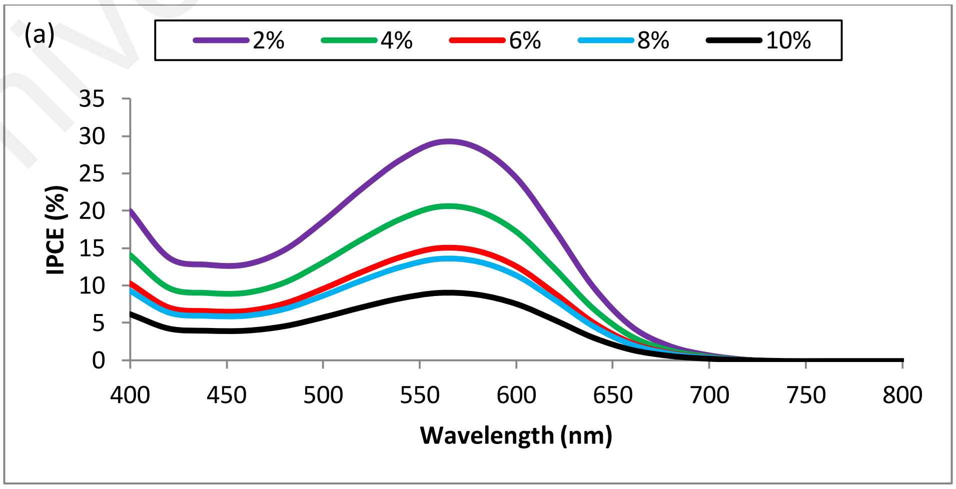

Figure 6.15: IPCE curve for anthocyanin-pigmented TiO_2 composite electrodes with 10 wt.% TiO_2 NRs at different weight percentage of (a) sucrose additives (2, 4, 6, 8 and 10 wt.% sucrose),(b) sucrose-DCA additive (2, 4, 6, 8 and 10 wt.% sucrose-DCA).

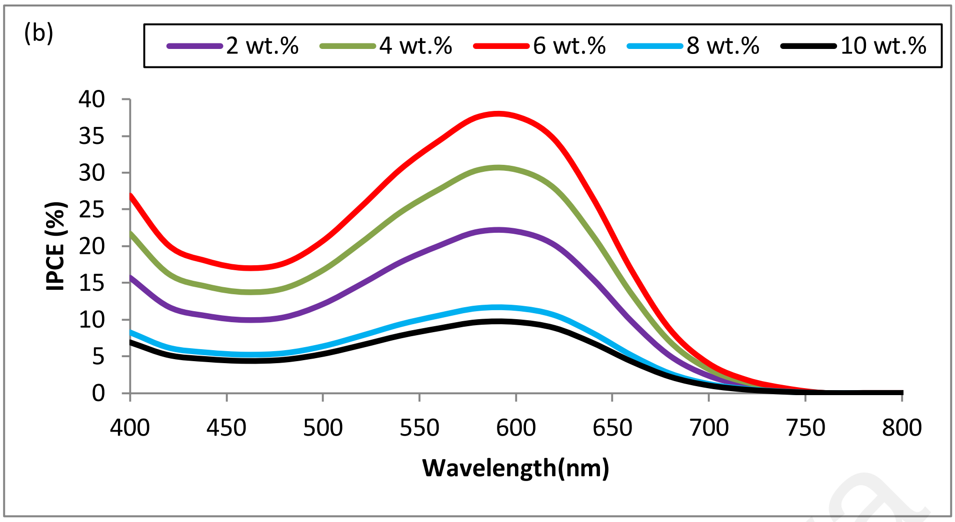

Figure 6.15, continued.

Previously, the IPCE of composite DSSCs with 10 wt.% NR without additives exhibits a maximum of 26% at 600 nm. The composites DSSCs with additives addition revealed higher IPCE values which is compatible with the J_{sc} value obtained by photocurrent-voltage measurement. The sucrose added samples shows the highest IPCE peak at 580 nm with 29% as in Figure 6.15 (a) which achieved by 2 wt.% sucrose. Addition of 6 wt. % sucrose-DCA as in Figure 6.15 (b) resulted in highest IPCE peak of 37% at 580 nm, which showed an increment from DSSC system without additives of almost 11%. These reveal that the addition of sucrose-DCA as additives resulted in a good impact towards DSSC performance. This positive outcome can be supported with EIS analysis which can confirm the positive roles of sucrose-DCA additives.

6.4.4 Electrochemical impedance spectroscopy (EIS) characterization at different weight percentages of additives

Figure 6.16 illustrated the Nyquist and fitting plots of the fabricated composite DSSCs with 10 wt.% NRs, assigned for D1 photoanode sensitized at 5 wt.% anthocyanin dyes with addition of different additive. The calculated values of R_s, R_1, R_2, R_3 for the composite DSSCs based anthocyanin dyes with added additives are presented in Table 6.7 and 6.8. As mentioned earlier, we were focusing on the R_2

variations. Based on the Figure 6.16, three semicircles observed. The R_2 is calculated after fitted the nyquist plot based on the equivalent circuit as mention before. It obviously seen in the Table 6.7, 2 wt.% sucrose added (C1) exhibit lower R_2. The R_2 value continues to increase when the wt.% of sucrose added increased. The lower R_2 values of (55.60 ± 0.29) Ω is observed for the cell with 2 wt.%, sucrose added but the values of R_2 increase to (115.00± 0.45) Ω when increased the percentages up to 10 wt.% (C5), as seen in Table 6.7.

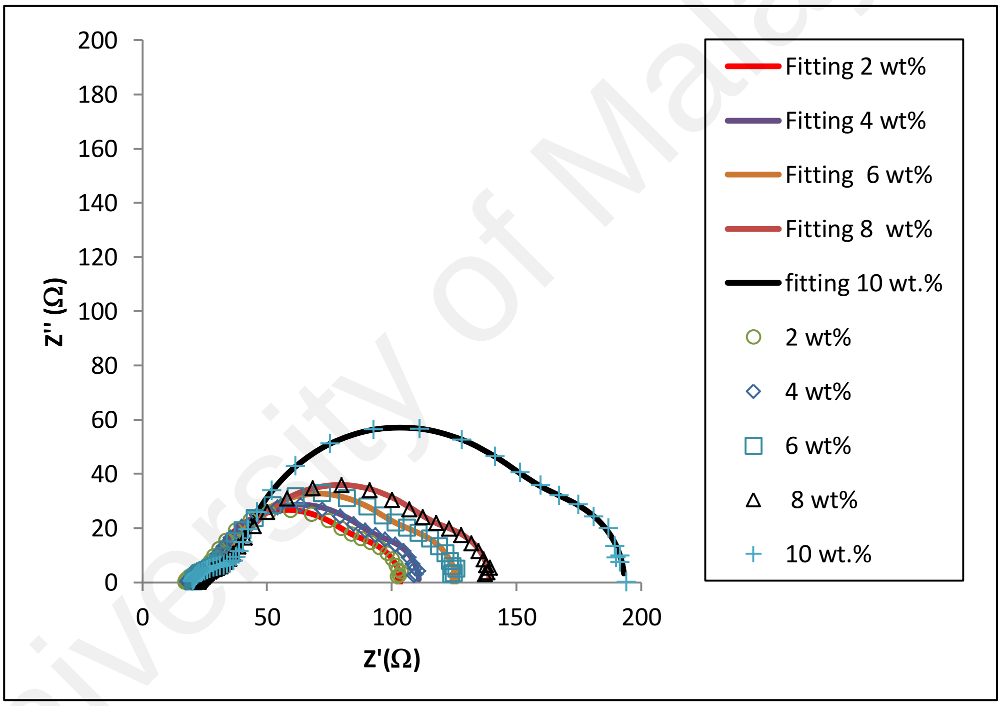

Figure 6.16: EIS for composite DSSCs fabricated with 10 wt.% TiO_2 NRs at different weight percentage of additives (2, 4, 6, 8 and 10 wt.% sucrose).

Table 6.7: *Rs, R_1, R_2, R_3* values for composite DSSCs fabricated with 10 wt.% TiO_2 NRs at different weight percentage of additives (2, 4, 6, 8 and 10 wt.% sucrose).

Wt.%	R_s (Ω)	R_1 (Ω)	R_2 (Ω)	R_3 (Ω)
2	19.90 ± 0.05	10.80 ± 0.12	55.60 ± 0.29	21.90 ± 0.12
4	18.07 ± 0.06	15.78 ± 0.15	65.45 ± 0.30	21.67 ± 0.18
6	21.00 ± 0.02	18.53 ± 0.13	72.45 ± 0.37	25.60 ± 0.13
8	22.60 ± 0.02	18.63 ± 0.10	85.04 ± 0.43	23.60 ± 0.10
10	19.83 ± 0.08	15.00 ± 0.19	115.00± 0.45	35.00 ± 0.12

Figure 6.17 show the nyquist and fitting plot for composite DSSCs fabricated with 10 wt.% TiO_2 NRs at different weight percentage of additives (2, 4, 6, 8 and 10 wt.% sucrose-DCA). For the sucrose-DCA added samples, the cell with 6 wt.% sucrose-DCA exhibited lower R_2 values of (38.20 ± 0.07) Ω. As can be observed in Table 6.8, The R_2 values value decreased with increased sucrose-DCA percentage from (56.40 ± 0.28) Ω (2 wt.%-D1) to (38.20 ± 0.17), Ω (6 wt.%-D5). Thus, these results are in agreement with highest efficiency performance associated with lowest R_2 values since the cell with 6 wt.% added sucrose-DCA also achieved highest efficiency (η) values.

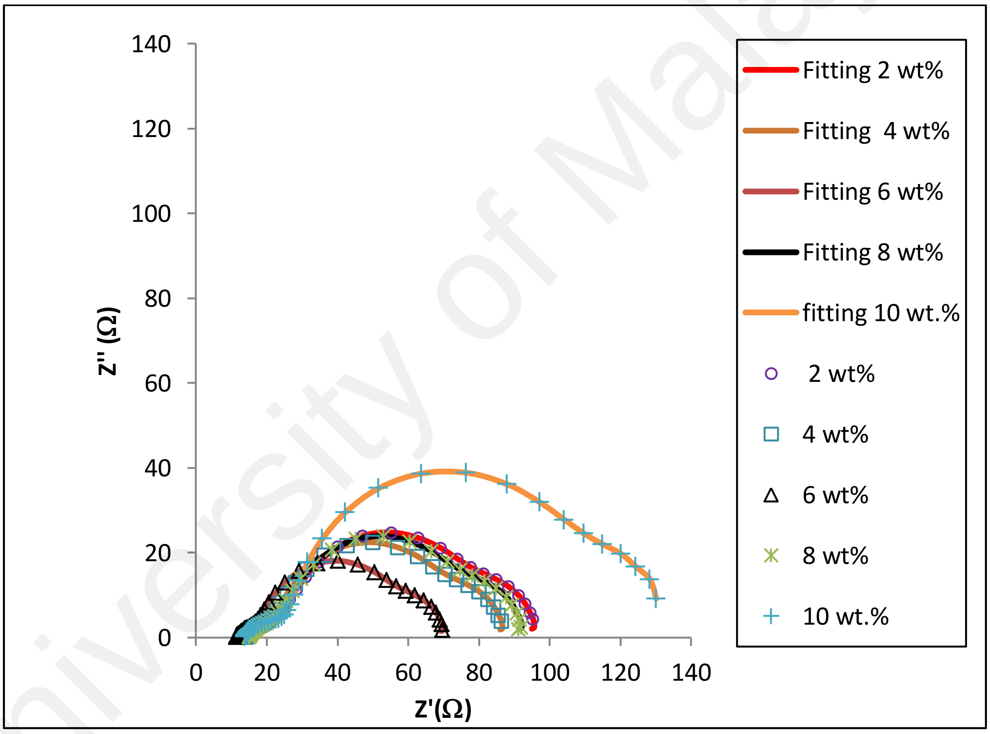

Figure 6.17: EIS for composite DSSCs fabricated with 10 wt.% TiO_2 NRs at different weight percentage of additives (2, 4, 6, 8 and 10 wt.% sucrose-DCA).

Table 6.8: R_s, R_1, R_2, R_3 values for composite DSSCs fabricated with 10 wt.% TiO_2 NRs at different weight percentage of additives (2, 4, 6, 8 and 10 wt.% sucrose-DCA).

Wt.%	R_s (Ω)	R_1 (Ω)	R_2 (Ω)	R_3 (Ω)
2	18.30 ± 0.03	11.70 ± 0.13	56.40 ± 0.28	21.90 ± 0.23
4	13.50 ± 0.02	6.00 ± 0.12	49.75 ± 0.19	14.75 ± 0.12
6	13.40 ± 0.02	4.80 ± 0.10	38.20 ± 0.17	14.00 ± 0.09
8	14.90 ± 0.08	9.00 ± 0.13	56. 98 ± 0.19	16.75 ± 0.13
10	13.30 ± 0.09	8.75 ± 0.12	80.15 ± 0.20	22.40 ± 0.09

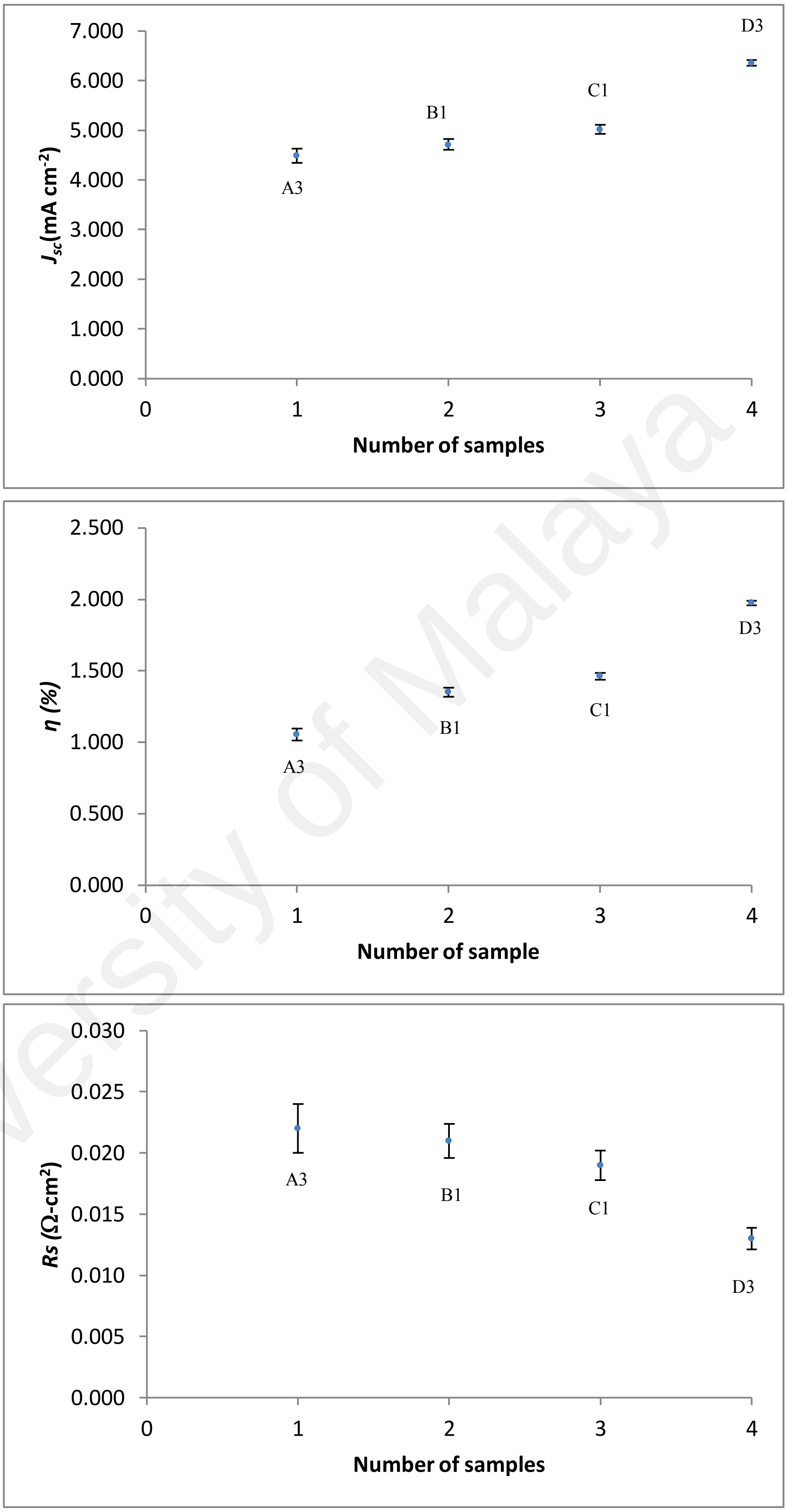

Figure 6.18: Summarized of (a) J_{sc} *(b)* η, (c) R_s, (d) R_{sh} and (e) R_2 values for four different sytems studied.

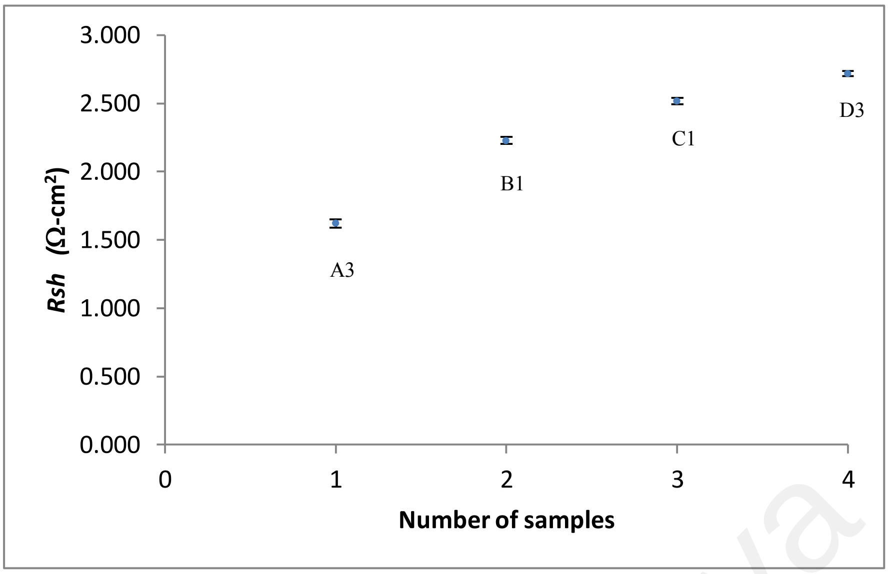

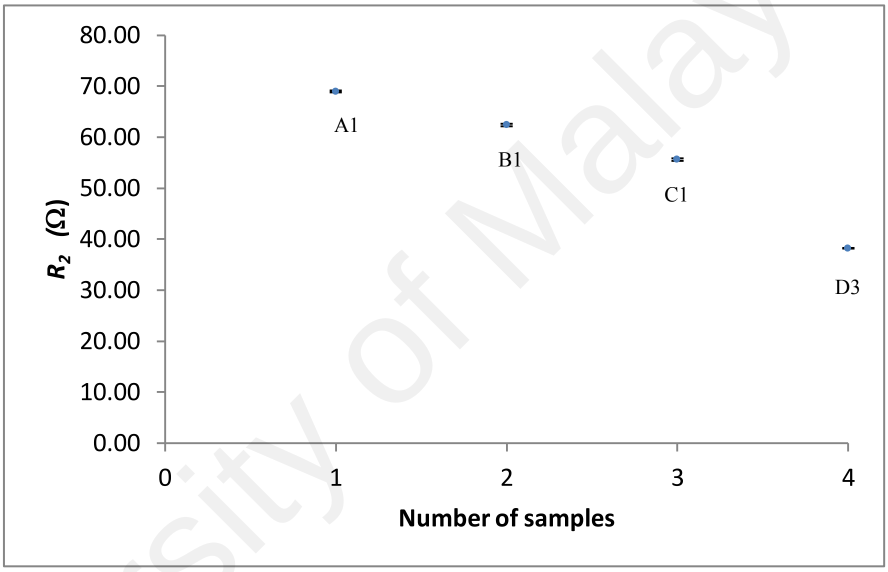

Figure 6.18, continued.

Figure 6.18 represents the summarized graph of (a) J_{sc}, (b) η, (c)R_s, (d) R_{sh} and (e) R_2 values for four different optimized sytems that studied in this work,which were: (Sample 1: commercial TiO_2 semiconductor with 5 wt.% anthocyanin extracts), (Sample 2: 10 wt.% NPs-NRs with 5 wt.% anthocyanin extracts), (Sample 3: 10 wt.% NPs-NRs with 5 wt.% anthocyanin extracts with addition of 2% sucrose), (Sample 4: 10 wt.% NPs-NRs with 5 wt.% anthocyanin extracts with addition of 6% sucrose-DCA) designated as A3, B1, C1 and D3 respectively. Based on the Figure 6.18(a) to (b), it show that (a) J_{sc}, and (b) η, continue to increase from sample 1 (A3) to sample 4 (D3). According to Figure 6.18(a) and (d), it can be summarized that the additions of 6%

sucrose-DCA (sample 4-D3) successfully enhanced the J_{sc} (4.487 ± 0.019) mA cm^{-2} and efficiency, η (1.054 ± 0.012) % of sample 1(A3) to J_{sc} (6.360± 0.019) mA cm^{-2} and efficiency, η (1.974 ± 0.014)%. TiO_2 nanoparticle/electrospun composite (sample 2-B1) electrodes have been designed to increase the efficiency of dye adsorption in DSSCs application. The efficiency, η and J_{sc}, of the DSSCs was observed to increase until it obtained the maximum of (1.351 ± 0.013)%, (4.711 ± 0.021) mA cm^{-2} respectively with the TiO_2 electrode soaked in 5 wt.% of dye solution. The performance of NPs-NRs composite based DSSC was further improved by addition of sucrose and sucrose-DCA additives. For the fourth fabricated DSSC (NP-NRs) composite systems, the use of sucrose-DCA successfully improved the performances of DSSCs based *Melastoma malabathricum* anthocyanin. It can be clearly observed that, since the efficiency of the performance increase, the R_{sh} value keep increase from sample 1(A3) to sample D3. While the R_s and R_2 value continue to decrease from sample 1(A3) to sample (D3) since low value of R_s and R_2 will be resulted in high efficiency. The performance was improved by addition of 6 wt.% sucrose-DCA (D3-sample 4) compared to sucrose without DCA additive, in which the J_{sc}, V_{oc}, FF, efficiency, R_s, R_{sh} and R_2 values (6.360 ± 0.059) mA cm^{-2}, (0.473 ± 0.0.005) V, (0.656 ± 0.006), (1.974 ± 0.014)%, (0.013 ± 0.003) Ω-cm^2, (2.918 ± 0.019) Ω-cm^2 and (38.20 ± 0.17) Ω, respectively.

6.5 Summary

DSSCs using anthocyanin based sensitizer extracted from fruit pulp of *Melastoma malabathricum* were successfully fabricated. This investigation shows positive result since 5 wt.% of anthocyanin managed to achieve 1.05% efficiency for commercial system. To improve the DSSCs performance, modification on the mesoporous layer were done by incorporating the TiO_2 nanorods (which have been produced through the electrospinning method) into the TiO_2 nanoperticles, hence it forms the composite mesoporous layer. The DSSC performance of 10 wt.% added NRs is further resulted in increased efficiency (1. 35%). Addition of 6 wt.% sucrose-DCA as additives successfull in enhancing the performance of (NPs- NRs) composite DSSC with efficiency of 1.97%.

CHAPTER 7: DISSCUSSIONS

Anthocyanin source used in this study was from the fruit pulp of *Melastoma mabathricum* which was freeze-dried in order to obtain particle powder of size ≤ 500 μm prior to extraction. As reported by Dutta et al (2007), turning fresh fruit sample into powder is a good approach. The size of particle that will be soaked in the appropriate solvent will be small and promotes solid particle diffusion into the solvent due to the larger area. The smaller the particle size the greater is anthocyanins content in the extract (Cissé et al., 2012). Since different approaches of extraction may exhibit different anthocyanin yield (Garcia-Viguera et al*.,* 1998), thus confirmation of major type of anthocyanin is a must. The results of UPLC-ESI-MS/MS analysis as Figure 4.1 showed that the fruit pulp extract from *Melastoma malabathricum* consists delphinidin glucoside, delphinidin-3,5-glucoside and proanthocyanindin. These results correlated well with study conducted by Bueno et al. (2012) and Dias et al. (2012) were stated that most anthocyanin in fruits exists in anthocyanin-glucoside form. Therefore, this species was proven to contain anthocyanin and pigment was extracted and was use as natural sensitizer for DSSC.

To get the highest extraction yield with minimum of degradation (Maciel et al., 2018) the experimental design to achieve high yield is very crucial. Extraction is the first step in this work. To get the highest yield, the extraction parameters must be optimized. The factors that affect extraction yields are type of solvent, solvent concentration, extraction temperature, and soaking time (Barnes et al*.,* 2009; Bridgers et al*.,* 2010; Tamaroh et al., 2018). Highest total anthocyanin that exist in glucoside form can be be obtain by extraction that using acidified methanol (Cacace &Mazza, 2002; Wallace and Giusti, 2013). Flavylium cation which is the stable anthocyanin form exists in acidic solutions. However, the excess use of acid can lead to hydrolysis of original anthocyanins (Li et al., 2010).

In this work, three parameters for extraction of anthocyanin is TFA content to be added to methanol. Secondly the time to soak the powdered of fresh fruit pulp of *Melastoma malabathricum* and the third is the temperature of extraction. BBD analysis in Table 4.1 revealed that different extraction parameters affected CIE colour and anthocyanin yield. Maximum anthocyanin yield of anthocyanin was the focus in this study prior to its use as dye sensitizer. Thus RSM approach was used in order to optimize extraction conditions of anthocyanins from *Melastoma malabathricum*. As mentioned in chapter 4, some evaluation steps were carried out in order to determine the appropriate model to represent the CIE colour responses and anthocyanin content. Based on Table 4.4 until 4.10, the results revealed that the reduced quadratic polynomial model was the best model since it significantly influenced the L*, a*, b*, C, H°, saturation and anthocyanin content responses. The appropriate polynomial equation generated from the selected quadratic model as displayed in Equation (4.1) to (4.7) were used to calculate the predicted responses of L*, a*, b*, C, H°, saturation and anthocyanin content. As depicted in Figure 4.2, there was good relationship between the experiment and predicted values since the residual is closely to a straight line and not obvious S-shape pattern were observed. As mention before by Shafie‟ et al., (2013), if obvious S-shape was observed indicates that there are some abnormalities with the experimental data. The residual is the different between experimental data and calculated predicted value. This also proved the successfully of all generated models since it capable to closely predict the outcome of the experimental data. The relationship and influence of solvent composition, soaking time and extraction temperature on the CIE colour indices and anthocyanin content can be deduced from the response model graphs in Figure 4.3 and 4.9. Through the optimization of selected model for responses of L*, a*, b*, C, H°, saturation and anthocyanin content as correspond to Table 4.12, the optimized conditions for anthocyanin extraction from fruit pulp of *Melastoma malabathricum* were successfully generated by RSM at combined parameters of 0.5% TFA content, 132 min soaking time and extraction temperature of 80 ºC. This optimized condition we will be used to extract anthocyanin from *Melastoma malabathricum* for further used as natural sensitizer in DSSCs application.

Based on RSM numerical optimization, 0.5% TFA is needed to enhance anthocyanin yield from *Melastoma malabathricum*. As stated before, the function of acid is to minimize the degradation of anthocyanins, weaker and volatile organic acids such as trifluoroacetic acid, about 0.5% - 3%, are used in the solvents (Ravilla et al., 1998). However, the amount of acid added cannot exceed the amount needed since excess medium that is strongly acidic may hydrolyse the glycosides bonds (Ju & Howard, 2003). Solvent acidification has led to higher extraction yield. The TFA addition can improve the anthocyanin yield when added to most solvents e.g. methanol (Barnes et al., 2009). Thus, the optimized 0.5% TFA content was adequate enough to increase anthocyanin yield in this research. The result obtained in good agreement with other study reported that anthocyanins are normally extracted with methanol containing 0.5% TFA (Barnes et al., 2009; Dai et al., 2010).

For this study, 80 °C was the optimized extraction temperature that yields highest anthocyanin content (4596.25 mg/L). The results showed that extraction temperature have an impact on the efficacy of extraction thus resulted in different CIE colour and anthocyanin content. The temperature to extract anthocyanin from *Melastoma malabathricum* is in agreement with the study conducted other researchers: (Ruenroengklin et al., 2008; Yang et al., 2008; Sharif et al*.,* 2010; Thirunavukkarasu &

Nithya, 2011; Duan et al., 2015) also investigated the effects of temperature on the extraction process. Sharif et al., (2010) reported the highest absorption of anthocyanin extract from onion (*Allium cepa)* using acidified methanol at 80 °C. Thirunavukkarasu & Nithya, (2011) obtained the ideal extraction temperature of 76.5 °C for extraction of anthocyanin from *Solanum melongena.* Duan et al., (2015) obtained the optimal extraction temperature for anthocyanin from Chinese bayberry, *Myrica rubra Sieb. & Zucc.* at 80 °C. Heating procedure is important to hydrolyze the bonds of bound phenolic compounds (phenol–protein or phenol–polysaccharide) and soften the plant tissue. This will enhance phenolics transfer to the solvent due to phenolics solubility (Shi et al*.,* 2003; Salar et al*.,* 2012). Nevertheless, oxidation and polymerization process of desired compound could occur if exposed too long exposure at high temperatures during extraction process (Shi et al*.,* 2003). Thus, soaking time at high temperature need to be optimized in order to ovoid degradation of polyphenolic compounds caused by hydrolysis and polymerizations which are unfavorable to the extraction yield (Abad-Garcia et al., 2007).

RSM results obtained from this work also revealed that soaking time play an important factor since altered extraction or soaking time resulted in different CIE colour and anthocyanin yield. The optimized soaking time to increase anthocyanin yield of 4596.25 mg/L in this research was 132 min. Solid to liquid diffusion will be enhanced if contact time between tissue of plant and extraction solvent increased. Diffussion is complete when solid to liquid diffusion and liquid to solid diffusion reaches equilibrium (Dutta, 2007). The time frame to reach equilibrium varies depending on temperature, solvent and plant material (Cacace & Mazza, 2002). These phenomena could be explained by Fick"s second law of diffusion which states that, after a certain time, solute concentrations in the solid matrix (plant matrix) and in the bulk solution (solvent) can reach a final equilibrium. Thus as stated by Silva et al. (2007), excess soaking time was not significant in extraction process after the final equilibrium is reach. The investigation of effect soaking time on anthocyanin extraction were also reported by other researchers : (Thirunavukkarasu & Nithya, 2011; Oancea et al., 2012; Lotfi et al., 2015; Yilmaz et al., 2015; Ramasamy et al., 2016).

Semiconductor photoanode also have important role in DSSCs applications. Thus, modification of photoanode properties is important in purpose to increase the performance of anthocyanin based DSSCs. In this work, TiO_2 nanorods have been successfully fabricated using the combination of sol-gel and electrospinning method followed with sintering and grinding process. Other researchers have obtained TiO_2 nanorods for used as photoanode in DSSCs in the same way (Lee et al., 2009; Rezvani et al., 2010; Huang et al., 2012; Park et al., 2013; Chen et al., 2013; Hong et al., 2014). The solution and process parameters influenced nanofiber properties as already discussed detail in chapter 2. Two parameters investigated in this study were polymer concentration and applied voltages on the morphology of TiO_2 nanofiber formations. FESEM image as depicted in Figure 5.1 showed the influence of different polymer concentrations on morphology of the nanofiber. At 12 wt.% (P5) polymer concentration, cylindrical fibres were formed compared to lower polymer concentrations. The average fiber diameter of electrospun TiO_2 at 12 wt.% PVP was bigger than that produced at lower polymer concentration as in Figure 5.2. This is caused by the greater resistance towards thinning of the jets (Deitzel et al., 2001). Polymer chain complexity and solution viscosity are inter-related (Deitzel et al., 2001). Hence, increased complexity of due to an increase in number of polymer concentration resulted in viscosity increase (Tungprapa et al., 2007). The increase in solution viscosity increased viscoelastic force, during electrosppining. This enables the viscoelastic force to overcome the electrostatic, and columbic repulsive forces that prevent the electrospinning jet from being stretched and break up. Therefore a low solution viscosity the electrospinning jet may breakup and surface tension force makes the high numbers of free solvent molecules in the solution to acquire a spherical shape and form a beads. This is the reason for the presence of beads and droplets at low polymer concentrations of 8 and 9 wt.% PVP compared to higher percentages. The bead diameter was formed to decrease with increasing polymer concentration as depicted in Figure 5.3. The increased solution viscosity enables the solvent to be distributed over the entangled polymer molecules which lead to formation uniform and beadless nanofibers (Mit-uppatham et al., 2004; Haider et al., 2018). The fibers are observed thickened and beads become thinner as listed in Table 5.1. This is due to increasing viscoelastic force that restricts the electrostatic and coloumbic forces from the electrospining jet (Veleirinho et al., 2008). Thus further increased in polymer concentration is insignificant because this will increase the solution viscosity which resulted in bigger fibers. Since the 12 wt.% resulted in less bead, this sanple was chosen for further study. In this work, in order to achieve beadless fiber, effect of process parameter (applied voltage) was intensively studied.

Figure 5.4 depicted the FESEM images on the influence of applied voltages on TiO_2 nanofibers formation. Based on the figure, it is clearly observed that 19 kV is the optimized voltage to fabricate uniform continuous nanofibers. In order to explain the diameter changes with voltage variation, many factors must be considered. These include gravitational, electrostatic and Coulombic forces. Coulombic forces stretches the jet. Viscoelastic force and surface tension prevent the charge jet from being stretched. The effect of applied voltages on the diameters of TiO_2 nanofibers as in Figure 5.5 may be undersood in terms of the Coulombic force, viscoelastic force and surface tension. At low voltages, the Coulombic force is lowered compared viscoelastic force and surface tension and nanofibers (NFs) with large diameters are formed. At moderate voltages, all three forces are inequilibrium. As a result in the NFs diameter decreased. At higher voltages, the coulombic force overcomes both viscoelastic force and surface tension. However, as there is both longitudinal and transverse stretching and the latter can result in increase of NFs diameter. The thicker nanofibers formed in this work can be ascribed to transverse stretching dominace over longitudinal stretching. Furthermore, as applied voltage was increased, the jet can be accelerated towards the collector. The solvent could not evaporate in time and thick nanofibers with larger diameter are formed. It is also indicates that at the lowest applied voltage, beads appear. This may be explained in terms of the viscoelastic force (Kim et al., 2018).

FESEM images in Figure 5.7 showed the morphology of rod-like TiO_2 structure of at different calcination temperature with the average nanorod diameters were evaluated and presented in Figure 5.8. The sizes of nanorod reduce from 180 nm to 93 nm after calcination temperature. This is due to removal of PVP polymer from the nanofibers and the crystallization of TiO_2 during the calcination process (Li and Xia, 2003; Nuansing et al., 2006 & Kumar et al., 2007). Elemental analysis in Figure 5.9 thus confirmed the removal of PVP polymer and showed the formation of pure TiO_2 material. XRD patterns in Figure 5.10 for the sample calcined at 500 °C yielded TiO_2 nanorods having anatase structure with the strongest peak being at 25.5° (Huang et al., 2012). PVP is reported to be thermally degraded at around 420 °C (Chrissafis et al., 2008; Lau & Mi, 2002). Anatse TiO_2 nanorods were mixed with commercial P25 TiO_2 nanoparticles in order to produce composite mesoporous layer. FESEM micrograph in Figure 5.11 revealed the morphologies of the composite mesoporous layer. Different addition of nanorods percentages resulted in randomly oriented interconnecting nanorods. Closer observation revealed the existence of interspaces and voids in the composite film. These voids enable easy loading of the dye into the composite (Huang et al., 2014; Hong et al., 2014). These composite photoanode systems were used in DSSCs.

In Chapter 6, characterization of dyes extracted from fruit pulp of *Melastoma malabathricum* via visible studies showed a maximum peak at λ=524 nm corresponding to the anthocyanins (Ludin et al., 2014) as in Figure 6.1. According to Figure 6.1 and Figure 6.2, increased in anthocyanin concentration up to 9 wt.% resulted in decreased in maximum absorption of visible spectroscopy as well as decreased in efficiency performance. This could be explained due to anthocyanin in *Melastoma malabathricum* extraction that easily to self- aggregate. According to Leydet et al. (2012), molecule of anthocyanin easily to undergo self-association, aggregations from simple to complex. Note that anthocyanin is a planar molecule with aromatic rings. They are prone to $\pi - \pi$ stacking interactions with themselves (self-association) and organizing into aggregations. Hence, increased in anthocyanin concentration up to 9 wt.% will increased the dye aggregation due to presence of hydroxyl group in anthocyanin extraction that can interact and aggregate with one another through hydrogen bonding (Spillmann & Burger, 1996). Dye aggregation will result in decrease of maximum absorption in visible spectrum which means that less adsorbed dye molecules harvest the light (Yang et al., 2014). Aggregation of anthocyanin couse the electron injection become inefficient thus decreases in DSSCs performance (Ehret et al., 2001; Pastore & Angelis, 2010).

Based on Figure 6.2, the maximum absorption wavelength for anthocyanin on TiO_2 was shifted to longer wavelength (lower energy), λ=526 nm due to the complexation between anthocyanin and Ti^{4+} (Calogero and Marco, 2008). This shift in maximum absorption is similar with other studies reports by Hao et al. (2006) and Fernando

&Senadeera (2008). Anthocyanin has hydroxyl group which can attach easily to TiO_2 as explained by Justus (2010). The adsorption of the anthocyanin dye is due to condensation of alcoholic-bound protons with hydroxyl groups in the TiO_2 surface. These chemical attachments affect the energy levels of the HOMO and LUMO of the anthocyanin pigment. The shift to the higher wavelength observed from the spectral response can be attributed to the electronic coupling between anthocyanin dye and TiO_2 (Wang et al*.,* 2004).

Based on the results shown in chapter 6, it can be inferred that sensitizer concentration significantly affected the dye adsorption and the resultant overall light conversion efficiency of DSSC. Figure 6.3 shows that DSSCs sensitized with 5 wt.% of anthocyanin concentration, A3 sample revealed the highest J_{sc} (4.487 ± 0.135) mA cm^{-2} and efficiency, η (1.054 ± 0.012)%. Beyond this anthocyanin concentration, both values started to decrease. The J_{sc} of DSSC is dependent on the electrons released by the dye molecules present and the number of dye molecules is dependent on the amount dye loaded. The amount of loaded dye will affect the quality of light harvested (Yang et al*.,* 2012). Tabulated data in Table 6.1 revealed that increasing the dye solution concentration increased efficiency of DSSCs and J_{sc} values. The increase in dye adsorbed on the TiO_2 surface will result in increasing DSSC efficiency and J_{sc} as stated by Ooyama & Harima (2012). J_{sc} value increased with increasing anthocyanin concentration because a larger area of TiO_2 will be adsorbed by the dye. However, beyond A3 sample, (5 wt.% of sensitizer concentration), DSSC perfomance started to deteriorate. This could be due to the inactive dye molecules on the TiO_2 surface hence restricting electron injection into the TiO_2 conduction band (Arifin et al., 2017).

As can be seen in Table 6.1, very high anthocyanin concentration (beyond 5 wt.%) lead to increase in series resistance (R_s) up to (0.046 ± 0.002) Ω-cm^2. Increasing R_s

means that some electrons are lost, thus results some voltage drop and decrease in photocurrent and efficiency value (Rho et al., 2015). Highly concentrated extracts which is beyond 5 wt.%, of anthocyanin concentration reduces the photocurrents hence lowering the cell efficiencies (Jasim et al., 2012). Since series resistance in DSSC is low, an improved *FF* is expected. The shunt resistance (R_{sh}) is due to the back electron transfer from TiO_2 to the electrolyte at the TiO_2/dye/electrolyte interface. A low shunt resistance (R_{sh}) gives an alternative substitute pathway for the light generated current. These alternative current pathways lower the power output and decreases fill factor. The shunt resistance (R_{sh}) results from the recombination of electrons with holes in the dye and/or with I_3^- component of the redox mediator. The decreasing R_{sh} means that there are few recombination sites (Rho et al., 2015). At high concentration of 7 and 9 wt.% of anthocyanin concentration the efficiency is lowers (0.704 ± 0.089)% and (0.551 ± 0.044)% respectively since the R_{sh} values were also lower which were (1.230 ± 0.054) Ω-cm^2 for 7 wt.%(A4) and (1.173 ± 0.060) Ω-cm^2 for 9 wt.% (A5) of anthocyanin concentration. It proposed that some adsorbed concentration of dye could facilitate the charge recombination in DSSC and lower electron transport properties of TiO_2 film (Tang et al*.*, 2015). In this study 5 wt.% of anthocyanin(A3 sample) was the sufficient concentration to improve the efficiency performance up to (1.054 ± 0.012)%. High efficiency can be achieved if the series resistance (R_s) is low and the shunt resistance (R_{sh}) high. Reducing the overvoltage for difusion and electron transfer also will cause to increase the *FF* and resulting in better efficiency (Gong et al., 2017). High R_{sh} values can boost J_{sc} . This due to R_{sh} restricts shunt currents on the cell structure. R_{sh} values had to be high to improve the fill factor for better DSSC efficiency (Yang et al.,2012) As predicted, the charge transport resistance (R_2) as listed in Table 6.2 is affecting the overall DSSC performance of the cell. Sample that immersed in 5 wt.% anthocyanin concentration resulted in lowest R_2 value which is (68.95 ± 0.38)Ω and highest efficiency. Hence appropriate amount of dye is needed to reduce charge recombination in DSSCs and improve the electron transport properties of TiO_2 film (Tang et al., 2015).

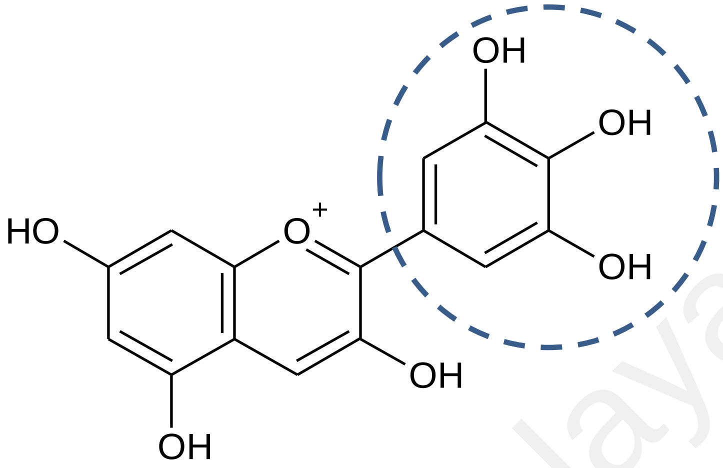

Figure 7.1 : Structure of delphinidin.

In addition, the results of DSSCs study showed that the presence of delpinidin as major type of anthocyanin extracted from *Melastoma malabathricum* could be used as sensitizer. Hamadanian et al. (2014) stated that, delphinidin gave the highest efficiency in DSSCs. Delphinidin has outstanding and promising physico-chemical properties. It is established that due to three hydroxyl groups in the B ring as in Figure 7.1, delphinidin can form strong bonding with TiO_2. This requires that a sufficient number of the OH binding sites to be available at the TiO_2 surface to form additional hydrogen bonds. Due to the mesoporous structure of TiO_2 anatase, the orientations of Ti(IV) sites and also the number of available binding OH sites onto TiO_2 surface determine the strongest and the most preferred binding mechanism (Fernando & Senadeera, 2008;Hamadanian et al. 2014).

In DSSC composite TiO_2 photoanode in the mesoporous layer is made up of TiO_2 NPs with addition of NRs at various percentages (10, 20, 30, 40 and 50 wt.%) and sensitized at 5 wt.% dye. This second system was designed to improve the performance of DSSCs based on anthocyanin extracted from *Melastoma malabathricum* sensitizer. 5 wt.% anthocyanin concentration exhibited highest efficiency in the first DSSC systems. Therefore 5 wt.% dye concentration (A3) was selected as the optimized concentration and further used in other DSSC systems studied in this thesis. Figure 6.8 and Table 6.3 showed the results of J_{sc} and η DSSC with composite mesoporous layer. Figure 6.8 and Table 6.3 showed that inclusion of 10 wt.% NR (B1) into the mesoporous layer, led to the highest of J_{sc} of (4.711± 0.109) mA cm^{-2} of (1.351± 0.013)% compared to the DSSC with purely commercial TiO_2 that exhibited J_{sc} value of (4.487 ± 0.135) mA cm^{-2} and efficiency *(η)* performance of (1.054 ± 0.012)% . These results showed that 10 wt.% NRs is sufficient to enhance the performance of DSSCs studied. The results agree with that of other researchers: Saji et al., (2010) and Park et al., (2013) that reported good photovoltaic cell efficiency with incorporation of 10 wt.% TiO_2 nanorods. However in their research synthetic dyes were used.

The improvement in J_{sc} and η in DSSCs systems containing TiO_2 nanoparticles-nanorods can be attributed to electron mobility and the specific contact area with the sensitizer. The electron transport through TiO_2 nanorods is more efficient than through nanoparticle due to their smaller grain interfaces. In contrast, nanoparticles improve the contact with the dyes due to their large specific surface area (Park et al*.,* 2013; Huang et al., 2012). The increase of J_{sc} may also cause by enhancing light scattering of the TiO_2 films containing nanorods (Huang et al., 2012; Chen et al., 2013). Although the high surface area of TiO_2 NP is required for dye to adsorb, however recombination of photoinjected electron limits their application. The TiO_2 electrodes such as NRs can enhance the light harvesting, straight pathway electron transport and also have no serious light loss due to back scattering. Hence, the design of the TiO_2 NPs-NRs composite film balances the surface area and the light scattering and resulted in highest efficiency compared to NP or NR electrode (Hafez et al., 2010).

The light scattering ability of composite photoelectrode was characterized by the visible analysis. As predicted the use of nanorod improved the light scattering ability. It maybe inferred that the porous structure inside nanorods helped to multiply the scattering and reflecting of the light and enhanced the optical pathway of the incident light. Figure 6.7 showed visible absorption spectra of the composite electrodes. The NPs-NRs electrodes resulted in increased visible light absorption. This may be attributed the due to light scattering of the TiO_2 nanorods that increased the optical path length of the longer wavelength incident light. This can be comfirmed by IPCE spectrum in Figure 6.9 that indicate efficient light harvesting. Light harvesting efficiency is improved when electrospun TiO_2 nanorods and nano particles were mixed together. The high scattering effect of porous nanorods will definitely increase the light harvesting efficiency of photoanode film, thus led to an enhanced J_{sc} density for the DSSCs (Huang et al., 2012; Chen et al., 2013). The increased in J_{sc} can be attributed to light scattering by the NRs and good dye uptake (Hong et al., 2014). In addition, the nanorods also helped to form the viscous stable TiO_2 colloid and prevent the film from being cracked after coating and sintering. A pure TiO_2 nanoparticles film from one deposition can sometimes contain cracks due to the excessive contractions during sintering. The addition of low percentage of TiO_2 nanorods can prevent the contraction and continuous crack-free films can be formed, which are beneficial to the diffusion and transport of the electrons (Huang et al., 2012).

Figure 6.10 showed the electrochemical impedance spectroscopy (EIS) analysis of TiO_2 NPs-NRs obtained at various nanorods weight percentage. Table 6.4 tabulated the

R_2 value. Obviously, the main research investigation is the middle voltage dependent region (second semicircle) which reveals the electron recombination process in the anode. R_2 value is analyzed in order to understand the process of charge transfer at the TiO_2/dye/electrolyte interface since it greatly affect the performance of DSSC (Akilavasan et al., 2013; Wang et al., 2006). The lowest R_2 is given by highest efficiency DSSC. TiO_2 NP-NR composite DSSC with inclusion of 10 wt.% NR resulted in R_2 value of (62.40 ± 0.28) Ω and also possessed the highest efficiency of (1.351 ± 0.013)%. Dense amorphous TiO_2 particles that formed on the surface of nanorods will facilitate electron transfer and increase the surface area for more light capture. This led to increased dye adsorption due to increased roughness of surface photoanode (Wang et.al. 2006). Improved light scattering and electron transport abilities are the main reasons for improved DSSCs performance (Huang et al., 2012). All these results obtained in this work revealed that TiO_2 nanorods is an efficient component in the composite photoanode of the DSSC due to their enhanced dye loading, strong light scattering ability, and excellent electron transport performance (Chen et al., 2013).

The performance of 10 wt.% NRs-NPs composite was further increased by addition of sucrose and sucrose-DCA additives. From Figure 6.13, it can be seen that addition of 2 wt.% sucrose increased the efficiency to (1.461 ± 0.024)%. Sucrose which is a disaccharide carbohydrate can interact and aggregate with one another through hydrogen bonding (Spillmann & Burger, 1996). The increment in the performances in DSSC could be due to molecules of sucrose interacting and aggregating to the glucosyl of anthocyanin. With anthocyanin molecules bound to the TiO_2 surface, molecules of carbohydrate would form a sugar layer on an array of the TiO_2-anthocyanin complex. This sugar layer could serve several purposes which affected the performance of DSSCs. First, it could act as a sealant which reduced electron recombination between the TiO_2 crystalline and electrolyte. Second, the presence of this sugar layer could prevent the self-aggregation of anthocyanin molecules. Note that anthocyanin easily to undergo self-association, aggregations from simple to complex (Hoshino, 1991; Houbiers et al., 1998; Leydet et al., 2012). Aggregation of anthocyanin is because the electron injection become inefficient thus decreases in DSSCs performance (Ehret et al., 2001; Pastore & Angelis, 2010). Separation of anthocyanin molecules by the sugar layer thus could result in a raise of J_{sc}. Third, the sugar layer could also force anthocyanin molecules to line up in the correct orientation for binding with the TiO_2 surface (Chien et al.,2014)

In this work, 6 wt.% sucrose-DCA (D3) addition resulted in improved DSSCs efficiency to (1.974 ± 0.014)% and indicated that sucrose-DCA is the better additive for 10 wt.% NRs-NPs composite DSSCs based on anthocyanin from *Melastoma malabathricum*. Figure 6.12 showed the absorption spectra of anthocyanin-pigmented TiO_2 composite electrodes with 10 wt.% TiO_2 NRs at different weight percentage of additives (2, 4, 6, 8 and 10 wt.% sucrose-DCA). 6 wt.% sucrose-DCA (D3) resulted in a shift in maximum wavelength from 528 nm (2 wt.%) to the longer wavelength, 532 nm or known as bathochromic shift and increase in absorbance intensity. The increase in peak absorption and shifted to lower energy wavelength (bathachromic shift) are important properties that affect the DSSC performance. This is because the absorption spectrum of the dye and the anchorage of the dye to the surface of TiO_2 are important parameters determining the efficiency of the cell. The mechanism of adsorption often involves chemical reaction between functional groups present on the TiO_2 (Chien et al., 2014).

The results from the visible spectroscopy are comparable with the results from the *J-V* curves. Figure 6.14 showed that DSSCs sensitized by anthocyanin added with 6 wt.%

sucrose-DCA revealed the highest of J_{sc} (6.360 ± 0.059) mA cm^{-2} and efficiency *(η)* of (1.974 ± 0.014)%. Beyond this concentration, at 10 wt.% of sucrose-DCA both values started to decreased to (4.386 ± 0.073) mA cm^{-2} and (1.213 ± 0.026)% respectively. As discussed before, the photocurrent of DSSCs depended on the number of dye molecules present. Maximum absorption in visible spectrum means that more adsorbed dye molecules harvest the light (Yang et al., 2012). Tabulated data in Table 6.6 revealed that increasing the sucrose-DCA concentrations added to anthocyanin increased the efficiency of DSSCs and J_{sc} values until 6 wt.% of sucrose-DCA added (D3). The increase in the amount of dye adsorbed by TiO_2 surface will result in increased DSSCs efficiency and J_{sc} as stated by Ooyama and Harima (2012). J_{sc} value increased due to increase in dye adsorption dye loading on the TiO_2 films (Arifin et al*.,* 2017). Compared with NPs-NRs composite immersed in 5 wt.% of anthocyanin without the addition of sucrose-DCA additive, the J_{sc} and *(η)* of samples with sucrose-DCA-anthocyanin increased up to 6.36 and 1.97% respectively. This showed that sucrose-DCA has helped to enhance the DSSCs performance. This can be explained in terms of the anchoring groups. Anthocyanin only has hydroxyl (OH) ligands and O ligands whereas sucrose-DCA contains –COOH that can combine with the OH groups of the TiO_2 particles and boost the coupling effect of the electrons in the TiO_2 conduction band and provide a rapid electron-transport rate. The sucrose-DCA helps to introduced more anchoring group inside dye molecule which increases electron transfer between the photosensitizer and TiO_2 surface (Kim et al., 2018). Since the J_{sc} and efficiency of 6% sucrose-DCA added sample (D3) increased resulted in decreased in R_2 value as in listed in Table 6.8. The observed increase in J_{sc} could be explained by the dispersion of anthocyanin aggregation by DCA, leading to the suppression of quenching process between molecules. It could also be due to the adsorption of DCA on the TiO_2 surface, which would positively shift the conduction band edge, resulting in a larger driving force for electron ejection from the excited anthocyanin molecules (Kay & Gra¨tzel, 1993). DCA induced an additional enhancement in the presence of the sugar layer, indicating that its enhancement mechanism was different from that of sucrose. DCA is generally used as the co-adsorbent to avoid dye aggregation in DSSCs (Lim et al., 2011; Sharma et al., 2012; Wang et al., 2007; Xia & Yanagida, 2011). The shielding provided by DCA was accomplished by direct binding to the TiO_2 surface, while sucrose formed an insulating layer above the TiO_2 surface. DCA dispersed anthocyanin aggregation by inserting in between molecules, while the sugar layer provided a web that could fix anthocyanin molecules in position. It is worthy to note that DCA, as a co-adsorbent, occupies binding sites on TiO_2, resulting in increased in DSSC performance. Besides, the sugar layer due to sucrose might scatter and reflect the incident light, increasing the light absorption of the anthocyanin molecules on the TiO_2 film (Chien et al., 2014). Thus, in this study the combination of sucrose and DCA (sucrose-DCA) additive significantly improved the performance of the composite NPs-NRs DSSCs based anthocyanin.

However at very high sucrose-DCA concentration (beyond 6 wt.%) increase in series resistant (R_s) was observed as in Table 6.6, thus decreasing in DSSCs efficiency due to electron loss and decreased in voltage and resulting in reduced photocurrent (Rho et al., 2015). This also may be due to electron scattering and trapping of electrons that led to the decreased in conversion efficiency of DSSCs (Pan et al., 2015). Since series resistance is increased as expected R_{sh} value decreased due to trapped electrons and also due to increase in recombination electron (Pan et al., 2015). Thus it is suggested that sufficient percentage of sucrose-DCA, in this case 6 wt.% is enough to increase the electron transport properties of NPs-NPs TiO_2 composite photoanode. As mention before increasing R_{sh} and decreasing R_{s} will lead to a higher *FF*, thus resulting in a greater efficiency (Liu et al., 2018). The larger R_{sh} originating from reduced charge recombination can be attributed to the field-assisted charge collection which leads to fewer opportunities for the electrons to backward reaction at the TiO_2/electrolyte interfaces (Liu et al., 2018).

CHAPTER 8: CONCLUSIONS AND SUGGESTIONS FOR FUTURE WORKS

In this thesis, DSSCs devices are fabricated from a combination of materials containing environmental friendly natural dye which is from fruit pulp of *Melastoma malabathricum* and inexpensive, inert and non-toxic TiO_2 photoanode. These two DSSC components have important roles in promoting good efficiency. In this chapter, some conclusion that has been made based on the results obtained from the study will be reported. Five objectives that stated earlier in chapter 1 were successfully accomplished. The first objective is to make a comfirmation of major anthocyanin in crude extract of *Melastoma malabathricum*. Thus, based on the result gained from analytical ultra performance liquid chromatography with electrospray ionization mass spectrometry (UPLC-ESI-MS/MS), the natural dyes extract in fruit pulp of *Melastoma malabathricum* has been comfirmed contain conthocyanin which are delphininidin-3-glucoside, delphinidin 3,5- glucoside and proanthocyanidin. The optimized extraction parameters for anthocyanin extraction from *Melastoma malabathricum* were well acquired using RSM method with the conditions of 0.5% TFA content in methanol, 132 min soaking time and 80 ºC of extraction temperature with resulted in anthocyanin content of 4597 mg/L. These optimized conditions were further applied to extract natural anthocyanin from fruit pulp of *Melastoma malabathricum* and be utilized as sensitizer in DSSCs application.

Smooth nanofibers of TiO_2 were successfully obtained by modification of polymer concentration and applied voltage. 12 wt.% of PVP polymer at 19 kV and distance of 14 cm exhibit beadless and uniform cylindrical fibers. To obtain anatase nanorod, the nanofibers were calcined at different temperatures. Effect of polymer concentration and applied voltage on morphology of electrospun TiO_2 was successfully examined using

FESEM analysis. The calcination temperature of 500 ^{0}C (heating rate 2 ^{0}C/min) resulted in average nanorod diameter in the range from 52 nm to 289 nm and most nanorod having diameter of 93 nm. XRD peaks at 2θ angles of 25.5°, 37.2°, 37.9°, 38.8°, 48.2° and 54° representing the planes of (101), (103), (004), (200) (112) and (211) (JCPDS No.21-1272) with strongest peak being at 2θ angles of 25.5° which proved that the presence of anatase TiO_2 phase. EDX studies also revealed the presence of titanium and oxygen element that confirmed the nanorods obtained were TiO_2. Hence, TiO_2 nanorods was successfully obtained from combining the sol-gel synthesis and electrospinning process, followed with sintering and grinding process and mixed with TiO_2 nanoparticles to form composite photoanode for DSSC application.

In this study, Four DSSC systems were successfully fabricated. For the first DSSC systems, 5 wt.% of anthocyanin dyes (A3) exhibited the maximum efficiency of (1.054 ± 0.012)% with J_{sc} of (4.487 ± 0.135) cm^{-2}, V_{oc} of (0.418 ± 0.004)V, *FF* of (0.569 ± 0.008), R_s of (0.022 ± 0.002) Ω-cm^2, R_{sh} of (1.620 ± 0.032) Ω-cm^2 and R_2 of (68.95 ± 0.38) Ω. In the second system, the DSSC performance further increased with inclusion of TiO_2 nanorods (NRs) into the mesoporous layer together with TiO_2 nanoparticles (NPs) to form composite photonaode. 10 wt.% NRs and 90 wt.% of NPs (B1) resulted in highest efficiency of (1.351± 0.013)%. with J_{sc} of (4.711 ± 0.109) mA cm^{-2}, V_{oc} of (0.458 ± 0.004) V, *FF* of (0.626 ± 0.007), R_s of (0.021 ± 0.002) Ω-cm^{2,} R_{sh} of (2.228 ± 0.025) Ω-cm^2 and R_2 of (62.40 ± 0.28) Ω.

The performance of NPs-NRs composite based DSSC was further improved by addition of sucrose (third system) and sucrose-DCA (fourth system) additives. For the fourth fabricated DSSC (NP-NRs) composite systems the use of sucrose-DCA successfully improved the performances of DSSCs based *Melastoma malabathricum* anthocyanin. The performance was improved by addition of 6 wt.% sucrose-DCA (D3) compared to sucrose without DCA additive, in which the J_{sc}, V_{oc}, *FF,* efficiency, $R_{s,}$ R_{sh} and R_2 values were (6.360 ± 0.059) mA cm^{-2}, (0.473 ± 0.0.005) V, (0.656 ± 0.006)*,* (1.974 ± 0.014)%*,* (0.013 ± 0.003) Ω-cm^2, (2.918 ± 0.019) Ω-cm^2 and (38.20 ± 0.17) Ω, respectively. The use of sucrose without DCA additive was not suitable for *Melastoma malabathricum* based DSSC since the performance of DSSC only slightly increased compared to NPs-NRs composite photoanode that immersed in non-added additive anthocyanin solution in which the J_{sc}, V_{oc}, *FF,* efficiency, $R_{s,}$ R_{sh} and R_2 values were (5.020 ± 0.093) mA cm^{-2}, (0.458 ± 0.010) V, (0.635 ± 0.005)*,* (1.461 ± 0.024)%*,* (0.019 ± 0.003) Ω-cm^2, (2.518 ± 0.024) Ω-cm^2 and (55.60 ± 0.29) Ω, respectively. Thus, based on result attained, fruit pulp of *Melastoma malabathricum* can be utilize as natural sensitizer for DSSCs application and the addition of 10 wt.% of TiO_2 nanorod onto TiO_2 nanoparticle is improve the DSSCs anthocyanin based. Apart from that, the addition of 6 wt.% of sucrose-DCA (D3) successfully improved the efficiency of DSSCs.

Several recommendations for future work also can be made in order to more improve the DSSCs based on anthocyanin from *Melastoma malabathricum*. Since sucrose-DCA additives showed great enhancement in energy conversion efficiency in this study, other possible additives can be consider to be added in order to improve the DSSCs performance such as fruitose, galactose and other carbohydrate. Besides that, Since the TiO_2 nanorods improve the DSSCs performance, using different preparation technique to obtain 1-D TiO_2 nanostructures such as hydrothermal, electrochemical anodization and template-assisted method also suggested. Different TiO_2 nanostructures such as nanofibers, nanotubes and nanowires also can be suggested to be utilized as photoanode material. This is due to different morphologies of TiO_2 nanostructure will generally affects the DSSC performance.

REFERENCES

Abad-Garcia, B. (2014). Polyphenolic contents in citrus fruit juices: authenticity assessment. *European Food Resources and Technology, 238*(5), 803-818.

Abad-Garcia, B., Berrueta, L. A., Marquez, D. L., Ferrer, I. C., Gallo, B., & Vicente, F. (2007). Optimization and validation of methodology based on solvent extraction and liquid chromatography for the simultaneous determination of several polyphenolic families in fruit juices. *Journal of Chromatography A, 1154*, 87-96.

Abbasi, T., & Abbasi, S. (2010). *Renewable energy sources: their impact on global warming and pollution*. New Delhi: PHI learning Private Limited Publisher.

Abdullah, J. O., Anuar, K., & Maziah, M. (2007). Anthocyanin stability studies in *Tibouchina semidecandra* L. *Food Chemistry, 101*(4), 1640-1646.

Adedokun, O., Awodele, M. K., Awodugba, A. O., & Kalawole, Y. (2018). Natural dye extracts from fruit peels as sensitizer in ZnO based dye-sensitized solar cells. *Earth and Environmental Science, 173*, 2-11.

Agarwala, S., Thummalakuma, L., Cook, C. A., Peh, C., Wong, A. W., & Ke, L. (2011). Co-existence of LiI and KI in filler-free, quasi-solid-state electrolyte for efficient and stable dye-sensitized solar cell. *Journal of Power Sources, 196*(3), 1651-1656.

Ahn, Y. C., Park, S. K., Kim, G. T., Hwang, Y. J., Lee, C. G., & Shin, H. S. (2006). Development of high efficiency nanofilters made of nanofibers. *Current Application in Phyics, 6*, 1030-1035.

Akilavasan, J., Wijeratne, K., Moutinho, H., Al-Jassim, M., Alamoud, A. M., & Rajapakse, R. G. (2013). Hydrothermally synthesized titania nanotubes as apromising electron transport medium in dye sensitized solar cells exhibiting a record efficiency of 7.6% for 1-D based devices. *Journal of Material and Chemistry A, 1*, 5377-5383.

Anderson, O. M., & Jordheim, M. (2006). The anthocyanins. In O. M. Arderson, & K. R. Markham (Eds.), *Flavoinoids Chemistry Biochemistry and Application* (pp. 471-551). London, Taylor & Francis Group, CRC publishers.

Arifin, Z., Soeparman, S., Widhiyanuriyawan, D., & Suyitno, S. (2017). Performance enhancement of dye-sensitized solar cells using a natural sensitizer. *International Journal of Photoenergy*, *5*, 120-128.

Asogoe, K., Suzuki, Y., Ngamsinlapasathian, S., & Yoshikawa, S. (2007). TiO_2-anatase nanowire dispersed composite electrode for dye-sensitized solar cells. *Journal of Physics, 61*, 1112-1116.

Asumadu-Sarkodie, S., & Owusu, S. (2015). Flood risk management in Ghana: a case study in Accra. *Advance in Applied Science Research, 6*, 196-201.

Bandara, T. M. W. J., Aziz, M. F., Fernando, H. D. N. S., Careem, M. A., Arof, A. K., & Mellander, B. E. (2015). Efficiency enhancement in dye-sensitized solar cells with a novel PAN-based gel polymer electrolyte with ternary iodides. *Journal of Solid State Electrochemistry, 19*, 2353-2359.

Barnes, J. S., Nguyen, H. P., Shen, S., & Schug, K. A. (2009). General method for extraction of blueberry anthocyanins and identification using high performance liquid chromatography-electrospray ionization-ion trap-time of flight-mass spectrometry. *Journal of Chromathography A, 1216*, 4728-4735.

Baxter, J. B., Walker, A. M., Ommering, K. V., & Aydi, E. S. (2006). Synthesis and characterization of ZnO nanowires and their integration into dye-sensitized solar cells. *Nanotechnology, 17*, 304-312.

Birse, M. J. (2007). *The Colour of Red Wine*. (Doctoral dissertation). School of Agriculture, Food and Wine, University of Adelaide, Australia.

Borges, G. S., Viera, F. K., Copetti, L. V., Gonzaga, L. V., & Fett, R. (2011). Optimization of the extraction of flavanols and anthocyanins from the fruit pulp of *Euterpe edulis* using the response surface methodology. *Food Research International, 44*(3), 708-715.

Bridgers, E. N., Cinn, M. S., & Truong, V. D. (2010). Extraction of anthocyanins from industrial purple-fleshed sweetpotatoes and enzymatic hydrolysis of residues for fermentable sugars. *International Crops Product, 12,* 613-620.

Bucior, I., Scheuring, S., Engel, A., & Burger, M. M. (2004). Carbohydrate-carbohydrate interaction provides adhesion force and specificity for cellular recognition. *Journal of Celular Biology, 165*, 529-537.

Bueno, J. M., Sáez-Plaza, P., Ramos-Escudero, F., Jiménez, A., Fett, R., & Asuero, A. (2012). Analysis and antioxidant capacity of anthocyanin pigments. Part ii: Chemical structure, color, and intake of anthocyanins. *Critical Reviews in Analytical Chemistry, 42*(2), 126-151.

Cacace, J. E., & Mazza, G. (2002). Extraction of anthocyanins and other phenolics from black currants with sulfured water. *Journal of Agriculture and Food Chemistry, 50*, 5939-5946.

Calogero, G., & Marco, G. D. (2008). Red Sicilian orange and purple eggplant fruits as natural sensitizers for dye-sensitized solar cells. *Solar Energy Materials and Solar Cells, 92*(11), 1341-1346.

Casteneda-Ovando, A., Pacheco-Hermandez, M. L., PaezHernandez, M. E., Rodriguez, J. A., & Galan-Vidal, C. (2009). Chemical studies of anthocyanins: A review. *Food Chemistry, 113*, 859-871.

Charles, C., Sunoa, S., & Janusz, N. (2005). *Materials for energy conversion devices*. London: CRC Publisher .

Chauhan, A., & Singh, B. (2011). X-Ray powder diffraction studies to determine the morphological transformations in *Hibiscus sabdariffa* graft copolymers. *International Journal of Polymer Analytical Characteristic, 16*, 319-328.

Chen, H. Y., Zhang, T. L., Fan, J., Kuang, D. B., & Su, C. Y. (2013). Electrospun hierarchical TiO_2 nanorods with high porosity for efficient dye-sensitized solar cells. *Application and Material Interfaces, 5*(18), 9205-9211.

Chien, Y. C., & Hsu, D. B. (2014). Performance enhancement of dye-sensitized solar cells based on anthocyanin by carbohydrates. *Solar Energy, 108*, 403-411.

Chew, S. Y., Wen, Y., Dzenis, Y., & Leong, K. W. (2006). The role of electrospinning in the emerging field of nanomedicine. *Current Pharmaceutical Design, 12*(36), 4751-4756.

Chrissafis, K., Paraskevopoulas, K., Papageorgiou, G. Z., & Bikialaris, D. (2008). Thermal and dynamic mechanical behavior of bionanocomposites: Fumed silica nanoparticles dispersed in poly(vinyl pyrrolidone), chitosan, and poly(vinyl alcohol). *Journal of Applied Polymer Science, 110*(3), 101-109.

Cisse, M., Bohuon, P., Sambe, F., Kane, C., Sakho, M., & Dornier, M. (2012). Aqueous extraction of anthocyanins from *Hibiscus sabdariffa*: Experimental kinetics and modeling. *Journal of Food Engineering, 109*, 16-21.

Cozzoli, P. D., Kornoski, A., & Weller, H. (2003). Low-temperature synthesis of soluble and processable organic-capped anatase TiO_2 nanorods. *Journal of American Chemistry and Society, 125*, 14539-14548.

Cuce, E., Riffat, S. B., & Young, C. H. (2015). Thermal insulation, power generation, lighting and energy saving perfomance of heat insulation solar glass as a curtain wall application in Taiwan: A comparative experimental study. *Energy Conversion and Management*, *96,* 31-38.

Cushing, B. L., Kolesnichenko, V. L., O‟Connor, C. J. (2004). Recent advances in the liquid-phase syntheses of inorganic nanoparticles. *Chemical Revision*, *104*, 3893-3946.

Dai, J., & Rusell, J. M. (2010). Plant phenolics: Extraction, analysis and their antioxidant and anticancer properties. *Molecules, 15*, 7313-7352.

Deitzel, J. M., Kleinmeyer, D., Harris, N. C., & Tan, B. (2001). The effect of processing variables on the morphology of electrospun nanofibers and textiles. *Polymer, 42*, 261-272.

Delgado-Vargas, F., Jimenez-Aparicio, A., & Paredes-Lopez, O. (2000). Natural pigments: carotenoids, anthocyanins, and betalains: characteristics, biosynthesis, processing, and stability. *Critical Reviews in Food Science and Nutrition, 40*, 173-289.

Demir, M. M., Yilgor, I., Yilgor, E., & Erman, B. (2002). Electrospinning of polyurethane fibers. *Polymers, 43*(11), 3303-3309.

Dias, A. L., Rozet, E., Chataigne, G., Oliveira, A. C., & Rabelo, C. A. (2012). A rapid validated UHPLC-PDA method for anthocyanins quantification from *Euterpe oleracea* fruits. *Journal of Chromathography B*, 108-116.

Doshi, J., & Reneker, D. H. (1995). Electrospinning process and applications of electrospun fibers. *Journal of Electrostatics, 16*(3), 1698-1703.

Duan, W., Jin, S., Zhoua, G., & Sun, P. (2015). Microwave-assisted extraction of anthocyanin from Chinese bayberry. *Food Science and Technology, 35*(3), 524-530.

Dutta, B. K. (2007). *Principles of Mass Transferand Separation Processes*. Prentice-Hall of India, New Delhi, India.

Dzenis, Y. (2004). Spinning continuous fibers for nanotechnology. *Science, 304*, 1917-1919.

Edenhofer, O., Pich-Madruga, R., Sokona, Y., Seyboth, K., & Matschoss, P. (2011). Renewable energy sources and climate change mitigation. Cambridge University Press.

Ehret, A., Stuhl, L., & Spitler, M. T. (2001). Spectral sensitization of TiO_2 nanocrystalline electrodes with aggregated cyanine dyes. *Journal of Physical Chemistry, 105*, 9960-9965.

Fernando, R., & Senadeera, G. R. (2008). Natural anthocyanins as photosensitizers for dye-sensitized solar devices. *Current Science, 95*, 663-666.

Florio, J. J., & Miller, D. J. (2004). *Handbook of Coatings Additives.* New York,USA: Marcel Dekker Publisher.

Fong, H., Chun, I., & Reneker, D. H. (1999). Beaded nanofibers formed during electrospinning. *Polymer, 40*(16), 4585-4592.

Furukawa, S., Hiroshi, L., Tomohisa, I., Koudai, K., & Shoji, Y. (2009). Characteristics of dye-sensitized solar cells using natural dye. *Thin Solid Films, 518*, 526-529.

Garcia-Viguera, C., Zafrila, P., & Tomas-Barberan, F. A. (1998). The use of acetone as an extraction solvent for anthocyanins from strawberry fruit. *Phytochemistry Analysis, 9*, 274-277.

Geng, X., Kwon, O.-H., & Jang, J. (2005). Electrospinning of chitosan dissolved in concentrated acetic acid solution. *Biomaterials, 26*(27), 5427-5432.

Gong, J., Sumathy, K., Qiao, Q., & Zhou, Z. (2017). Review on dye-sensitized solar cells (DSSCs): Advanced techniques and research trends. *Renewable and Sustainable Energy Reviews, 68*, 234-246.

Gratzel, M. (2003). Dye-sensitized solar cells. *Journal of Photochemistry and Photobiology C: Photochemistry Reviews, 4*, 145-153.

Gratzel, M. (2005). Solar energy conversion by dye-sensitized photovoltaic cells. *Inorganic Chemistry, 44*, 6841-6851.

Guisti, M. M., & Wrostald, R. E. (2003). Acylated anthocyanins from edible sources and their applications in food systems. *Biochemical Engineering Journal, 14*, 217-225.

Hafez, H., Wu, J., Lan, Z., Li, Q., Xie, G., & Lin, J. (2010). Enhancing the photoelectrical performance of dye sensitized solar cells using $TiO_2:Eu^{3+}$ nanorods. *Nanotechnology, 21*, 459-501.

Haghi, A. K., & Akbari, M. (2007). Trends in electrospinning of natural nanofibers. *Physica Status Solidi (A) Applications and Materials, 204*(6), 1830-1834.

Haider, A., Haider , S., & Kang, I. K. (2018). A comprehensive review summarizing the effect of electrospinning parameters and potential applications of nanofibers in biomedical and biotechnology. *Arabian Journal of Chemistry, 11*, 1165-1188.

Hamadanian, M., Safaei-Ghomi, J., Hosseinpour, M., Masoomi, R., & Jabbari, V. (2014). Uses of new natural dye photosensitizers in fabrication of high potential dye-sensitized solar cells (DSSCs). *Materials Science in Semiconductor Processing, 27*, 733-739.

Hamman, T. W., Jensen, R. A., Martinson, A. F., Ryswyk, H. V., & Hupp, J. T. (2007). Advancing beyond current generation dye-sensitized solar cells. *Energy & Environmental Science, 1*(1), 66-78.

Hao, S., Wu, J., Huang, Y., & Lin, J. (2006). Natural dyes as photosensitizers for dye-sensitized solar cell. *Solar Energy, 80*(2), 209-214.

Haugan, J. A., Aakermann, T., & Liaaen-Jensen, S. (1992). Isolation of fucoxanthin and peridinin. *Methods in Enzymology, 213*, 231-245.

Hegedus, S., & Luque, A. (2011). *Handbook of Photovoltaic Science and Engineering, In Second Edition*. Weinheim,Germany: Wiley-VCH Publisher.

Heo, N., Jun, Y., & Park, J. H. (2013). Dye molecules in electrolytes: new approach for suppression of dye-desorption in dye-sensitized solar cells. *Scientific Reports, 3*, 1712-1734.

Hilliard, S., Baldinozzi, G., Friedrich, D., Kressman, S., Strub, H., Artero, V., & Laberty-Robert, C. (2017). Correction: Mesoporous thin film WO_3 photoanode for photoelectrochemical water splitting: A sol–gel dip coating approach. *Sustainable Energy & Fuels, 1*, 145-153.

Hong, C. K., Jung, Y. H., Kim, J., & Park, K. H. (2014). Electrochemical properties of TiO_2 nanoparticle/nanorod composite photoanode for dye-sensitized solar cells. *Current Applied Physics, 14*(3), 294-299.

Hosenuzzaman, M., Rahim, N. A., Selvaraj, J., Malek, A., & Nahar, A. (2015). Global prospects, progress, policies, and environmental impact of solar photo-voltaic power generation. *Renewable and Sustainable Energy Reviews, 41*, 284-297.

Hoshino, T. (1991). An approximate estimate of self-association constants and the self-stacking conformation of malvin quinonoidal bases studied by 1H NMR. *Phytochemistry, 30*, 2049-2056.

Houbiers, C., Lima, J. C., Macanita, A. L., & Santos, H. (1998). Color stabilization of malvidin 3-glucoside: Self-aggregation of the flavylium cation and copigmentation with the Z-chalcone form. *Journal of Physical Chemistry, 102*, 3578-3588.

Huang, K., Chen, L., Deng, J., & Xiong, J. (2012). Enhanced visible-light photocatalytic performance of nanosized anatase TiO_2 doped with CdS quantum dots for cancer-cell treatment. *Journal of Nanomaterials*, *120,* 1-12.

Huang, L., Arena, J., Manickam, S., Jiang, X., & Willis, B. (2014). Improved mechanical properties and hydrophilicity of electrospun nanofiber membranes for filtration applications by dopamine modification. *Journal of Membrane Science, 460*, 241-249.

Huang, Z. M., Zhang, Y. Z., Kotaki, M., & Ramakrishna, S. (2003). A review on polymer nanofibers by electrospinning and their applications in nanocomposites. *Composite Science and Technolology, 63*, 2223-2253.

Hug, H., Bader, M., Mair, P., & Glatzel, T. (2014). Biophotovoltaics: Natural pigments in dye-sensitized solar cells. *Applied Energy, 115*, 216-225.

Husain, A. A., Hasan, W. Z., & Hamidon, M. N. (2018). A review of transparent solar photovoltaic technologies. *Renewable and Sustainable Energy Reviews*, *94*, 779-791.

Jasim, K. E., Al-Dallal, S., & Hassan, A. M. (2012). Henna (*Lawsonia inermis* L.): Dye-sensitized nanocrystalline titania solar cell. *Journal of Nanotechnology*, *90*, 1-6.

Jinchu, I., Sreekala, C. O., & Sreelatha, K. S. (2014). Dye sensitized solar cell using natural dyes as chromophores: review. *Materials Science Forum, 771*, 39-51.

Ju, Z., & Howard, L. R. (2003). Effects of solvent and temperature on pressurized liquid extraction of anthocyanins and total phenolics from dried red grape skin. *Journal of Agricultural and Food Chemistry, 51*, 5207-5213.

Jun, Z., Hou, H., Schaper, A., Wendorff, J. H., & Greiner, A. (2003). Poly-L-Lactic nanofibers by electrospinning-influence of solution viscosity and electrical conductivity on fiber diameter and fiber morphology. *Polymer, 3*(1), 102-110.

Jung, J. H., Ono, Y., & Shinkai, S. (2000). Sol-gel polycondensation in a cyclohexane-based organogel system in helical silica: creation of both right- and left-handed silica structures by helical organogel fibers. *Chemical European Journal, 6*, 4552-4557.

Jung, Y. H., Park, K. H., Oh, J. S., Kim, D. H., & Hong, C. K. (2013). Effect of TiO_2 rutile nanorods on the photoelectrodes of dye-sensitized solar cells. *Nanoscale Resource Letter, 8*(1), 1-37.

Justus, S. (2010). *Characterization of anthocyanin dyes and investigation of charge transport in TiO_2 dye and sensitized solar cells.* Department of Physics, University of Nairobi, Kenya.

Kang, M., Ahn, K., Lee, J., & Kang, Y. (2008). Dye-sensitized solar cells employing non-volatile electrolytes based on oligomer solvent. *Journal of Photochemistry and Photobiology A*: *Chemistry, 195*, 198-204.

Kaur, G., Kumar, V., Goyal, A., Tanwar, B., & Kaur, J. (2018). Optimization of nutritional beverage developed from radish, sugarcane and herbal extract using response surface methodology. *Nutrition & Food Scienc*e, *78*, 145-154.

Kay, A., & Gratzel, M. (1993). Artificial photosynthesis. 1. Photosensitization of TiO_2 solar cells with chlorophyll derivatives and related natural porphyrins. *Journal of Physical Chemistry, 97*, 6272-6277.

Kaygusuz, K. (2012). Energy for sustainable development: A case of developing countries. Renewable and Sustainable. *Energy Reviews, 16*, 1116-1126.

Ki, C. S., Baek, D. H., Gang, K. D., Lee, K. H., Um, I. C., & Park, Y. H. (2005). Characterization of gelatin nanofiber prepared from gelatin-formic acid solution. *Polymer, 46*, 5094-5102.

Kidoaki, S., & Kwon, I. K. (2005). Mesoscopic spatial designs of nano- and microfiber meshes for tissue-engineering matrix and scaffold based on multilayering and mixing electrospinning techniques. *Biomaterials, 26*, 1-37.

Kim, J., Han, S., Lei, A., Miyano, M., Bloom, J., & Srivastana, V. (2018). Characterizing cellular mechanical phenotypes with mechano-node-pore sensing. *Microsystem Nanoengineering, 4*, 134-139.

Kim, B., Park, H., Lee, S. H., & Sigmud, W. (2005). Poly(acrylic acid) nanofibers by electrospinning. *Materials Letters, 59*(7), 829-832.

Kumar, A., Jose, R., Fujihara, K., Wang, J., & Ramakrishna, S. (2007). Structural and optical properties of electrospun TiO_2 nanofibers. *Chemistry and Material, 19*, 6536-6542.

Kumar, E. N., Jose, R., Archana, P. S., Vijila, C., & Yusoff, M. M. (2012). High performance dye-sensitized solar cells with record open circuit voltage using tin oxide nanoflowers developed by electrospinning. *Energy and Environmental Science, 5*(1), 5401-5407.

Kushwaha, R., Srivastana, P., & Bahadur, L. (2013). Natural pigments from plants used as sensitizers for TiO_2 based dye-sensitized solar cells. *Journal of Energy, 2013,* 1-8.

Lau, C., & Mi, Y. (2002). A study of blending and complexation of poly(acrylic acid)/poly(vinyl pyrrolidone). *Polymer 4, 3*(3), 823-829.

Lee, J. C., Kim, T. G., Lee, W., Han, S. H., & Sun, Y. M. (2009). Growth of CdS nanorod-coated TiO_2 nanowires on conductive glass for photovoltaic applications. *Crystal Growth, 9*, 4519-4523.

Levy, Z., & Zayat, M. (2015). *The Sol-Gel Handbook: Synthesis, Characterization and Applications.* Weinheim,Germany: Wiley-VCH Publisher.

Leydet, Y., Gavara, R., Petrov, V., Diniz, A. M., Parola, A. J., & Lima, J. C. (2012). The effect of self-aggregation on the determination of the kinetic and thermodynamic constants of the network of chemical. *Phytochemistry, 83*, 125-135.

Li, D., & Xia, Y. (2003). Fabrication of titania nanofibers by electrospinning. *Nanotechnology and Letter, 3*, 555-560.

Li, Z., Qiu-Hong, P., Xiangyun, C., & Chang-Qing, D. (2010). Optimization on anthocyanins extraction from wine grape skins using orthogonal test design. *Food Science and Biotechnology, 19*, 1047-1053.

Lim, J., Park, T., & Kwon, Y. S. (2011). Effect of coadsorbent properties on the photovoltaic performance of dye-sensitized solar cells. *Chemical Communication, 47*, 4147-4149.

Liu, H., Zhang, L., & Li, T. (2018). A study of controllable synthesis and formation mechanism on flower-like TiO_2 with spherical structure. *Crystal*, *34*, 457-466.

Lotfi, L., Kalbasi-Ashtari, A., Hamedi, M., & Ghorbani, F. (2015). Effects of enzymatic extraction on anthocyanins yield of saffron tepals (*Crocus sativus*) along with its color properties and structural stability. *Journal of Food Drug Analysis, 23*(2), 210-218.

Ludin, N. A., Mahmoud, A. M. A., Mohamad, A. B., Kadhum, A. A. H., Sopian, K., & Karim, N. S. A. (2014). Review on the development of natural dye photosensitizer for dye-sensitized solar cells. *Renewable and Sustainable Energy Reviews*, *31*, 386-396.

Lund, P. D. (2009). Effects of energy policies on industry expansion in renewable energy. *Renewable Energy*, *34,* 53-64.

Maran, P., Mekala, J., & Manikandan, S. (2013). Modeling and optimization of ultrasound assisted extraction of polysaccharide from *Cucurbita moschata. Carbohydrate Polymers, 92*, 2018-2026.

Mazza, G., & Brouillard, R. (1990). The mechanism of co-pigmentation of anthocyanin in aqueous solutions. *Phytochemistry*, *25*, 1097-1102.

Maciel, L. G., Vieira, M. A., Azevedo, L., Daguer, H., Molognoni, L., & Almeida, M. (2018). *Hibiscus sabdariffa* anthocyanins-rich extract: Chemical stability, in vitro antioxidant and antiproliferative activities. *Food and Chemical Toxicology, 113*, 187-197.

Mazza, G., & Miniati, E. (1993). *Anthocyanins in fruits, vegetables and grains*- Second edition. London, UK: CRC Publisher.

McConell, R. D. (2002). Assessment of the dye sensitized solar cell. *Renewable and Sustainable Energy Reviews, 6*, 273-295.

Megelski, S., Stephen, J. S., Chase, D. B., & Rabolt, J. F. (2002). Micro and nanostructured surface morphology on electrospun polymer fibers. *Macromolecules, 35*(22), 8456-8466.

Michael, J., Laudenslager, I., Raymond, H., Scheffer, I., & Wolfgang, M. (2010). Electrospun materials for energy harvesting, conversion, and storage: A review. *Pure Application Chemistry, 82*(11), 2137-2156.

Mikroyannids, J., Stylianakis, M. M., Roy, M. S., Suresh, P., & Sharma, G. D. (2009). Synthesis, photophysics of two new perylene bisimides and their photovoltaic performances in quasi solid state dye sensitized solar cells. *Journal of Power Sources, 194*(2), 1171-1179.

Mit-Upphatham, C., Nithianakul, M., & Suphapol, P. (2004). Ultrafine electrospun polyamide-6 fibers: Effect of solution conditions on morphology and average fiber diameter. *Macromolecular Chemistry and Physics, 205*(17), 2327-2338.

Naczk, M., & Shahidi, F. (2006). Phenolics in cereals, fruits and vegetables: Occurrence, extraction and analysis. *Journal of Pharmaceutical and Biomedical Analysis, 41*(5), 1523-1542.

Navas, M., Jiminez-Moreno, A. M., Bueno, M. J., Saez-Plaza, P., & Asuero, A. (2012). Analysis and antioxidant capacity of anthocyanin pigments. Part IV: Extraction of anthocyanins. *Critical Reviews in Analytical Chemistry, 42*(4), 313-334.

Nazeeruddin, M. K., Kay, A., Rodicio, I., Humphry-Baker, R., Muller, E., & Liska, P. (1993). Conversion of light to electricity by cis-X2bis (2,2'-bipyridyl-4,4'-dicarboxylate) ruthenium(II) charge-transfer sensitizers (X = Cl-, Br-, I-, CN-, and SCN-) on nanocrystalline titanium dioxide electrodes. *Journal of the American Chemical Society, 115*, 6382-6390.

Nazeeruddin, M. K., Penchy, P., Renouard, T., Zakeeruddin, S. M., Baker, R. H., & Comte, P. (2001). Engineering of efficient panchromatic sensitizers for nanocrystalline TiO_2-based solar cells. *Journal of the American Chemical Society, 123*, 1613-1624.

Norris, D., Shaker, M. M., Ko, F. K., & MacDiarmid, A. G. (2000). Electrostatic fabrication of ultrafine conducting fibers: polyaniline/polyethylene oxide blends. *114*(2), 109-114.

Nuansing, W., Ninmuang, S., Jarernboon, W., Maensiri, S., & Seraphin, S. (2006). Structural characterization and morphology of electrospun TiO_2 nanofibers. *Material Science and Engineering B, 131*, 147-155.

Oancea, S., Stoia, M., & Coman, D. (2012). Effects of extraction conditions on bioactive anthocyanin. *Procedia Engineering, 42*, 489-495.

Ooyama, Y., & Harima, Y. (2012). Photophysical and electrochemical properties and molecular structures of organic dyes for dye-sensitized solar cells. *Chemical and Physical Chemistry, 13*(18), 4032-4080.

O'Regan, B., & Gratzel, M. (1991). A low-cost, high-efficiency solar cell based on dye-sensitized colloidal TiO_2 films. *Nature, 353*, 737-740.

Pan, M., Liu, H., Yao, Z., & Zhong, X. (2015). Enhanced efficiency of dye-sensitized solar cells by trace. *Journal of Nanomaterials*, *120,* 111-123.

Panwar, N., Kaushik, S., & Kothari, S. (2011). Role of renewable energy sources in environmental protection: A review. *Renewable and Sustainable Energy, 15*, 1513-1524.

Park, S. H., Seo, S. Y., Kim, S. H., & Wan, S. H. (2006). Surface roughness and strain effects on ZnO nanorod growth. *Applied Physics Letters, 88*(25), 251-259.

Park, Y. D., Anabuki, K., Kim, S., Park, K.-W., Lee, D. H., & Um, S. H. (2013). Fabrication of stable electrospun TiO_2 nanorods for high-performance dye-sensitized solar cells. *Mollecular Research, 21*(6), 636-640.

Patore, M., & Angelis, F. D. (2010). Aggregation of organic dyes on TiO_2 in dye-sensitized solar cells models: an ab initio investigation. *ACS Journal, 4*, 556-562.

Perera, F. (2018). Pollution from fossil-fuel combustion is the leading environmental threat to global pediatric health and equity: Solutions exist. *International Journal of Environmental Research and Public Health, 15*(16), 2-17.

Peter, L. M. (2007). Characterization and modeling of dye-sensitized solar cells. *Journal of Physical Chemistry C, 111*, 6601-6612.

Polo, A. S., & Iha, N. Y. (2006). Blue sensitizers for solar cells: Natural dyes from *Calafate* and *Jaboticaba*. *Solar Energy and Solar Cells, 90*, 1936-1944.

Pujiarti, H., Arsyad, W. S., Shobih, Muliani, L., & Hidayat, R. (2018). Efficient and stable photovoltaic characteristics of quasi solid state DSSC using polymer gel electrolyte based on ionic liquid in organosiloxane polymer gels. *Journal of Physics: Conference Series, 1011*, 12-20.

Ramakrishna, S., Fujihara, K., Teo, W. E., Yong, T., Ma, Z., & Ramaseshan, R. (2006). Electrospun nanofibers: solving global issues. *Materials Today, 9*(3), 1-13.

Radwan, I. M. (2015). Dye-sensitized solar cells based on natural dye extracted from plant roots. *Skripsi Palestina: Islamic University of Gaza*, Gaza.

Ramakrishna, S., Fujihara, K., Teo, W. E., Lim, T. C., & Ma, Z. (2005). An introduction to electrospinning and nanofibers. *World Scientific Journal, 21,* 1-19.

Ramasamy, S., Mazlan, N. F., Ramli, N. A., Asyiqin, W. N., & Manickam, S. (2016). Bioactivity and stability studies of anthocyanin-containing extracts from

Garcinia mangostana L. and *Etlingera elatior jack*. *Sains Malaysiana, 45*(4), 559-565.

Ravilla, E., Ryan, J. M., & Martin-Otega, G. (1998). Comparison of several procedures used for the extraction of anthocyanins from red grapes. *Journal of Agricultural and Food Chemistry, 46*(11), 12-20.

Razykov, T. M., Ferekides, C. S., Morel, D., Stefanakos, E., Ullal, H. S., & Upadhayaya, H. M. (2011). Solar photovoltaic electricity: current status and future prospect. *Solar Energy, 85*, 1580-1608.

Reneker, D. H., & Yarin, A. L. (2008). Electrospinning jets and polymer nanofibers. *Polymer, 49*(10), 2387-2425.

Rezvani, F., Parvazian, E., & Hosseni, S. A. (2016). Dye-sensitized solar cells based on composite TiO_2 nanoparticle-nanorod single and bi-layer photoelectrodes. *Bulletin of Material Sciences, 39*(6), 1397-1402.

Rho, Y. W., Jeon, H., Kim, S. H., Chung, J. W., Suh, S. J., & Jun, H. B. (2015). Recent progress in dye-sensitized solar cells for improving efficiency: TiO_2 nanotube arrays in active layer. *Journal of Nanomaterials*, 56, 111-119.

Rogelj, J., McCollum, D. L., Reisinger, A., Meinshausen., M., & Riahi, K. (2013). Probabilistic cost estimates for climate. *Nature, 493,* 79-83.

Ruenroengklin, N., Zhong, J., Duan, X., Yang, B., Li, J., & Jiang, Y. (2008). Effects of various temperatures and pH values on the extraction yield of phenolics from Litchi fruit pericarp tissue and the antioxidant activity of the extracted anthocyanins. *International Journal of Molecular Sciences, 9*(7), 1333-1341.

Rus, A. Z. M., Abdullah, N. M., & Abdullah, M. F. L. (2013). Characterization and treatment of titanium dioxide via ultrasonic process with *Melastoma malabathricum* as sustainable sensitizer for photovoltaic solar cell. *Journal of Chemistry, 2013,* 1-10.

Sahin, S., & Samli, R. (2013). Optimization of olive leaf extract obtained by ultrasound-assisted extraction with response surface methodology. *Ultrasonics Sonochemistry, 20*, 595-602.

Sahin, S., Samli, R., Tan, A. S. B., Barba, F. J., Chemat, F., Cravotto, G., & Lorenzo, J. M. (2017). Solvent-free microwave-assisted extraction of polyphenols from olive tree leaves: antioxidant and antimicrobial properties. *Molecules, 7*, 1045-1054.

Saji, V. S., & Pyo, M. (2010). Dye sensitized solar cell of TiO_2 nanoparticle/nanorod composites prepared via low-temperature synthesis in oleic acid. *Thin Solid Films, 518*, 6542-6546.

Salar, R. K., Certik, M., & Brezova, V. (2012). Modulation of phenolic content andantioxidant activity of maize by solid state fermentation with Thamnidium elegans CCF-1456. *Biotechnology and Bioprocess Engineering, 17*(1), 109-116.

Saleem, M., & Somá, A. (2015). Design of experiments based factorial design and response surface methodology for MEMS optimization. *Microsystem Technolology, 21*, 263-276.

Sarkar, A., Schukarev, A., Leino, A. R., Kordas, K., Mikkola, J. P., & Petrov, P. O. (2012). Photocatalytic activity of TiO_2 nanoparticles: effect of thermal annealing under various gaseous atmospheres. *Nanotechnology, 23*(47), 475-711.

Senecal, K. J., Ziegler, D. P., He, J., Mosurkal, R., Schreude-Gibson, H., & Samuelson, L. A. (2002). Photoelectric response from nanofibrous membranes. *Materials Research Society Symposium Proceedings, 708*, 285-289.

Senthil, T. S., Muthukumarasamy, N., & Kang, M. (2013). Applications of highly ordered paddle wheel like structured ZnO nanorods in dye sensitized solar cells. *Materials Letters, 102,* 26-29.

Shafiʿi, S., Ahmad, N., Abidin, M. Z., Hani, M. N., & Ismail, N. (2013). Optimization of hydrocolloids and maltodextrin addition on roselle-based fruit leather using two-level full factorial design. *International Journal of Bioscience and Biochemestry Bioinformation, 3*, 387-391.

Sharif, A., Saim, N., Jasmani, H., & Ahmad, W. (2010). Effects of solvent and temperature on the extraction of colorant from onion (*Allium cepa*) skin using pressurized liquid extraction. *Asian Journal of Applied Sciences, 3*, 262-268.

Sharma, G., Kurchania, R., Ball, R. J., Roy, M. S., & Mikroyannidis, J. A. (2012). Effect of deoxycholic acid on the performance of liquid electrolyte dye-sensitized solar cells using a perylene monoimide derivative. *International Journal of Photoenergy*, *2012,* 1-7.

Sharma, S., Jain, K. K., & Saharma, A. (2015). Solar cells: In research and applications: A review. *Materials Sciences and Applications, 6*, 1145-1155.

Shelke, R. S., Thombre, S. B., & Patrikar, S. R. (2013). Status and perspectives of dyes used in dye sensitized solar cells. *International Journal of Renewable Energy Resources, 3*, 54-61.

Shi, J., Yu, J., Pohorly, J., Young, J. C., Bryan, M., & Wu, Y. (2003). Optimization of the extraction of polyphenols from grape seed meal by aqueous ethanol solution. *Journal of Food Agricultural and Environment, 1*(2), 42-47.

Silva, E. M., Rogez, H., & Larondelle, Y. (2007). Optimization of extraction of phenolics from *Inga edulis* leaves using response surface methodology. *Separation and Technology, 55*, 381-387.

Song, P., & Vasyliunas, V. (2005). Solar wind-magnetosphere-ionosphere coupling: Neutral atmosphere effects on signal propagation. *Journal of Geophysical Research*, *110*, 1-13.

Spillmann, D., & Burger, M. M. (1996). Carbohydrate-carbohydrate interactions in adhesion. *Journal of Cellular Biochemistry, 68*, 562-568.

Subbiah, T., Bha, G. S., Tock, R. W., Parameswaran, S., & Ramkuma, S. S. (2005). Electrospinning of nanofibers. *Journal of Applied Polymer Science, 96*, 557-569.

Sui, R., & Charpentier, P. (2011). Synthesis of metal oxide nanostructure by direct sol-gel chemistry in supercritical fluids. *Chemical Revison, 112*, 3057-3082.

Sukigara, S., Ghandi, M., Ayutsede, J., Mikclus, M., & Ko, F. (2003). Regeneration of *Bombyx mori* silk by electrospinning, part 1: processing parameters and geometric properties. *Polymer, 44*(19), 5721-5727.

Susanti, D., Nafi, M., Purwaningsih, H., Fajarin, R., & Kusuma, G. E. (2014). The preparation of dye sensitized solar cell (DSSC) from TiO_2 and *Tamarillo* extract. *Procedia Chemistry, 9,* 3-10.

Tachan, Z., Ruhle, S., & Zaban, A. (2010). Dye-sensitized solar tubes: A new solar cell design for efficient current collection and improved cell sealing. *Solar Energy Materials and Solar Cells, 94*, 317-322.

Tamaroh, S., Raharjo, S., Mdianti, A., & Anggrahini, S. (2018). Total phenolic content and antioxidant activity of anthocyanin extract from purple yam (*Dioscorea alata* L.) flour using different solvents. *Pakistan Journal of Nutrition, 17*, 260-267.

Tang, Q., Zhang, H., Meng, Y., He, B., & Yu, L. (2015). Dissolution engineering of platinum alloy counter electrodes in dye-sensitized solar cells. *Chemical International, 23*, 11448-11452.

Thirunavukkarasu, A., & Nithya , R. (2011). Response surface optimization of critical extraction parameters for anthocyanin from *Solanum melongena*. *Journal of Bioprocess Biotechnology*, *1*, 99-103.

Tungprapa, S., Puangparn, T., Weerasombut, M., Jangchud, I., & Semongkhol, S., Meechaisue, C. (2007). Electrospun cellulose acetate fibers: effect of solvent system on morphology and fiber diameter. *Cellulose, 14*(6), 563-575.

Veleirinho, B., Rei, M. F., & Silva, J. L. (2008). Solvent and concentration effects on the properties of electrospun poly(ethylene terephthalate) nanofiber mats. *Journal of Polymer Science Part B: Polymer Physics, 46*(5), 460-471.

Wallace, T. C., & Giusti, M. (2013). Anthocyanins in health and disease. *Boca Raton, Florida, USA: Taylor & Francis Group.*

Wang, P., Dai, Q., Zakeeruddin, S. M., Forsyth, M., MacFarlane, D. R., & Gratzel, M. (2004). Ambient temperature plastic crystal electrolyte for efficient, all-solid-state dye sensitized solar cell. *Journal of American Chemical Society, 126*(42), 13590-13591.

Wang, T., Jonsdottir, R., & Olafsdottir, G. (2009). Total phenolic compounds, radical scavenging and metal chelation of extracts from *Icelandic* seaweeds. *Food Chemistry, 116*(1), 240-248.

Wang, W., Du, J., Ren, Z., Peng, W., Pan, Z., & Zhong, X. (2006). Improving loading amount and performance of quantum dot-sensitized solar cells through metal salt solutions treatment on photoanode. *ACS Application Material Interfaces, 8*(45), 31006-31015.

Wang, Z. S., Cui, Y., Dan-oh, Y., Shinpo, A., & Hara, K. (2007). Thiophene-functionalized coumarin dye for efficient dye-sensitized electron lifetime improved by coadsorption of deoxycholic. *Journal of Physical Chemistry, 111*, 7224-7230.

Watthanaarun, J., Pavarajarn, V., & Supaphol, P. (2005). Titanium (IV) oxide nanofibers by combined sol–gel and electrospinning techniques preliminary report on effects of preparation conditions and secondary metal dopant. *Science and Technology of Advanced Materials, 6*, 240-245.

Wenger, S., Bouit, Q., Chen, J., Teuscher, J., & Censo, D. D. (2010). Efficient electron transfer and sensitizer regeneration in stable π-extended tetrathiafulvalene-sensitized solar cells. *Journal of America Chemistry Society, 132*, 5164-5169.

Wijingaard, H. H., & Brunton, N. (2010). The optimisation of solid-liquid extraction of antioxidants from apple pomace by response surface methodology. *Journal of Food Engineering, 96*(1), 134-140.

Wong, W. (2008). *Melastoma malabathricum: Too Beautiful to Be Called a Weed.* Green Culture, Singapore.

Wrolstad, R. E., Durst R. W., & Lee, J. (2005). Tracking color and pigment changes in anthocyanin products. *Trends in Food Science and Technology, 16*, 423-428.

Wurfel, U., Peter, M., & Hinsch, A. (2008). Detailed experimental and theoretical investigation of the electron transport in a dye solar cell by means of a three-electrode configuration. *Journal of Physical Chemistry C, 112*, 1711-1720.

Xia, J., & Yanagida, S. (2011). Strategy to improve the performance of dye sensitized solar cells: interface engineering principle. *Solar Energy*, *85*, 3143-3159.

Yang, R. Y., Chen, H. Y., & Lai, F. D. (2012). Performance degradation of dye-sensitized solar cells induced by electrolytes. *Advances in Materials Science and Engineering, 23*, 1-4.

Yang, Z., Zheng, Y., & Cao, S. (2008). Effect of high oxygen atmosphere storage on quality, antioxidant enzymes, and DPPH-radical scavenging activity of Chinese bayberry fruit. *Journal of Agricultural and Food Chemistry, 57*, 176-181.

Yılmaz, F., Karaaslan, M., & Vardin, H. (2015). Optimization of extraction parameters on the isolation of phenolic compounds from sour cherry (*Prunus cerasus* L.) pomace. *Journal of Food Science and Technology, 52*, 2851-2856.

Yu, Z., Vlachopoulos, N., Gorlov, M., & Kloo, L. (2011). Liquid electrolytes for dye-sensitized solar cells. *Dalta Transition Journal, 40*, 10289-10303.

Yuan, J., Geng, J., Xing, Z., Shen, J., Kang, I. K., & Byun, H. (2010). Electrospinning of antibacterial poly(vinylidene fluoride) nanofibers containing silver nanoparticles. *Journal of Applied Polymer Sciences, 116*(2), 668-672.

Yuan, X. Y., Zhang, Y. Y., Dong, C. H., & Sheng, J. (2004). Morphology of ultrafine polysulfone fibers prepared by electrospinning. *Polymer International, 53*(11), 1704-1710.

Yusuf, S. N. F., Azzahari, A. D., Yahya, R., Majid, S. R., Careem, M. A., & Arof, A. K. (2016). From crab shell to solar cell: A gel polymer electrolyte based on N-127 phthaloylchitosan and its application in dye-sensitized solar cells. *RSC Advances, 6*, 27714-27724.

Zhou, H., Wu, L., Yurong, G., & Tigli, M. (2011). Dye-sensitized solar cells using 20 natural dyes as sensitizers. *Journal of Photochemistry and Photobiology A: Chemistry, 219*, 188-194.

Zhou, Z., Li, J., Yuan, X., Zhang, Y., & Sheng, J. (2005). Preparation and properties of electrospun poly(vinylidene fluoride) membranes. *Journal of Applied Polymer Science, 97*(2), 466-474.

Ziegler, G. R., Creek, J. A., & Runt, J. (2005). Spherulitic crystallization in starch as a model for starch granule initiation. *Biomacromolecules, 6*(3), 1547-1554.

Zong, X., Kim, K., Fang, D., Ran, S., Hsiao, B. S., & Chu, B. (2002). Structure and process relationship of electrospun bioabsorbable nanofiber membranes. *Polymer, 43*(16), 4403-4412.

Zukalova, M., Zukal, A., Kavan, L., Nazeeruddin, M. K., Liska, P., & Graetzel, M. (2005). Organized mesoporous TiO_2 films exhibiting greatly enhanced performance in dye-sensitized solar cells. *Nano Letters, 5*(9), 1789-1792.

LIST OF PUBLICATIONS AND PAPERS PRESENTED

PUBLICATIONS

1. Arof, A. K., Mat Nor, N. A., Noor, I. M., & **Aziz, N.** (2017). Utilization of saffron (*Crocus sativus* L.) as sensitizer in dye-sensitized solar cells (DSSCs). *Optical and Quantum Electronics*, *49*, 1-8.
2. **Aziz, N.,** & Arof, A. K. (2016). A model to investigate extraction parameters for anthocyanin from *Melastoma malabathricum*. *Optical and Quantum Electronics*, *48*(205), 205-211.
3. **Aziz, N.,** Mat Nor, N. A., Mohd-Adnan, A. F., Taha, R. M., & Arof, A. K. (2016). Colour properties of poly(vinyl alcohol)–anthocyanin blends. *Optical and Quantum Electronics, 48* (451), 2-8.

PAPERS PRESENTED

1. **Aziz, N.,** Mat Nor, N. A., & Arof, A. K. (2016). *Optimization of natural dye from M. malabathricum by response surface method as photo-sensitizer in dye sensitized solar cells*. Paper presented at 2nd International Conference on Solar Energy Photovoltaic (ICSEP-16), 17-19th December 2016, Bhubaneswar, India.
2. **Aziz, N.,** Mat Nor, N. A., & Arof, A. K. (2014). *Studies on natural dye from M. malabathricum as photo-sensitizer in dye sensitized solar cells*. Paper presented at National Workshop on Functional Materials (NWFM 2017), 17-18th January 2017, Kuala Lumpur, Malaysia.
3. **Aziz, N.,** & Arof, A. K. (2014). *Spectroscopic analysis of co-pigmentation effects on fruit pulps of melastoma malabathricum*. Paper presented at International Conference on Science and Engineering of Materials (ICSEM-2014), 6-8th January 2014, Uttar Pradesh, India.

BOOK CHAPTER

1. Arof, A. K., Aziz, N., Mat Nor, N. A., Rahim, A. S., & Kufian, M. Z. (2017). Imaging of electrospun nanoparticle electrode materials. In A. Méndez-Vilas, (Eds.), Microscopy and imaging science: practical approaches to applied research and education (pp. 438-449). Spain: Formatex Research Center. ISBN-13: 978-84-942134-9-6.